DISS. ETH NO. 27485

Performance of detector modules for the CMS Pixel Phase 1 upgrade and search for $t\bar{t}H, H \to b\bar{b}$ events in the boosted regime

A thesis submitted to attain the degree of

DOCTOR OF SCIENCES OF ETH ZURICH
(Dr. sc. ETH Zurich)

presented by

Maren Tabea Meinhard
MSc. Physics, ETH Zurich
Born on 21.09.1992
Citizen of Germany

accepted on the recommendation of

Prof. Dr. Rainer Steffen Wallny, examiner
Prof. Dr. Günther Dissertori, co-examiner

2021

Abstract

This thesis presents two contributions to the research programme in particle physics of the Compact Muon Solenoid (CMS) experiment at the Large Hadron Collider (LHC).

The increasingly stringent operating conditions of the LHC accelerator led to the replacement of the innermost component of the CMS experiment, its pixel detector, with an upgraded version in early 2017. This improved its performance and allowed operation up to instantaneous luminosities of $2 \times 10^{34}\,\mathrm{cm}^{-2}\,\mathrm{s}^{-1}$. The functionality of the readout chip used for the innermost layer of the detector has been investigated in this thesis, in particular its tolerance towards radiation damage. For this purpose, the characteristics of the readout chip have been studied at increasing irradiation doses. This proved that no property of the chips is problematically altered by irradiation, and provides essential calibration parameters to successfully operate the chips in the experiment throughout their expected lifetime. Moreover, the quality of the modules built from these readout chips for the final detector has been monitored during the course of this work. This allowed to identify and reject modules with defects such as clusters of irresponsive pixels or faulty connections between the sensor and the readout electronics.

When measuring the properties of the Higgs boson with the highest possible accuracy, the $\mathrm{t\bar{t}H}$, $\mathrm{H}\rightarrow\mathrm{b\bar{b}}$ process is of particular interest, as it allows a direct measurement of the Yukawa coupling between the top quark and the Higgs boson. This work focuses on a search for such events where either of these particles are produced at large transverse momentum (p_T), which is a region of phase space for which many theories predict deviations from Standard Model expectations. Two different discriminators are studied in this context. The matrix element probability is a powerful variable to differentiate between the signal and the main background, $\mathrm{t\bar{t}}+\mathrm{b\bar{b}}$. During this thesis a numerical instability during its computation was discovered, however a promising method to use this discriminant in a search for events with objects produced at large p_T is presented nonetheless. Another approach has been developed, that uses a set of kinematics and b tagging related variables, to measure a best-fit signal strength for the $\mathrm{t\bar{t}H}$, $\mathrm{H}\rightarrow\mathrm{b\bar{b}}$ process of $0.47^{+3.34}_{-3.41}$. This result is largely driven by events with objects produced at lower p_T. Events with a Higgs bosons or a top quark with a larger p_T are expected to improve the analysis sensitivity when using state of the art identification methods for these objects.

Zusammenfassung

Diese Arbeit stellt zwei Beiträge zum Forschungsprogramm des Compact Muon Solenoid (CMS) Experiments am Large Hadron Collider (LHC) in der Teilchenphysik dar.

Die erhöhte Strahlungsintensität des LHC Beschleunigers hat Anfang 2017 zu dem Austausch der innersten Komponente des CMS Experiments, dem Pixeldetektor, durch einen neu entwickelten Detektor geführt. Dadurch verbesserte sich die Auflösung der Rekonstruktion der Interaktion der Teilchen mit dem Detektor und erlaubte den Betrieb bis zu einer instantanen Luminosität von $2 \times 10^{34}\,\mathrm{cm}^{-2}\,\mathrm{s}^{-1}$. Die Eigenschaften und insbesondere die Strahlenhärte des Auslesechips, welcher in der innersten Detektorlage verwendet wird, wurden in dieser Arbeit untersucht. Hierzu wurde eine Bestrahlungsstudie bei unterschiedlichen Gesamtionisierungsdosen durchgeführt. Diese Untersuchungen ergaben, dass keine der grundlegenden Charakteristika der Chips problematisch durch die Bestrahlung verändert werden. Zusätzlich konnten essenzielle Kalibrierungsparameter vermessen werden, mit welchen die Eigenschaften der Chips während des Betriebs angepasst werden können. Weiters wurde eine Qualitätsprüfung von Detektormodulen, die mit diesen Auslesechips ausgestatteten wurden, durchgeführt. Dadurch konnten fehlerhafte Module, zum Beispiel aufgrund von Anhäufungen von defekten Pixeln oder fehlenden Verbindungen zwischen Sensor und Ausleseelektronik, aussortiert werden.

Bei der genauen Bestimmung der Eigenschaften des Higgs Bosons spielt der $\mathrm{t\bar{t}H}$, $\mathrm{H}\rightarrow\mathrm{b\bar{b}}$ Prozess eine entscheidende Rolle, da er eine direkte Messung der Yukawa-Kopplung zwischen dem top Quark und dem Higgs Boson ermöglicht. Der Schwerpunkt dieser Arbeit liegt auf Ereignissen, bei denen eines dieser Teilchen mit großem transversalen Impuls (p_T) produziert wird, da etliche Theorien in diesem Phasenraum Abweichungen vom Standardmodell vorhersagen. Zwei verschiedene Diskriminanten wurden untersucht. Die Matrixelementmethode ermöglicht, zwischen dem Signal und dem wichtigsten Hintergrundprozess $\mathrm{t\bar{t}}+\mathrm{b\bar{b}}$ zu unterscheiden. Es wurde eine Methode entwickt, um diese Diskriminante in einer Suche nach Ereignissen mit Objekten, welche mit hohem p_T produziert werden, einzusetzen. Im Rahmen dieser Dissertation wurde eine numerische Instabilität in der Berechnung des Matrixelements entdeckt, weshalb in einem anderen Ansatz kinematische Variablen und Observablen zur Beobachtung von b Quarks verwendet werden. Hiermit wurde eine Signalstärke für den $\mathrm{t\bar{t}H}$, $\mathrm{H}\rightarrow\mathrm{b\bar{b}}$ Prozess von $0.47^{+3.34}_{-3.41}$ gemessen. Dieses Ergebnis beruht hauptsächlich auf Ereignissen mit Objekten, welche bei niedrigerem transversalen Impuls entstehen. Mit verbesserten Methoden um Objekte mit höherem transversalem Impuls zu rekonstruieren, wird erwartet, dass diese Ereignisse auch stärker zur Sensitivität der Analyse beitragen werden.

Contents

Chapter 1

Introduction

A scientific search, almost spanning a century, has found its — temporary — conclusion with the discovery of the Higgs boson in 2012. The Higgs boson was the last missing piece of the Standard Model (SM) of particle physics and is famously responsible for providing masses to elementary particles. However, while the SM is complete, our understanding of Nature at the most fundamental level is not.

Experimental evidence clearly points to the existence of new physics which is not described by the SM. Astrophysical observations predict the existence of a so far unknown form of matter, and a new manifestation of energy is needed to explain the acceleration patterns of distant galaxies. Looking back far into the past it is not known how the Big Bang, where according to today's knowledge matter and antimatter should have been produced in equal amounts, led to the current matter dominated universe. Particle physicists specifically puzzle over anomalies observed in the flavour sector and seemingly fine-tuned parameters of the SM, and ambitious theorists dream of a grand theory unifying all forces of Nature.

Given these unanswered questions and the lack of direct observations of new manifestations of physics beyond the SM in the past years, focus has shifted towards searching for discrepancies with SM predictions. In this context, precise investigations of the properties of the Higgs boson are a promising way forward. Specifically the Higgs boson coupling to the top quark, which is the heaviest known elementary particle and implicated in many models of physics beyond the SM, is of great interest. With the associated production of a Higgs boson with a top quark pair this property can be measured directly, which provides a large advantage over other production channels where top quarks are only present as virtual particles, such that contributions from so far unknown physics processes cannot be excluded. However, this production mechanism is challenging to reconstruct because of its complex final

state, and the presence of backgrounds with a cross section several orders of magnitude larger than that of the sought signal process.

Dedicated analysis techniques are necessary to reconstruct such events. However, their performance is bounded by the quality of the recorded data. In particular, correctly identifying traces of bottom quarks in the detector is of utmost importance when reconstructing Higgs bosons produced in association with a top quark pair, as top quarks decay almost exclusively to a bottom quark and a W boson, and the Higgs boson branching fraction to two bottom quarks is almost 60%. The predominant characteristic of jets originating from bottom quarks is the presence of a secondary vertex several millimetres away from the main interaction point. To reconstruct these vertices, a pixel detector with high granularity and excellent temporal resolution is required.

This is why a newly designed pixel detector has been installed in the CMS experiment in January 2017. The development of the so-called Phase 1 upgrade necessitated almost a decade of work, including its design, its production, its quality assessment and the preparations for installation. Amongst other tests, the radiation tolerance of all components has been verified to prevent degradation during operation of the detector. Additionally, each of the elements that are installed in the final version of the detector has been thoroughly tested to exclude faulty pieces. This applies especially to the modules which hold the sensors with which incoming particles interact.

This thesis is organised as follows. Chapters 2 and 3 give an introduction to the SM and to Higgs boson physics, and describe the CMS experiment. Part I details the characteristics of the CMS pixel detector, and in particular of its Phase 1 upgrade. It also summarises the effects of radiation in electronic circuitries, and presents a study of the radiation tolerance of the readout chip that is installed in the innermost layer of the detector. Finally, results of the quality assessment of modules built from these readout chips for installation in the detector are shown. In Part II of the thesis, an analysis of the associated production of a Higgs boson with a top quark pair, in which the Higgs boson decays to two bottom quarks, is presented using the dataset collected by the CMS experiment in 2017. Special focus is placed on events with a Higgs boson or a top quark produced at large transverse momentum, as this region is particularly sensitive to beyond the SM physics effects.

Chapter 2

The Standard Model of particle physics

For thousands of years, mankind has been thriving to understand Nature. From attempts to categorise all known matter into elements and the first ideas of elementary particles emerging in ancient Greece and India [1, 2], it wasn't until the nineteenth century that the atomic theory was confirmed by John Dalton who correlated chemical reaction rates to the atomic content of the reactor materials [3]. Further studies on the inner structure of atoms lead to the discovery of electrons by Joseph Thomson [4] and of the nucleus by Ernest Rutherford while studying the scattering of α particles on a gold foil [5]. In the twentieth century, the inner structure of the nucleus was resolved, showing that it consists of protons and neutrons [6], which in turn are made of quarks [7, 8]. As of today, electrons and quarks are believed to be elementary particles.

All known fundamental particles as well as their interactions are described in the Standard Model (SM). This quantum field theory provides the theoretical background for current research in particle physics.

Section 2.1 summarises the essential concepts of the SM. In particular, the particles which are described by the theory as well as their interactions are presented. The Higgs mechanism, which occurs via spontaneous symmetry breaking and which provides mass to the particles is illustrated in Section 2.2. While a vast majority of measurements have confirmed predictions of the SM in the past years, there exists a number of open questions which cannot be solved by the current theoretical framework. Examples of such questions are listed in Section 2.3. This Section also briefly summarises theoretical models which could potentially solve these questions.

2.1 The Standard Model Lagrangian

The Standard Model (SM) is a quantum field theory (QFT) which describes matter particles, and three of the four existing fundamental forces: the strong, the weak and the electromagnetic force [9]. The fourth fundamental force is gravity, which is not included in the SM. The SM can be described by a Lagrangian density $\mathcal{L}$ depending on the fields $\Psi(x)$ and their derivatives. The Lagrangian density must obey the principle of least action $\delta S = 0$ where the action S is defined as the integral over space-time of the Lagrangian density:

$$S = \int d^4x \mathcal{L} \tag{2.1}$$

Furthermore, the Lagrangian density must remain invariant under local field transformations which can be described by the gauge group

$$\mathcal{G}_{SM} = SU(3)_C \otimes SU(2)_L \otimes U(1)_Y \tag{2.2}$$

where $SU(3)_C$ corresponds to the gauge group of the strong interaction, and $SU(2)_L$ and $U(1)_Y$ represent the gauge groups of the weak isospin and hypercharge respectively [10].

2.1.1 Fundamental particles of the Standard Model

All particles described by the SM can be divided into fermions and bosons, which differ by their spin quantum number. For fermions, it equals $s = \frac{1}{2}$, and for bosons, it is an integer number ($s = 0, 1$).

Four bosons with a spin quantum number of one are described by the SM. These are the mediators of the fundamental forces. The photon is a massless and uncharged boson, which mediates the electromagnetic force. In contrast, the weak force is mediated by two massive bosons, a charged $W^{\pm}$ boson, and a neutral Z boson. While the gluon is massless, it carries colour charge. Thus is doesn't only interact with coloured fermions, but it is also involved in gluon self-couplings. These interactions will be described in more detail in the following Sections. The generation of the mass of the weak bosons can be derived when considering the last boson of the SM, which is the Higgs boson. The Higgs mechanism is described in Section 2.2.

Fermions are matter particles and are represented by spinor fields in the Lagrangian. There exist two different types of fermions, leptons and quarks. Both have three generations, differing amongst each other only by their increasing mass, but otherwise having identical quantum numbers.

Each lepton generation consists of a charged lepton and its associated uncharged neutrino. With increasing mass, these leptons are the electron (e), the muon (μ) and the tau (τ). As neutrinos do not carry electric charge, they do not interact electromagnetically. All six leptons however interact via the weak force. This makes the neutrinos peculiar amongst all fundamental particles. Since they only interact weakly and the weak force only interacts with left-handed chiral states, right-handed neutrinos cannot be produced. Furthermore, no mechanism in the SM gives mass to the neutrinos. However, already in 1957, Bruno Pontecorvo postulated that neutrinos must be massive [11], which has been confirmed in 1998 by the Superkamiokande experiment with the discovery of neutrino oscillations [12]. As such, the non-zero mass of neutrinos disagrees with SM expectations, as will be detailed in Section 2.3.

There exist six flavours of quarks, split into up-type quarks (up, charm and top) which carry a charge of $\frac{2}{3}e$, and down-type quarks (down, strange, and bottom) with a charge of $-\frac{1}{3}e$, where e corresponds to the elementary charge. Contrary to leptons, quarks also interact via the strong force and thus carry an additional charge known as the colour charge, which exists in three flavours termed as red, green and blue.

As the quark types represent mass eigenstates instead of eigenstates of the weak interaction, they can mix by the exchange of a $\mathrm{W}^{\pm}$ boson. The amplitude of these processes is described by the Cabibbo-Kobayashi-Maskawa (CKM) matrix [13, 14]:

$$\begin{pmatrix} d' \\ s' \\ b' \end{pmatrix} = \begin{pmatrix} V_{ud} & V_{us} & V_{ub} \\ V_{cd} & V_{cs} & V_{cb} \\ V_{td} & V_{ts} & V_{tb} \end{pmatrix} \begin{pmatrix} d \\ s \\ b \end{pmatrix} \tag{2.3}$$

Here, the i' quarks designate the weak eigenstates of the down-type quarks, and the i quarks represent the mass eigenstates. In the CKM matrix, the diagonal elements are much larger than the off-diagonal ones, thus encouraging quark mixing within families rather than across families.

Amongst the quarks, the top quark plays a special role, since it is the most massive elementary particle known to date ($m_t = 173.0 \pm 0.4\,\mathrm{GeV}$ [15]), and is therefore considered as a portal to the discovery of physics processes which are not described by the SM [16, 17]. Furthermore, it is the only particle which decays before it hadronises, having a lifetime of $\tau_t = 5 \times 10^{-25}\,\mathrm{s}$.

Additionally, an antiparticle is associated to each of the 12 leptons and quarks described above. The antiparticle only differs from the parent particle by its opposite charge. Antiparticles have been postulated by Paul Dirac in 1926 [18] and experimentally discovered in 1933 by Carl Anderson [19]. All particles described above are summarised in Figure 2.1 [10].

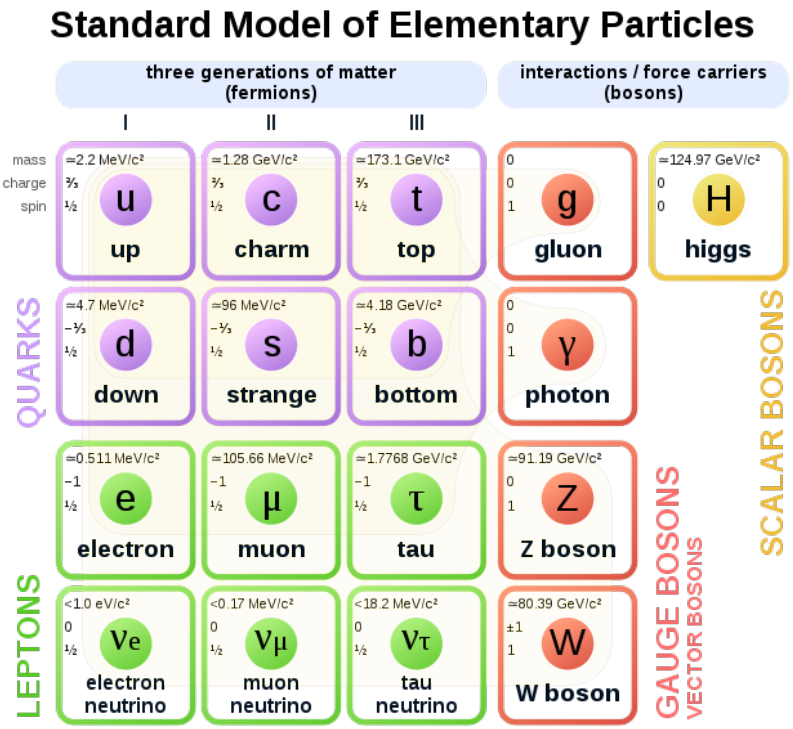

Figure 2.1: Summary of all particles of the Standard Model. Particles belonging to the three generations of quarks and leptons interact with each other via gauge bosons, which are the force mediators. The only scalar boson of the SM is the Higgs boson [20].

2.1.2 Fundamental interactions

As mentioned above, three of the four fundamental forces of Nature are described in the SM: the electromagnetic, the weak and the strong force. These are described in more detail in the following.

Quantum electrodynamics

The electromagnetic force is described in the theory of quantum electrodynamics (QED). The QED Lagrangian density must be invariant under gauge transformations of the U(1) group. It can be written as

$$\mathcal{L}_{\mathcal{QED}} = \bar{\Psi}(i\gamma^{\mu}\mathcal{D}_{\mu} - m)\Psi - \frac{1}{4}F_{\mu\nu}F^{\mu\nu} \tag{2.4}$$

Here, Ψ is the spinor that represents the field of the interacting fermions and γ^{μ} the gamma matrices. In order to maintain gauge invariance, the covariant derivative $\mathcal{D}_{\mu} = \partial_{\mu} + ieA_{\mu}$ is used instead of the classical derivative. The electromagnetic potential is given by the vector field A_{μ} which represents the photon field, and $F^{\mu\nu} = \partial^{\mu}A^{\nu} - \partial^{\nu}A^{\mu}$ is the field strength tensor. Thus, the Lagrangian in Equation 2.4 describes the coupling between charged fermions and the photon with a coupling strength e, presents a mass term for the fermions, and describes the kinematics of the photon field. Because of the gauge invariance of the Lagrangian, the gauge field A_{μ} is required to be massless, thus making the photon a massless particle [10].

Electroweak theory

In the 1950s and 1960s, Sheldon Glashow, Abdus Salam and Steven Weinberg established the electroweak formalism, which unifies the electromagnetic force with the weak force [21, 22, 23]. This was motivated by the fact that both forces conjectured the existence of a massless gauge boson, which was then thought to originate from the superposition of the electromagnetic and the weak force.

The electroweak theory is characterised by conserving $\mathrm{SU}(2)_L \otimes \mathrm{U}(1)_Y$ gauge symmetry. This symmetry enforces the conservation of the electric charge q, the weak isospin I_3 and the hypercharge Y, the later ones being the generators of the $\mathrm{SU}(2)_L \otimes$ and $\mathrm{U}(1)_Y$ groups respectively. These quantities are related by

$$q = I_3 + \frac{1}{2}Y. \tag{2.5}$$

The generators give rise to three weak isospin fields ($\mathrm{W}_{1,2,3}$) and a field B_0 coupling to the hypercharge current. The neutral fields can be related to the physical boson fields by introducing the Weinberg mixing angle θ_W:

$$\begin{pmatrix} \gamma \\ Z_0 \end{pmatrix} = \begin{pmatrix} \cos\theta_W & \sin\theta_W \\ -\sin\theta_W & \cos\theta_W \end{pmatrix} \begin{pmatrix} B_0 \\ W_3 \end{pmatrix} \tag{2.6}$$

which is fundamentally a rotation in the (W_3, B) plane.

Finally, the $\mathrm{W}_{2,3}$ bosons give rise to the charged $\mathrm{W}^{\pm}$ bosons:

$$W^{\pm} = \frac{1}{\sqrt{2}}(W_1 \mp iW_2) \tag{2.7}$$

The electroweak theory however cannot explain the mass of the $W^{\pm}$ and Z bosons as is explained in Section 2.2 [9].

The electroweak theory has been validated in 1983 by the discovery of the $W^{\pm}$ and Z bosons at CERN [24, 25, 26].

Quantum Chromodynamics

The strong force, which is mediated by gluons, is described by quantum chromodynamics (QCD). As quarks exist in three different colour states (red, green and blue), they are represented by a three-component spinor field Φ_i. The Lagrangian density which describes the strong interaction is given by

$$\mathcal{L}_{\mathcal{QCD}} = \bar{\Psi}_i((i\gamma^\mu \mathcal{D}_\mu)_{ij} - m\delta_{ij})\Psi_j - \frac{1}{4}G^a_{\mu\nu}G^{\mu\nu}_a \tag{2.8}$$

which is invariant under SU(3) gauge transformations. In the case of QCD, the covariant derivative is given by $\mathcal{D}_\mu = \partial_\mu - \frac{1}{2}igA^\alpha_\mu\lambda_\alpha$, where λ_α are the Gell-Mann matrices which span the Lie algebra of the SU(3) group. Similarly to the electromagnetic interaction, the Lagrangian describes the kinematics of the gluons, and presents a mass term for the quarks. However, the interaction terms in the gluon field strength tensor differs:

$$G^a_{\mu\nu} = \partial_\mu A^a_\nu - \partial_\nu A^a_\mu + g_s f^{abc} A^b_\mu A^c_\nu \tag{2.9}$$

In equation 2.9, f^{abc} are the structure constants of the SU(3) group. A^a_μ are the gluon fields, which exist in eight massless colour variations. Contrary to the electromagnetic interaction, the field strength tensor now also provides a gluon self-coupling term with a colour charge g_s. The Lagrangian describes both a triple-gluon vertex and a quadruple-gluon vertex. This implies, as mentioned above, that gluons now themselves carry colour charge, namely one colour and an anticolour charge. Hence colour charge is conserved in the strong interaction [10].

The strong coupling constant α_s, which is related to the coupling g_s as $\alpha_s = \frac{g_s^2}{4\pi}$ also exhibits a special behaviour. Indeed, it approaches zero at high transferred transverse momentum Q^2, thus leading to asymptotic freedom, as quarks in this regime can be approximated as free particles. This allows to use perturbation theory to calculate QCD processes in this regime. At low Q^2 however, the coupling strength rises to infinity. This implicates that is not possible to observe individual quarks, as they would carry infinite energy. Therefore, when increasing the distance between two quarks, two new quarks are created from the vacuum when it becomes energetically favourable. This property is named colour confinement and it implies that only

hadrons, which are colour neutral particles, can be observed. There are two possibilities to form these colourless states, either by assembling three quarks forming a colour singlet which are then named baryons, or by combining a quark and an antiquark, in which case mesons are constructed. The process of hadron formation is named hadronisation, which at high energies ultimately leads to the creation of jets as is detailed in Section 3.1 [9].

2.2 The Higgs mechanism in the Standard Model

In addition to the gauge bosons presented in Section 2.1.1, a spin-zero boson has been postulated in 1964 by Peter Higgs, François Englert, Robert Brout and others [27, 28, 29]. The existence of this boson is necessary in order to account for the mass of the $W^{\pm}$ and Z bosons. Indeed, including a mass term in the Lagrangian for gauge bosons similar to that of fermions and leptons would break its gauge invariance.

Instead, spontaneous symmetry breaking (SSB) is used to introduce mass terms for these bosons in the Lagrangian. In practice, SSB conserves gauge invariance, but breaks the invariance of the vacuum of the theory.

The mechanism is illustrated using a Lagrangian invariant under U(1) gauge transformations:

$$\mathcal{L} = (\mathcal{D}_\mu \phi)^* (\mathcal{D}^\mu \phi) - \mu^2 \phi^* \phi - \lambda (\phi^* \phi)^2 - \frac{1}{4} F_{\mu\nu} F^{\mu\nu} = T(\phi) - V(\phi) \tag{2.10}$$

Here, ϕ represents a complex scalar field which remains invariant under gauge transformations $\phi \rightarrow e^{i\theta(x)}\phi$, where $\theta(x)$ depends on the space-time coordinates. Under these, the gauge field transforms as $A_\mu \rightarrow A_\mu + \frac{1}{g}\partial_\mu \theta$. In the equation above, the Lagrangian has been split into its kinetic part $T(\phi)$ and its potential $V(\phi) = \mu^2 \phi^* \phi + \lambda (\phi^* \phi)^2$.

The parameters μ and λ are free parameters of the SM. When choosing $\mu^2 < 0$ and $\lambda > 0$, the potential has an infinite number of minima as is illustrated in Figure 2.2. These minima are degenerate and form a circle around the local maximum at $\phi(x) = 0$ with radius $-\frac{\mu^2}{\lambda}$.

Choosing a particular minimum of the potential such as $\mathrm{Im}(\phi) = 0$ and $\mathrm{Re}(\phi) = -\frac{\mu^2}{\lambda}$ breaks the invariance of the Lagrangian. The complex field can then be expressed in terms of fluctuations around the chosen ground state using the vacuum expectation value v and the real fields h and ξ as

$$\phi \rightarrow \frac{1}{\sqrt{2}}(v + h(x)) e^{i\frac{\xi(x)}{v}} \tag{2.11}$$

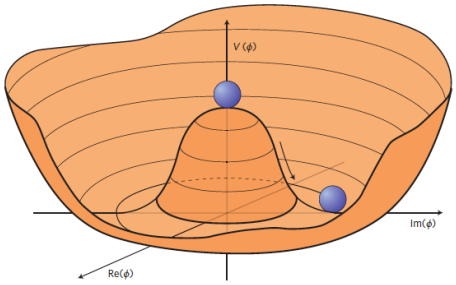

Figure 2.2: Illustration of the potential $V(\phi)$ of a complex scalar field ϕ. The minima of the potential are located on a circle with radius $-\frac{\mu^2}{\lambda}$ around the origin [30].

Redefining the gauge field as

$$\hat{A}_\mu = A_\mu - \frac{1}{v}\partial_\mu \xi. \tag{2.12}$$

the Lagrangian in Equation 2.10 now reads as:

$$\mathcal{L} = \frac{1}{2}(\partial_\mu h)^2 - \lambda v^2 h^2 + \frac{1}{2}g^2 v^2 \hat{A}_\mu^2 - \lambda v h^3 - \frac{1}{4}\lambda h^4 \tag{2.13}$$

$$+ \frac{1}{2}g^2 \hat{A}_\mu^2 h^2 + v g^2 \hat{A}_\mu^2 h - \frac{1}{4}\hat{F}_{\mu\nu}\hat{F}^{\mu\nu} \tag{2.14}$$

This rewriting reveals the presence of a massive scalar Higgs field h. The corresponding mass term $\lambda v^2 h^2$ yields a Higgs boson mass of $m_h = \sqrt{2\lambda v^2}$. While the Lagrangian in Equation 2.10 was written as a function of two fields ϕ and A^μ each of which had two degrees of freedom, the Lagrangian in Equation 2.13 now contains a real, scalar field h with only 1 degree of freedom, and the vector field $\hat{A}_\mu$. This vector field thus gained an additional degree of freedom by incorporating the massless Goldstone boson ξ. This is predicted by the Goldstone theorem which states that a massless boson appears for every spontaneously broken symmetry [31, 32, 33]. The additional third degree of freedom of the vector field thus gives the mass $m_A = gv$ to the gauge boson. Hence, adding a scalar Higgs field to the SM Lagrangian allows the existence of massive vector bosons while conserving gauge invariance, under the condition that the vacuum expectation value v is non-zero [9, 34].

Extending this mechanism to the breaking of the local gauge symmetry $SU(2)_L \times U(1)_Y$, SSB can explain the non-zero masses of the $W^\pm$ and Z bosons. In this case, the covariant derivative can be written as

$$\mathcal{D}_\mu = \partial_\mu - \frac{1}{2}ig\tau_i \cdot W_\mu^i - \frac{1}{2}ig' B_\mu \tag{2.15}$$

with the coupling constants g and g' of the $SU(2)_L$ and $U(1)_Y$ fields and the Pauli matrices τ_i, which are the generators of the $SU(2)$ group. The Lagrangian itself can be written as

$$\mathcal{L} = -(\mathcal{D}^\mu\phi)^\dagger(\mathcal{D}_\mu\phi) - \mu^2\phi^\dagger\phi - \lambda(\phi^\dagger\phi)^2 \tag{2.16}$$

which is identical to the previous case, but using the hermitian adjoint instead of the complex conjugate.

The parameters of the Lagrangian potential are chosen as $\mu^2 < 0$ and $\lambda > 0$, which leads to the following minimum of the potential:

$$< \phi^\dagger\phi >= v^2 = -\frac{\mu^2}{\lambda}. \tag{2.17}$$

.

The Higgs doublet is now written as

$$\phi = \frac{1}{\sqrt{2}}\begin{pmatrix} 0 \\ v + h(x) \end{pmatrix}. \tag{2.18}$$

Here, $h(x)$ represents fluctuations around the vacuum in the direction of the generator $Q = I_3 + Y$.

Using the given expression of the Higgs doublet, the Lagrangian now contains the following terms:

$$M_W^2 W_\mu^+ W^{-\mu} + \frac{1}{2}M_Z^2 Z_\mu Z^\mu \tag{2.19}$$

where

- $W^\pm = \frac{(W^1 \mp W^2)}{\sqrt{2}}$
- $Z_\mu = \frac{gW_\mu^3 - g'B_\mu}{\sqrt{g^2+g'^2}}$
- $M_W = \frac{1}{2}vg$
- $M_Z = \frac{1}{2}v\sqrt{g^2+g'^2}$

As expected, introducing spontaneous symmetry breaking of the vacuum states introduces mass terms for the electroweak bosons Z and $W^\pm$ in the SM Lagrangian while conserving gauge invariance [34].

A further complication regards the masses of the fermions. Indeed, a mass term of the form $\mathcal{L}_m = -m\bar{\Psi}\Psi$ would not be invariant under the $\mathrm{SU}(2)_L$ gauge group. To solve the issue, an interaction between the fermions and the Higgs boson is introduced:

$$\mathcal{L}_Y = -\frac{c_Y}{\sqrt{2}}(v+h)\Psi\bar{\Psi} \tag{2.20}$$

The mass term for fermions can then be written as

$$m_f = c_Y \frac{v}{\sqrt{2}} \tag{2.21}$$

where c_Y designates the Yukawa coupling constant between the fermion and the Higgs boson. These couplings are specific for each fermion, such that each fermion has a different mass which is directly proportional to their coupling strength to the Higgs boson. Additionally, these masses and couplings are free parameters of the theory, so that only experimental measurements can determine their values [21].

The validity of this theory has been proven in 2012 with the discovery of a new particle that is compatible with the Higgs boson at the CERN LHC accelerator [35, 36]. The most precise measurement of the Higgs boson mass to date is $125.35 \pm 0.15\,\text{GeV}$ [37]. Furthermore the vacuum expectation value is related to the coupling constant of the weak interaction G_F and has been measured in the decay of muons to $v = 246\,\text{GeV}$ [38, 39, 40]. Both measurements are compatible with their theoretically predicted relation $m_h = \sqrt{2\lambda v^2}$ where λ is the Higgs self-coupling parameter. Its theoretically predicted value is $\lambda_{SM} \approx 0.13$, and its current exclusion limit at 95% confidence limit is $-0.8 < \lambda/\lambda_{SM} < 7.7$ [15].

2.3 Limitations of the Standard Model

The SM has experienced vast success in the last decades, correctly describing many physics processes. This is exemplified in Figure 2.3, which shows measurements of cross sections of many processes performed by the CMS collaboration, including well known SM processes such as diboson production, as well as Higgs boson production measurements. The measured cross sections range over almost ten orders of magnitude and all agree well with predictions.

Despite this tremendous success, a number of physical observations and theoretical considerations indicate that the SM cannot be the final theory of Nature. One example has already been described, which is the non-zero mass of the neutrinos. Another obvious example is the matter-antimatter asymmetry in the universe. Shortly after the Big Bang, matter and antimatter should have been produced in equal amounts. Today however, no antimatter is naturally present in the universe, so unknown phenomena must have led to its disappearance.

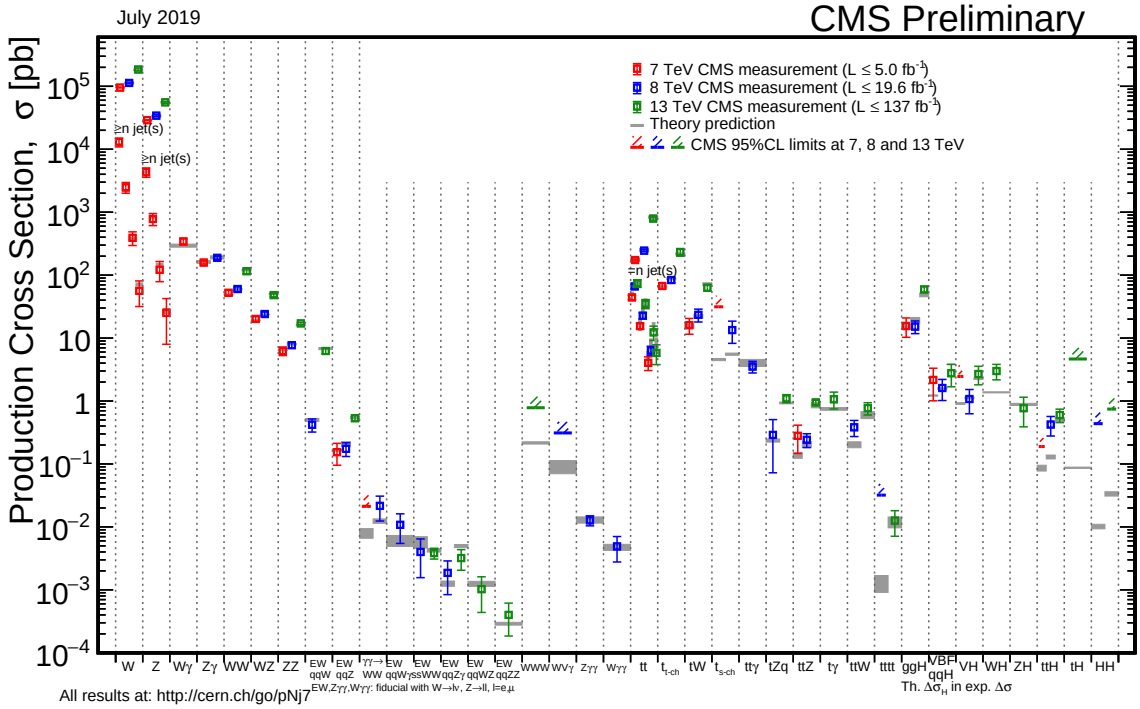

Figure 2.3: Measurements of cross sections for various SM processes by the CMS collaboration. These agree with theoretical predictions over many orders of magnitude [41].

Furthermore the SM does not include a description of the gravitational force. This is because so far, gravity could not be formulated as a renormalisable theory. While the gravitational force is negligible at energies under test at high energy physics experiments, this approximation no longer holds when considering energy regimes around the Planck scale $\Lambda_P \sim 10 \times 10^{19}\,\text{GeV}$, where the strength of the gravitational force is comparable to the forces described by the SM.

Another puzzle regards the mass of the Higgs boson, which is formally known as the hierarchy problem. Indeed, it is surprising that the Higgs mass is several orders of magnitude lower than the Planck scale, when it is subject to large corrections from virtual fermion and boson loops, such as depicted in Figure 2.4. These corrections can be written as

$$\Delta m_H^2 = -\frac{|\lambda_f^2|^2}{8\pi^2}\Lambda_{NP}^2 \tag{2.22}$$

where λ_f is the coupling strength of the Higgs to fermions, and Λ_{NP} the scale

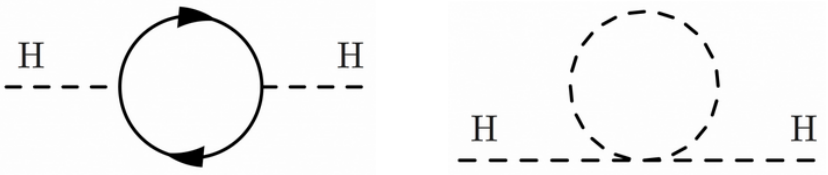

(a) Fermionic corrections (b) Bosonic corrections

Figure 2.4: Quantum corrections to the Higgs boson mass by virtual fermion (a) and boson (b) loops.

at which physics that isn't described by the Standard Model appears. If that scale corresponds to the Planck scale, the corrections quickly surpass the measured mass of the Higgs boson. In principle, these corrections could cancel, since the contributions from bosons and fermions enter with opposite signs. This is however quite unlikely as it would require an unreasonable fine-tuning of the corrections.

Finally, the matter observed today only describes about 4% of the entire energy present in the universe. Indeed astrophysical observations such as measurements of rotation curves of galaxies indicate the presence of an unknown substance named dark matter. It can be excluded that this matter arises from one of the particles of the SM, so that it must consist of a new type of particle, for example weakly interacting massive particles (WIMPs). Observations such as from gravitational lensing indicate that dark matter accounts for $\sim$ 27% of the total energy of the universe. The remaining 68% percent are attributed to dark energy, which must exist to explain the expansion of the universe. However, dark energy is so far not understood [42].

Many theoretical models, commonly grouped as beyond the Standard Model (BSM) theories, have been developed to explain these shortcomings of the SM. A very promising theory is called supersymmetry (SUSY), which not only solves the hierarchy problem, but also naturally provides a candidate for dark matter and unifies all fundamental forces at high energies [43]. Supersymmetry predicts partners for all SM particles — bosons for fermions and vice-versa, of which experiments aim to find traces to test the theory. However, despite intensive searches in the past years, no measurements compatible with the existence of SUSY particles have been published to date [44, 45].

Extra dimension models, such as the Arkani-Dimopoulos-Dvali [46] and Randall-Sundrum [47] predict additional dimensions which would lower the Planck scale, thus solving the hierarchy problem. Other theories directly study the properties of the Higgs boson, such as composite Higgs models, which postulate that it is not an elementary particle, or hidden valley theories, where the Higgs boson couples to a

series of new particles [48, 49].

Particle physics experiments are probing these proposed models by theorists. However, in the absence of direct observations of new physics phenomena in the past years, focus has now shifted towards indirect detections of BSM physics by searching for discrepancies with respect to SM expectations. For example, slight tensions with respect to SM predictions in measurements of lepton flavour universality have been observed. These deviations are present both in decays of b mesons to strange quarks and to charm quarks in association with leptons [50, 51, 52, 53].

Chapter 3

The CMS experiment at the LHC

Today's research in high energy particle physics is driven by increasingly powerful particle accelerators reaching previously unattainable collision energies. The currently used machine, which is in operation since 2009, is the Large Hadron Collider (LHC) which accelerates protons and heavy ions [54]. After first ideas about a future utilisation of the tunnel that had been built for the LEP collider emerged in the early 1980s, the LHC project was approved in December 1994, and construction began in 1996 [42]. Several experiments were constructed along the accelerator ring, aiming to answer fundamental open questions in particle physics. One of those experiments is the Compact Muon Solenoid (CMS) detector, which is characterised by its powerful solenoid magnet.

Section 3.1 reviews the fundamental physical processes involved in hadron collisions. In particular, the various components of these interactions such as the hard process, the parton shower and hadronisation are described, and it is explained how jets, which are predominantly produced in hadron colliders, are reconstructed. This Section also discusses the production and decay modes of the Higgs boson at hadron colliders. In Section 3.2 the LHC accelerator is described, while Section 3.3 outlines the different components of the CMS experiment which allow the reconstruction of collisions.

3.1 Physics at hadron colliders

In this Section, Standard Model processes described in the previous Chapter are exemplified in the case of hadron colliders. In particular, the parton model is discussed, and the processes involved in the interaction are detailed.

3.1.1 Properties of circular hadron colliders

Circular particle colliders are very versatile machines, and are powerful tools for studying known physical processes, in particular because they provide large datasets. This is because beams can be conserved for several hours and collided at multiple interaction points every few nanoseconds, in contrast with linear accelerators, where beams are destructed after each collision. Furthermore particles circulate in bunches through the accelerator, providing multiple interactions per collision point. This enables to collect large datasets to perform precision measurements of parameters of the SM, such as particle masses or coupling strengths. By measuring these quantities with increasingly high precision, it is also possible to find hints for new physics phenomena when measurements deviate from theoretical predictions.

Additionally, hadron colliders are the prevalent tool for searches for BSM physics. Indeed, the collision of hadrons presents several large advantages with respect to the collision of leptons, even though the later ones are typically cleaner and easier to reconstruct. Most importantly, the collision energy is not fixed but depends on the momentum fraction of the colliding partons. Thus, hadron colliders intrinsically scan a wide range of energies.

In addition, reaching higher energies is much facilitated when accelerating hadrons such as protons rather than electrons in circular colliders. This is explained by synchrotron radiation losses during acceleration. The power radiated by relativistic electrons and protons undergoing a circular motion can be written as

$$P = \frac{2}{3}\frac{e^2 c}{R^2}\Big(\frac{E}{mc^2}\Big)^4 \tag{3.1}$$

where e designates the Coulomb charge, c the speed of light, R the curvature radius of the particle's trajectory, E its energy and m its mass [55]. Because of the mass difference of protons and electrons, the power losses for both particles differ by a factor $\frac{P_e}{P_p} = \left(\frac{m_p c^2}{m_e c^2}\right)^4 \simeq 10^{13}$. Thus, energy losses from synchrotron radiation are considerably larger at circular lepton colliders than at hadron colliders.

Collisions are typically characterised by their centre-of-mass energy, which is the total energy available in the collision. It is beneficial to increase this energy as much as possible, as this enables the experiments to access so far unexplored phase space regions.

The number of observed collisions in a specified amount of time is given by

$$N_{events} = \varepsilon \mathcal{A} \sigma \mathcal{L}_{int}. \tag{3.2}$$

where ε stands for the detection efficiency, $\mathcal{A}$ for the geometrical detector acceptance, σ for the cross section of the process, and $\mathcal{L}_{int}$ for the integrated luminosity. It is defined as the integral over time of the instantaneous luminosity $\mathcal{L}$

$$\mathcal{L}_{int} = \int_t \mathcal{L} dt, \tag{3.3}$$

which in turn is defined as

$$\mathcal{L} = \frac{N_1 N_2 n f}{A} \tag{3.4}$$

where N_i designates the number of particles per bunch in beam i, n gives the number of bunches, f the rotation frequency around the ring, and $A = 4\pi\sigma_x\sigma_y$ the cross section area of the beam [56].

3.1.2 Production cross section

Collisions produced at hadron accelerators are highly complicated processes, in particular because of the composite nature of the hadrons. Contrary to electrons or positrons, hadrons have an inner structure. For instance, protons consist of three valence quarks (two up quarks and one down quark) as well as sea quarks and gluons. All these particles inside hadrons are named partons.

At high energies, the momentum transfer between the colliding particles is large enough to resolve the inner structure of hadrons, such that collisions do not occur between the protons themselves, but between partons. Such events are called hard scattering events.

A crucial feature of QCD is factorisation. This implies that the hard interaction process can be described separately from fragmentation processes occurring at lower energies. Both regimes are separated by the factorisation scale μ_F. The fragmentation process involves hadronisation, where each final state parton creates stable hadrons. This process is inevitable as single partons cannot exist because of colour confinement.

The interaction cross section between hadrons thus depends on the parton interaction cross section using the factorisation theorem [57]:

$$d\sigma^{h_1 h_2 \to X} = \int_0^1 dx_1 \int_0^1 dx_2 \sum_{a,b} f_{a/h1}(x_1, \mu_F^2) f_{b/h2}(x_2, \mu_F^2)\, d\hat{\sigma}^{ab\to X}(Q^2, \mu_F^2) \tag{3.5}$$

where a is a parton in hadron h_1 with momentum fraction x_1, b a parton in hadron h_2 with momentum fraction x_2, X the final state of an event and Q^2 the momentum transfer in the collision [58].

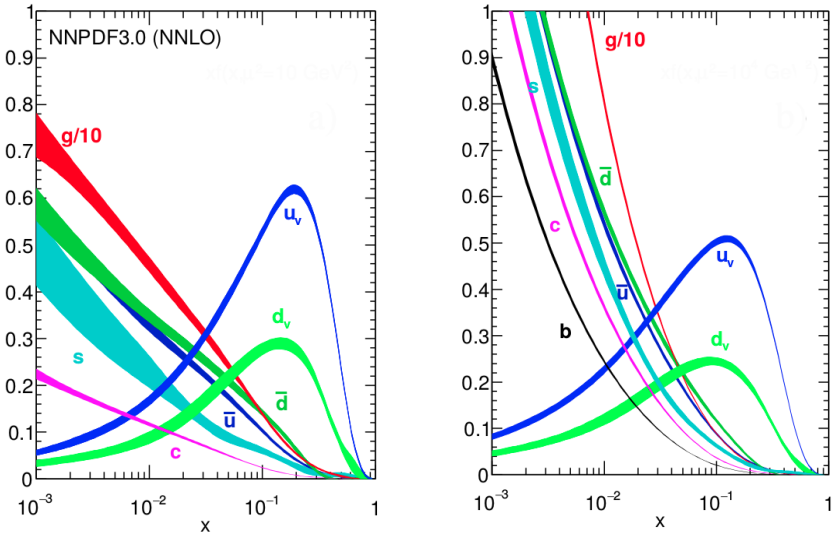

(a) $Q^2 = 10\,\mathrm{GeV}^2$ (b) $Q^2 = 10^4\,\mathrm{GeV}^2$

Figure 3.1: Parton density functions of the NNPDF3.0 set at energy scales of $Q^2 = 10\,\mathrm{GeV}$ (left) and $Q^2 = 10^4\,\mathrm{GeV}$ [15]. At low values of momentum fraction x, interactions are most likely to occur between gluons.

Importantly the hadron interaction depends on the interaction cross section between the two partons a and b, $d\hat{\sigma}^{ab\to X}(Q^2, \mu_F^2)$. However, the exact momentum of the interacting partons is not known as it cannot be inferred from the total hadron momentum. This is why the cross section in Equation 3.5 contains so-called parton density functions (PDFs) $f_i(x, \mu_F^2)$. These PDFs describe the probability that the interacting parton carries a momentum fraction x of the total hadron momentum. PDFs cannot be derived theoretically such that precise measurements are necessary to evaluate them [59, 60]. One example can be found in Figure 3.1, which shows the NNPDF3.0 PDF set at different factorisation scales. In can be seen that at the regime at which current hadron colliders operate, protons consist mostly of gluons, such that the most probable interactions occur between a pair of gluons. The PDFs depend on the energy scale and are typically calculated at a particular value of that scale. To extrapolate these functions to different values of the energy scale, the Dokshitzer, Gribov, Lipatov, Altarelli and Parisi (DGLAP) equations can be used. This also allows to combine measurements from various experiments performed at different scales to evaluate the PDFs [61, 62, 63].

3.1.3 Jet algorithms

Because of hadronisation and parton showering, which describe QCD radiation processes from quarks or gluons, partons produced in hard interactions manifest themselves as collimated "sprays" of hadrons. These sprays are called jets, and dedicated clustering algorithms exist to construct them such that all particles that originate from the same parton produced in the hard interaction are grouped together [64]. While in the past, cone-type algorithms such as Midpoint Cone, Iterative Cone or SISCone [65, 66, 67] were used, sequential clustering algorithms are nowadays preferred. This is because they intrinsically guarantee infrared safety, which means that jet construction is independent from adding a low-energetic particle to the input constituents, and collinear safety, which also leaves the jet formation unchanged when replacing one constituent by two collinear constituents.

Sequential clustering algorithms define a set of two distances. One of them is the distance of one constituent to the beam axis $y_{iB} = p_{T_k}^n$. The second distance y_{ij} is defined between two constituents i and j:

$$y_{ij} \;=\; \min(p_{T_i}^{2n}, p_{T_j}^{2n}) \frac{\Delta R_{ij}^2}{R^2} \;=\; \min(p_{T_i}^{2n}, p_{T_j}^{2n}) \; \frac{(\eta_i - \eta_j)^2 + (\phi_i - \phi_j)^2}{R^2} \tag{3.6}$$

Here, ΔR_{ij} denotes the angular distance between two constituents, R is the jet's distance parameter which is given to the algorithm and p_T is the momentum tranverse to the beam axis.

Sequential clustering algorithms proceed iteratively. First, the minimum distance $y_{\min} = \min_{ij}(y_{ij}, y_{iB})$ is determined for all combinations of two constituents. If $y_{\min} = y_{ij} < R$, both constituents are combined into a single constituent with the four-momentum $p_k = p_i + p_j$, removing i and j from the constituent list. If $y_{\min} = y_{iB} < R$, constituent i is associated to beam radiation and removed from the algorithm. Otherwise if $y_{\min} > R$, both constituents are conserved and are declared as jets [68].

Three different algorithms arise from this formalism, which differ by the value of the parameter n. The k_T algorithm uses $n = 1$ [69]. The Cambridge-Aachen (CA) algorithm uses $n = 0$ [70, 71], and the anti-k_T algorithm sets $n = -1$ [72]. While the anti-k_T algorithm forms almost circular jets with a radius close to the given distance parameter, the distance measure for the CA algorithm only depends on spatial separation and not on momentum or energy considerations as is illustrated in Figure 3.2. It is therefore particularly well suited to study the substructure of jets.

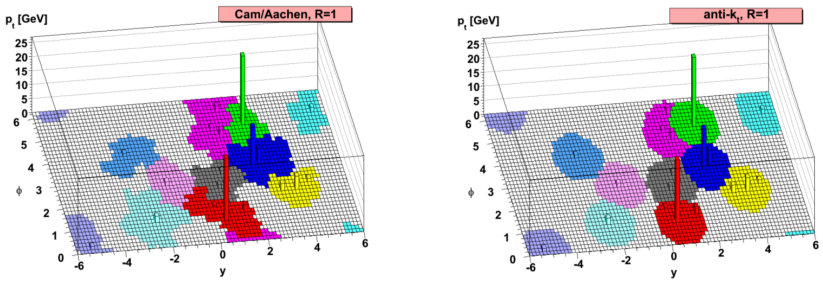

(a) CA algorithm (b) anti-k_T algorithm

Figure 3.2: Illustration of the jet clustering algorithms CA and anti-k_T [72].

3.1.4 Pileup and underlying event

Since particles are accelerated in bunches, several collisions can occur during the same bunch crossing, which is called pileup. At the LHC, up to 70 collisions have been recorded simultaneously in 2017 [73]. Furthermore, collisions occur every 25 ns at experiments around the LHC ring. Given that the shower creation in the calorimeters, the detector readout and triggering are not instantaneous, it cannot be excluded that particles originating from a previous bunch-crossing interfere with the event of interest, leading to so-called out-of-time pileup. Many efforts go into correctly identifying and removing particles created by pileup events during event reconstruction [74, 75, 76].

In addition to the hard scattering process, other particles are produced in the interaction between the protons. These can be partons which took part in the primary interaction, products of multiple parton interactions, and contributions from initial and final state radiation. These processes are commonly grouped as the underlying event [77]. Similarly to contributions from pileup events, they lead to additional particles in the detector which interfere with those originating from the hard scattering process.

3.1.5 Higgs physics at hadron colliders

The Higgs boson which represents the last missing piece of the SM has eluded discovery for many years. This is because large collision energies are required to produce this very massive particle. Furthermore its production cross section is small, such that large datasets are needed. A new particle compatible with the SM Higgs boson was finally discovered at the LHC in 2012 [35, 36].

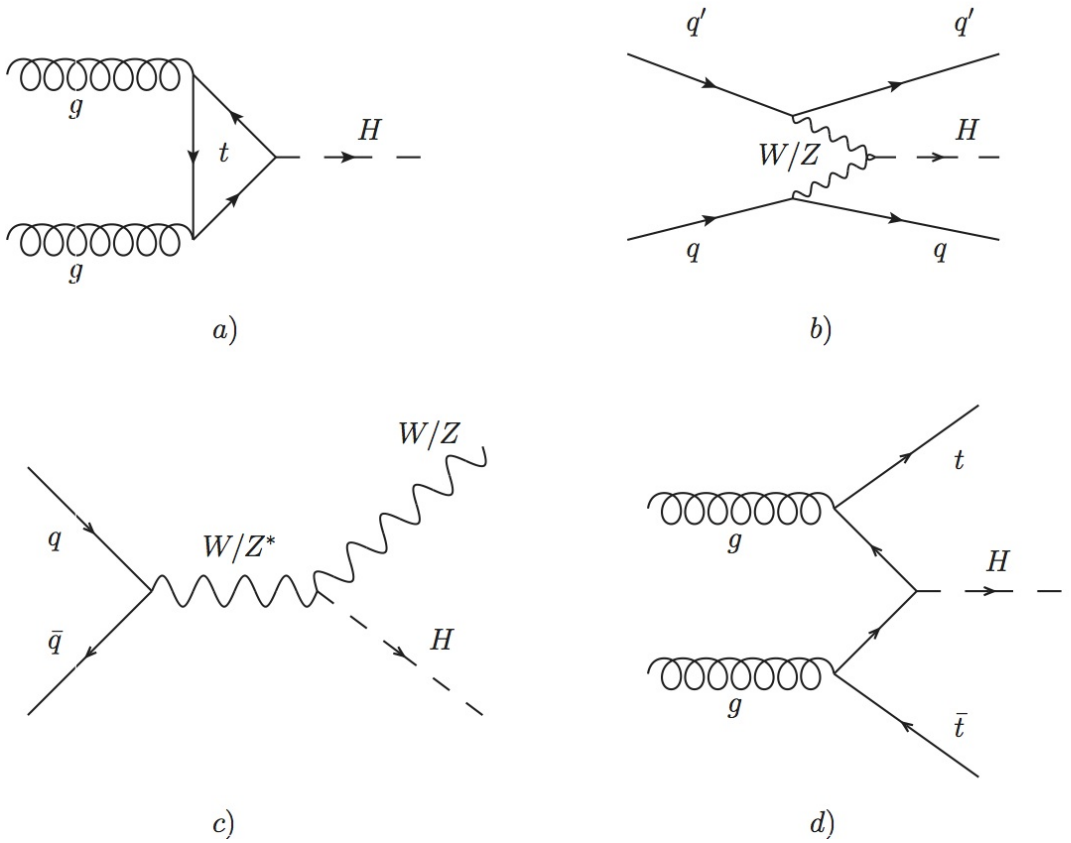

Figure 3.3: Feynman diagrams of the four main Higgs boson production mechanisms: gluon fusion (a), vector boson fusion (b), Higgs strahlung (c) and associated production with top quarks(d).

The Higgs boson is produced via four main production modes at hadron colliders which are illustrated in Figure 3.3:

- Gluon fusion (ggF): A Higgs boson is produced in the interaction between two gluons via a fermion loop.
- Vector boson fusion (VBF): Two quarks radiate a weak boson, which can merge by emitting a Higgs boson.
- Higgs strahlung (WH, ZH): Off-shell $W^{\pm}$ or Z bosons radiate a Higgs boson
- Associated production ($t\bar{t}H$, $b\bar{b}H$): Production of a Higgs boson in association with a top quark or a bottom quark pair.

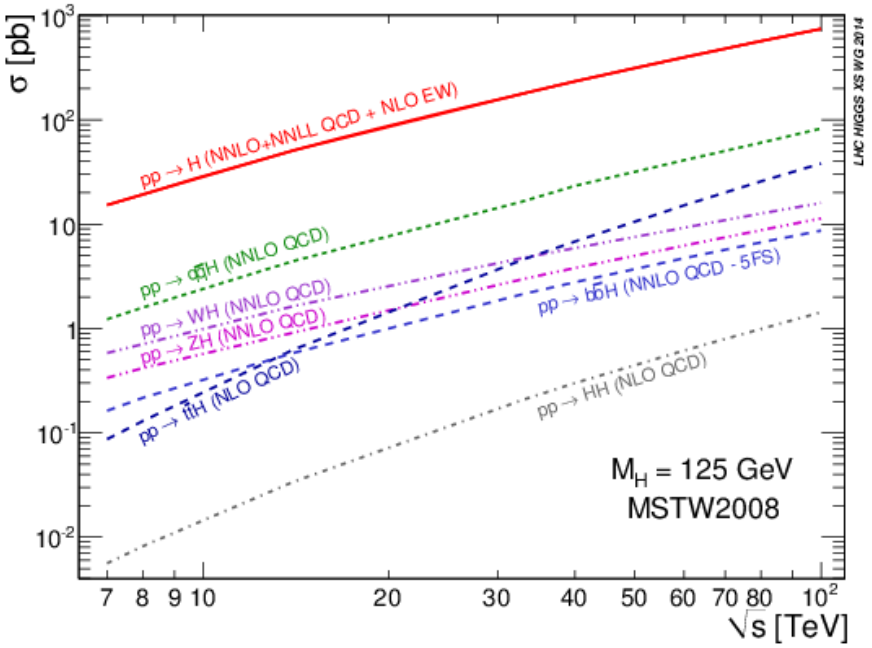

Figure 3.4: Higgs production cross section as a function of centre-of-mass energy [79]. The production cross section increases with higher collision energies, in particular for the $t\bar{t}H$ process.

Figure 3.4 illustrates the dependence of the different Higgs boson production cross sections as a function of the centre-of-mass energy, while the values of the cross sections at centre-of-mass energies of 13 TeV and 100 TeV are summarised in Table 3.1. A reference of 100 TeV has been chosen as this is the target energy of a proposed future collider, the Future Circular Collider [78].

The dominant production mechanism at the centre-of-mass energies at which the LHC collider operates is gluon fusion. Typically the fermion in the loop is a top quark, since it has the largest mass and therefore the largest coupling to the Higgs boson. However, as the quark is only present in a virtual loop, contributions from BSM physics cannot be excluded. Conversely, for the associated production of a Higgs boson with a pair of top quarks ($t\bar{t}H$), top quarks are present in the final state of the event, thus allowing a direct measurement of the Yukawa coupling with the Higgs boson. This justifies the importance of this measurement, and explains why the large increase in cross section that is observed with increasing centre-of-mass energies is highly beneficial for studying this production mode.

Like most SM particles, the Higgs boson is not stable and decays almost instantly.

Table 3.1: Higgs production cross sections at $\sqrt{s} = 13\,\text{TeV}$ and $\sqrt{s} = 100\,\text{TeV}$ assuming a Higgs mass of 125 GeV [79, 80].

Process	$\sigma = 13\,\text{TeV}$ (pb)	$\sigma = 100\,\text{TeV}$ (pb)	$\sigma(100\,\text{TeV})/\sigma(13\,\text{TeV})$
ggF	43.92	740.3	16.86
VBF	3.748	82.0	21.88
WH	1.380	15.9	11.52
ZH	0.8696	11.26	12.95
$t\bar{t}H$	0.5085	37.9	74.53
$b\bar{b}H$	0.5116	8.64	16.89

Indeed, the predicted lifetime is around $10^{-22}\,\text{s}$ [81], and experiments constrain the lifetime to less than $\tau_H < 1.9 \times 10^{-13}\,\text{s}$ [82]. There exist multiple decay mechanisms of the Higgs boson as it couples to all massive particles. Since the coupling strength is proportional to the particle's mass, it implies that the Higgs decays preferentially to more massive particle, as long as the decay is still kinematically allowed [68]. Further decays to massless particles, for instance to two photons, are possible via virtual loops. The decay probability into the various final states is described by the branching ratio

$$\mathcal{BR}(H \to X) = \frac{\Gamma(H \to X)}{\Gamma_{total}} \tag{3.7}$$

where $\Gamma(H \to X)$ is the decay width of channel X and Γ_{total} the total decay width of the Higgs boson.

The branching ratio of various decay modes as a function of the Higgs boson mass is illustrated in Figure 3.5. At the measured Higgs boson mass of around 125 GeV, the decays $H \to b\bar{b}$ and $H \to W^+W^-$ are the most prominent. However, the $H \to b\bar{b}$ decay channel is challenging to observe experimentally because of large background contributions. This is why the Higgs boson was discovered in 2012 in the $H \to \gamma\gamma$, $H \to ZZ \to 4l$, and $H \to WW \to l\nu l\nu$ decay channels [35, 36].

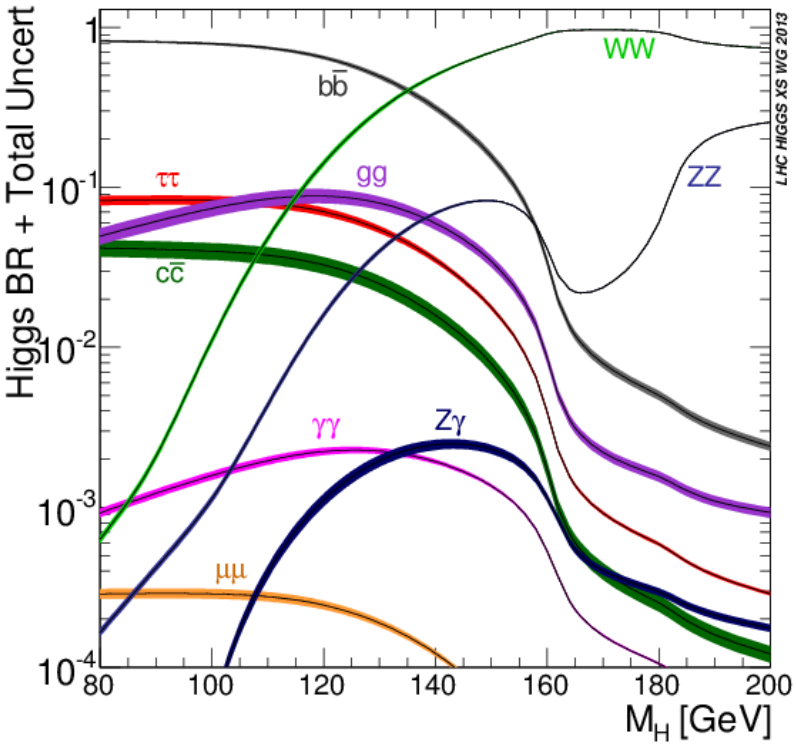

Figure 3.5: Higgs boson branching ratios as a function of Higgs boson mass [80]. The largest branching ratio at a mass of 125 GeV is the decay into a pair of bottom quarks.

3.2 The Large Hadron Collider at CERN

The large hadron collider (LHC) is a proton-proton collider operated by CERN (Organisation Européene pour la Recherche Nucléaire [83]) and located in Geneva, Switzerland. In addition to the LHC, CERN operates a large accelerator complex which enables research in many areas of nuclear and particle physics.

3.2.1 The CERN accelerator complex

The CERN accelerator complex is illustrated in Figure 3.6. Most of the accelerators feed into each other aiming to produce particles at higher and higher energies. Protons, which are used in collisions that are analysed in this work, are produced by ionising hydrogen atoms. In a first linear section (Linac 2), they are accelerated to an energy of 50 MeV. This section has been replaced in 2020 by the Linac 4, which

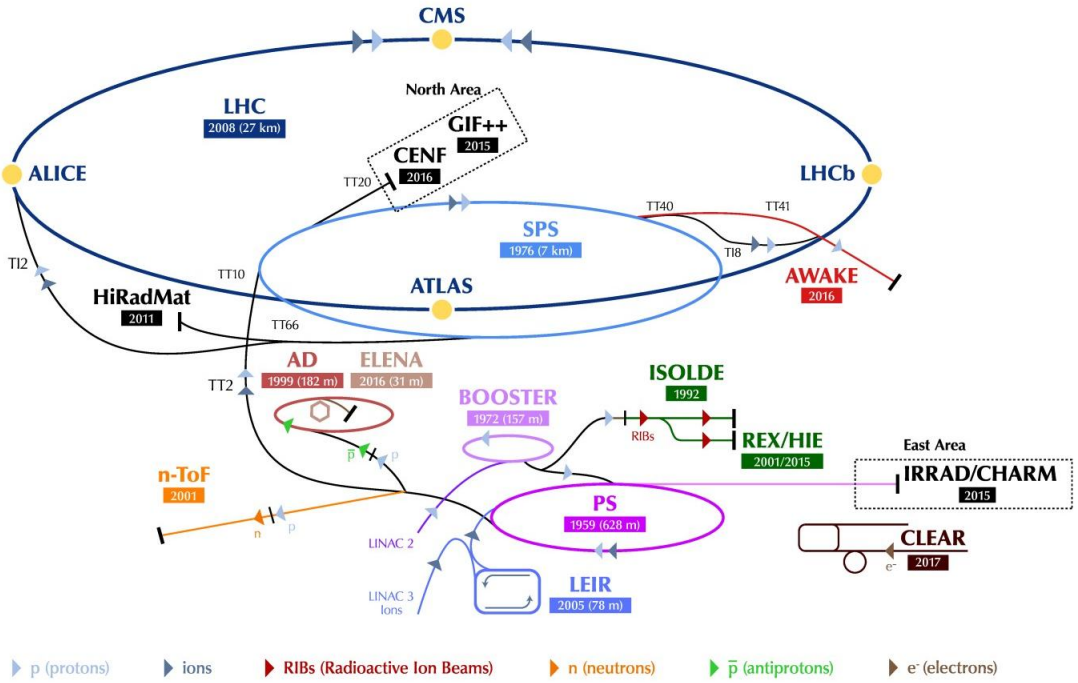

Figure 3.6: Schematics of the CERN accelerator complex. Protons go through several consecutive accelerator rings, each gradually increasing the particles' energy before injection in the LHC ring [87].

will increase the energy of protons to 160 MeV [84]. Afterwards, they are propagated successively to the Proton Synchrotron Booster (PSB), the Proton Synchrotron (PS) and the Super Proton Synchrotron (SPS), where their energy reaches 450 GeV. Protons are finally injected in the Large Hadron Collider, which will be described in Section 3.2. This chain is also used to accelerate heavy ions, however this thesis focuses on the collisions of protons [42].

In addition to this accelerator chain, the CERN infrastructure provides many other facilities for instance for research on antimatter (at the antiproton decelerator [85]) or for the production of radioactive ion beams (at ISOLDE [86]).

3.2.2 The LHC

The Large Hadron Collider (LHC) has been built 100 m below ground in the tunnel which previously hosted the Large Electron-Positron Collider (LEP) and has a circumference of 27 km [88, 54]. The LHC consists of two beam lines in which protons

circulate in opposite directions. The protons are arranged in 2808 bunches, spaced by 25 ns and each consisting of 1.15×10^{11} protons [54].

Particles are accelerated using eight radio frequency cavities per beam, each of which is fed with a voltage of 2 MV. Thus, the energy of each proton increases by 485 keV per turn in the LHC. In order to guide the proton bunches through the beam pipe, 1232 Niobium-Titanium dipole magnets are installed in the accelerator ring. These magnets are operated at a temperature of 1.9 K using liquid helium. At this temperature, the magnets become superconductive and provide a magnetic field of 8.3 T. Additional magnets are used to focus the beam, which is necessary in particular in the upfront of the collision points [54].

Collisions with a design centre-of-mass energy of 14 TeV occur at four interaction points. At each of these an experiment is located. Both CMS (Compact Muon Solenoid) [89] and ATLAS (A Toroidal LHC ApparatuS) [90] are multi-purpose detectors and target a wide physics programme, from precision Standard Model measurements to searches for physics beyond the Standard Model such as supersymmetry or dark matter candidates. ALICE (A Large Ion Collider Experiment) [91] uses heavy ions collisions to produce matter at very high energy densities to study the quark-gluon plasma which is believed to have existed shortly after the big bang. Finally, LHCb (Large Hadron Collider beauty) [92] is a experiment specialised on the study of physics involving b quarks, which might be a key to understand CP violation.

3.3 The CMS experiment

The Compact Muon Solenoid (CMS) experiment is one of the two large multi-purpose experiments at the LHC. With a diameter of 15 m and a length of 28.7 m it is one of the largest particle physics experiments ever built [89]. An illustration of the detector is shown in Figure 3.7.

The structure of the CMS detector is cylindrical, consisting of a barrel part, which is parallel to the beam pipe, and endcaps which are orthogonal to it. This ensures coverage over most of the phase space. A right-handed coordinate system is used by CMS whose centre lies at the collision point. The x-axis is directed towards the centre of the accelerator, while the y-axis is pointing in the direction of the Earth's surface. More commonly however, polar coordinates are used. The angle ϕ marks the angle with respect to the x-axis. In addition, the polar angle θ is measured with respect to the y-axis and is used to define the pseudorapidity η as

$$\eta = -\ln \tan \frac{\theta}{2}. \tag{3.8}$$

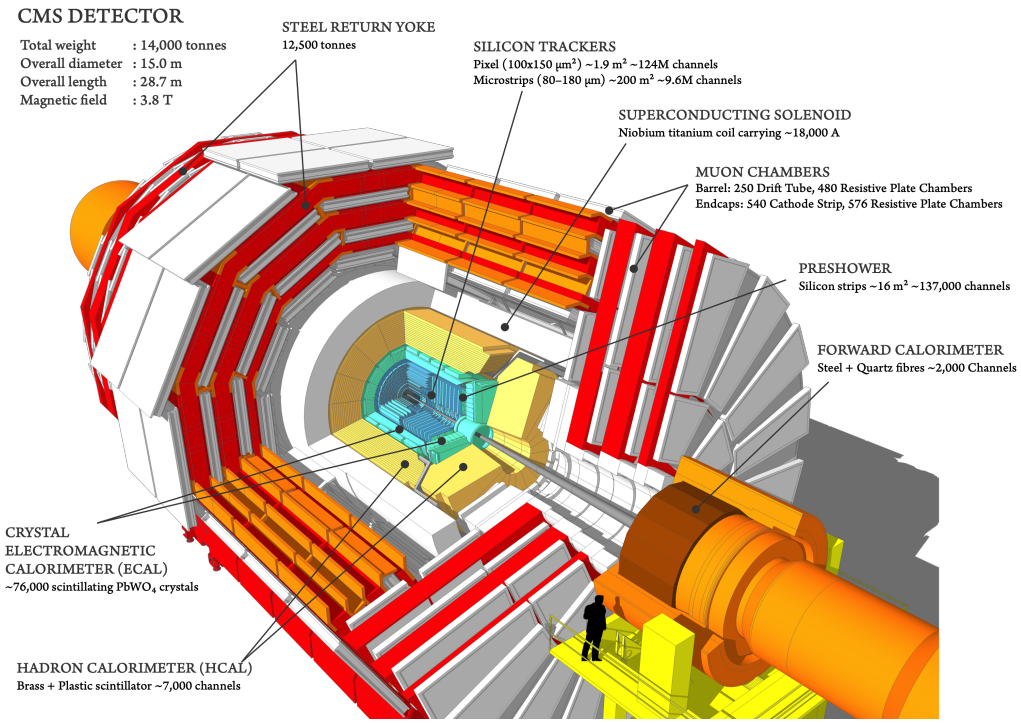

Figure 3.7: Illustration of the CMS detector. In its centre lies the tracking system, which is surrounded by the calorimeters. All these are enclosed in the solenoid magnet. The outermost components are the muon chambers [93].

In addition to the pseudorapidity and the angle ϕ, the transverse momentum p_T and energy E_T are used to denote the momentum and energy transverse to the beam [58].

The detector consists of several layers of material. In its centre lies the tracking system which measures the trajectory of charged particles. At larger distances to the interaction point, an electromagnetic and a hadronic calorimeter are located to measure the energy of particles. These detector components are all contained within a solenoid magnet which provides a magnetic field to bend the particles' tracks. Muon chambers are installed outside of the solenoid volume. By combining the information from all layers, each particle interacting with the detector can be identified.

In the following, specifications about the different detector components are given.

3.3.1 The tracking system

A fully silicon-based tracking system lies at the centre of the CMS detector, covering the space up to pseudorapidities of $|\eta| < 2.5$ as is illustrated in Figure 3.8. It has a total active area of $200\,\mathrm{m}^2$. This detector enables the measurement of tracks and the transverse momentum of particles as is described in Section 4.1. The CMS tracking system consists of two subdetectors: the pixel detector which is closest to the beam line and covers radii up to 16 cm, and the strip detector which surrounds the pixel detector up to radii of 120 cm.

With several thousand particles emerging from collisions during every bunch crossing, excellent spatial resolution and thus fine granularity are required. Additionally, the detector must be radiation tolerant to prevent performance degradation due to continued exposure to large particle fluxes. Furthermore, while increasing the number of detecting layers improves the reconstruction of tracks, a low material budget is required to minimise multiple scattering. The material budget can be expressed in terms of the radiation length, after which a highly energetic electron looses all but $1/e$ of its energy. Across the entire tracking system, the material budget amounts to between 0.4 and 1.8 radiation lengths. Driven by the excellent performance of the pixel detector, the current system achieves a vertex resolution of up to 10 µm for high momentum tracks [94].

The CMS pixel detector

The pixel detector, being closest to the beam line features a particularly high granularity with a pixel size of $100\,\mu\mathrm{m} \times 150\,\mu\mathrm{m}$. It consists of four layers spaced at radii between 3 cm and 16 cm to the beam line in the barrel part and of three layers in the endcaps. These layers are equipped with modules, which consist of a silicon sensor and readout electronics. These components are connected via metallic bonds. The detector is cooled using a two phase CO_2 cooling system [95]. A detailed description of this subdetector is given in Chapter 4.

The strip detector

This detector supplements the pixel detector in order to extrapolate the tracks to larger radii. The sensor of this detector is not pixelated but segmented in strips with a typical size of $10\,\mathrm{cm} \times 80\,\mu\mathrm{m}$. This facilitates the readout of the detector and reduces the manufacturing costs. The strips provide a one-dimensional spatial information. To obtain a two-dimensional hit position, the layers of adjacent strips are rotated by a stereo angle of around 100 mrad with respect to each other. While

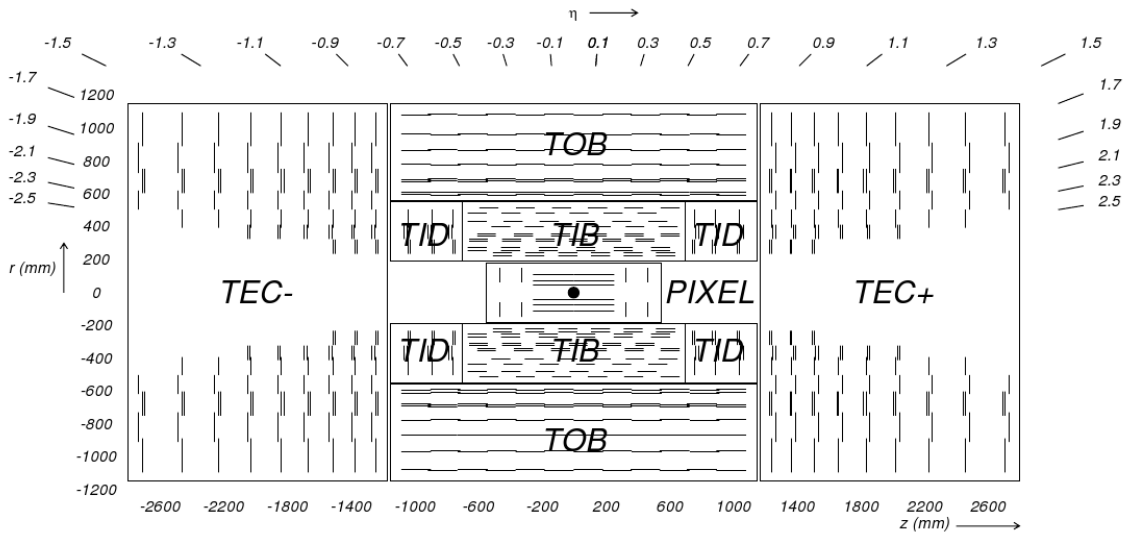

Figure 3.8: Illustration of the different layers of the CMS tracking system. The detector consists of the tracker inner barrel (TIB) and the tracker inner disks (TID) in the central part of the detector and of the tracker outer barrel and the tracker endcaps in regions further away from the interaction point [95]. Here, the Phase 0 detector, which was in use until 2016, is depicted [96].

the granularity is reduced with respect to the pixel detector, the spatial resolution remains sufficient for trajectory reconstruction as the particle fluxes are lower in this region of the detector [97, 98].

3.3.2 Calorimetry

To measure the energy of particles, an electromagnetic (ECAL) and a hadronic calorimeter (HCAL) are installed in the CMS detector. Both cover a large solid angle to ensure maximum detection efficiency. This is particularly important for the correct reconstruction of the missing transverse energy (MET), which is evaluated from the momentum imbalance in a plane orthogonal to the beam line. The missing transverse energy is associated to particles such as neutrinos or so far unknown BSM particles which do not interact directly with the detector.

The energy resolution of calorimeters can be parametrised as following:

$$\left(\frac{\Delta E}{E}\right)^2 = \left(\frac{c_s}{\sqrt{E}}\right)^2 + \left(\frac{c_n}{E}\right)^2 + c_c^2 \tag{3.9}$$

with the stochastic term c_s, which takes into account intrinsic shower and sampling fluctuations, the noise term c_n which parametrises the electronic noise, and the constant term c_c which describes detector inhomogeneities and calibration uncertainties [99].

ECAL

The electromagnetic calorimeter is a homogeneous calorimeter which fully absorbs the energy of electrons, positrons and photons. The energy is measured by collecting the scintillation light produced by electromagnetic showers in the crystals of the detector. These showers are produced by successive steps of pair production and Bremsstrahlung. This excites the atoms of the crystal lattice, which emit light when returning to their ground state. On average 4.5 photoelectrons are produced per deposited MeV of energy.

The ECAL consists of 75848 lead-tungsten ($PbWO_4$) crystals. Contrary to the tracking system which intents to disturb particles as little as possible, the calorimeter aims to completely stop the particles mentioned above, such that they deposit all of their energy in the detector. This explains the choice of the material, as $PbWO_4$ possesses a high density of $8.3\,\mathrm{g\,cm^{-3}}$ and thus a small radiation length ($\chi_0 = 0.89\,\mathrm{cm}$). Therefore, with a length of only $\sim$20 cm, the crystals contain the shower produced by the particles mentioned above. The crystal sizes vary between $2.2\,\mathrm{cm} \times 2.2\,\mathrm{cm}$ in the barrel part and $2.9\,\mathrm{cm} \times 2.9\,\mathrm{cm}$ in the endcaps. Together with the lower occupancy and radiation damage, this justifies the improved resolution in the barrel part with respect to the endcaps. The deposited scintillation light is collected by avalanche photodiodes in the barrel and vacuum phototriodes in the endcaps [100].

In addition, a preshower detector is installed in front of the ECAL endcaps, which improves the discrimination between photons produced in the hard interaction and photons created in the decay of neutral pions. The preshower detector is made of two lead planes connected to silicon sensors [100].

The detector resolution obeys to Equation 3.9 with $c_s = 2.8\%$, $c_n = 12\%$ and $c_c = 0.3\%$. This equates to an energy resolution between 1.7% and 4.5% for electrons with $p_T \sim 45\,\mathrm{GeV}$, as has been measured in decays of the Z boson into e^+e^- [101, 102, 100].

HCAL

The hadronic calorimeter determines the energy of the hadrons by measuring the shower produced in their interaction with the detector. The structure of these showers is more complex than for pure electromagnetic showers, as strong interactions with the absorber need to be taken into account, involving processes such as nuclear

excitations or spallation. Often hadronic and electromagnetic showers coexist, since electromagnetic showers also arise from hadrons such as in the decay of neutral pions into two photons. To take into account all of these processes, the thickness of the HCAL is characterised by the number of nuclear radiation lengths, which is the mean distance covered by highly energetic hadrons before undergoing inelastic interactions with the absorber. Typically, a material's nuclear radiation length is larger than its radiation length, which explains why the thickness of the HCAL of around 1 m is larger than that of the ECAL [99, 103].

The HCAL is a sampling calorimeter and consists of steel or brass plates, interfaced with plastic scintillating tiles, which collect the hadronic showers. The produced scintillation light is read out using photodiodes and photomultipliers. This detector has been designed to sustain large radiation doses as particle fluxes are particularly high especially in the endcaps.

Similarly to the other detector components, the HCAL consists of a barrel part which covers pseudorapidities up to $|\eta| < 1.3$ and endcaps which reach $|\eta| < 3.0$. To extend coverage of the solid angle, a very forward calorimeter has been installed, covering pseudorapidities $|\eta| < 5.2$. This subdetector is also used for the measurement of the luminosity delivered to CMS [104]. Furthermore, an outer calorimeter is mounted outside of the magnet in order to collect showers which are not fully contained within the HCAL. This is necessary because of the limited space inside of the solenoid, so that only between 5.8 and 10.6 nuclear interaction lengths can be inserted. The outer calorimeter adds 11.8 nuclear interaction lengths to the absorber [103]. The resolution of the HCAL is lower than that of the ECAL, with a stochastic term of 115% and a constant term of 5.5% [105]. However combining its information with that of the ECAL and other subdetectors enables to improve the resolution using the particle flow algorithm which is described in Section 3.3.6.

3.3.3 The solenoid

A large solenoid is installed within CMS, primarily to bend the trajectory of charged particles. This allows to identify the charge of the particle and provides a measurement of its momentum. The magnet consists of a Niobium–titanium (Nb-Ti) coil through which a current of around 20 kA circulates. This produces an magnetic field of 3.8 T at the centre of the experiment. The coil is cooled to $-268.5\,^{\circ}\mathrm{C}$ so that the Nb-Ti becomes superconductive.

A three layered iron return yoke is installed to guide the magnetic field through the muon chambers. The resulting magnetic field of 2 T in the muon chambers improves the resolution on the momentum of muons [89].

3.3.4 Muon detection

The CMS muon system consists of four detecting layers interleaved with the solenoid return yoke [106]. While all other particles interacting with the detector are stopped in the solenoid at the latest, muons traverse the entire detector and are the only particles to interact with the muon chambers. The detecting layers consist of gaseous detectors, three different types of which are in use:

- Drift tubes (DT): These devices are used in the barrel part of the subdetector. A metallic, positively charged wire lies inside the tubes, such that when incoming muons ionise the atoms of the gas in the tube, the liberated electrons drift towards the positively charged wire and induce a current in the wire. These detectors have a spatial resolution of around 260 µm [107].

- Cathode strip chambers (CSD) are used in the endcap regions, where the magnetic field is less homogeneous and where higher particle rates are expected. Inside of the gas volume of these devices lies an array of wires, whose charge is opposite for vertical and horizontal wires. Thus, not only electrons are collected, but also the positively charged ions. By combining the hit information of electrons and ions a two dimensional hit information for each particle is obtained. As the wires are close to each other, drift times are short so that the cathode strip chambers can be used by the trigger system which will be described in Section 3.3.5. Depending on the chamber type, resolution ranges between 47 µm and 243 µm [108].

- Resistive plate chambers (RPC) are installed in both the barrel part and the endcaps and improve the time resolution of the detector to 1 ns. These detectors also contributes to the trigger decision. The chambers consist of two parallel plates which are oppositely charged. Electrons produced in the gas (mostly $C_2H_2F_4$) through ionisation create avalanches by in turn ionising other atoms. The charge is collected by readout strips [109].

Combining all three technologies and information from the tracking system, a transverse momentum resolution of 1.0% in the barrel and 3% in the endcaps for muons with $p_T < 100\text{GeV}$ is reached. This resolution deteriorates to up to 7% for transverse momenta up to 1 TeV [110].

3.3.5 Trigger system and data acquisition

The CMS detector operated at a peak instantaneous luminosity reaching around $2 \times 10^{34}\,\text{cm}^{-2}\,\text{s}^{-1}$ in 2017 and 2018, and on average 35 collisions occurred every

25 ns [73]. It is therefore not possible to analyse and store the information of every single event, as this would result in a data rate of approximatively 60 Tbit s^{-1}. A dedicated triggering system has been designed to filter out events which reveal physics processes of interest from already well-known interactions. One major requirement of the system is that it performs extremely fast in order to cope with the bunch crossing rate of 25 ns [111].

For this purpose, CMS employs a two-staged trigger system. In a first step, the L1 trigger utilises information from calorimeters and muon detectors, selecting events containing muons or large p_T jets or MET. This reduces the event rate by several orders of magnitude to around 100 kHz. The L1 trigger decision is taken within 4 µs. After passing the L1 trigger, data from different parts of the detector, which are buffered until validation from the L1 trigger, are accumulated and synchronised. From this, high level objects are reconstructed and transmitted to the high-level trigger (HLT). These trigger paths are designed specifically to meet the needs of physics analyses carried out by CMS. Events are recorded if they fulfil the selection criteria of at least one of those HLT trigger paths. The final event rate is then approximatively 1 kHz [112].

The data of the selected events are propagated to the Worldwide LHC Computing Grid, from where it is accessible for analysis to the entire world [113]. The Grid is divided into three Tiers. The Tier 0 centre located at CERN hosts the HLT farm which together with other computing resources performs the first event reconstruction. Data is typically stored at Tier 1 centres while data analysis and production of Monte Carlo datasets are performed on Tier 2 and Tier 3 sites, which are spread over all countries contributing to the LHC efforts.

3.3.6 Particle and object reconstruction

After validation from the HLT trigger, events are fully reconstructed. For this purpose, information gathered from the tracking detectors and the muon chambers is combined with that of the calorimeters. This is because particles cross multiple components of the detector and typically leave a trace on several of them. Combining all these traces enables to reconstruct each individual particle that was created in the event [114].

In a first step, the trajectory of particles is reconstructed using the combinatorial track finding algorithm [115]. This algorithm utilises both hits in the muon chambers and in the tracking system. Tracks are identified by interpolating hits in the different detector layers. In order to minimise the misidentification rate while maintaining a high reconstruction efficiency, the algorithm uses an iterative tracking strategy. Thus

in a first step, tight selection criteria are applied to reconstruct unambiguous tracks. These criteria are then loosened as more tracks are reconstructed.

Signals in both calorimeters are gathered in so-called clusters. For that purpose, cluster seeds are placed in each calorimeter cell where the energy deposit exceeds a fixed threshold. Adjacent cells which also recorded an energy deposit above a defined threshold are then combined to this cluster. It is assumed that each cluster seed originates from a single particle.

After building track seeds and calorimeter clusters, these traces are combined into blocks, each block ideally containing all traces left in the detector by a single particle. To that aim, a link algorithm has been developed. This algorithm defines link distances between different objects such as a track and a calorimeter cluster, or between an ECAL and an HCAL cluster. The blocks are then built by simultaneously minimising the number of built blocks and the link distances [114].

The type of the particle creating each block is then determined using the particle flow algorithm [114]. This algorithm uses an iterative procedure. In a first step, blocks originating from muons are identified, as these particles are the only ones leaving traces in the muon chambers. After muon reconstruction, electrons are identified. This is complicated by the presence of Bremsstrahlung photons, which must be correctly associated to the emitting electron to reconstruct its original energy. This is verified if they are tangent to the trajectory of the electron.

After removing blocks corresponding to leptons, the remaining particles are reconstructed. To distinguish blocks originating from photons and charged and neutral hadrons, the momentum measured from the trajectory of particles is compared with the deposited energy in the calorimeter clusters. If the energy of a cluster is incompatible with the momentum of a track or if no track is pointing in the direction of the cluster, neutral particles are identified. Depending on whether the largest energy deposit lies in the ECAL or the HCAL, photons or neutral hadrons are reconstructed. Remaining blocks are associated to charged hadrons. Following this strategy, all particles interacting with the detector can be identified.

Using the particle flow algorithm allows to considerably improve the particle reconstruction performance and the momentum and energy resolution. In particular the measurement of jet kinematics using solely information from the calorimeters is limited by the low resolution of the HCAL, such that the jet energy resolution of the ECAL and HCAL lies between 5% and 40% depending on the jet p_T. Combining that information with that of other subdetectors improves the jet energy resolution to between 4% and 15% [116]. Furthermore the jet momentum response (which is defined as the ratio between the measured momentum and the momentum of the jet at generator level) improves from ∼65% to ∼90% for jets with $p_T \sim 100\,\text{GeV}$.

Similarly, the efficiency to correctly identify muons is slightly improved while considerably lowering the mistag efficiency of hadrons by more than an order of magnitude compared to previously available identification algorithms [114].

In the following, details about the reconstruction of objects used in physics analyses are given.

- `Primary vertex`
  The primary interaction vertex which originates from the hard scattering process is reconstructed from the particle tracks measured by the tracking system. In a first step, tracks compatible with the main interaction region are selected by setting requirements on their transverse impact parameter with respect to the beam spot position, the number of hits in the pixel and in the strip layers, and on the χ^2 of the fit. A dedicated algorithm clusters the selected tracks which originate from the same vertex. The selected primary vertex is the reconstructed vertex with the largest sum over the p_T^2 of all its tracks. The selected primary vertex must be within 24 cm to the nominal interaction point in the z direction and 2 cm in the orthogonal plane [115].

- `Photons`
  Photons interact primarily with the electromagnetic calorimeter (ECAL). To reconstruct these particles, all measured energy deposits in the ECAL are grouped in clusters, because the energy is usually shared amongst several adjacent crystals. Typically, 97% of the particle's energy is recorded within a crystal array of size 5×5. A cluster is built from a seed, which is a crystal with a local maximum in deposited energy. Neighbouring crystals are then incorporated in the cluster if their energy exceeds 80 MeV in the barrel and 300 MeV in the endcaps. Additionally, photon conversion into an electron-positron pair ahead of the ECAL is taken into account by merging clusters into so-called superclusters. These regroup clusters compatible with an electron-positron pair which separated in the ϕ direction because of the applied magnetic field [117].

- `Muons`
  Depending on the use case, muons are reconstructed using solely information from the tracking system or from the muon chambers, or by combining the information from both detector systems. Additional selection criteria are applied to identify so-called prompt muons, which originate directly from the hard scattering process and to discriminate them from cosmic muons or non-prompt muons. These identification criteria use the fact that prompt muons are typically produced at large angular distances to other final state particles,

whereas muons originating from hadronic processes are typically surrounded by hadrons. Additional selection criteria involve the quality of the track fitting, and the impact parameter of the track with respect to the primary vertex of the interaction [118].

- `Electrons`
  Reconstructing electrons is more difficult than reconstructing muons as they do not leave such a distinct signal in the detector, and because of the presence of Bremsstrahlung photons mentioned earlier. These photons are mostly emitted in the ϕ-direction because of the bending of the electron path in the magnetic field. Electron tracks are reconstructed using the Gaussian sum filter algorithm, which considers additional photon radiation, as well as interrupted tracks from multiple scattering on the tracking layers [119]. A multi-variate analysis is used to combine these tracks with electromagnetic clusters that are reconstructed using the same algorithm than is used for photons. This enables to identify prompt electrons from electrons produced in photon conversions, decays of heavy quarks, or from jets with large energy deposits in the ECAL [101].

- `Jets`
  Hadronisation products emitted by partons are collected using jet algorithms as described in Section 3.1.3. Additionally, special algorithms are used to identify and remove contributions from pileup and to align the detector resolution in simulation with that of data as is explained in Section 9.2.2. Jets are only selected for analysis if they satisfy a number of quality requirements, such as a minimum number of constituents, and a given fraction of charged and neutral components.

- `Jets originating from b quarks`
  With a lifetime of around 1.5 ps, b hadrons travel up to 1 cm in the detector before decaying [15]. This decay produces a secondary vertex, which is distinct from the location of the hard scattering. Thus, jets originating from such a decay can be reconstructed for example with the DeepCSV algorithm [120]. This deep neural network based algorithm uses track and secondary vertex properties such as track impact parameters, or the mass and flight distance significance of the secondary vertex for the discrimination [120].

- `Missing transverse momentum`
  The missing transverse momentum is reconstructed as the negative vectorial sum of the momentum of all reconstructed particles in the event. This explains why hermeticity of the detector is crucial to correctly reconstruct the missing transverse energy in an event, as particles escaping detection can falsify the measurement.

3.3.7 Monte Carlo event generators

While the previous Sections detailed the acquisition and reconstruction of data from the CMS detector, many analysis also use Monte Carlo (MC) generators to produce simulated events to directly compare expectations from theory with measurements. These generators have vastly improved in the last years thanks to considerable efforts by theorists, for instance by taking into account higher order corrections for matrix element calculations. The simulated events greatly resemble those originating from real collisions as not only the hard interaction process can be modelled, but also initial and final state radiation, particle decays and hadronisation, as well as pileup effects and underlying events [121, 122]. This is done by using probabilistic methods to approximate non analytically solvable equations, such as the complex phase space integrals describing the cross section of processes. Examples for such generators are MADGRAPH5_aMC@NLO or Powheg. Madgraph is used to calculate matrix elements and process cross sections to leading or next-to-leading order in perturbation theory [123]. Powheg operates similarly, and allows for one additional radiation jet in the calculation of the matrix element [124, 125, 126, 127]. Another generator which specialises on the computation of matrix elements at tree and one-loop level is OpenLoops [128, 129]. The parton shower and underlying events is usually simulated using the Pythia generator [130].

Additionally, the interaction of particles produced in a generated event with the CMS detector can be simulated. This provides theoretically based expectations for many processes which can be compared to the data collected by the CMS experiment or to calibrate analysis methods. In this work, the Geant4 software is used to model the interactions of particles with our detector. This C++ based framework contains a detailed description of the geometry and material distribution of CMS. This model is used to evaluate interactions with the detector, such as particle ionisation or annihilation, scattering processes or photon interactions [131].

Part I

Performance of the modules for the innermost layer of the CMS Phase I pixel detector upgrade

Chapter 4

The pixel detector of CMS and its Phase I upgrade

In the centre of the CMS experiment lies a silicon tracking detector which reconstructs the trajectory of charged particles. It is composed of two subdetectors: the microstrip and the pixel detector as is presented in Section 3.3.1. This thesis focuses on the CMS pixel detector, which is the innermost component of the experiment. It is therefore exposed to particularly high particle rates and confronted with large radiation damage. This challenge is solved in the CMS experiment by using dedicated technologies both on the sensor side as well as for the readout electronics.

As the LHC gradually increases its instantaneous luminosity, the pixel detector needs to be adapted to these more stringent conditions. To meet these demands, the Phase 0 pixel detector which was developed for the beginning of Run I in 2008 was replaced with an improved version, the Phase 1 upgrade, in early 2017.

After presenting basic concepts of tracking detectors in Section 4.1, the CMS pixel detector is described in Section 4.2. This Section also discusses the impact of the Phase 1 upgrade on the physics programme of the CMS experiment. Finally planned developments after the Phase 1 upgrade are summarised in Section 4.3.

4.1 Semiconductor tracking devices

Tracking devices are a key component of many high energy particle physics (HEP) experiments, measuring the trajectory of charged particles, as well as their charge and momentum when the detector is placed in a magnetic field. Typically located close to the interaction point, they are exposed to very large particle hit rates in the ATLAS and CMS experiments, so that high granularity and excellent spatial resolution are

required of these detectors. These devices typically use silicon as detecting material, in which particles create charge via ionisation. This section reviews the basic mechanisms of the interaction of particles with matter, and elucidates how charge is created and processed within a tracking device. Finally, the basic working principles of tracking detectors are described.

4.1.1 Interaction of particles with matter

Particles interact with matter via two main mechanisms: ionising and non-ionising energy losses. The precise interaction mode depends on the particle type, its charge and its mass.

Particles with a mass significantly larger than the electron mass ($m_e = 0.51\,\mathrm{MeV}$ [15]) interact via sequential collisions in the absorption medium. These interactions typically ionise the atoms in the medium. The fundamental force involved is the electromagnetic force, which is why neutral particles cannot cause direct ionisation and are therefore not detected by tracking devices.

The mean energy loss per distance travelled through the medium $\left\langle -\frac{dE}{dx} \right\rangle$, also called the stopping power, is described by the Bethe-Bloch equation [15]:

$$\left\langle -\frac{dE}{dx} \right\rangle = K z^2 \frac{Z}{A} \frac{1}{\beta^2} \left[\frac{1}{2} \ln \frac{2 m_e c^2 \beta^2 \gamma^2 W_{max}}{I^2} - \beta^2 - \frac{\delta(\beta\gamma)}{2} \right] \tag{4.1}$$

with:

- $K = 4\pi N_A r_e^2 m_e c^2$ a constant with c the speed of light, N_A the Avogadro constant, and r_e the classical electron radius,
- z the charge of the incident particle in units of the electron charge,
- Z, A the atomic number and atomic mass of the absorption medium,
- $\beta = v/c$, v being the velocity of the incident particle,
- γ its Lorentz factor,
- $m_e c^2$ the electron's rest energy,
- I the medium dependent excitation energy,
- W_{max} the maximum kinetic energy that can be transferred in a single collision
- $\delta(\beta\gamma)$ a correction term leading to a saturation at high energies.

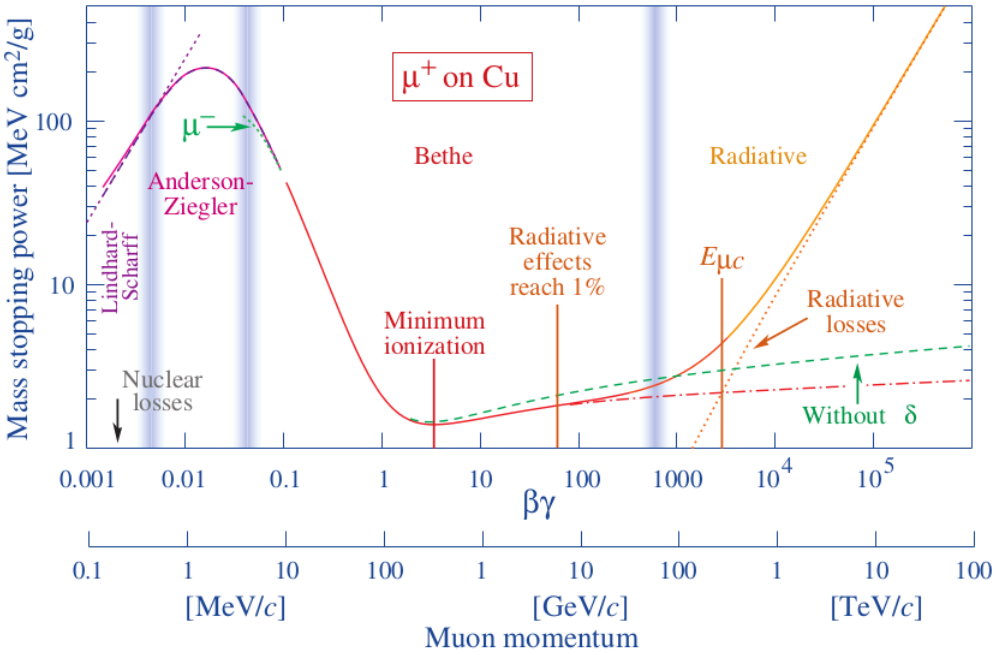

Figure 4.1: Mass stopping power for antimuons in copper as a function of $\beta\gamma$ [15].

The Bethe equation is valid for particles whose velocity lies in the range $0.1 < \beta\gamma < 1000$ and which interact with materials with an intermediate atomic number. An example is shown in Figure 4.1 in the case of incident antimuons in copper. In the range $0.1 < \beta\gamma < 1$, the kinematic term $\frac{1}{\beta^2}$ dominates. For energies in the range $1 < \beta\gamma < 1000$, the logarithmic term provokes a rise in the mass stopping power which however saturates at even higher $\beta\gamma$.

For electrons and positrons, the Bethe formula does not hold, as radiative energy loss processes have to be taken into account. While ionisation remains the dominant energy loss mechanism at energies of a few MeV, Bremsstrahlung dominates at larger energies as is shown in Figure 4.2. The mass stopping power as a function of the energy of electrons and positrons is described in [132, 133]. While the energies relevant in HEP experiments are above the critical energy where the energy losses from ionisation and Bremsstrahlung are equal, the contribution from ionisation is sufficient to create detectable charge in the detector [15].

When interacting with matter, particles not only loose energy but are also deflected by many scatterings with the nuclei in the material via the Coulomb force or the strong force in the case of hadrons. The average deviation angle is however very small ($\Sigma_{dev} \sim 0.1°$) for detector widths typical of LHC experiments [134].

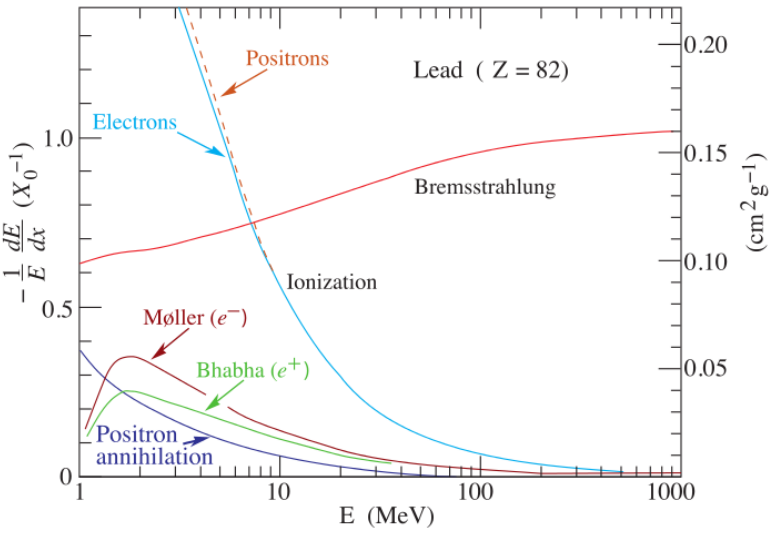

Figure 4.2: Energy loss per radiation length in lead as a function of electron energy [15]. At energies relevant in high energy physics experiments, Bremsstrahlung is the dominant mechanism of energy loss, while a small contribution from ionisation remains.

4.1.2 Signal creation

In order to detect a signal, charge has to be produced and collected. A brief review of these processes in silicon detectors is given here.

Properties of semiconductors and doping

Semiconductors are frequently used for tracking devices since their electric properties and their conductivity can easily be controlled by the addition of impurities in the material. Silicon in particular is heavily used because its properties are well studied, and it is comparatively cheap to manufacture. Its conductivity arises from the excitation of electrons which move from the valence band to the conduction band. The valence band corresponds to the highest energy band in which electrons are present at absolute zero temperature, and the conduction band to the lowest energy level which, when filled with electrons, makes the material conductive. While the energy gap of insulators is too large to thermally excite electrons and elevate them from the valence to the conduction band, this does not apply for semiconductors. Indeed silicon has a relatively small mean ionisation energy of 3.6 eV. Because of momentum conser-

vation, this energy is however larger than the band gap energy of 1.12 eV, which is why the band gap of silicon is called an indirect band gap. The additional energy is carried off by phonons, and dissipates as thermal energy [134].

An electron can be excited when energy is deposited in the material. If the electron is propagated to the conduction band, it becomes a free charge carrier. Additionally, an empty position in the valence band is created, called a hole, which can also carry charge, although its mobility is reduced with respect to that of electrons in silicon.

The conductivity of silicon can be further increased by doping the material. In this process, atoms of adjacent atomic groups replace certain silicon atoms in the crystal lattice. Elements of the higher group have an additional electron that occupies the conduction band, which is called n-doping. Similarly, elements of lower atomic groups will present a hole in their valence band, which is called p-doping. Practically, n-doping introduces impurity levels near the conduction bands, while p-doping creates impurity levels near the valence band. This reduces the band gap between the conduction and the valence bands, and therefore facilitates the creation of charge carriers in the material.

pn-junctions

Materials with p-doping and n-doping can be combined to form pn-junctions which are the building blocks of sensors used in tracking detectors. When brought together, electrons and holes diffuse across the junction and recombine, leading to a region without free charge carriers in the material, the depletion zone. In the depletion zone, atoms used for doping are now ionised, either by accepting an additional electron, or by losing one. This creates an electric field which generates a built-in voltage.

To increase the width of the depletion zone, an external bias voltage V_b reinforcing the built-in voltage V_{bi} is applied. In case of a diode composed of a strongly p-doped silicon layer associated with a thicker, less strongly n-doped layer, the depletion width can be written as

$$w_d = \sqrt{\frac{2\varepsilon(V_b + V_{bi})}{Ne}} \tag{4.2}$$

with the dopant concentration N in the n-doped layer and the dielectric constant ε [135].

In this zone, no free charge carriers are present. Therefore, when an incoming particle interacts with the material, the charge deposited by it drifts through the sensor because of the applied electric field. A current is then induced in the electrodes which can be measured [136, 137]. Ideally the entire width of the sensor is depleted.

The voltage that needs to be applied for this purpose is called the depletion voltage.

Leakage current

In reality, the depletion zone will not be completely deprived of charge carriers. This has two reasons:

- Charge can diffuse from the non-depleted region into the depletion zone.
- Thermal excitations can free electrons from the valence band.

The current that therefore still flows within the material is called leakage current. Since thermal excitations become more likely at higher temperatures, it strongly depends on temperature:

$$I(T) \propto T^2 \exp^{-E/2kT} \tag{4.3}$$

where $E = 1.2\,\mathrm{eV}$ is the activation energy, and k the Boltzmann constant. Thus the leakage current roughly doubles when the temperature increases by 7 °C [135].

For operation, the leakage current needs to be much lower than the current that originates from the interaction with incident particles, otherwise the deposited charge will not be discernible. This is why detector modules are cooled during data taking.

Charge sharing and spatial resolution

In a fully depleted sensor, an incoming particle creates one electron-hole pair per 3.6 eV of deposited energy. The accumulated charge drifts through the sensor because of the electric field in the depletion zone. The drift velocity is given by $\vec{v} = \mu\vec{E}$ and is proportional to the mobility μ of charge carriers. However, the drift does not fully follow the field lines due to multiple effects:

- Random thermal motion. This leads to a Gaussian distribution of the arrival position with a width:

  $$\sigma = \sqrt{2Dt} \tag{4.4}$$

  where t is the charge collection time and D is the diffusion constant that depends on the temperature and on the mobility of the charge carriers. The effect of random thermal motion is however rather small and typically amounts to a few micrometers.

- Presence of a magnetic field. In order to measure a particle's charge and momentum, a magnetic field is applied in HEP experiments. This magnetic field also modifies the trajectory of the collected charge in the silicon through the Lorentz force. The Lorentz angle describes the lateral deflection of particles due to this effect:

$$\tan \theta_L = \mu_H B_\perp \tag{4.5}$$

  where $B_\perp$ is the component of the magnetic field that is orthogonal to the electric field and μ_H is the Hall mobility. The Hall mobility is directly proportional to the mobility by a temperature dependent factor.

Both effects lead to distributing the acquired charge over several pixels which is called charge sharing. This helps to increase the position resolution as is briefly illustrated below.

For a basic binary detector with a pitch size p, the hit information is a uniform distribution over the pitch size described by the function $P(x) = 1/p$. Therefore, the position measurement will be at the centre of the pixel. Without charge sharing between neighbouring pixels, the spatial resolution is given by the square root of the variance:

$$\sigma_x = \Big(\int_{-\frac{p}{2}}^{\frac{p}{2}} x^2 P(x) dx \Big)^{\frac{1}{2}} = p/\sqrt{12} = 0.29 \cdot p. \tag{4.6}$$

The resolution can be improved using charge sharing described above if pulse height information is available. For this, dedicated methods such as weighted interpolation, where the hit position is calculated from the charge weighted pixel positions, or the η algorithm [138] exist. The η algorithm can be used if the charge is shared between two pixels, and gives the hit position as $x_h = p \cdot f(Q_{\text{left}}/(Q_{\text{left}} + Q_{\text{right}})) + x_{\text{left}}$, with p the pitch size, Q_i the collected charge in pixel i, $f(\eta)$ the normalised distribution of the η variable and x_{left} the position of the pixel on the left. This increases the position resolution by on average a factor two, depending on the pitch size and the quality of the pulse height measurement [135, 134].

4.1.3 Signal processing

Several steps are necessary to convert the charge deposited by a particle in the sensor to an electronic signal which can be analysed. Figure 4.3 shows a generic case of a processing chain before digitisation of the signal. As explained in Sections 4.1.1 and 4.1.2, particles create charge in sensors by ionisation. The induced current is measured and transferred to the readout electronics. In a first step, the signal is amplified, as the collected signal is typically very small ($\sim 4 \times 10^{-15}$ C). The amplified pulse is

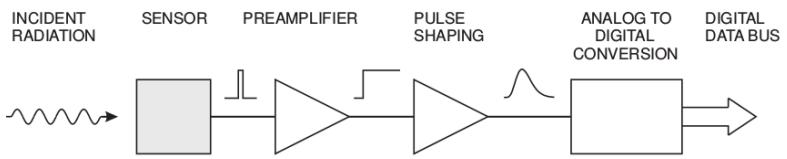

Figure 4.3: Processing chain of a signal in the readout electronics. An incident particle creates charge by ionisation in the sensor. This signal is collected, amplified and shaped before being digitised [135].

then shaped to increase the signal-to-noise ratio. Both the pulse amplifier and the pulse shaper belong to the main producers of electronic noise in the readout chain. After shaping, the signal is digitised for further processing. A concrete example is given in Section 4.2.5 which describes the readout chip used in the CMS pixel detector [135].

4.1.4 Hybrid detector technology

In most current tracking detectors, sensors and readout electronics are manufactured separately. A connection is assured via a metallic bond, such as a bump bond. A pixelated metallised layer at the interface between the sensor and the bump bond ensures electric conductivity. A sketch illustrating this process is given in Figure 4.4.

For pixel detectors, several thousand pixels are placed on the same structure both in the sensor and in the readout electronics. In the sensor, each pixel corresponds to a highly doped region in the silicon bulk, forming a pn-junction.

Today, new detector technology developments aim at producing monolithic technologies in which the sensor and the readout electronics are produced together. This would simplify the production of pixel detectors, as the bump bonding process would become unnecessary. As this process is prone to many technical challenges and is not fully efficient as is discussed in Section 6.3.3, removing the bump bonding process from the production chain would be advantageous.

4.1.5 Working principle of tracking detectors

Using the processes described above, tracking detectors measure the positions of the interactions of particles with the detector material. With their excellent spatial resolution, trajectories of charged particles can be recorded, vertices can be deducted, and a particle's energy and momentum can be reconstructed.

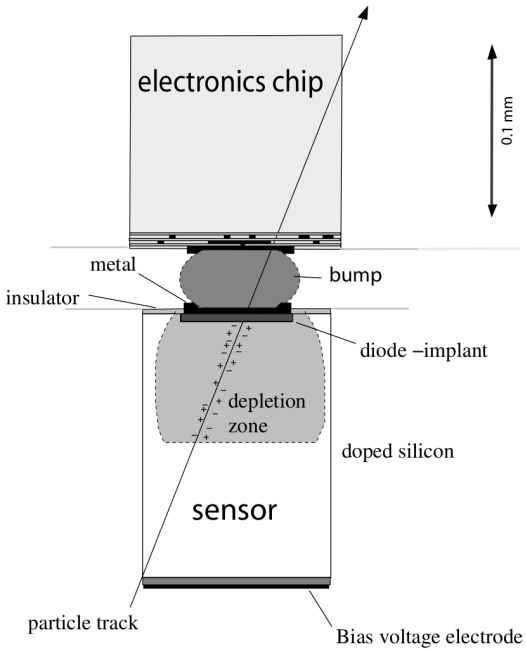

Figure 4.4: Illustration of the hybrid detector technology. A cell in the sensor is connected to readout electronics using a metallic bump [134].

The working principle of a tracking detector is illustrated in Figure 4.5 in the case of a pixel detector with four layers. Each particle crossing the detector leaves a signal in the detecting material. By using multiple detecting layers, several space points can be recorded per particle. Making use of the high granularity of this type of detector, these interaction points can be interpolated to reconstruct the trajectory of particles with a high precision.

When applying a magnetic field B in the detector volume, a tracking detector can also be used to infer on the momentum of an incoming charged particle. The Lorentz force will bend the path of charged particles, leading them onto a helix trajectory. The momentum of the particle in GeV is then linked to the curvature radius R in meters of the measured trajectory as

$$p_T = 0.3 \cdot B \cdot R \cdot q \tag{4.7}$$

with q the charge of the particle, and B the applied magnetic field. Furthermore, the direction of the curvature of the path reveals the sign of the charge of the particle.

However, several factors complicate the reconstruction of the trajectory, as is illustrated in Figure 4.5. One issue are fake signals which are not associated to any

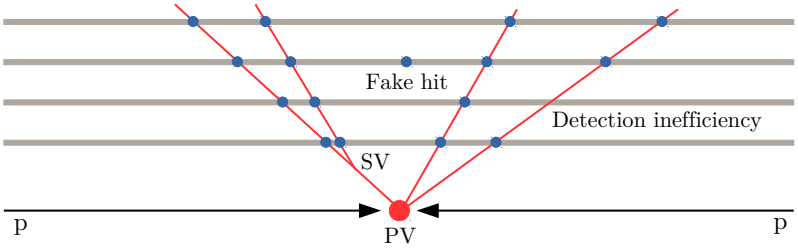

Figure 4.5: Illustration of the working principle of a multi-layered pixel detector. Two protons collide with each other at the primary vertex (PV). The collision creates particles which leave a trace (blue dots) in all four layers of the pixel detector. Red lines represent the trajectories reconstructed from the hits in all detecting layers. Secondary vertices (SV) can be reconstructed from tracks that don't originate from the primary vertex. Detection inefficiencies and fake hits complicate the reconstruction of tracks and vertices.

trajectory and which arise for instance from detector noise. Pileup events or scattering processes can also create additional signals in the detector. Another issue are detector inefficiencies, leading to missing interpolation points in one or several detector layers.

The number of measurement points strongly impacts the performance of the trajectory reconstructing algorithm as is illustrated with a trajectory defined by $N+1$ equally spaced measurement points. These points are located at the positions $z_0, ..., z_N$ and σ designates the measurement error on the position. The parameter $L = z_N - z_0$ gives the distance between the first and the last measurement point, and the parameter $z_c = \frac{z_N - z_0}{2}$ describes the distance between the centre of the trajectory and the interaction point.

A straight line can be fitted to these measurement points, where the errors on the two fit parameters (slope and offset) are described by

$$\sigma_a = \sqrt{\frac{\sigma^2}{N+1}} \tag{4.8}$$

$$\sigma_m = \sqrt{\frac{\sigma^2}{N+1}\frac{12N}{N+2}\frac{1}{L^2}} \tag{4.9}$$

where the errors are uncorrelated if the origin of the reference system is located at the centre of the trajectory.

Thus the impact parameter d_0, giving the distance of closest approach of the trajectory to the interaction point can be written as a function of the slope m and

offset a of the fit as $d_0 = a - mz_c$. The error on the impact parameter is then obtained using error propagation:

$$\begin{aligned}\sigma_{d_0} &= \sqrt{\sigma_a^2 + \sigma_m^2 z_c^2} \\ &= \sqrt{\frac{\sigma^2}{N+1} + \frac{\sigma^2}{N+1}\frac{12N}{N+2}\frac{1}{L^2}}\end{aligned} \tag{4.10}$$

which depends on the number of measurement points, the spatial resolution and the parameter L [139, 140].

Similarly, the resolution on the momentum measurement can be approximated by the Gluckstern formula, where N denotes the number of measurement points:

$$\frac{\sigma_{p_T}}{p_T} = \sqrt{\frac{720}{N+4}}\frac{\sigma}{aBL^2}p_T \tag{4.11}$$

Here, $a = 0.3\,\mathrm{GeV\,T^{-1}\,m^{-1}}$ is a constant, σ denotes the spatial resolution of the detector and L is the length of the trajectory, when projected onto a plane orthogonal to the magnetic field B [141].

These examples show how the reconstruction of trajectories and consequently the resolution on the impact parameter and the momentum depend on the number and the spacing of the interaction points. More precisely, the error on these parameters decreases with additional measurement points, which is achieved by increasing the number of detector layers, which however increases the material budget and thus intensifies multiple scattering processes, and by improving the efficiency of the detector to avoid missing measurement points. Similarly, larger distances L between the outermost measurement points reduce the uncertainty on the impact parameter. As explained in the following Section, the Phase 1 upgrade of the CMS pixel detector uses these approaches together with a more uniform spacing between the detector layers to improve upon the performance of the previous version of the detector while coping with denser environments.

Properly reconstructing particle trajectories allows to resolve the primary vertex of the interaction. Furthermore, trajectories which do not originate from the primary vertex can be associated to a secondary vertex which indicates the presence of a short lived particle decaying within the detector volume. This occurs for instance for b quarks which hadronise and decay with a lifetime of around $\tau = 0.5\,\mathrm{ps}$ to $1.5\,\mathrm{ps}$ [15]. Assuming that particles travel at the speed of light, this means that a secondary vertex is created around $c\tau = 1\,\mathrm{mm}$ away from the main vertex. Bottom quarks arise in the decay of particles under study at the LHC experiments, such as top quarks,

which decay almost exclusively into a b quark and a W boson, and Higgs bosons in the $b\bar{b}$ pair decay channel, as is described in the second part of this work. However, secondary vertices can also originate from the decay of so far unknown particles, which decay back to SM particles after travelling for a certain distance. Several BSM models predict short lived particles which decay at distances down to $c\tau \sim 10\,\mu\text{m}$ from the vertex [142], which is why pixel detectors are crucial in detecting this kind of particles.

4.2 The Phase I upgrade of the CMS pixel detector

As presented in Section 3.3.1, the pixel detector is the innermost component of the CMS detector, and has a considerable impact on the performance of the particle flow algorithm described in Section 3.3.6, since it allows to precisely measure the trajectory of charged particles, their momentum and their charge. The Phase 0 detector was installed before the start of the LHC in 2009 and performed excellently until the end of the year 2017 when it was replaced with the Phase 1 detector [96, 94]. The reasons for this replacement were twofold:

- During its seven years of operation, the detector degraded due to the large particle fluxes crossing the detector, called radiation damage. The innermost layer for instance accumulated a dose of around 10 Mrad, where one rad corresponds to a deposited energy of 0.01 J per kilogram of detecting material.

- The Phase 0 detector, which was installed in 2009, was designed for an instantaneous luminosity of $1 \times 10^{34}\,\text{cm}^{-2}\,\text{s}^{-1}$ corresponding to 25 pileup events per bunch crossing, and a bunch crossing time of 25 ns. This luminosity was exceeded in 2016 and was doubled in 2018 as is illustrated in Figure 4.6. While the CMS detector is currently not operating for the long shut down 2 (LS2), it will resume its activity in 2021 running at the same luminosity of $2 \times 10^{34}\,\text{cm}^{-2}\,\text{s}^{-1}$. Operating the detector above its design luminosity would lead to large inefficiencies. These arise for instance from an insufficient buffer length, where data is temporarily stored until validation from the trigger system, or from a readout that is too slow to cope with large amounts of signals arriving simultaneously. These inefficiencies would seriously impact the reconstruction of trajectories and thus degrade the performance of physics analyses as is shown in Figure 4.7, which gives the efficiency and mistag rate for reconstructing tracks in $t\bar{t}$ events at different luminosities and bunch spacing times. Doubling the instantaneous

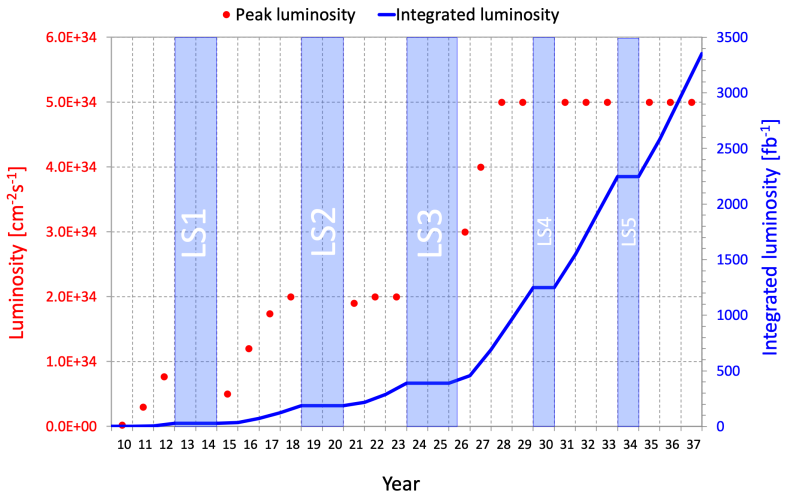

Figure 4.6: Instantaneous and integrated luminosity of the LHC as a function of time [143]. Three Runs are taking place between 2009 and 2023 which are separated by long shut downs 1 and 2 (LS1,2) during which technical work on the accelerator and the experiments is taking place. A considerable increase in instantaneous luminosity is planned starting from 2027 after LS3.

luminosity at the same bunch crossing rate would lead to a 10% loss in efficiency in reconstructing such events.

To maintain or even surpass the performance of the Phase 0 detector in more stringent conditions, the Phase 1 upgrade pixel detector has been installed in the Extended Year End Technical Stop (EYETS) in the winter 2016/2017. After a brief summary on the expected improvement on physics analyses of the Phase 1 upgrade pixel detector, a detailed description of the detector is given.

4.2.1 Impact on physics analyses

The improved performance of the Phase 1 upgrade pixel detector results in higher efficiencies and lower mistag rates in the identification of muons, b hadrons, taus, and in the discrimination between electrons and photons. This indirectly also improves the reconstruction of the missing transverse energy, which is calculated as the negative vectorial sum of the kinematics of all measured objects. Figure 4.8 shows the efficiency and mistag rate for tracks in $t\bar{t}$ events for different pileup scenarios with the Phase 1 upgrade detector which can be compared with the same result for the Phase 0

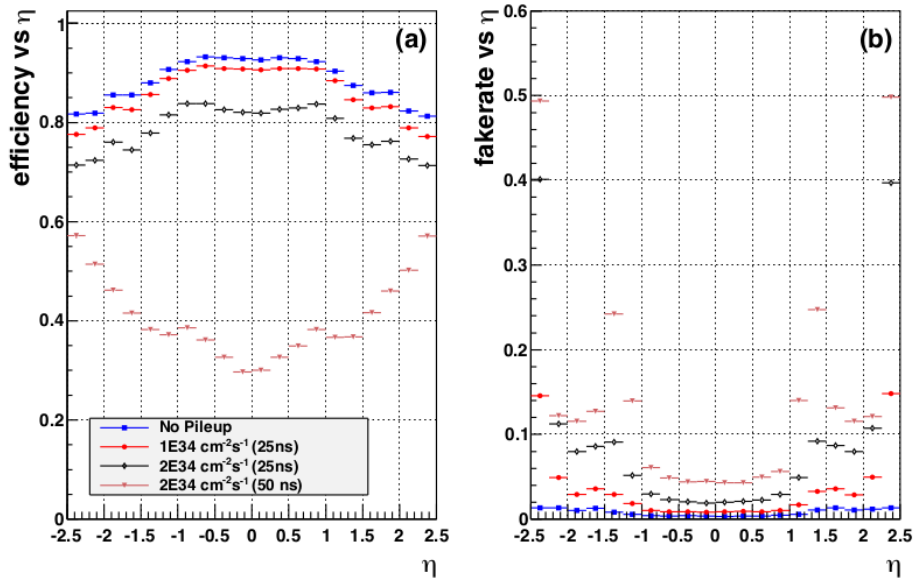

Figure 4.7: Projected efficiency and mistag rate in simulated $t\bar{t}$ events as a function of the pseudorapidity η for different pileup scenarios for the Phase 0 detector. Red dots correspond to a pileup of 25, black diamonds to a pileup of 50, and magenta triangles to a pileup of 100 [95].

detector, that is presented in Figure 4.7. Clearly the performance of the upgraded detector leads to higher reconstruction efficiencies and lower mistag rates for all tested pileup conditions, and the performance is stable up to a pileup of 50.

Another benchmark to quantify the relative performance of the Phase 1 detector with respect to the previous version is the separation of jets originating from b quarks (b jets) from jets produced by light quarks or gluons, referred to as b tagging. This process heavily relies on the precise reconstruction of secondary vertices, which are the points where the B hadrons decay. The resolution of the reconstruction is improved when moving the innermost detector layer closer to the beam line as is demonstrated for a simplified detector model consisting of two layers at radii R_1 and R_2 from the collision point, with $R_1 < R_2$. R_0 describes the radius of the beam pipe. The pitch size in both layers is d. The hit resolution in both layers is expressed as a function of the spatial resolution of the detector, which is derived in Section 4.1.2, and as a function of a term describing the effect from multiple scattering at the beam pipe and the inner detector layer. The resolutions σ_1 and σ_2 can then be written as

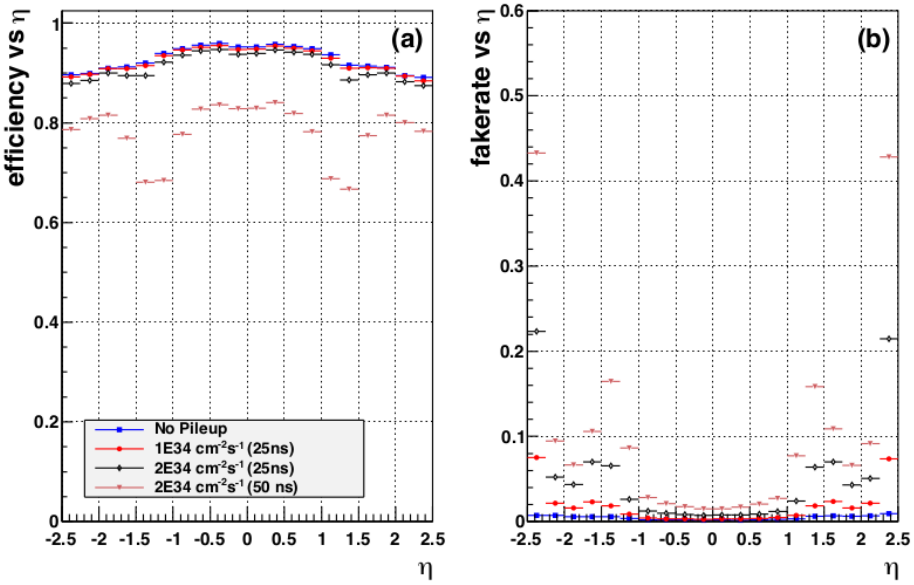

Figure 4.8: Projected efficiency and mistag rate in simulated $t\bar{t}$ events as a function of the pseudorapidity η for different pileup scenarios using the Phase 1 pixel detector. Red dots correspond to a pileup of 25, black diamonds to a pileup of 50, and magenta triangles to a pileup of 100 [95].

$$\sigma_1 = \sqrt{\left(\frac{d}{\sqrt{12}}\right)^2 + \left((R_1 - R_0)\sigma_\Theta^0\right)^2} \tag{4.12}$$

$$\begin{aligned}\sigma_2 &= \sqrt{\left(\frac{d}{\sqrt{12}}\right)^2 + \left((R_2 - R_0)\sigma_\Theta^0\right)^2 + \left((R_2 - R_1)\sigma_\Theta^1\right)^2} \\ &\simeq \sqrt{\left(\frac{d}{\sqrt{12}}\right)^2 + \left((R_2 - R_0)\sigma_\Theta^0\right)^2}\end{aligned} \tag{4.13}$$

where $\sigma_\Theta^{0,1}$ designate the standard deviation of the Gaussian distribution describing the scattering angles at the beam pipe and the innermost layer. It is assumed that $\sigma_\Theta^0 \gg \sigma_\Theta^1$.

The vertex position can then be calculated by interpolation of the two hit positions, and its resolution is expressed as a function of the position resolution of both hits, and also takes into account the correlation of the error due to the multiple scattering at the beam pipe:

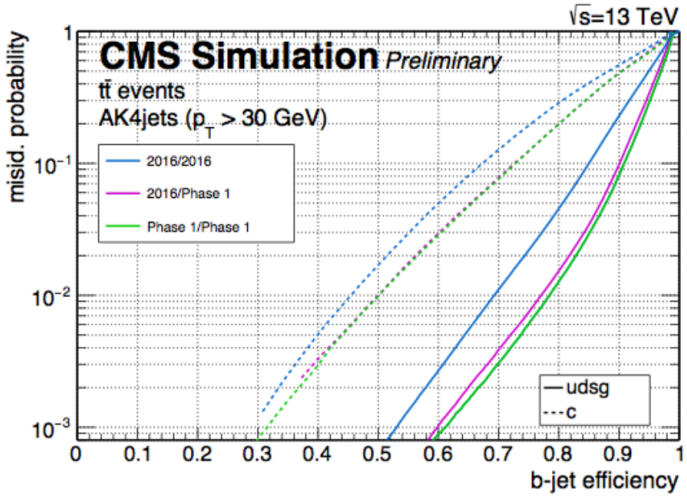

Figure 4.9: Efficiency versus mistag rate for light (u, d, s) jets and gluons (g), and charm quarks (c) of the DeepCSV b tagger [120] which identifies jets originating from b quarks. The performance using the geometry of the Phase 0 pixel detector is shown in blue. The green lines shows the efficiency of the tagger using the Phase 1 pixel detector. In pink is the performance of the Phase 1 detector, but where the neural network on which the b tagging algorithm is based is trained using the 2016 detector geometry [144].

$$\begin{aligned}\sigma_{vertex} &= \sqrt{\left(\frac{R_2}{R_2-R_1}\sigma_1\right)^2 + \left(\frac{R_1}{R_2-R_1}\sigma_2\right)^2 + \frac{2R_1R_2(R_2-R_0)(R_1-R_0)}{(R_2-R_1)^2}\sigma_\Theta^2} \\ &\simeq \sqrt{\left(\frac{d}{\sqrt{12}}\right)^2 \cdot \left(1+\frac{R_1^2}{(R_2-R_1)^2}\right) + (2R_1-R_0)^2\cdot\sigma_\Theta^2}\end{aligned} \tag{4.14}$$

This calculation explicitly shows that the resolution improves as expected with smaller detector segmentation but also with smaller R_1, such that moving the innermost detector layer closer to the beam line improves vertex reconstruction [140]. This has been done for the Phase 1 upgrade detector.

Using this improved vertex resolution, the mistag rate of identifying b jets from light jets is reduced for the same tagging efficiency as is shown in Figure 4.9 in the case of the DeepCSV b tagger [120].

These features lead to an improvement in the sensitivity of many physics analyses as is discussed in [95]. For example, an improvement in event selection efficiency of

65% is expected in the analysis of the associated production of a Z boson with a Higgs boson, where the Higgs boson decays to bottom quarks and the Z boson into electrons or muons. Similarly, in the search for supersymmetric particles using the M_{T2} variable in the hadronic final state, a gain of 20% in event selection efficiency is expected. These gains arise from improved b tagging and lepton identification performances [95]. Another example is the analysis of the associated production of a Higgs boson with a top-antitop quark pair, where the Higgs boson decays into two b quarks, which will be discussed in Part II of this thesis. Since this decay channel has four b quarks in the final state, an improvement in the b tagging efficiency directly reflects on the analysis sensitivity. Furthermore, the production of $t\bar{t}$ events with additional QCD radiation is the main background of the analysis, so that the improvement in the identification of such events shown in Figure 4.8 also directly impacts the search for $t\bar{t}H$, $H \to b\bar{b}$ events.

4.2.2 Detector geometry

The CMS pixel detector consists of a cylindrical barrel part (BPIX) that is parallel to the beam pipe and has a length of 548.8 mm, and two endcaps (FPIX), which are perpendicular to it. A significant change of the Phase 1 detector with respect to the Phase 0 detector is the installation of one additional layer in both the BPIX and in the FPIX, resulting in 4 layers in the barrel and 3 layers in the endcaps. In the barrel part, layer one has been moved closer to the beam line (requiring the installation of a new beam pipe during the LS1). This considerably improves the reconstruction of short-lived particles such as b quarks, as explained in Section 4.2.1. Furthermore a fourth layer has been installed to provide an additional interpolation point between the pixel detector and the strip detector. Table 4.1 gives the distances of the barrel layers to the beam line for the Phase 0 and 1 detectors. An illustration of the detector is also given in Figure 4.10.

[in cm]	Phase 0	Phase 1
Layer 1	4.4	3.0
Layer 2	7.3	6.8
Layer 3	10.2	10.2
Layer 4	-	16.0

Table 4.1: Distance of the layers of the barrel Phase 0 and Phase 1 detectors to the beam line.

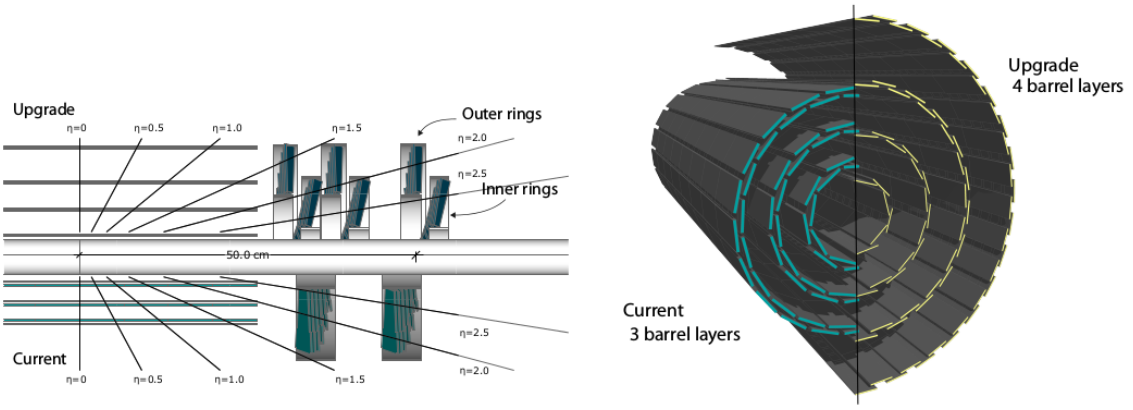

Figure 4.10: Illustration of the Phase 1 upgrade of the CMS pixel detector. The side view on the left illustrates the excellent spatial coverage of the detector up to $\eta = 2.5$. The front view on the right shows the positioning of the layers with respect to the Phase 0 detector [95].

Generally, the additional layers of the detector would increase the material budget of the detector. This would have negative consequences on the detector's performance, as photon conversion, multiple scattering and nuclear interactions can modify the trajectory of incoming particles as well as their energy from prolonged interaction with the tracking layers, thus increasing the uncertainty on the energy measurement in the calorimeters.

To counteract these effects, considerable efforts were put into reducing the material budget of the detector supply system. Moving most of the passive components to outside of the detector volume, as well as installing a newly developed CO_2 cooling system allowed to maintain the same material budget in the region with $|\eta| < 1$ and to reduce it by approximately 1/3 in higher η regions [95].

4.2.3 Powering system and data readout

For communication with the detector modules, a service cylinder and a supply tube are installed outside of the detector volume at large η values. They provide power and signal to the modules, and implement a data link for reading out the acquired data. Figure 4.11 shows an illustration of the service area of the detector.

Data collected by the modules are transferred via twisted pair cables towards the supply tube where the data are converted to an optical signal by Pixel-Opto-Hybrid (POH) elements. They are then propagated via fibres to the front end drivers (FEDs)

located in the service cavern of the CMS experiment. These buffer and synchronise the obtained data. From there, they are propagated to the central data acquisition system, where they are used in the decision making process of the HLT trigger.

The 40 MHz clock and other signals such as resets are propagated to the detector by pixel front end controllers (FECs) via optical fibres. The FEDs and FECs are controlled using the μTCA technology.

DC-DC converters are used to set the required input voltage of the modules to a controlled value. These converters are a novelty of the Phase 1 detector design, triggered by the requirement to use the same power supplies and supply cables while coping with a power consumption twice larger for the Phase 1 detector with respect to the Phase 0 design. Thus higher voltages are applied to the cables. This voltage is reduced again in proximity to the modules to meet the requirements of the modules using "buck" type converters, where the output voltage is lower than the input voltage. Consequently, the output current is increased. Two types of DC-DC converters are installed. One of them delivers an output voltage of 2.4 V and an output current between 0.4 and 1.7 A to the analog circuitry of the readout chips. Similarly, DC-DC converters serving the digital components of the readout chips and the modules have an output voltage of 3 V and an output current between 0.7 and 2.4 A. With an input voltage to the converters of around 10 V, this powering system reduces the power losses in cables by a factor of around 10 with respect to a traditional powering scheme [95, 145].

4.2.4 Cooling system

Cooling of the detector is essential in order to dissipate heat produced by the modules (around 200 mW cm^{-2}). Furthermore it reduces the temperature of the sensors to control the leakage current and prevent thermal runaway as illustrated in Section 4.1.2.

To that end, the cooling system of the pixel detector has been completely revised for the Phase 1 detector. Previously, a C_6F_{14} cooling has been used, which was replaced with a two-phase CO_2 cooling. The choice of the cooling system is largely responsible for the massive reduction in material budget, as much smaller and thinner pipes can be used with a CO_2 cooling. A coolant temperature of $-20\,°C$ is chosen, which ensures that the temperature of the sensors remains below $-4\,°C$ [95]. The system was designed for a total cooling power of 15 kW, which suffices to dissipate the heat produced by all modules of the detector.

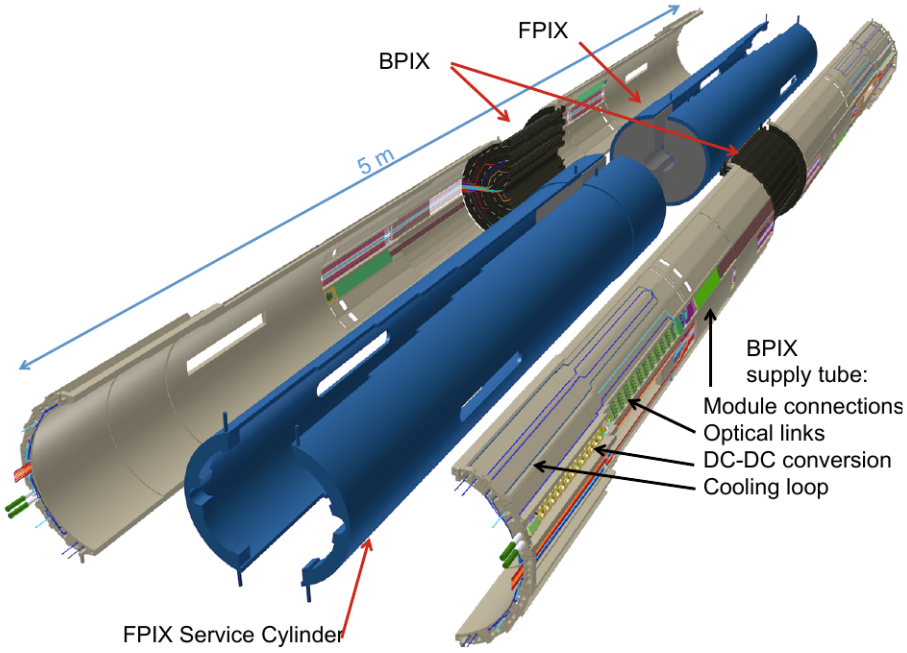

Figure 4.11: Sketch of the BPIX supply tube and FPIX service cylinder providing power and a data readout link to the detector [95].

4.2.5 Detector modules

The central part of the pixel detector are the detector modules. They are fixed to a light-weight carbon fiber structure. This section focuses on the modules produced for the BPIX detector.

The BPIX detector holds 1184 modules, each of which having 16 readout chips (ROCs) which are responsible for the signal processing. The ROCs and sensors are segmented into individual pixels, forming an array of 52 x 80 pixels per ROC. This amounts to a total of 79 million pixels, instead of the 48 million for the Phase 0 detector. The pixel size of 100 µm × 150 µm remains unchanged.

Figure 4.12 illustrates the module components. Modules for the FPIX and for layers 2 to 4 of the BPIX are mounted on base strips by which they can be screwed onto the support structure. Glued on these strips is the array of 16 ROCs which is bump bonded to the silicon sensor. A printed circuit board, known as high density interconnect (HDI) is glued onto the sensor. Wirebonds ensure the connection to the ROCs. Finally, a twisted pair cable provides power and signal to the module, and is used for data readout. Modules for layer 1 of the BPIX exhibit certain differences

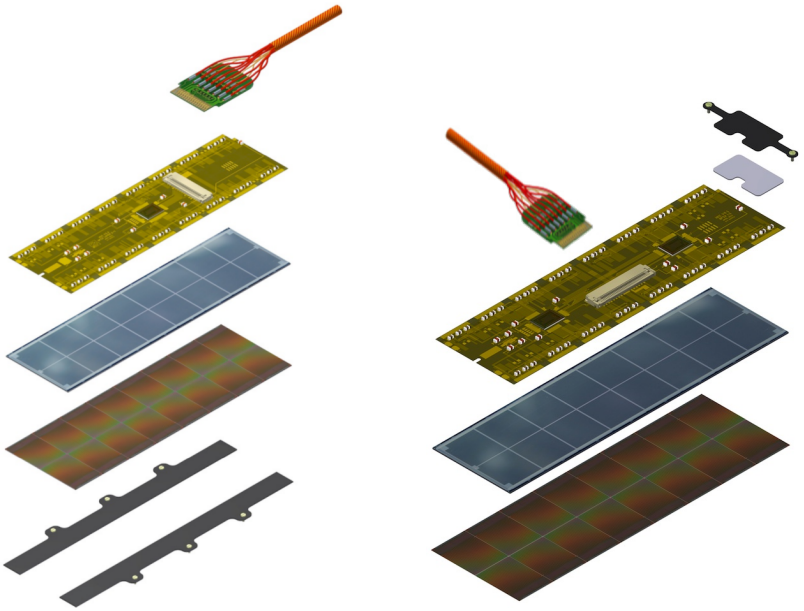

(a) Layer 2-4 modules (b) Layer 1 modules

Figure 4.12: Illustration of the modules used for layers 2-4 of BPIX (a) and for layer 1 (b). Modules for layers 2-4 consist from bottom to top of base strips for fixation on the support structure, an array of 16 readout chips, the silicon sensor, a printed circuit board and a cable for power and readout. Modules for layer 1 differ by the fixation to the structure using a carbon fiber clip. Furthermore, these modules have a dedicated readout chip and HDI.

to the modules described before. They are fixed using carbon fiber clips instead of base strips as the space at the small radius at which the modules are located is very restricted. Furthermore a dedicated readout chip was developed specifically to meet the demands of the innermost layer. For similar reasons, a new HDI has been designed [95]. In order to protect the wirebonds from mechanical damage, a thin polyimide foil is applied on the HDI.

HDI and TBM

The HDI is a printed circuit board which distributes power and signal to all ROCs on the module, as well as to another chip called the token bit manager (TBM). The TBM is glued on the HDI and is responsible for coordinating the readout of the ROCs on the module. It also distributes clock, trigger and reset signals. Furthermore, the

TBM constructs the data format which is transmitted to the FEDs. In particular, it attaches a header to the data stream identifying the module and the ROC from which the data is sent. TBMs are separated in two cores. Each ROC produces a 160 Mbit s^{-1} data stream, which are combined to one or multiple 400 Mbit s^{-1} readout links.

Different types of TBM chips are used in the Phase 1 upgrade detector, adapted to the data rates expected in each part of the detector. All TBM versions possess two cores, but differ in the number of ROCs which are processed simultaneously and in the number of readout links. Layers 3 and 4 use a TBM that builds two token chains of eight ROCs, which are merged to a single readout link. Modules in layer 2 have a different TBM chip as they are closer to the beam line and must therefore cope with larger hit rates. This TBM has four token chains of four ROCs each, which are processed simultaneously and merged into two output links. Layer 1 modules are exposed to even higher rates. Thus two TBM chips are glued on the HDI, creating readout chains of only 2 ROCs [95], resulting in four data streams.

Sensor

Each module has a segmented silicon sensor with a thickness of 285 µm and a pitch size of 100 µm × 150 µm.

As for the previous version of the detector, a n^+-in-n sensor technology has been chosen. Sensors using this technology are built from a n-substrate, with a p^+ backside contact, and n^+ implants (with a higher doping concentration than in the substrate) on the other sensor side. Before type inversion arising from irradiation which is described in Section 5.1.1, a bias voltage of −150 V is applied to the sensor to expand the depletion region towards the implants, where the connection to the readout electronics is implemented. After type inversion, the pn-junction moves to the interface between the pixel implants and the n-substrate. This is illustrated in Figure 4.13. Therefore, the sensor is depleted around the implants even after irradiation, when the sensor cannot be fully depleted any more with the available detector infrastructure.

Readout chip

Two new readout chips (ROC) have been designed for the Phase 1 upgrade pixel detector. While layers 2 to 4 of the BPIX and the FPIX share a common ROC, named *psi46digV2.1respin*, a dedicated ROC, *PROC600V2*, was developed for layer 1 of the BPIX detector to face the larger particle fluxes close to the interaction point. Indeed, the expected hit rate in layer two is around 120 MHz cm^{-2} and in layer one 600 MHz cm^{-2} [146]. This section describes the properties of *PROC600V2*, while

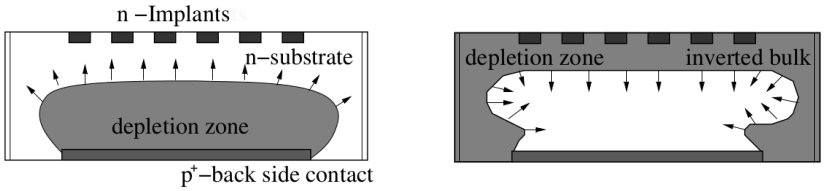

(a) Before type inversion (b) After type inversion

Figure 4.13: Illustration of the n^+-in-n technology. Before type inversion, the depletion zone expands from the p^+ backside into the substrate (a). After type inversion, it reaches the n^+ implants where the readout electronics are located (b). Arrows indicate how the depletion zone expands when biasing the sensor. Modified from [134].

psi46digV2.1respin is extensively reviewed in [147]. This document also serves as a reference in the description below for all features common to both ROCs.

For operation, the ROC needs to be supplied with a digital and an analog voltage of 2.9 V for *PROC600V2*. These are further regulated on the chip, providing a regulated digital voltage V_{dig} and tuning the current necessary for operation of the ROC to 24 mA. The operation of the ROC can be adjusted using 19 digital-to-analog converters (DACs), which are described in Table 4.2.

The ROC is designed in a 250 nm CMOS technology and measures 7.9 mm × 10.6 mm [146]. It consists of three building blocks as illustrated in Figure 4.14:

- The pixel array: As mentioned above, the sensor is segmented into pixels. Each of these pixels is bump bonded to a cell in the pixel array, called the pixel unit cell (PUC). The PUCs are arranged into 26 double columns (DCs) of 180 pixels each.

- The double column interface (DCI) which holds data and timestamp buffers where hit information is stored until validation from the L1 trigger. One major difference between both ROC versions lies in the number of these buffers. While *psi46digV2.1respin* has 24 timestamp and 80 data buffers per double column, *PROC600V2* has 40 timestamp and 4×56 data buffers per double column.

- The control interface block (CIB), in which DACs, voltage regulators and registers are hosted. Test pads are also accessible on the CIB.

All three blocks are now described in greater detail.

	DAC	Description
Regulators	Vdig	Regulator for the digital voltage supply
	Vana	Regulator for the analog voltage supply
	Vsh	Regulator for the sample and hold circuit
	Vcomp	Regulator for the comparator
Readout	VwllPr	Preamplifier feedback
	VwllSh	Shaper feedback
	Vtrim	Setting of the trim bit strength
	Vthrcomp	Comparator threshold
Trigger	PHOffset	Voltage amplifier offset
	PHScale	Voltage amplifier gain
	Vcomp_ADC	ADC comparator voltage
Others	Vcal	Calibration signal pulse height
	CalDel	Delay of calibration signal
	WBC	Trigger latency
	CtrlReg	Control register and zero suppression
	readback	Readback register

Table 4.2: Summary of all tunable DACs in use for *PROC600V2*. Adapted from [148].

The pixel unit cell The pixel unit cell is responsible for the readout of one pixel of the segmented sensor. Each PUC has an analog domain and a digital part. Both are represented in Figure 4.15. The analog part follows closely the general description shown in Figure 4.3. The induced current is measured and propagated to the ROC via the bump pad. The signal is first amplified and shaped to increase the signal to noise ratio. The resistance of the amplifier and the shaper can be tuned using VwllPr and VwllSh. Signals are then compared to an adjustable threshold which is tuned via Vthrcomp and four trim bits per pixel whose strength is set using Vtrim. Signals above the threshold enter a sample and hold circuit where the pulse height information is sampled and temporarily stored. At this point, the pixel is blocked from processing further hits. A continuous column drain initiates an entry in the timestamp buffer so that hits can later be associated to the correct bunch crossing. Furthermore, the pulse height information and the address of the firing pixel are propagated to the DCI. After this, the pixel is available to process new signals. The pixel dead time during signal processing leads to an inefficiency of around 1% at the

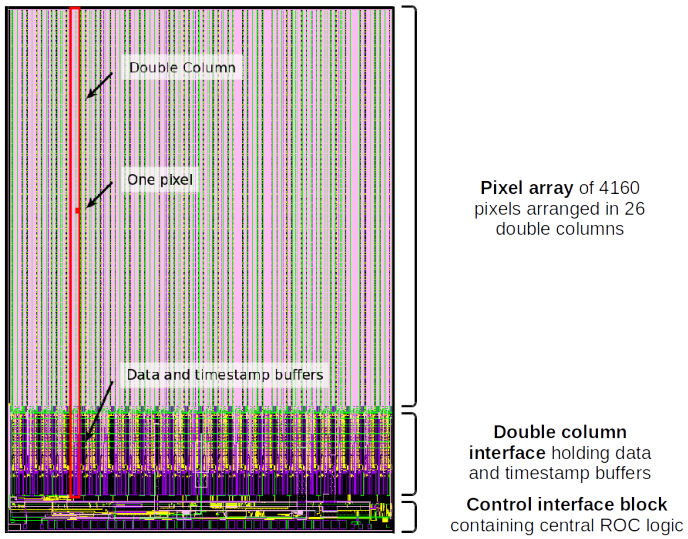

Figure 4.14: Layout of the *PROC600V2* chip. Pixels are organised in double columns forming a pixel array. Each double column owns data and timestamp buffers in the double column interface. A control interface block contains central ROC readout logic. Adapted from [149].

maximum rates expected in the CMS detector.

The propagation of hit information to the double column periphery has been reworked for *PROC600V2* in order to accommodate higher hit rates. The fundamental idea originates from the fact that charge is typically shared amongst neighbouring pixels, creating so-called clusters. This has been described in Section 4.1.2. Given the Lorentz angle in the CMS experiment, clusters will consist on average of 1.95 pixels. Therefore, the new Dynamic Cluster Column Drain (DCCD) mechanism reads out clusters of 2 $\times$ 2 pixels simultaneously, instead of individual pixels. An additional improvement arises from the fact that 7 pending column drains are supported instead of two, which reduces the dead time, since on average 1.2 clusters are formed per event per double column. Thus, with n the number of pixels and m the number of clusters per DC, m+2 clock cycles are needed to read out m clusters in one column drain, which typically equals to 3.2 clock cycles. With the readout mechanism of *psi46digV2.1respin*, 2n+3 clock cycles are necessary, which on average amounts to 7.7 cycles. A gain of a factor of 2.4 in the readout speed is thus achieved.

For testing purposes, an internal mechanism is implemented in the PUC which enables to artificially inject a test charge or calibration signal into the bump pad. The amplitude of the signal can be set with `Vcal` and `CtrlReg`. The time at which

the pulse is injected is set with `CalDel`, so that it is injected in the bunch crossing on which is later triggered. This test charge can also be capacitively coupled into the sensor instead of being deposited onto the bump pad as illustrated in Figure 4.15. With that functionality the quality of the bump bond is investigated by verifying if injected test pulses can be read out.

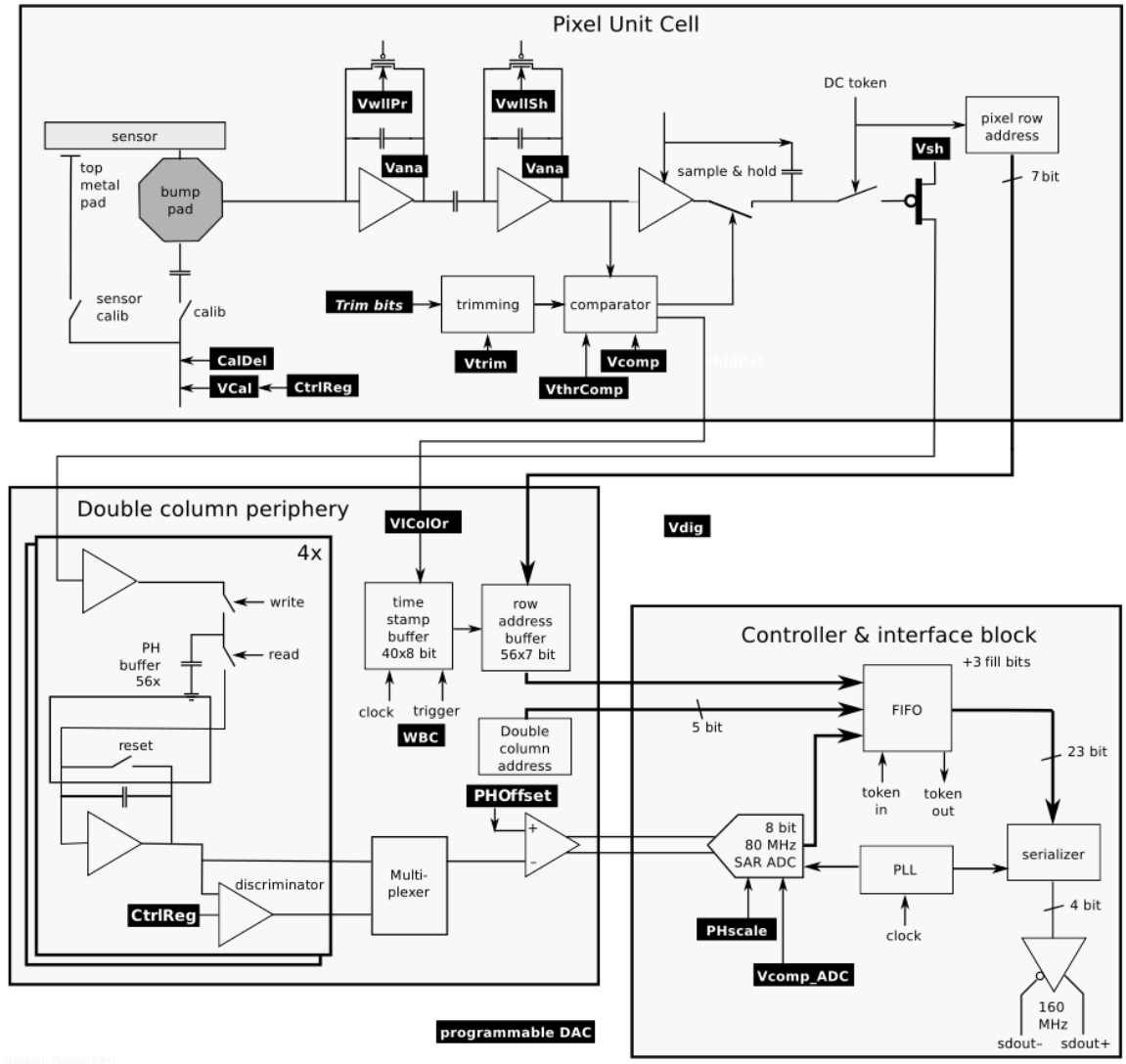

Figure 4.15: Schematic design of the *PROC600V2* chip readout [150].

The double column interface The main component of the DCI are the timestamp and data buffers which temporarily store hit information. The bunch crossing in which the hit occurred is saved in a time stamp buffer. This entry is created as soon as a hit passes the threshold because the pixel immediately sends a fast column OR-signal (*colOR*) to the double column periphery. This signal also triggers the double column readout, thus saving pixel addresses as well as pulse height information in the data buffers. Correspondence of hits in data and timestamp buffers is thus ensured. If the L1 triggers the event, data taking is halted to prevent overwriting of hit information and the hit is read out, otherwise the information is discarded. Inefficiencies in the chip operation can arise when either one of the buffers are full before validation by the trigger. Then, new hits cannot be processed. This is why the number of buffers has been increased for the *PROC600V2* chip. Additional inefficiencies arising in the double column periphery originate from the limited number of simultaneous column *colOR* signals and column drains, which is why the *PROC600V2* chip features a larger number of pending column drains than its predecessor.

The control interface block One main feature of the CIB is the control of the readout of each DC. This is governed by an internal token. By arrival of the token, the pulse height information is digitised. This is achieved using a per ROC analog-to-digital converter (ADC). The gain and the offset of the output of the ADC are tuned using `PHSlope` and `PHOffset`. The digitised data is then stored in a readout buffer, until a token sent from the TBM finally propagates the hit information away from the ROC.

Furthermore, the CIB provides the voltage regulators, holds the DACs controlling the chip performance, and provides a temperature independent voltage reference for the DACs: the band gap reference voltage.

The CIB also features a readback mechanism which can be used to extract different parameters of the ROC operation. The desired parameter can be chosen by setting the register of the readback DAC accordingly. Parameters that can be read back involve information from the last transmitted hit, unregulated analog and digital voltages, regulated analog voltage and current and the band gap reference voltage [95].

ROC readout format The readout format of *PROC600V2* is illustrated in Figure 4.16. The readout is initiated by a token sent by the TBM. After the token, a ROC header is sent. This header consists of a zero followed by 8 ones and another zero. Next, the readback information is sent as a start marker, and an information bit. Only one bit can be sent per readout chain, therefore readback information is split over the readout of 16 events. Last, the row and column addresses as well as

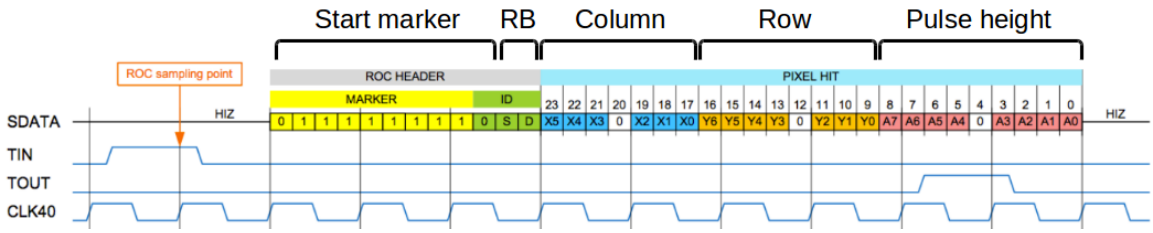

Figure 4.16: Format of the readout of *PROC600V2*.

the pulse height information are transmitted. These addresses are separated by zeros to prevent confusion with ROC headers. The pixel hit information is repeated for all hits in the ROC. A token is sent from the ROC to the TBM to signal the end of the readout chain.

These characteristics guarantee a successful operation of the Phase I pixel detector upgrade up to instantaneous luminosities of $2 \times 10^{34}\,\mathrm{cm}^{-2}\,\mathrm{s}^{-1}$ with 50 or more pileup interactions.

4.3 Future developments

As illustrated in Figure 4.6 the LHC programme extends to the year 2037. After the successful Runs I and II in which close to $200\,\mathrm{fb}^{-1}$ of data have been collected, the LHC is undergoing an upgrade and maintenance period between 2019 and 2021. After resuming operation in 2022, Run III aims to collect further data at double the LHC design luminosity for three years. The programme culminates in the High-Luminosity Large Hadron Collider (HL-LHC) project [151], during which the instantaneous luminosity will reach $5 \times 10^{34}\,\mathrm{cm}^{-2}\,\mathrm{s}^{-1}$ starting from 2027. This will allow to collect over $3000\,\mathrm{fb}^{-1}$ of data by the year 2036, providing ample data for precision measurements of the newly discovered Higgs boson, and for searches of very rare signals.

These developments come with new demands on the detectors in terms of efficiency at high rates and radiation hardness. To that end, layer 1 of the Phase I upgrade of the pixel detector will be replaced during the LS2, and a Phase II upgrade is in preparation to be installed during the LS3, before the start of the HL-LHC programme.

4.3.1 Replacement of the innermost layer of the Phase 1 upgrade pixel detector

As the first layer of the detector is closest to the interaction point, it will accumulate more radiation damage than the rest of the detector. Therefore it is planed to equip layer 1 with new modules during LS2 [95]. While the sensor remains unchanged, a new version of the HDI and an improved version of the *PROC600V2* chip, *PROC600V4*, will be used.

During operation of the Phase 1 detector, it has been observed that sparks can be created between the voltage test pads on the HDI and the guard rings of the silicon sensor, as the pads lie close to the edge of the HDI. To prevent this, the size of the HDI has been increased by 1.2 mm to increase the space between the pads and the edge of the HDI. Furthermore, the HDI will be equipped with a new version of the TBM chip. One reason for this is a timing difference in the readout between layers one and two. As both layers share the same clock, no optimal readout timing exists with the current TBM version, which creates inefficiencies when reading out the detector. Furthermore, single event upsets could only be recovered after a power cycle. This has been corrected in the new version of the chip by ensuring that it is properly responding to the reset token sent by the module periphery [152].

The *PROC600V4* chip has been improved from *PROC600V2* in order to overcome issues of the ROC which have been observed during operation in 2017 and 2018:

- A crosstalk between the trim lines and the injector capacitor was observed. This led to a large noise level, which is discussed in Section 5.3.2. Consequently the operation threshold was set considerably higher for *PROC600V2* than for *psi46digV2.1respin*.

- It has been observed that *PROC600V2* presents inefficiencies both at low and high hit rates, which could be traced back to a problem in the buffer logic, leading to a wrong assignment between the data and the timestamp buffers. Frequent resets of the chip can circumvent the problem [153].

- The pulse height resolution of the chip is reduced because of a large spread in the analog pulse height between the different pixels. This affects the spatial resolution of the detector.

The improved ROC is expected to facilitate the operation of the detector and to optimise its performance during Run III of the LHC programme.

4.3.2 Phase II pixel detector upgrade

The HL-LHC will provide over 3000 fb^{-1} of data at an instantaneous luminosity reaching $5 \times 10^{34}\,\mathrm{cm}^{-2}\,\mathrm{s}^{-1}$. To cope with such large hit rates, a Phase 2 upgrade of the CMS pixel detector is being developed [154]. It will be exposed to doses reaching 1.2 Grad within its ten years of operation.

Similarly to the Phase 1 upgrade, the detector will consist of a barrel part and endcaps. In addition, an extended pixel detector will cover the region up to a pseudorapidity of $|\eta| < 4$. This detector will use silicon as a detecting material. The pitch size will be reduced to 50 µm × 50 µm to reduce inefficiencies and for better spatial resolution.

A new readout chip is being developed by the CERN RD53 collaboration [155] in a joint effort of the ATLAS and the CMS collaborations. The feature size is reduced from the Phase 1 detector to 65 nm as a higher logic density is needed with the reduced pixel size.

A serial powering concept has been designed for the Phase II upgrade pixel detector, in which modules are powered in series [156]. This helps to reduce the amount of cables and therefore also reduces the power losses (which amount to up to 2/3 of the supplied power). To split the current between the chips on the module, shunt-LDO regulator blocks are installed on the chips [157].

A similar CO_2 cooling system will be used for the Phase II detector, but with a coolant temperature of −33 °C [154].

Chapter 5

Radiation tolerance of PROC600V2

The pixel detector is the component of CMS closest to the beam line, and is therefore exposed to very high hit rates. This leads to considerable radiation damage. For instance, the innermost layer of the pixel detector surrounds the beam line at a radius of only 3 cm, where an accumulated dose of 35 Mrad is expected per 100 fb^{-1}. Therefore, all detector components must be tested for their radiation hardness. This chapter focuses on studying radiation effects on the chip used for layer 1 of the upgraded pixel detector, *PROC600V2*. A similar study has been performed with the chip used in the three outer layers of the detector, which is presented in [147].

Section 5.1 gives an introduction to radiation effects that occur in silicon detectors, detailing the processes taking place in the sensor material and in the readout electronics. Section 5.2 describes the conditions of the irradiation campaign of *PROC600V2* as well as the setups used for testing. Finally, the results are presented in Section 5.3.

5.1 Radiation effects in semiconductor devices

This section details the mechanisms leading to radiation damage in semiconductor devices, focusing on damage in silicon sensors and in transistors, which are the building blocks of the readout electronics. Many studies on this subject have been performed, and are compiled for instance in [135] and [158], on which the summary presented here is based.

Radiation effects primarily arise from two different processes, displacement and ionisation damage. Displacement damage originates from the non-ionising energy loss of highly energetic particles, leading to the dislocation of atoms or clusters of atoms

from the lattice. These dislocations modify the electrical properties of the crystal. Displacement damage is thus particularly relevant in the bulk of sensors, and for instance leads to a decrease in charge collection efficiency. While these effects are not the main focus of this work, a short summary is nonetheless given in Section 5.1.1 as the *PROC600V2* samples under study are linked to a silicon sensor such that both components are irradiated during the campaign.

On the other hand, ionisation damage originates from energy losses of incoming radiation in the insulating components of the detector (typically silicon dioxide (SiO_2) in silicon devices). This generates free charge carriers within the insulator by ionising the electrons from the atoms. The damage created from these free charge carriers is directly proportional to the absorbed energy, such that the radiation damage can be characterised by the total ionising dose (TID). Ionisation damage is the dominant mechanism leading to the deterioration of transistors and thus of the properties of readout electronics. These effects are detailed in Section 5.1.2.

5.1.1 Radiation effects in sensors

Ionisation damage has no impact on the bulk of sensors since electrons and holes can drift in the sensor because of the applied electric field and therefore do not permanently modify the structure and properties of the crystal. Ionisation damage only affects the surface of the sensor, where isolating structures are positioned. While this is the prevalent problem in sensors used in photon science, the dominant source of radiation damage in silicon sensors in high energy physics arises from the displacement of atoms in the lattice.

Atoms can be dislocated from their position in the lattice if they receive a recoil energy above 25 eV in the collision. This can be provided by incident protons or neutrons with an energy above 190 eV [134]. Atomic displacements create vacancies at lattice positions previously occupied by an atom, and interstitials when atoms are placed at unusual places in the crystal. The likelihood of such defects greatly increases for incident particles with larger masses and energies, but is not directly proportional to the total energy deposited in the crystal. In a HEP experiment environment, the energy of incoming particles is often of the order of several MeVs up to GeVs, such that the recoil energy is much larger than 25 eV. Thus recoiling silicon atoms can themselves displace other atoms in the lattice, leading to a cluster of defects, which can reach 0.1 nm in size, and displacing up to 1000 atoms. Some of the vacancies and interstitials will recombine, but individual pairs remain, leading to permanent point-like damages. The magnitude of the damage is typically compared to the displacement damage created by neutrons with an energy of 1 MeV, given in

units of $n_{eq}\,\mathrm{cm}^{-2}$. For this, a hardness factor is measured to scale the damage caused by a particle with a given energy to that of 1 MeV neutrons [134, 135].

The atomic displacements lead to three macroscopically observable effects:

- Increase of leakage current
- Change in doping concentration
- Decrease of charge collection efficiency

Increase of leakage current

The microscopic origin of the increase of the leakage current is the creation of localised mid-gap states due to the vacancies and interstitials. The current as a function of the fluence is parametrised as follows, when assuming a uniform distribution of the defects in the crystal:

$$I_{irr} = I_0 + \alpha \cdot \Phi \cdot A \cdot d \tag{5.1}$$

where I_0 gives the leakage current before irradiation, Φ is the particle fluence, α is the damage constant which depends on the irradiating particle and the fluence, and A and d are the area and thickness of the detector [135].

The leakage current is strongly dependent on temperature, as described in Section 4.1.2. Therefore, a radiation induced increase in leakage current can be mitigated by lowering the temperature of the sample under test [135].

Change in doping concentration

Prior to irradiation, the doping concentration is given by the number of donor or acceptor atoms in the lattice. The apparent doping concentration changes with irradiation due to impurities in the crystal. Thus an effective doping level N_{eff} is defined as

$$|N_{eff}| = \frac{2\varepsilon_0\varepsilon_{\mathrm{Si}}V_{\mathrm{depletion}}}{ed^2} \tag{5.2}$$

where $V_{\mathrm{depletion}}$ is the depletion voltage of the sensor, d is its thickness, e is the elementary charge, and ε_{Si} and ε_0 are the permittivity of silicon and the vacuum respectively.

This can lead to type inversion in n-type sensors. With irradiation, acceptor states are created in the material, which resemble impurities of p-type materials. The

effective doping level decreases for low fluences and almost disappears at a fluence around $\Phi \sim 3.5 \times 10^{12}\, n_{eq}\, \mathrm{cm}^{-2}$. At higher fluences, N_{eff} increases again, but with opposite polarity, leading to a sensor with p-type characteristics.

As the effective doping concentration increases after type inversion, the depletion voltage must be increased after irradiation. However, this leads to a decrease in charge sharing, which reduces the position sensitivity of the device [134, 135].

Decrease of charge collection efficiency

Displacement defects are not only responsible for the two effects mentioned above, but also create trapping centres. These trap charge carriers for a certain amount of time, thus reducing the amplitude of the signal. The trapping time linearly increases with the fluence Φ and can be parametrised as

$$\frac{1}{\tau_t(\Phi)} = \frac{1}{\tau_t(\Phi = 0)} + \gamma\Phi \tag{5.3}$$

The constant γ depends on the irradiating particles and was measured to be $0.56 \times 10^{-6}\, \mathrm{cm\, s}^{-2}$ for electrons and $0.77 \times 10^{-6}\, \mathrm{cm\, s}^{-2}$ for holes after proton irradiation.

The number of collected electrons within the charge collection time t_C thus decreases as

$$N_e(t_C) \propto \exp^{-\frac{t_C}{\tau_t(\Phi)}} \tag{5.4}$$

Therefore, the charge collection efficiency decreases with larger irradiation doses i.e. smaller $\tau_t(\Phi)$. To compensate for this effect, sensor architectures with smaller collection times can be used, such as three dimensional sensor technologies [134, 135].

5.1.2 Radiation effects in integrated circuits

The ROC under study [146] contains more than two million transistors [146], most common of which are metal-oxide-semiconductor field-effect (MOSFETs) transistors. The dominant source of radiation defects in MOS devices is ionisation damage rather than displacement damage. This is because the main effect of displacement damage is a reduction in the minority carrier lifetime in the silicon, which however does not drastically affect the functionality of MOS devices [159]. Therefore the created damage depends strongly on the total ionisation dose (TID), and concentrates on the insulating parts of the transistors.

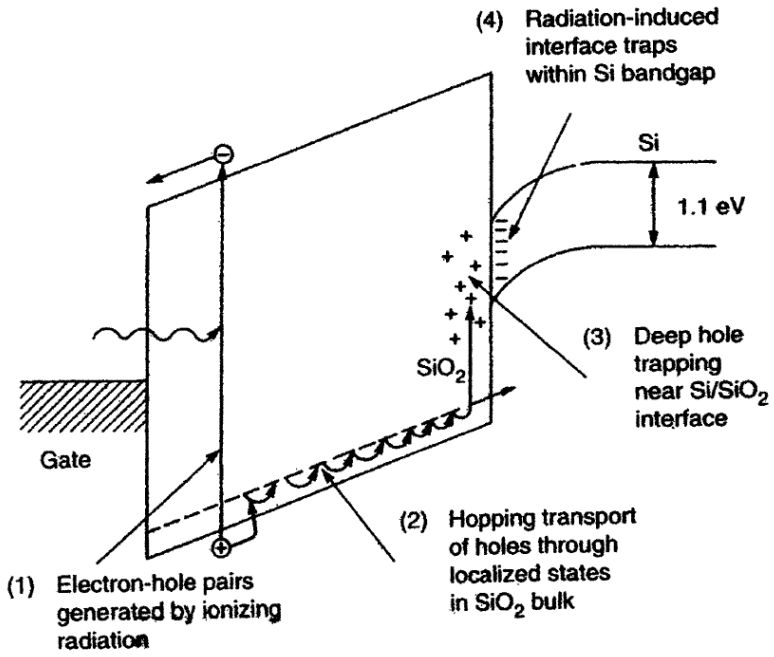

Figure 5.1: Illustration of charge trapping in silicon dioxide [159]. Holes created by ionising radiation propagate in the silicon through a hopping mechanism. They can then be trapped at the interface between the oxide and the silicon, or in a region of deep holes in the oxide itself.

Ionising radiation with a large enough energy (in SiO_2 for instance, an energy of 18 eV is required) creates electron-hole pairs in the gate oxide of MOSFET devices. Because of their several orders of magnitude larger mobility, electrons quickly drift towards the gate of the transistor following the applied electric field. Holes however have a much lower mobility and move only slowly using a hopping mechanism through free states in the oxide bulk [159] and are often trapped either directly in the oxide or at the interface between the oxide and the silicon substrate, as is illustrated in Figure 5.1.

Most holes are captured in a region close to the interface to the substrate which has a large concentration of deep hole traps. As electrons can tunnel through the interface, these hole traps are limited to the region between 5 nm and 20 nm from the interface. Macroscopically this lowers the threshold voltage of the transistor. For NMOS devices this can ultimately lead to a negative threshold voltage and the unability to change the transistor's logic state while PMOS transistors become more and more ohmic for larger irradiation doses. The usage of thin gate transistors reduces

the size of this deep hole trap region, thus limiting the number of captured holes.

However, holes are also trapped in the shallow trench isolation which surrounds the entire transistor to isolate it from neighbouring components. This leads to a positive space charge in the isolation. For NMOS devices, this introduces a leakage current between the source and the drain of the transistor. Conversely the effective width of the gate is decreased for PMOS type devices because of the electric field originating from this space charge.

A transition between a cristalline and an amorph material exists at the interface between the silicon and the oxide. So-called dangling bonds are thus formed at the interface which act as charge traps. To prevent this, manufacturers insert hydrogen atoms to occupy these trapping centres, however they become active after irradiation as the bonds to the hydrogen atoms break. The type of particles that are captured by these traps depends on the Fermi level and thus on the doping characteristics of the materials. Effectively holes are captured in PMOS and electrons in NMOS devices. For PMOS devices, this enhances the degradation of the transistor. Conversely for NMOS devices, the electric field created by these traps actually compensates the electric field originating from trapped holes in the oxide. Trapped particles at the interface lower the gain of the transistor, which increases its response time. Thus larger gate voltages are required to reach the same change in current [159, 160, 161, 162].

The magnitude of the defects depends on a variety of factors, such as the TID, the irradiation rate or the temperature and applied bias voltage during irradiation. Furthermore, annealing can change the properties of the transistor after irradiation. For instance, high temperatures can free trapped holes within the oxide, but simultaneously also increase the trapping probability at the interface. As these effects further complicate the analysis of radiation induced damage, annealing effects are thwarted by lowering the temperature after irradiation [135].

To mitigate these radiation induced losses in performance of devices, special techniques are used in the chip design. In particular enclosed layout transistors are used which have a lower leakage current compared to standard, linear transistors as they do not have trench isolations between the different transistor components. Additionally guard rings can be used to isolate structures. While these features do not prevent radiation damage, they reduce its impact on the device's performance [163].

In addition to TID effects, ionisation damage can also affect the electronics of the detector when a single ionising particle interacts with a sensitive component of the device. These events are called single event upsets, and are typically recoverable with a reset of the device [134, 158]. However, this work focuses on damage created by TID.

5.2 Irradiation campaign

To study the impact of these defects on the performance of the ROCs, an irradiation campaign has been performed with *PROC600V2* chips bump bonded to a silicon sensor, as described in Section 5.2.2 [1].

5.2.1 Irradiation facility

Samples are irradiated at the proton irradiation facility at the Karlsruhe Institute of Technology in Germany[2] [164] and operated by ZAG Zyklotron AG [165]. The facility provides a proton beam with an energy of ∼23 MeV. To produce the beam, H^- ions (hydrogen atoms which gained an additional electron) are accelerated and directed towards a foil, where the two electrons are stripped away from the ion as shown in Figure 5.2. The beam exit window consists of a 7 µm foil made of a cobalt, chromium and nickel alloy. The last beam stop is located 20 cm ahead of the foil. The samples under irradiation are located in a climatic chamber with controlled temperature, 50 cm away from the foil. The chamber is installed on a XY-stage in order to scan over the whole sample. This is necessary because the beam spot's diameter is between 4 mm and 8 mm, which is smaller than the sample size. The scan is performed in rows with a width of 1 mm. The desired proton fluence F_{prot} is therefore obtained by multiple scans over the test sample using the following equation:

$$F_{prot} \simeq \frac{n \cdot I}{q_{el} \cdot v_x \cdot \Delta y} \tag{5.5}$$

with:

- n the number of scans over the sample
- I=2 µA, the beam current
- q_{el} the electron charge
- v_x=115 mm s^{-1}, the horizontal velocity of the XY-stage
- Δy=1 mm, the step size in the vertical direction

[1] This project has received funding from the European Union's Horizon 2020 Research and Innovation programme under Grant Agreement no. 654168.

[2] KIT Campus Nord, Hermann-von-Helmholtz-Platz 1, 76344 Eggenstein-Leopoldshafen

The fluence can be converted to the TID acquired by the test sample using the stopping power of silicon (S_p=18.1 MeV cm^2 g^{-1} [166]) as:

$$I_d = F_{prot} \cdot S_p. \tag{5.6}$$

All samples are powered and cooled to -30°C using cold nitrogen gas during irradiation [165].

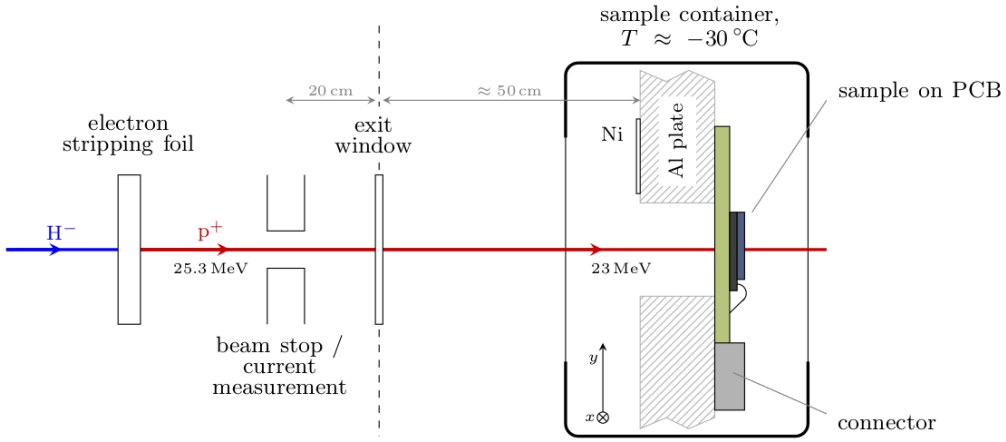

Figure 5.2: Schematics of the irradiation setup [147].

5.2.2 Testing setup

After irradiation, the samples are tested in three steps, each performed using a dedicated test setup.

- To measure parameters on test pads located on the chip periphery, a probe needle and a microscope are available. The temperature in this setup cannot be controlled, which is why testing times are limited to prevent annealing effects.
- A chamber with temperature and humidity control is available for testing the electronic properties of the samples. Cooling is assured by four Peltier elements mounted on a copper block. Water is used to evacuate the heat transported by the Peltier elements.
- To test the properties of the ROC when interacting with real particles instead of internal calibrate signals, an X-ray source is used. The device used

for testing has a Chromium anode and a power of 1.8 kW. X-rays are generated by accelerating electrons which create photons when colliding with the anode. The obtained spectrum consists of a continuous part that originates from Bremsstrahlung, and of several peaks that arise from characteristic X-rays of the atoms of the target anode. The electrons are accelerated using a voltage of up to 60 kV. The current of the tube can be adjusted between 2 mA and 30 mA allowing to vary the hit rate between several MHz cm^{-2} to up to 1 GHz cm^{-2} at the location of the test samples, which is approximatively 60 cm below the X-ray source.

In addition to the direct X-ray source which produces a high intensity polychromatic beam, different metallic fluorescent targets are available to produce a monochromatic beam with a lower intensity. When exposed to X-rays, atoms in these targets become excited, as electrons are ejected from inner atomic orbitals. In order to reduce the atom's internal energy, electrons from higher orbitals occupy the vacated spaces in lower orbitals. The energy that is lost by the atoms in this process is radiated by photons with a precise energy, corresponding to the energy difference between the orbitals. The obtained spectrum therefore consists of emission lines whose energies are characteristic of the target material. In practice, two lines are observed:

- The Kα_1 line arises from photons originating from the migration of an electron from the 2p to the 1s orbital
- The Kβ_1 line is formed by photons created when electrons move from the 3p state to the 1s state.

The energy resolution of the ROC under study is too poor to distinguish between the two lines, therefore in the presented measurements, only the Kα_1 line is taken into account as the amplitude of the Kβ_1 line is negligible. It has been verified that the energy calibration of ROCs is not impacted by the presence of the Kβ_1 line [167].

Samples are placed in a small climatic chamber with humidity control. Similarly to the cooling box of the main testing setup, temperature is controlled using Peltier elements and water cooling. This enables to test samples at a temperature below -15°C.

In all setups, connection to the sample under test is available through a chip adapter, in which the printed circuit board on which the ROCs are mounted can be inserted. This adapter is linked to a digital test board (DTB). The DTB is connected

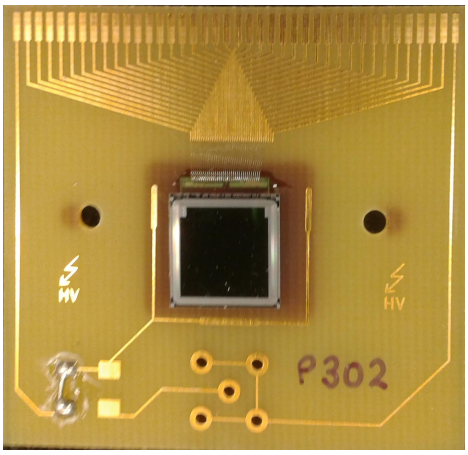

Figure 5.3: Photography of a single chip module consisting of a *PROC600V2* chip with sensor on a printed circuit board irradiated to 10 Mrad. The brown frame around the sample shows the effect of irradiation on the PCB.

to a computer using a USB connection. Furthermore, bias voltage is provided to the sensor via the DTB by a power supply. The software *pxar* [168, 169] is used for running the testing procedure. All devices (including the X-ray tube, the metallic targets, the power supply, the temperature and humidity controls of the cooling chamber and *pxar*) are controllable by the software *elComandante* [170].

5.2.3 Irradiation conditions and procedure

For the irradiation campaign, ten *PROC600V2* chips were bump bonded to a sensor, forming single chip modules (SCMs). Unlike the modules used for the phase 1 detector which are presented in Section 4.2.5, SCMs possess only one chip, and they have no HDI regulating the read out of the module. Instead SCMs are glued onto a printed circuit board (PCB). The connection to the PCB is assured via wirebonds, in the same way as a ROC would be wirebonded to the HDI on a phase 1 module. A photography of a SCM is shown in Figure 5.3.

The irradiation is performed iteratively, so that it is possible to test the same ROC at increasing irradiation doses. Five doses up to 80 Mrad with steps of 10 Mrad to 20 Mrad are considered, requiring a thorough testing of the samples before and after each irradiation step. The tested doses are summarised in Table 5.1.

The dose delivered by the irradiation facility can be determined by fixing a Nickel (Ni^{57}) foil on the aluminium mask holding the samples during irradiation. The activity measurement of those foils is performed using a Germanium detector system

Target irradiation dose [Mrad]	Measured irradiation dose [Mrad]	Fluence [Neq/cm^2]	Integrated luminosity [fb^{-1}]	Equivalence
0	0	0	0	/
10	10 ± 2	6.7 ·10^{13}	30	/
20	20 ± 4.47	1.3 ·10^{14}	60	∼ End 2017
40	38.97 ± 5.84	2.6 ·10^{14}	120	∼ End 2018
60	60.05 ± 7.20	3.9 ·10^{14}	180	/
80	77.95 ± 8.08	5.2 ·10^{14}	240	∼ Run III

Table 5.1: Summary of the tested irradiation doses. The target and measured irradiation doses are given in Mrad and in Neq/cm^2, assuming a hardness factor of 2 [165]. The corresponding integrated luminosity accumulated by CMS is also noted, as well as the data acquisition period the luminosity corresponds to.

[165]. An uncertainty of 20% is assumed on the dosimetry measurement. For the two initial irradiation steps which each contributed 10 Mrad to the total dose to which the ROCs were irradiated, the deposited dose was too small for performing a Ni^{57} dosimetry measurement. However, measurements on other samples irradiated to larger doses on the same days provided a measurement within 4% of the target dosis. Assuming a stable beam operation, this uncertainty was extrapolated to the *PROC600V2* samples under study.

Table 5.1 also indicates the accumulated fluence in order to estimate the radiation damage accumulated by non-ionising processes. Furthermore, the integrated luminosity delivered to CMS corresponding to the various irradiation doses is given. The irradiation dose of 20 Mrad is equivalent to the TID the detector has accumulated by the end of 2017 and the dose of 40 Mrad to the end of Run II in December 2018. For Run III, which will start in 2021, a TID of 80 Mrad is expected, corresponding to the maximum dose tested in the irradiation campaign.

Results up to doses of 20 Mrad are summarised in [171]. In addition, an irradiation campaign with *PROC600V1*, which serves as prototype for the ROC under study, was performed to doses up to 480 Mrad. This study, which is documented in [172], showed that the electronic circuitry of the ROCs is still functioning properly after such large radiation doses when adjusting its operation parameters. It was also shown that the efficiency of the ROCs is almost unchanged with respect to their pre-irradiation value after a dose of 120 Mrad.

A total of 10 samples were available at the start of the campaign, however, 5 of

those samples were not responding any more after the fourth or the fifth irradiation step. The observed failure modes varied. Some samples could not be programmed any more, on other ROCs no readout was obtained. While it cannot be excluded with certitude that these defects originate from irradiation, the predominant hypothesis is that these issues arose from mechanical damage during handling. Indeed the samples were brought to the irradiation facility five times, and have been exposed to the testing procedure six times (each of which involving handling, and large variations in temperature). The hypothesis is supported by the fact that similar effects have been observed on test samples which have not been used in an irradiation campaign.

After irradiation, all ROCs are stored and tested in a controlled environment with low temperatures ($< -15°C$) and low humidity. This is necessary to prevent annealing effects and to reduce condensation which would damage the samples. An exception to this are tests involving the measurement of currents and voltages on the test pads using a probe needle. Testing times for these measurement are below 10 min, therefore annealing effects occurring during this time are neglected.

5.3 Irradiation campaign results

This section presents the results of the irradiation campaign performed with the *PROC600V2* chip, which follows the procedures and strategy of the irradiation of the *psi46digV2.1respin* chip presented in [147]. The steps necessary for the commissioning of the ROC after irradiation are presented in Section 5.3.1. The electronic properties of the chip and its response to the interaction with X-rays are discussed in Sections 5.3.2 and 5.3.3. Finally, the radiation dependence of the readback mechanism is studied in Section 5.3.4. These results provided necessary input for the successful operation of the detector in 2017 and 2018, such as dose dependent calibration parameters needed to update the detector configuration.

5.3.1 Chip commissioning after irradiation

Before measurements can be performed, the operation parameters of the ROCs must be determined. This involves finding the correct voltage to supply the required currents, as well as setting specific DACs that enable the readout of signals. This commissioning is performed after each irradiation step instead of reusing pre-irradiation parameters which often do not lead to successful readout of the chip after irradiation.

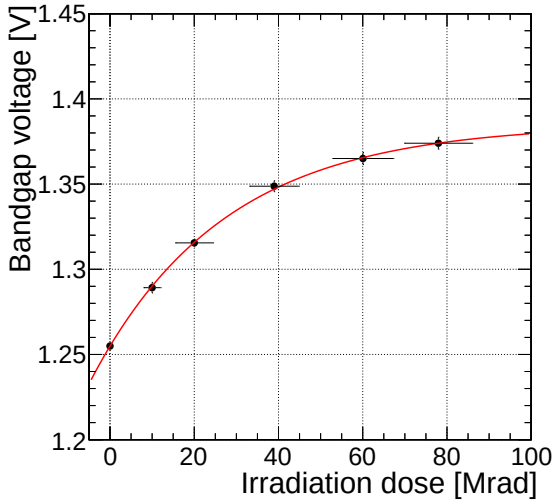

Figure 5.4: Band gap reference voltage as a function of irradiation dose. The BGV increases by 0.12 V at the largest tested irradiation dose.

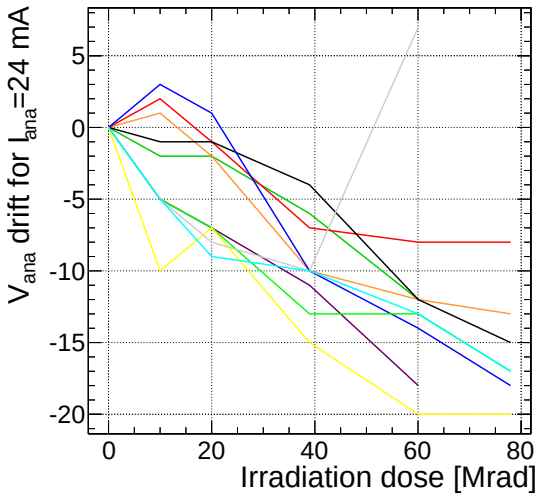

Figure 5.5: Change with irradiation dose of the `Vana` setting necessary to provide an analog regulated current of 24 mA to the ROC. Each line represents one sample, and the data point in gray at 60 Mrad originates from a defective sample at this rate. Large differences are observed between the samples. On average, a decrease of 16 DAC units in the `Vana` setting is observed at the largest tested irradiation dose.

Bandgap reference voltage

To serve as a reference voltage defining the amplitude of each DAC unit on the ROC, a band gap reference system is installed on the chip. It is based on voltage drops across a resistor and across a pn-junction operated with a forward bias voltage [147, 173]. The circuit defining the band gap reference voltage (BGV) is designed such that it is independent of the temperature and input voltage [174]. However it is not stable with respect to radiation damage as it modifies the doping concentrations in the pn-junction. Thus it is measured before and after all irradiation steps on a test pad on the ROC using a probe needle. The results are presented in Figure 5.4, which shows the average BGV for all samples as a function of irradiation dose. The errors represent the spread amongst all samples. The data points have been fitted with an

Dose [Mrad]	Δ V / V_0 (probe) [%]	Δ V / V_0 (readback) [%]
10	2.73 ± 0.18	3.15 ± 0.63
20	4.83 ± 0.17	5.13 ± 1.06
40	7.48 ± 0.25	7.72 ± 0.69
60	8.77 ± 0.28	9.50 ± 1.08
80	9.48 ± 0.32	9.89 ± 0.78

Table 5.2: Relative shift of the band gap reference voltage with respect to before irradiation at all tested irradiation doses. Results are presented for the measurement on the test pad on the ROC and for the measurement using the readback mechanism of the ROC.

exponential function, such that the evolution of the band gap reference voltage as a function of the irradiation dose d is described by the function

$$\mathrm{BGV}(d) = -0.13\,\mathrm{V} \cdot \exp^{-3.13 \times 10^{-2}\,\mathrm{Mrad}^{-1} \cdot d} + 1.38\,\mathrm{V}. \tag{5.7}$$

This leads to a saturation level of 1.38 V at large irradiation doses. Table 5.2 gives the relative drift of the BGV with respect to before irradiation. Before irradiation, a value of 1.255 V is measured, which is close to the band gap voltage of silicon as expected. At low doses, a large increase of the voltage is observed, with an increase of 4.83 ± 0.17 % for the first 20 Mrad. The BGV begins to saturate at higher irradiation doses, reaching a drift of close to 10% at 80 Mrad.

The BGV can also be extracted from the readback mechanism on the ROC which is described in Section 4.2.5. For comparison, the obtained ADC value has been converted to a voltage using a voltage calibration which is repeated after each irradiation step, since this calibration is not stable with irradiation as will be described in Section 5.3.4. While the values of the BGV measured using the readback mechanism are typically between 1% and 3% higher than those measured with the probe needle, the shifts with respect to before irradiation are compatible within errors, as shown in Table 5.2.

This shift is largely responsible for the necessary readjustment of certain DACs after irradiation. Therefore, in the following measurements, the shift as measured using the probe needle is taken into account. Since the readback response measured in the setup can be influenced by voltage drops in cables or by different ground levels on the chip and the DTB, this measurement is less accurate than the direct measurement on the test pad.

Analog and digital supply voltage

Two supply voltages are provided to the ROC to power the analog and digital circuitries of the chip. These are given as input to two regulators which deliver a regulated analog current and digital voltage to the circuits. The regulators are adjusted using `Vana` and `Vdig`.

The analog circuitry of the chip requires a current of 24 mA for operation. At each irradiation step, the setting of `Vana` is optimised to provide the required current. This setting is impacted by radiation processes, such as the change in the band gap reference voltage. Therefore `Vana` must be adjusted with increasing TID. This is illustrated in Figure 5.5, which shows the difference of the optimised value of `Vana` with respect to the value before irradiation in order to supply the necessary analog current for all ten samples under study. It can be noted that while there is a large discrepancy between the individual ROCs, there is a clear trend towards lower values of `Vana` after irradiation. A correction factor to the `Vana` setting after irradiation is estimated by measuring the average drift of the 10 ROCs under test. The six data points are fitted with a linear function yielding the following parametrisation of the `Vana` setting as a function of the irradiation dose d:

$$\texttt{Vana}\,(d) = \texttt{Vana}_{\,0} - [0.199^{\pm 0.069} \cdot d + 0.94^{\pm 3.24}] \tag{5.8}$$

This parametrisation is used to correct the setting of `Vana` during detector operation.

Previous irradiation campaigns have shown that the regulated analog current of the *psi46digV2.1respin* chip presents a dose dependent saturation [147]. For instance, the maximum analog current that can be obtained after a TID of 420 Mrad is approximatively 14 mA using an unregulated analog voltage of 1.6 V. The saturation can be mitigated by raising the unregulated analog voltage [147]. The design of the *PROC600V2* chip was therefore modified to enable operation at higher irradiation doses without increasing the unregulated analog supply voltage.

The digital voltage supplied to the chip is regulated with `Vdig`, and allows for a dynamic range in currents of approximatively 8 mA. Irradiation effects lead to an increase in the current for a given DAC value, which directly follows from the radiation induced drift of the band gap reference voltage. This is verified in Figure 5.6 where each line corresponds to the mean of all ROCs, and the error to their spread. Despite this slight increase, the range of available currents is conserved, and is sufficient for operation at all tested irradiation doses.

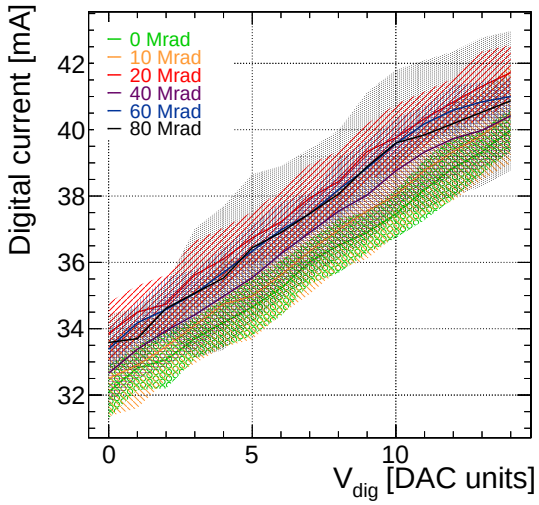

Figure 5.6: Digital current as a function of `Vdig` for all tested irradiation doses. A small increase in current for a given DAC setting is observed after irradiation.

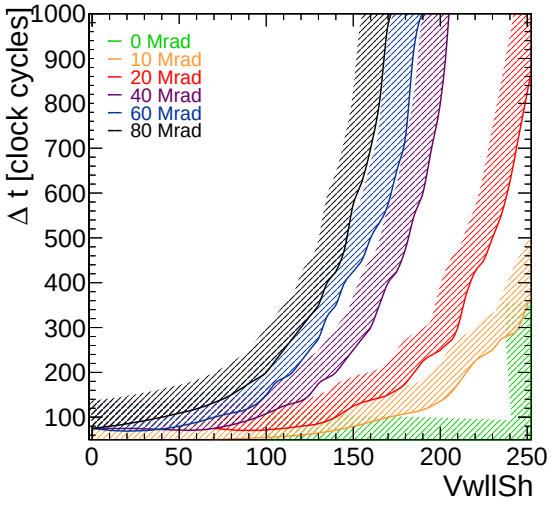

Figure 5.7: Test pulse response as a function of `VwllSh` and the time ΔT between the injection of two test pulses. The space into which the filled area expands indicates the region of the phase space in which the second test pulse is read out. This region shrinks to larger values of ΔT and smaller values of `VwllSh` with irradiation.

Shaper response time

After guaranteeing appropriate voltage supplies to the ROC, it has to be ensured that calibrate signals can be correctly processed by the readout chain. To enable this, `VwllSh` requires adjusting after irradiation, because irradiation leads to an increase in the resistance of the shaper due to a threshold drift in a MOSFET transistor [147]. Higher resistances of the shaper imply that the recovery time of the shaper to return to its ground line increases. Thus signals arriving before the shaper has fully recovered from the previous hit will not be processed. As a consequence `VwllSh` is lowered to reduce the shaper resistance.

This behaviour is tested by modifying the standard pattern generator used to inject calibrate signals in the ROC. Typically, the pattern generator consists of a RESET, a CALIBRATE, a TRIGGER, and a TOKEN signal, the last one replacing the functionality of the HDI on a module to initiate the readout of the ROC. This pattern

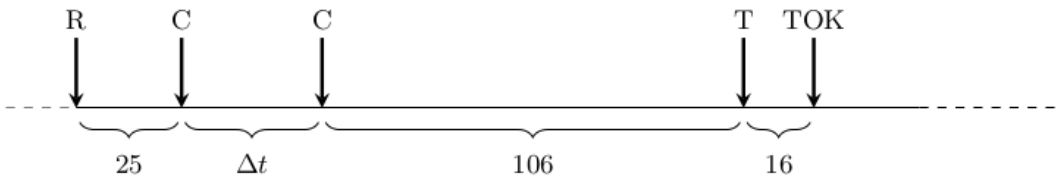

Figure 5.8: Pattern generator sequence used to study the impact of the setting of `VwllSh` on the readout of calibrate pulses [147]. The time between signals is given as a function of number of clock cycles.

generator is amended by a second CALIBRATE signal following the first one after a time Δt, while triggering on the second signal as illustrated in Figure 5.8.

Figure 5.7 shows the result of the two dimensional scan of Δt and `VwllSh` for one pixel on a ROC at different irradiation doses. The region in which the second test pulse is read out expands from the solid line to the top left corner of the phase space. For unirradiated ROCs, all combinations of Δt and `VwllSh` lead to a successful readout of the second test pulse. However, with larger irradiation doses, regions with small Δt and large `VwllSh` become unresponsive, as the shaper has not yet reached its ground line when the second signal arrives. To amend this, either Δt has to be increased (which is not possible during operation), or the resistance of the shaper needs to be reduced which is achieved by lowering `VwllSh`.

For operating the samples in further tests, `VwllSh` was set to 150 for unirradiated samples and samples irradiated to up to 20 Mrad, and Δt was set to 194 clock cycles. For higher irradiation doses, Δt remains unchanged, but the value of `VwllSh` was lowered to 10. It was chosen not to modify the values for the lower irradiation doses as previous irradiation campaigns have shown that the noise level strongly depends on `VwllSh`, and modifying this value can thus mask irradiation effects on the noise, as will be discussed in Section 5.3.2. The chosen values enable a readout without any efficiency losses at all tested irradiation doses.

5.3.2 Electric properties of PROC600V2

After adjusting all parameters of the ROC to enable a successful readout of internal calibrate signals, several essential electronic properties of the chip such as its noise and its accuracy in setting a threshold are studied as well as their response to irradiation.

Pulse height calibration

The amplitude of a signal is measured in terms of its pulse height. A charge proportional to the pulse height is transferred to the buffers and stored. The conversion and digitisation into an 8-bit energy expressed in `Vcal` units is performed using an ADC in the control interface block of the ROC. This mostly linear conversion is tuned using `PHSlope` and `PHOffset`, which adjust the slope and the offset of the ADC. The signals measured during operation in CMS are expected to stay below an energy of 100 `Vcal` units, so that the entire available ADC range of the pulse height should cover this energy range. A detailed explanation of the algorithm used to optimally choose the settings of both DACs is given in [175]. After optimising the two DACs, the conversion between the pulse height and the injected charge is measured for each pixel by injecting signals with increasing amplitude, and recording the measured pulse height as shown in Figure 5.9, which illustrates the conversion for one pixel on an unirradiated *PROC600V2*. This Figure already hints to one major problem of this chip, as the full available pulse height range is not exploited. The used phase space is indicated by the shaded area, and the range only maps onto 150 out of the 250 available ADC units for describing the amplitude after optimisation of both DACs. This is explained by a large non-linearity between the pixels on a ROC. Indeed the pulse height response of pixels to a calibrate signal with a fixed amplitude are vastly disparate, differing by more than 100 ADC units as is illustrated in Figure 5.10. Thus it is impossible to adjust `PHSlope` and `PHOffset` such that the pulse height of all pixels is perfectly tuned.

This feature and its evolution with irradiation are further described by fitting the range below an energy of 100 Vcal with a linear function. The slope (s) and the offset (o) of the fit provide the gain and the pedestal of all pixels, which effectively invert the calibration:

- Gain $= 1/s$ [Vcal/ADC]
- Pedestal $= o/s$ [Vcal], which is a good indicator of the non-linearity of the pixels.

These two parameters are measured for each irradiation step after readjusting `PHSlope` and `PHOffset`. The evolution of the pedestal with irradiation dose is shown in Figure 5.11 where the error bars correspond to the spread among the ROCs and the data points to their mean. The pedestal is larger than 130 Vcal and its mean value increases with irradiation to above 160 Vcal at the largest irradiation dose. For comparison, the *psi46digV2.1respin* chip has a pedestal of around 50 Vcal, which

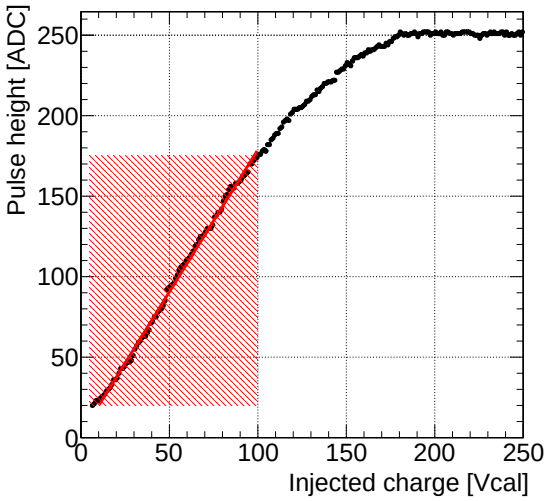

Figure 5.9: Illustration of a pulse height calibration. The area coloured in red is the region of interest in the CMS experiment.

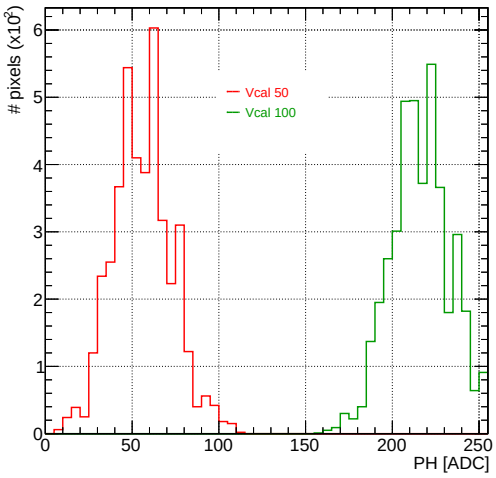

Figure 5.10: Pulse height reponse to test pulses of amplitudes of 50 and 100 `Vcal` units for all pixels of an unirradiated sample. The spread of the pulse height amongst the pixels exceeds 100 ADC units.

is almost three times smaller. This large disparity and the correlated reduction in dynamic range is however not expected to significantly impact the position sensitivity of the detector [152]. The evolution of the gain for all ROCs is shown in Figure 5.11. Each data point corresponds to mean of all pixels of a ROC and the errors to their spread. The order of the ROCs in each series of measurements per dose remains the same. It can be concluded that the gain remains constant at around 3.7 Vcal/ADC, and that there is no systematic trend caused by irradiation.

Loss in pulse height resolution

Irradiation studies of the *psi46digV2.1respin* revealed a loss in accuracy of the pulse height measurement after irradiation [147]. This effect was traced back to an increasingly ohmic behaviour of a transistor responsible for mirroring the current that propagates the pulse height information. Therefore, the rise time of the potential of the capacitor is too long to reach the nominal value within the sampling time of 25 ns. This results in an incorrect sampling of the pulse height information. At low irradiation doses, this issue can be remediated by increasing the digital supply voltage,

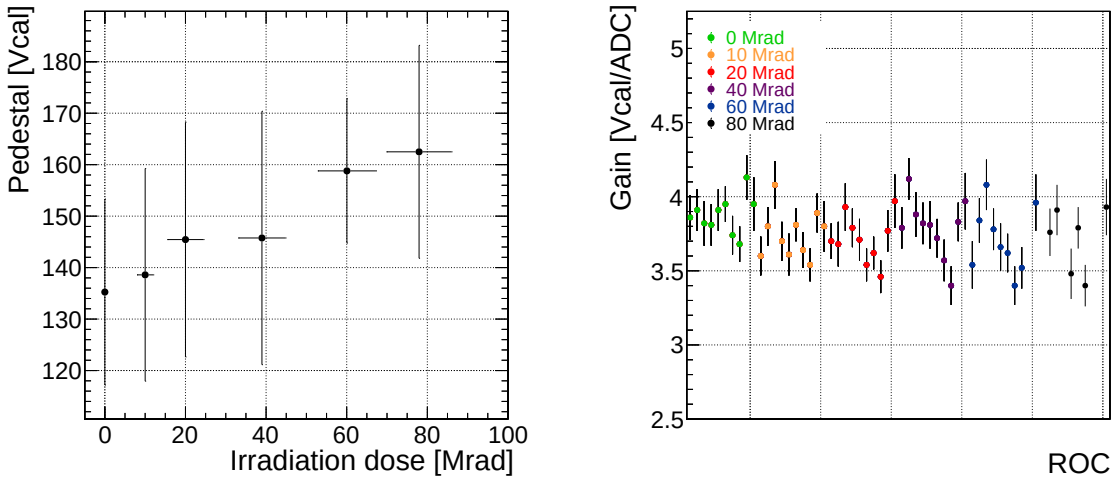

(a) Pedestal (b) Gain

Figure 5.11: Pedestal (a) and gain (b) of the pulse height calibration. No clear conclusions towards the effects of irradiation on those parameters can be drawn given the sensitivity of the measurement.

which allows to safely use *psi46digV2.1respin* for layers 2-4 of the detector.

For the expected dose for layer 1 however, increasing the digital supply voltage would not suffice to mitigate the problem. Therefore the responsible transistor has been replaced with a more radiation tolerant transmission gate. It was verified for irradiated *PROC600V1* ROCs that this change is effective. For this purpose, 20 calibrate signals with a constant and low amplitude are injected in a test pixel, followed by 20 test pulses with a larger amplitude. The measured pulse height is recorded for each pulse. The test results are given in Figure 5.12 for a *PROC600V1* sample irradiated to 240 Mrad. Each line corresponds to a different digital supply voltage setting. It is shown that also for low digital voltages, the pulse height already reaches its expected value for the first calibrate signal of both series, even after the large jump in pulse height from signal 20 to 21. This result differs for *psi46digV2.1respin*, where the recorded pulse height asymptotically reaches the nominal value as is shown Figure 5.12. These test results verify the successful chip design change to eliminate this issue for the *PROC600* chip series.

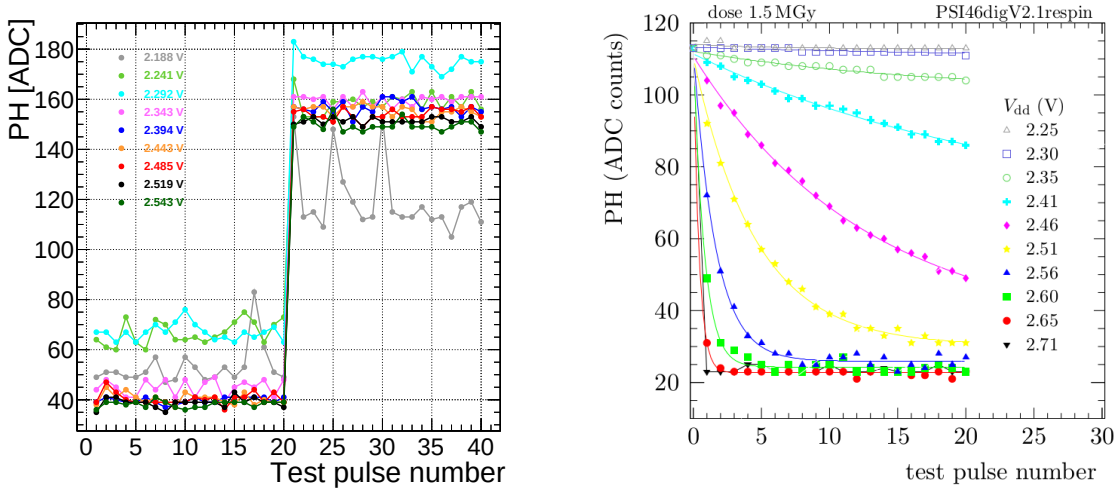

(a) *PROC600V2* (b) *psi46digV2.1respin*

Figure 5.12: Pulse height response to 20 consecutive test pulses with constant amplitude for the *PROC600V2* (a) and *psi46digV2.1respin* (b) ROCs. In the case of *PROC600V2*, these are followed by 20 test pulses with larger amplitude. Here, the measured pulse height reaches the nominal value already for the first test pulse of both series. This is not the case for the *psi46digV2.1respin* ROC, where the time after which the pulse height reaches its stable value depends on the supplied digital voltage [147].

Energy calibration

It was shown previously how the amplitude of a recorded signal is converted into a digitised value expressed in `Vcal` units. A further calibration is necessary to obtain the corresponding charge deposited in the sensor. This calibration is performed using monochromatic X-ray beams. As described in Section 5.2.2, the X-ray beam can be directed towards metallic targets to obtain monochromatic photon sources. The three target materials used in the calibration are Molybdenum (Mo), Silver (Ag), and Tin (Sn).

A spectrum is recorded for each of the three metallic targets, as is illustrated in Figure 5.13. These are fitted with a double Gaussian distribution. The mean of the highest Gaussian corresponds to the Kα_1 emission line of the target. The energy of these lines are compiled for instance in [176] and are reported for the relevant targets in Table 5.3. Considering that on average a deposited energy of 3.6 eV is required to produce one electron-hole pair in silicon [135], the peaks in the spectra can be

Element	Kα_1 [keV]	Kβ_1 [keV]
Mo	17.479	19.607
Ag	22.162	24.943
Sn	25.271	28.486

Table 5.3: Kα_1 and Kβ_1 X-ray transition energies for Molybdenum (Mo), Silver (Ag), and Tin (Sn) [176].

related to the deposited charge in the sensor as is illustrated in Figure 5.14. The energy calibration is then obtained by fitting the three measurement points with a linear function, and extracting the slope and offset.

This calibration is performed for all ROCs after each irradiation step, and the average of the slope of the calibration for all ROCs is shown in Figure 5.15. Before irradiation, a slope of $49.91 \pm 2.68\,\mathrm{e^-Vcal^{-1}}$ is measured, which is used as a conversion factor in various measurements in this Section. As expected from the drift in the bandgap reference voltage, the slope increases with irradiation. The offset of the calibration is shown in Figure 5.16. A large spread between the different ROCs is observed without any clear trend with respect to TID.

Noise

The electronic noise originating for the most part from the preamplifier and the shaper of the readout chain has to be controlled as it can fake signals, and falsify the pulse height of a hit. The amount of noise in the chain is measured by injecting pulses into the pixel under test with increasing amplitude, and measuring the pixel efficiency. Ideally, this would result in a step function, with pulses below the threshold having zero efficiency, and signals above the threshold a full efficiency. However, a turn-on curve is obtained instead because of the gaussian-shaped noise contribution. The curve is fitted using an error function:

$$\mathrm{erf}(x) = \frac{2}{\sqrt{\pi}} \int_0^x e^{-t^2} dt \tag{5.9}$$

The width of the function corresponds to the noise of the ROC, and the amplitude at 50% efficiency gives the threshold of the ROC as illustrated in Figure 5.17.

The measured noise as a function of irradiation dose is illustrated in Figure 5.18, where each data point corresponds to the mean noise of all samples, and the error to their standard deviation. The extracted value in ROC internal `Vcal` units is converted to a charge in electrons, using the conversion constant of $50\,\mathrm{e^-Vcal^{-1}}$ derived

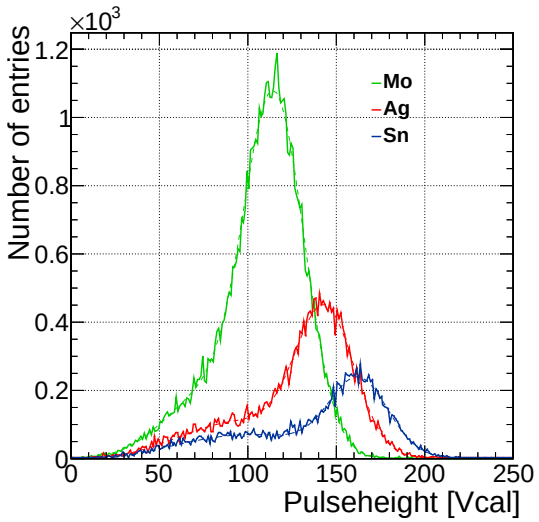

Figure 5.13: Spectrum of the Molybdenum, Silver and Tin targets measured with an unirradiated *PROC600V2*. The peaks of the spectra correspond to the Kα_1 emission line of the elements. Dashed lines show the fit to the spectra.

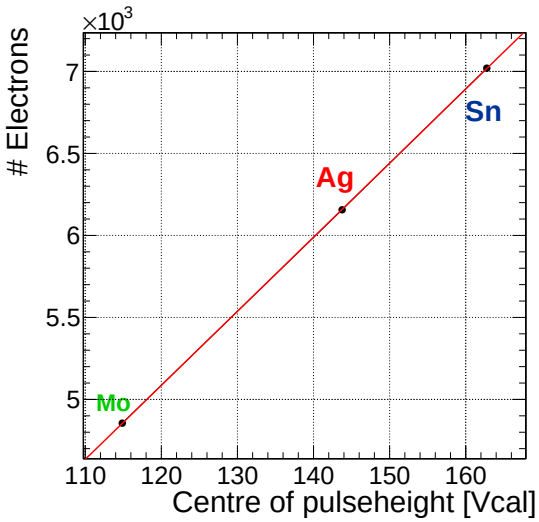

Figure 5.14: Example of an energy calibration using three targets for an unirradiated *PROC600V2*. The measured slope and the offset are used to convert a pulse height expressed in units of `Vcal` into a charge in electrons.

previously. This constant is updated at each irradiation dose, taking into account the drift of the band gap reference voltage.

It is noted that the noise varies between 105 e^- to 130 e^- for all irradiation doses. A direct conclusion regarding the effect of irradiation on the noise cannot easily be drawn, as the noise strongly depends on the values of `VwllPr` and `VwllSh`. This is illustrated in Figure 5.19 which shows that the noise of an unirradiated ROC varies between 80 e^- to 200 e^- depending on the setting of both DACs. In order to factor out this effect, it was attempted to leave the value of `VwllSh` unchanged for the first two irradiation doses. However this was unsuccessful as the pattern observed in Figure 5.19 changes with irradiation, while the noise range remains constant. Thus, it was not possible to disentangle effects from radiation and from the settings of the preamplifier and shaper on the noise. However, the variations in noise observed in Figure 5.18 are much smaller than the variations due to the setting of both DACs. A considerable increase of electronic noise with irradiation can therefore be excluded, and the amount of noise in the ROC depends more on the settings of `VwllSh` and `VwllPr` than on the TID.

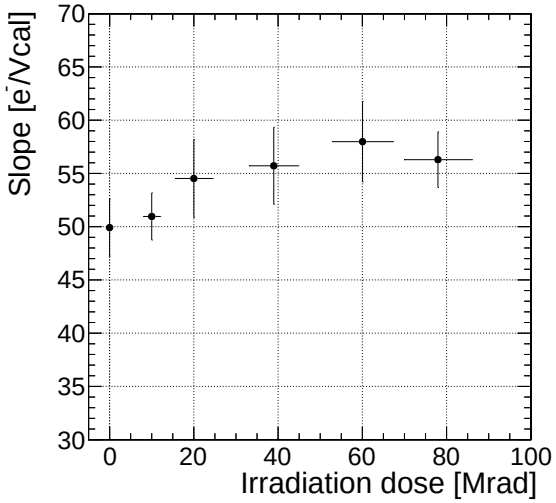

Figure 5.15: Slope of the Vcal calibration as a function of irradiation dose. Following the increase of the bandgap reference voltage, the slope increases with TID.

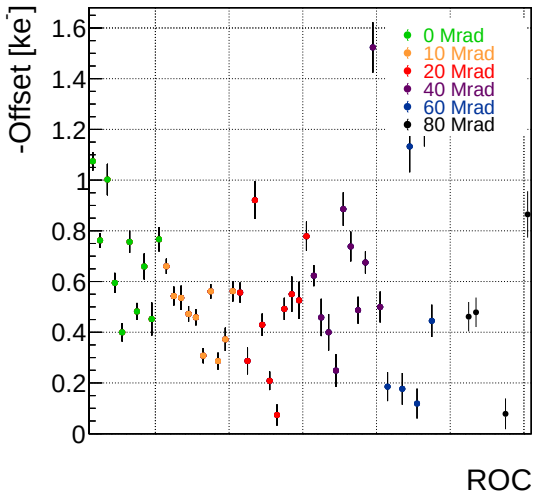

Figure 5.16: Offset of the Vcal calibration for each ROC at all irradiation steps. No clear dependence on TID is observed.

Threshold

In order to establish a constant response of the whole detector, the threshold of every individual pixel is tuned. The procedure to set a ROC's threshold, called trimming, is summarised in the following:

- In a first step, the global DAC `VthrComp` is adjusted. For that purpose, pulses with an amplitude corresponding to the desired threshold are injected at increasing values of `VthrComp`. A turn-on curve similar to Figure 5.17 is obtained for each pixel. From these, the turn-on threshold is extracted, and `VthrComp` is set to the minimal turn-on threshold obtained amongst all pixels of a ROC. At this `VthrComp` value, the threshold of all pixels is at the desired value or higher.

- In a second step, the value of `Vtrim` is set. In combination with the trim bits, its purpose is to lower the threshold of individual pixels. Concretely, `Vtrim` determines the strength of the individual trim bits. In order to maximise the accuracy of the trimming algorithm, `Vtrim` is set as small as possible while allowing the correct threshold setting for all pixels. The pixel with the highest threshold after adjusting `VthrComp` is thus selected for the optimisation of `Vtrim`. All

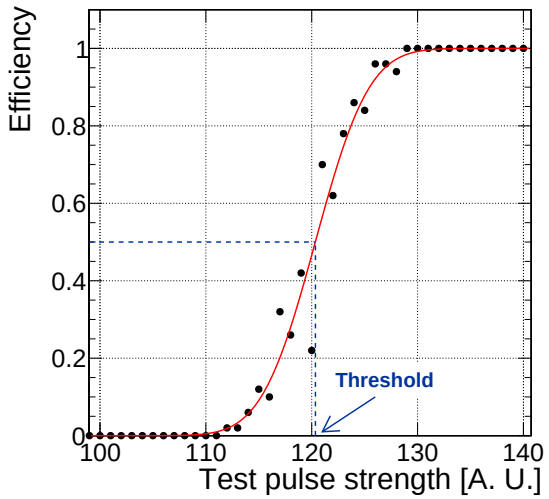

Figure 5.17: Illustration of the measurement of the threshold and the noise on a ROC. The noise corresponds to the width of the error function, and the threshold to the amplitude where an efficiency of 50% is reached.

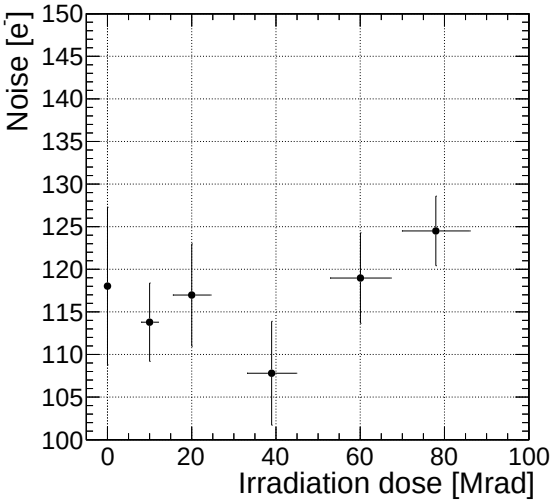

Figure 5.18: Electronic noise as a function of irradiation dose. The noise fluctuates around the pre-irradiation value.

trim bits for this pixel are enabled and `Vtrim` is lowered until calibrate signals with an amplitude corresponding to the desired threshold are recorded.

- In a last step, the trim bits of all pixels are adjusted for fine-tuning. For that purpose, turn-on curves are measured while performing a binary search.

The threshold set on the ROC is expressed in `Vcal` units. As typically a threshold in units of electric charge is of interest, it is converted to a `Vcal` value as detailed in the previous Section, taking into account the change in band gap reference voltage which modifies the step width of the DAC. In this study, a constant threshold of 2000 e^- is used, leading to varying settings of the threshold in `Vcal` values with irradiation as illustrated in Table 5.4. The small deviations from the 2000 e^- baseline arise from the fact that the chip can only be trimmed to integer values of `Vcal`. Therefore, the ROCs are trimmed to the integer value closest to the one obtained in the conversion.

Figure 5.20 shows the threshold in `Vcal` units for all ROCs at all irradiation doses. The data points show the average of the threshold of all pixels on the ROC, and the error bars their spread. It is confirmed that the trimming algorithm operates as

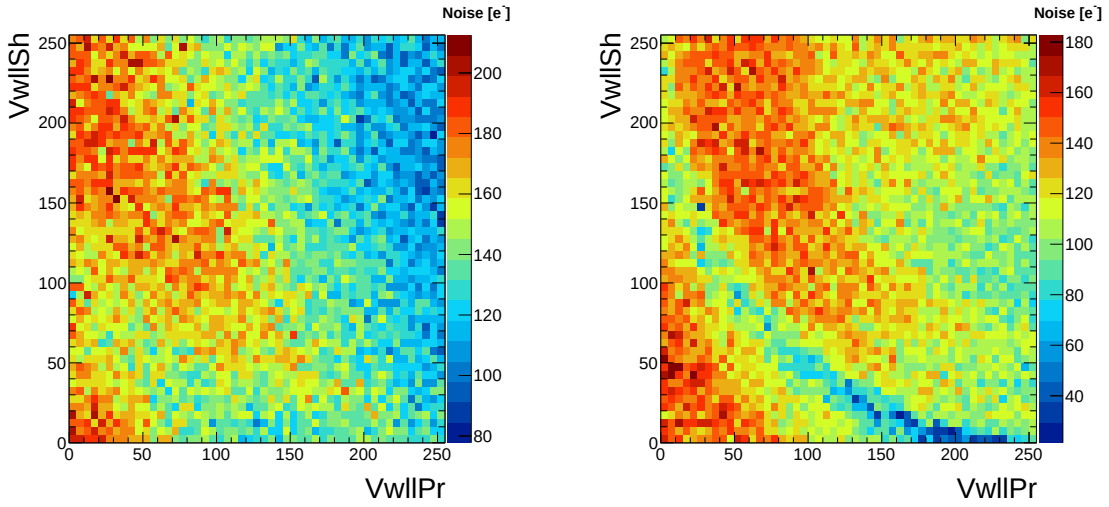

(a) Unirradiated (b) 10 Mrad

Figure 5.19: Noise of a ROC as a function of `VwllPr` and `VwllSh` before irradiation (a) and after a dose of 10 Mrad (b). Large fluctuations of up to 120 e^- are observed. The regions with low and high noise change with irradiation.

TID [Mrad]	Threshold [`Vcal`]	Target threshold [e^-]	Measured threshold [e^-]	Distribution width [e^-]
0	40	2000	1996.8 ± 1.8	72.2 ± 2.2
10	39	2003.2	2003.6 ± 3.2	70.7 ± 2.5
20	38	1991.8	1990.8 ± 5.4	72.3 ± 7.4
40	37	1988.4	1985.7 ± 7.0	63.3 ± 3.3
60	37	2012.2	2007.9 ± 6.0	77.1 ± 6.4
80	36	1970.6	1970.5 ± 6.1	71.2 ± 7.9

Table 5.4: Summary of the target threshold in `Vcal` units and in electrons set at each irradiation dose. The average of the measured threshold after optimisation and the threshold distribution width are listed as well. The measured threshold is well compatible with the target one.

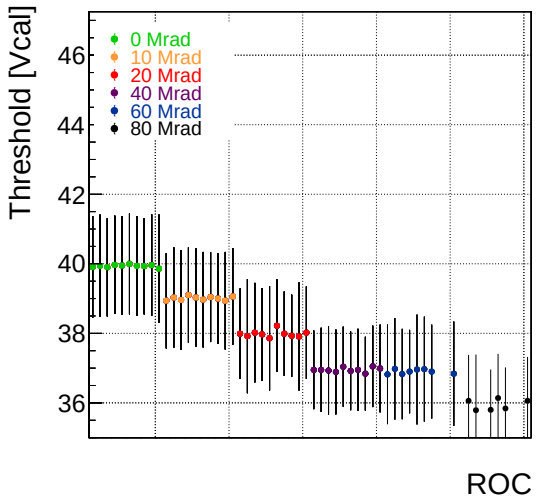

Figure 5.20: Average threshold of the ROCs at all irradiation doses. It corresponds to the target threshold o 2000 e^-.

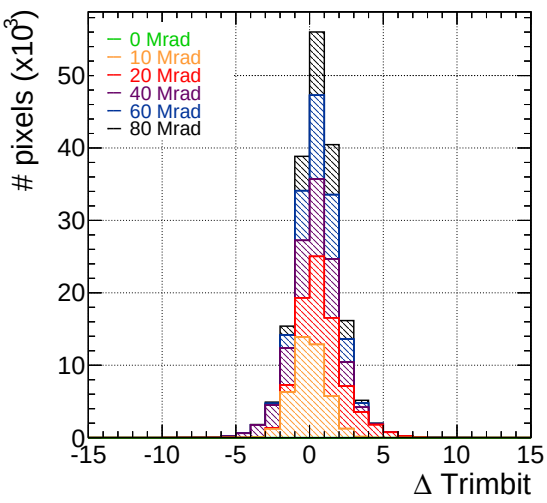

Figure 5.21: Trim bit setting difference between before and after irradiation. Small deviations are present, but most trim bit values remain close to the pre-irradiation ones.

expected and allows to set the desired threshold at all tested irradiation doses. This is also verified in Table 5.4, which shows the average threshold set by the optimisation procedure as a function of the irradiation dose.

For the individual adjustment of the pixels, four trim bits per pixel are available. During operation in the detector, these trim bits cannot be readjusted as turn-on curves are not measurable for the whole detector via the FEDs. As pre-operation settings must be used, it is necessary to verify the validity of the trim bit settings after irradiation. This is shown in Figure 5.21, which gives the difference between the trim bit value set before irradiation and the value determined by the trimming algorithm after irradiation. It can be noted that there is no systematic trend in the evolution of the trim bit settings, and that the optimal trim bit setting changes by less than five units after irradiation. This justifies the use of the trim bit settings obtained during the initial testing of the detector for the entire detector operation.

Timewalk

Depending on their amplitude, signals cross the threshold after a certain delay, which is larger for signals with smaller amplitudes than for those with larger amplitudes.

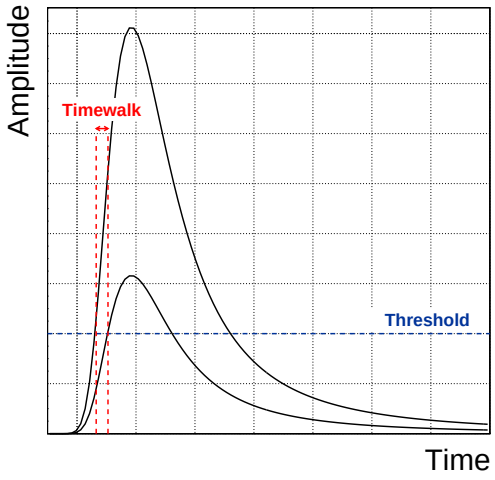

Figure 5.22: Illustration of the measurement of the timewalk. One contribution arises from the delay in arrival time between pulses with different amplitudes.

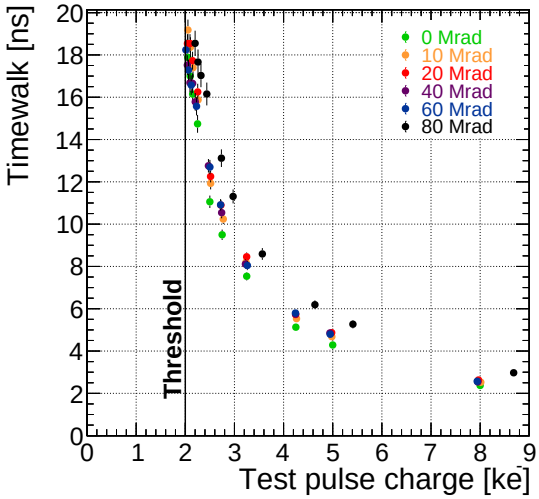

Figure 5.23: Timewalk between a test pulse and pulse with an amplitude of $\sim$ 83000 e. The timewalk increases for test pulses close to the threshold, but for most pixels remains below the CMS bunch crossing time.

This difference is called timewalk and is illustrated in Figure 5.22. It is important that the maximum timewalk, which is reached for signals just above the threshold, is smaller than the bunch crossing time of 25 ns in the CMS experiment. Otherwise, hits from one bunch crossing will be associated to a later bunch crossing, leading to missing hits in the tracker in the original bunch crossing, and to noise hits in the next one. Both reduce the tracking efficiency.

To measure the timewalk, the time delay between a pulse with large amplitude of $\sim$83 000 e^- and a test charge is evaluated in Figure 5.23. For each test charge one hundred pixels are randomly chosen on the ROC and their mean timewalk is extracted. The errors indicate the standard deviation of all tested pixels. As expected, the timewalk increases with smaller test pulses. For test pulses right above the threshold, the mean timewalk stays below 20 ns, which is less than the LHC bunch crossing time of 25 ns. Few individual pixels however reveal a timewalk larger than the bunch crossing time. This is why efforts have been made to reduce the timewalk further for the following iterations of the ROC. Irradiation effects lead to a maximal increase in the timewalk of 2 ns after a TID of 80 Mrad. However, as it still remains

below 25 ns, this increase does not affect the performance of the ROC.

5.3.3 Behaviour of PROC600V2 under X-ray illumination

In this Section, the properties of the *PROC600V2* chip when exposed to X-rays are studied in order to test the interaction of the ROC with real particles instead of internally generated calibrate signals.

Noise

The noise measurement presented in Section 5.3.2 is restrictive in the sense that estimates the noise of the analog readout chain of the ROC, factoring out the impact of incident particles on the noise, and the crosstalk between different pixels. In real detector conditions however, all pixels are operational simultaneously, and exposed to radiation. These more stringent conditions have a large impact on the noise level, as is verified by repeating the previous measurement under X-ray illumination.

Indeed, the noise level strongly depends on the hit rate to which the ROC is exposed to during the measurement as is verified in Figure 5.24, which shows the noise as a function of hit rate for one ROC at different irradiation doses. It is shown that the noise increases by about 150 e^- from a hit rate of 50 MHz cm^{-2} to 250 MHz cm^{-2}. This is why the exact hit rate during the measurement is recorded in order to disentangle effects on the noise from irradiation and from varying hit rates. The result of the noise measurement performed in the high rate environment is shown in Figure 5.25. Two features can be extracted: as presented before, the noise increases with larger hit rates, and exceeds the noise measured in the ideal case presented in Section 5.3.2 by more than a factor two. In addition it also becomes clear that the noise level increases with TID, especially at doses above 60 Mrad where the noise increases by 100 e^- on average at a constant hit rate. Already the noise level before irradiation considerably impacts the operation of the detector, which is why a high threshold of 4000 electrons was chosen to operate the modules built with the *PROC600V2* chip.

With the help of this result, the origin of the noise has later been understood to originate from a crosstalk between the trim lines and the injection capacitor. After setting the threshold of the chip, the trim lines lie on the last value of the trimbits that was set. In most cases, this value will be different from the ground level. When the chip is exposed to a high hit rate environment, the crosstalk between the ground lines and the injector capacitor causes the creation of additional noise hits in the capacitor. The schematics of the ROC illustrating the origin of the large noise are shown in Figure 5.26. To solve the issue, the position of the injection capacitor has

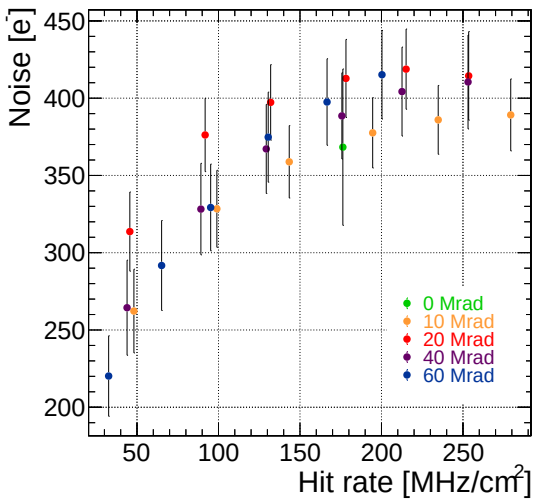

Figure 5.24: Noise measured for one ROC for increasing hit rates at irradiation doses up to 60 Mrad. The noise increases considerably with larger hit rates.

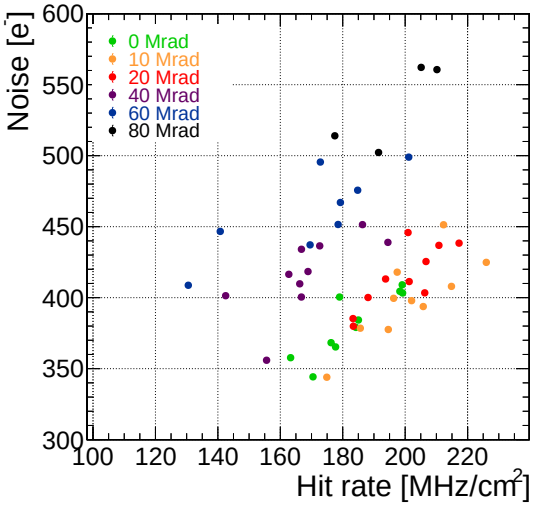

Figure 5.25: Noise per ROC as a function of irradiation dose and hit rate. The noise increases with larger TID by several tens of electrons, independently of the hit rate.

been moved for the *PROC600V4* chip, and is now located below the bump pad, therefore removing possible crosstalk between the trim lines and that capacitor [177].

Efficiency

Specifications of the chip indicate that the efficiency should surpass 98% at the maximum hit rate expected in the CMS detector. For layer 1, which is located only 3 cm away from the beam line, a proton hit rate of around 600 MHz cm^{-2} is expected (thereby giving the ROC its name). As mentioned in Section 4.2.5, hadrons create clusters of size two on average in the sensor. Photons produced in the available X-ray setup primarily interact with the sensor via the photoelectric effect, such that no charge sharing occurs. Therefore each hit leads to an entry in both the timestamp and the data buffers. On the contrary for clusters of hits, only one entry in the timestamp buffers is created for multiple hits. The equivalent hit rate of X-rays is thus estimated to be on average twice larger than for charged particles, and the maximum hit rate expected in the CMS experiment corresponds to a photon hit rate of 300 MHz cm^{-2}.

The efficiency measurement consists in recording an efficiency map while enabling all pixels and exposing the ROC to X-rays. The efficiency is calculated as the frac-

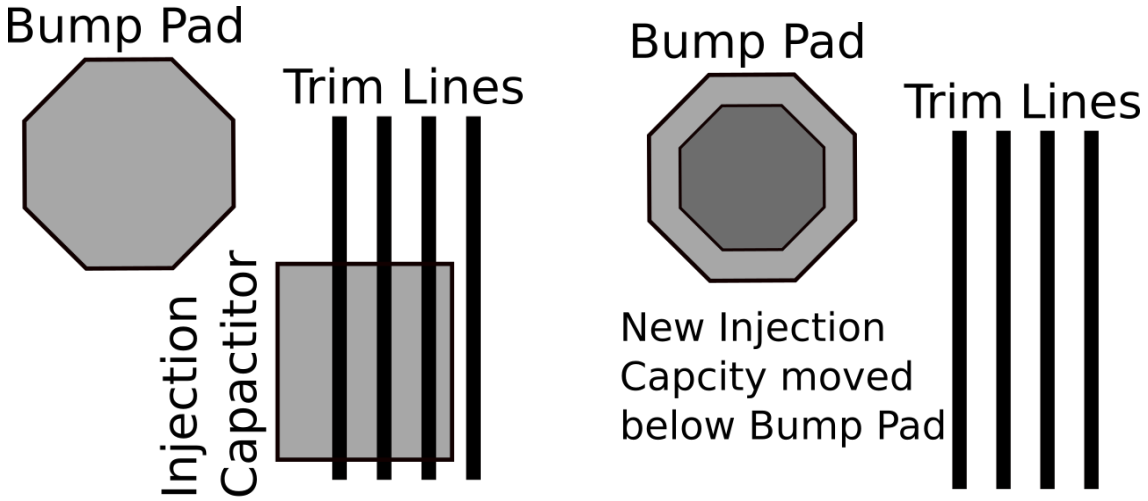

(a) *PROC600* versions 1,2 and 3 (b) *PROC600V4*

Figure 5.26: Positioning of the injection capacitor for *PROC600* versions 1,2, 3 (a) and 4 (b) [177]. For ROCs up to version three, crosstalk between the trim lines and the injector capacitor creates large noise in a high rate environment. Moving the injection capacitor underneath the bump pad reduces the noise of the *PROC600V4* chip.

tion of correctly read out test pulses. The corresponding hit rate is extracted from the number of hits detected on the whole ROC area, and corrected for the measured efficiency, assuming that the efficiency of detecting hits from X-rays and calibration signals is similar. The estimated efficiency as a function of hit rate is shown in Figure 5.27, where each data point corresponds to the efficiency of one double column in the ROC. When considering the overall trend of the efficiency up to a rate of $1300\,\mathrm{MHz\,cm^{-2}}$, which is a factor 4 larger than the rate expected in the CMS experiment, two regimes can be identified. Below rates of $\sim 600\,\mathrm{MHz\,cm^{-2}}$ a small linear decrease in efficiency is observed, which is explained by the analog dead time of the amplifier. For larger rates, the efficiency drops much faster. There, buffer overflows become the dominating source of inefficiencies as hits arrive in the pixels faster than they can be read out. However, this problem only arises at rates much higher that those expected in CMS. At lower rates the efficiency is well above the specification of 98% for all ROCs at all irradiation rates, with the exception of one test sample at 80 Mrad. The low efficiency of this sample is explained by the high level of noise originating from the large irradiation dose. Globally, it can be concluded that the efficiency is above specifications at the rates and irradiation levels expected to be

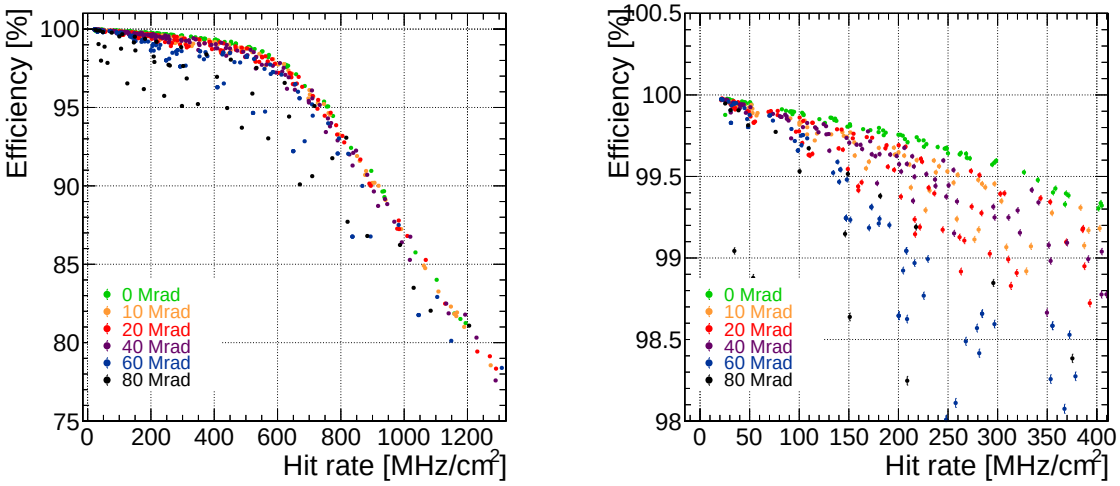

(a) Hit rates up to 1300 MHz cm^{-2}

(b) Hit rates up to 300 MHz cm^{-2}

Figure 5.27: Efficiency as a function of hit rate (a), and zoom into the low rate region (b). While different sources of inefficiencies are noticeable, the efficiency remains above 98% up to hit rates of 300 MHz cm^{-2}.

reached in the CMS experiment.

This measurement is performed using the standard pattern generator which sends a reset before each calibrate signal. After conclusion of this study, it was observed that when removing these resets, a large drop in efficiency is observed both at low and at high rates which is caused by a synchronisation failure between the data and the timestamp buffers. This occurs when the ROC signals that its buffers are full simultaneously to a the arrival of a new signal. The detector is thus operated with resets sent with a frequency of 70 Hz in order to reach the targeted efficiency.

5.3.4 Readback calibration

As explained in Section 4.2.5, the ROC possesses a readback mechanism which allows to extract certain information from the ROC during operation. Of particular interest are

- the bandgap reference voltage, as it is known from Section 5.3.1 that it decreases with irradiation
- the analog current provided to the chip to verify that it is sufficient for operation

- the unregulated analog and digital voltage as they are used to supply the regulated analog and digital voltage which are provided to the ROC.

In order to make use of the information obtained via the readback mechanism, it needs to be calibrated before installation. This is done via the DTB by comparing the voltage or current supplied to the chip with the value obtained from the readback mechanism.

Voltage calibration

The voltage that is read back by the ROC scales linearly with the input voltage, such that it can be described as

$$V(R) = p_0 + p_1 \cdot R,$$

where R is the value provided by the readback mechanism, $V(R)$ the corresponding physical voltage and p_0 and p_1 two parameters to be determined.

The average of the calibration curves obtained for all ROCs at each irradiation dose is shown in Figure 5.28 for the calibration of the digital and the analog voltage. This calibration strongly depends on the TID. The bottom panels of this Figure show the ratio between the pre- and the post-irradiation curves. At the TID collected by layer 1 of the detector during operation in 2017 and 2018, the curve shifts by 20%, meaning that using the calibration curves collected during module testing before installation leads to wrongly interpreted voltage measurements. Noticeably only the offset of the calibration curve is affected, but not its slope.

In order to compensate for this drift, a dose dependent correction factor is extracted from the measured calibration curves and is shown in Figure 5.29 for the analog and digital voltage calibrations. The correction factor $C(d)$ is well parametrised by the function

$$C(d) = c_1 \cdot (c_2 - e^{-d \cdot c_3})$$

where d stands for the accumulated TID in Mrad. The fit parameters are given in Table 5.5. It can be noticed both from the Figures and from the fit parameters that the calibration for the analog and the digital voltage are comparable with each other. The extracted correction factor for the offset of the calibration is independent on the reference voltage and enables to correctly interpret the readback information after irradiation.

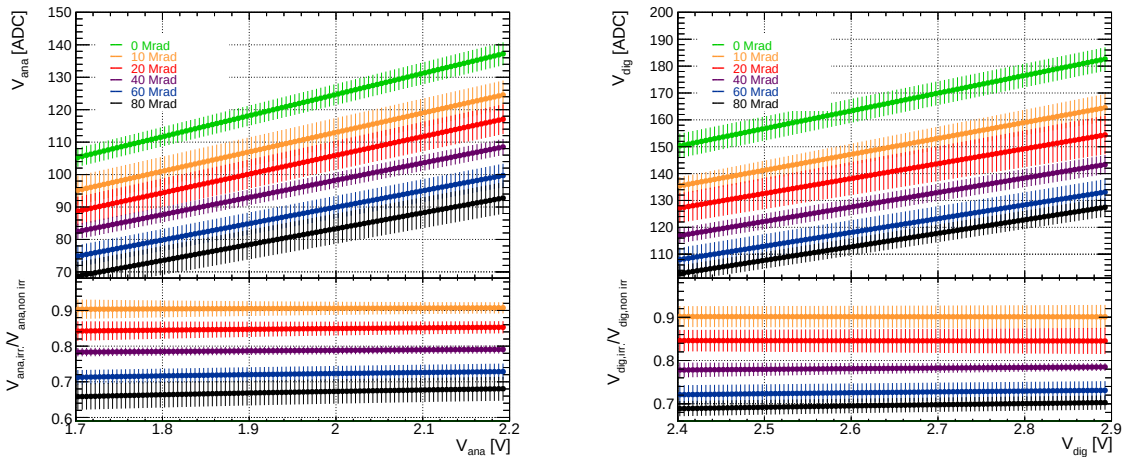

(a) Analog voltage

(b) Digital voltage

Figure 5.28: Calibration of the readback of the analog (a) and digital (b) voltage as a function of irradiation dose. The calibration strongly depends on TID and the offset of the calibration curve decreases by more than 30% at the largest tested dose.

Current calibration

Similarly to the readback of voltages, the readback of the analog current is calibrated. In a first step, the evolution of the analog current, which is measured with the DTB, with respect to the setting of `Vana` is evaluated and fitted with a second order polynomial:

$$I_{ana}(V_{ana}) = m_0 + m_1 \cdot V_{ana} + m_2 \cdot V_{ana}^2$$

In a second step, the amplitude of `Vana` is related to the measured readback

Readback calibration	c_1	c_2	c_3
Analog voltage	-0.37 ± 0.07	-1.74 ± 0.53	0.025 ± 0.009
Digital voltage	-0.34 ± 0.04	-1.96 ± 0.36	0.029 ± 0.009
Analog current	-0.48 ± 0.14	-1.10 ± 0.62	0.022 ± 0.012

Table 5.5: Fit parameters for the correction factor that rectifies the readback calibration after irradiation presented in Figure 5.29.

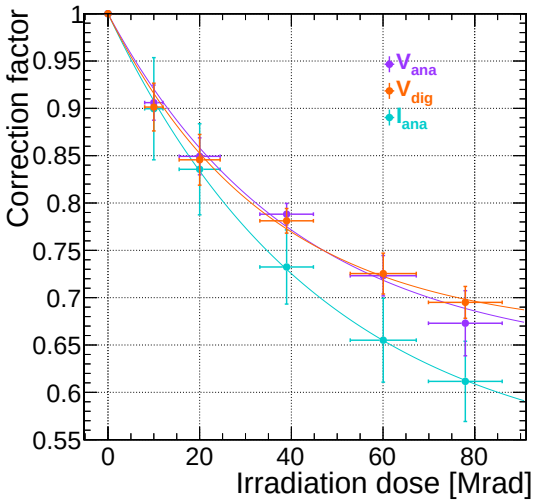

Figure 5.29: Correction curve for the voltage and current calibration after irradiation. The correction factor increases with larger TID.

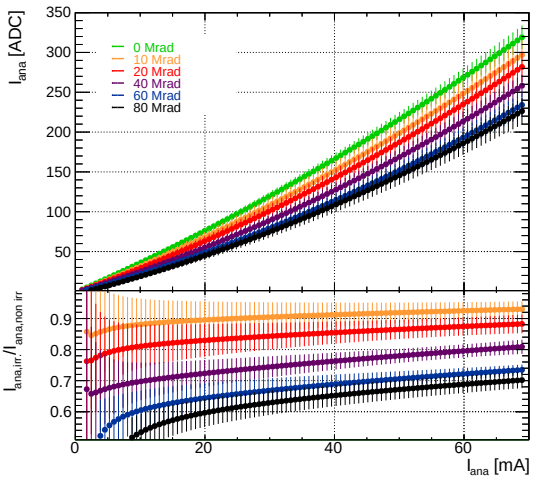

Figure 5.30: Calibration of the readback of the analog current as a function of irradiation dose. The calibration curve is impacted by the TID and results in larger physical currents for the same readback currents after irradiation.

response using a linear function:

$$R = n_0 + n_1 \cdot V_{ana}$$

Combining both steps allows to find the analog current as a function of the readback value:

$$I_{ana}(R) = m_0 + m_1 \cdot \left(\frac{R - n_0}{n_1}\right) + m_2 \cdot \left(\frac{R - n_0}{n_1}\right)^2$$

The calibration is performed for each ROC at all tested irradiation steps, and the calibration curves are averaged for all samples. The result is presented in Figure 5.30. As expected, the calibration is parabolic and not linear in this case. Furthermore, while the current calibration also strongly depends on the TID, the radiation induced drift varies with the value of the current. A correction factor has been derived for correcting the calibration for a current of 24 mA, as this is the current required to operate the chip. The correction factor is given in Figure 5.29, and the parameters of the exponential fit are listed in Table 5.5. The given parameters can be used to

correct the calibration curves during operation knowing the TID accumulated by the detector in order to properly interpret the output of the readback.

5.3.5 Conclusion

This study intensively investigated the effect of TID on the readout chip used for layer 1 of the Phase 1 upgrade pixel detector, *PROC600V2*. Test samples were exposed to doses up to 80 Mrad, which exceed the accumulated dose during the operation of the detector in 2017 and 2018 by a factor two. Various intermediate doses were tested in order to establish a clear picture on the evolution of TID effects with irradiation dose. The knowledge gained during this work was instrumental in the excellent performance of the detector.

During the course of the study, several shortcomings of the chip became apparent, such as its large noise when exposed to X-rays, and the reduced pulse height sensitivity arising from the large non-linearity between the pixels. None of these issues originate from radiation defects, and are present already for non-irradiated ROCs. Identifying these flaws enabled to correct them for the development of the *PROC600V4* chip, from which modules are built to replace the innermost layer of the pixel detector for Run III of the LHC.

The irradiation campaign did not reveal additional issues arising from accumulated TID, which was confirmed during the two years of operation in CMS. It was shown that the ROCs can well be commissioned and trimmed at all tested irradiation doses. It was also shown that using frequent resets, the chip efficiency is above 98% at the maximum hit rate expected in the CMS experiment. It was observed that the noise of the ROC when exposed to X-rays increases even further with irradiation, particularly at higher irradiation doses above 40 Mrad. However, this dose exceeds the maximum TID accumulated during the two years of operation, and the increase of the noise level at lower rates is acceptable.

This study also provided several essential calibration parameters which are needed to adapt the operation parameters during data taking. In particular, a TID dependent correction factor which enables to correctly interpret the output of the ROC readback mechanism was derived. Additionally another dose dependent correction factor is provided to adjust the input current to the analog circuitry of the chip during detector operation. This contributed to a successful operation of the detector during the years 2017 and 2018.

Chapter 6

Module qualification for the Phase 1 upgrade pixel detector

All individual components are thoroughly tested before assembly of the full modules. In dedicated setups any electrical shortcomings of single HDIs are identified, and the properties of all sensors are evaluated. In addition, the ROC wafers are probed after dicing to identify ROCs with severe damages. These tests are performed in order to maximise the production yield of full modules, already rejecting faulty components before module assembly. However, a complete analysis of the assembled modules is still necessary in order to verify the modules' functionality, to set certain operation parameters, as well as to recognise potential defects occurring during module production. The testing procedure involves electrical tests and measurements performed under X-ray illumination and verifies the thermal stress tolerance of the modules.

Module assembly took place in October and November 2016 at the Paul Scherrer Institute in Switzerland (PSI) [178]. This included the bump bonding of the sensor to the array of readout chips, the gluing of the HDI and the wirebonding of the HDI to the readout chips. The first series of tests were also performed at PSI, and modules were afterwards transported to ETHZ [179] to study the modules' performance when exposed to X-rays.

Section 6.1 details the test series performed on all assembled modules and describe the testing conditions. Section 6.2 gives a brief overview of the results of the electric tests performed on the modules. In Section 6.3, their properties when exposed to X-rays are described and the main observed defects are outlined. Section 6.4 summarises the results of the module qualification procedure. Finally, selected test results of prototype modules equipped with the *PROC600V4* chip are presented in Section 6.5.

6.1 Test sequence and conditions

A standardised testing procedure is used to assess the quality of all modules before installation in the Phase 1 pixel detector. Similarly to the tests performed on single chip modules which are presented in Section 5.3, the procedure involves tests verifying the electric properties of the readout chain of the individual ROCs, as well as measurements using X-rays in order to evaluate the detection efficiency in a high radiation environment. In addition, the sensor quality is evaluated. The full qualification procedure used for layer 1 modules which are described in Section 4.2.5 is outlined in the following:

- Thermal cycling: Three temperature cycles between 17 °C and −20 °C are performed to verify that the sensor does not develop defects when exposed to changes in temperature. As the coolant temperature in the CMS experiment is −20 °C [95], this constitutes a lower bound for the modules.

- Electrical test at −20 °C: In this part of the qualification procedure, the functionality of the module and the tuning of its operation parameters is verified. This involves setting the timings of the TBM chip, studying the ROCs' programmability, adjusting their supply voltages as well as their threshold, measuring their noise, and evaluating the pulse height response. In addition, the bump bonding quality is assessed and the readback mechanism of the ROCs is calibrated.

- Sensor test at −20 °C: The leakage current of the sensor is measured at increasing bias voltages to display the sensor properties. In particular, a high leakage current or a voltage breakdown occurring at unusually low bias voltages indicates defects in the silicon.

- Electrical test at 17 °C: This test is repeated at higher temperatures to ensure the good functionality of the modules over the entire possible temperature range in the CMS experiment.

- Sensor test at 17 °C: For similar reasons, the sensor quality is also assessed at larger temperatures.

- High rate test at 17 °C: The ROCs' efficiency when exposed to X-rays is measured as well as their noise. Pixels recording unusually many hits (hot pixels) are also identified and either trimmed to a higher threshold value or masked. Hit maps are recorded to identify further irregularities in the modules' functionality.

A total of 96 modules are needed to equip the innermost layer of the pixel detector. To account for some defective modules and to provide spares in case of unexpected issues during mounting, 141 modules are produced and qualified. The qualifications are performed in similar setups than those described in Section 5.2.2. In this case, modules are connected via a copper cable to an adapter card, which in turn is connected to the DTB. The tests are performed using the *pxar* [168, 169] and the *elComandante* [170] software. Test results are analysed with the *MoreWeb* package [180], allowing an automatic, consistent and fast grading of the modules.

6.2 Electric and sensor properties

An extensive overview of the results of the electrical tests is given in [181], of which the key points are summarised here.

The test results confirm the ROC characteristics which were observed during the irradiation campaign presented in Section 5.3. In particular, the threshold setting is successful for almost all modules, and the supply voltages can be adjusted correctly. However the large non-linearity in the pulse height response between all pixels becomes apparent in the test results as well. While globally the sensor quality is very good, three modules are rejected because their leakage current exceeds 10 µA at 17 °C.

Additional issues are observed, which are also confirmed by tests performed in a high hit rate environment which are described in Section 6.3. In particular, some modules present a poor bump-bonding quality. In addition to this, specific electric defects are identified. One example are address decoding problems, which are illustrated using the efficiency map shown in Figure 6.1. In this case, one column shows a problematic behaviour as the hits received by every second pixel are read out with the address of the pixel in the previous row. These type of defects impact the efficiency in a high rate environment and affected modules are therefore rejected.

6.3 Interaction with X-rays

A key part of the module qualification is the verification of their functionality when interacting with real particles instead of internally generated test pulses. Thus, 134 modules which did not reveal serious issues in the electric test (such as a particularly high leakage current) were tested using X-rays between October and November 2016. All modules are assigned a grade after qualification. Grade A modules exhibit a good performance and are suited for installation in the detector. Modules with a few not disqualifying problems are assigned grade B and are still considered for installation,

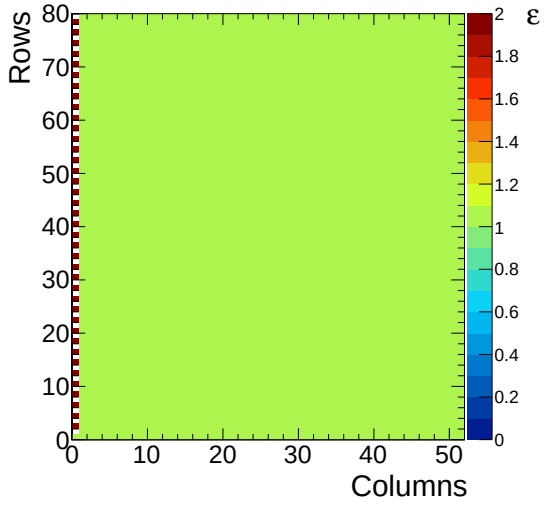

Figure 6.1: Efficiency map of a ROC presenting address decoding problems in column 0. Hits in every second pixel are recorded in the wrong pixel.

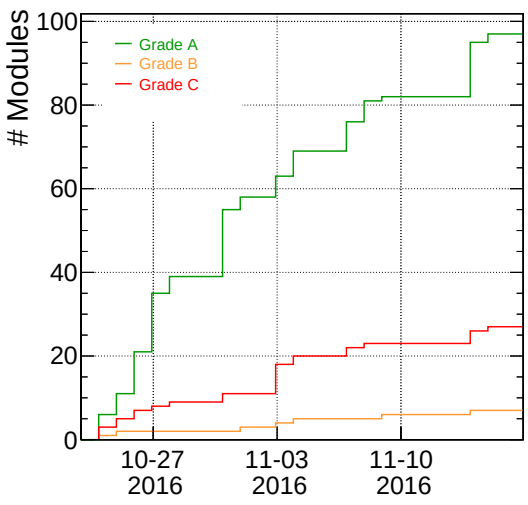

Figure 6.2: Number of tested modules as a function of time and assigned performance grade. A total of 134 modules were tested within three weeks.

while modules with severe issues are downgraded to grade C. Figure 6.2 shows the evolution of the number of modules of each grade as a function of time. Most modules are graded A, however approximatively 30% of the modules revealed major defects in the qualification and are thus rejected from installation in the detector.

Because of the shortcomings of the *PROC600V2* ROC which are observed in various tests such as the irradiation campaign presented in Section 5.3, dedicated testing conditions are designed for layer 1 modules. In particular the threshold at which modules are tested is raised to $4000\,\mathrm{e}^-$ because of the large noise observed when exposing the module to X-rays. However, this higher threshold is also necessary because with the additional activity occurring in the chip at lower thresholds, the power consumption of the ROC increases and exceeds the capabilities of the DTB, such that a proper readout cannot be assured. This issue is not relevant when performing tests on single chip modules because the DTB only has to power one ROC instead of 16 as is the case for a layer 1 module.

When increasing the threshold to that value, it is not possible to perform an energy calibration for all modules as the energy of the fluorescent lines lies below the threshold. Thus the calibration is only performed on only one module in dedicated testing conditions, yielding a calibration with a slope of $52.23 \pm 3.55\,\mathrm{e}^-\mathrm{Vcal}^{-1}$ and

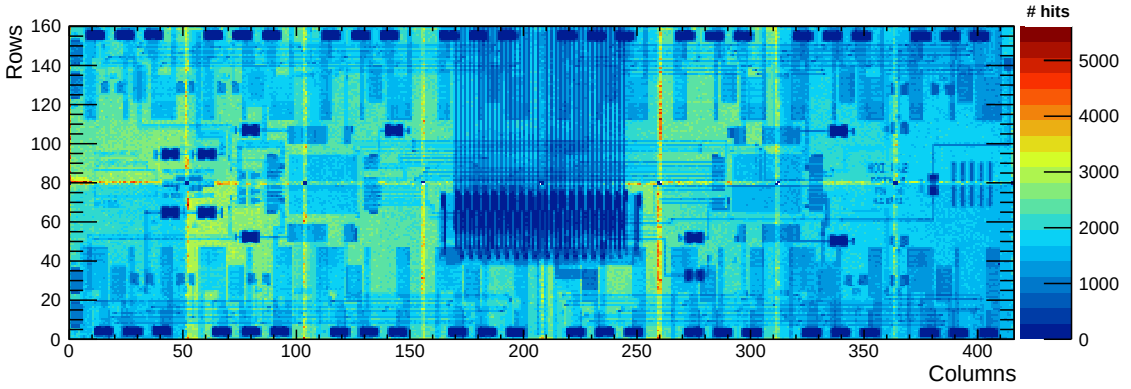

Figure 6.3: X-ray image of a module used for layer 1 of the pixel detector. Features such as the cables and the capacitors placed on the module's edges are clearly recognisable.

an offset of $-2046 \pm 616\,\mathrm{e}^-$.

To further counteract effects from noise, two corner pixels of the ROC, whose size is four times that of the other pixels are masked for the qualification. Furthermore, the threshold of all edge pixels, whose size is twice larger than the size of pixels in the middle of the array is increased to even larger values. In these conditions, it is possible to operate the modules when exposed to X-rays as is illustrated in Figure 6.3, which shows a hit map of an entire module. The features of the HDI shown in Figure 4.12 are clearly recognisable, since parts of this printed circuit board are more transparent to X-rays than others. In particular, the dark rectangles show the location of capacitors glued on the HDI. The module cable is also identifiable. As the energy of particles which are produced in the CMS experiment is much higher than that of the X-rays used for testing, the stopping power of the HDI does not impact the operation of the pixel detector.

Before taking any measurements in the high hit rate environment, modules are configured. As mentioned above, the threshold of the pixels is adjusted. Furthermore, pixels which record considerably more hits than surrounding ones are identified as hot pixels, and their threshold is either increased or the entire pixel is masked. Lastly, `CalDel` is optimised for reaching the highest possible efficiency.

6.3.1 Efficiency

A crucial feature which is tested during the qualification procedure is the modules' efficiency in a high rate environment. The test is performed as is described in Sec-

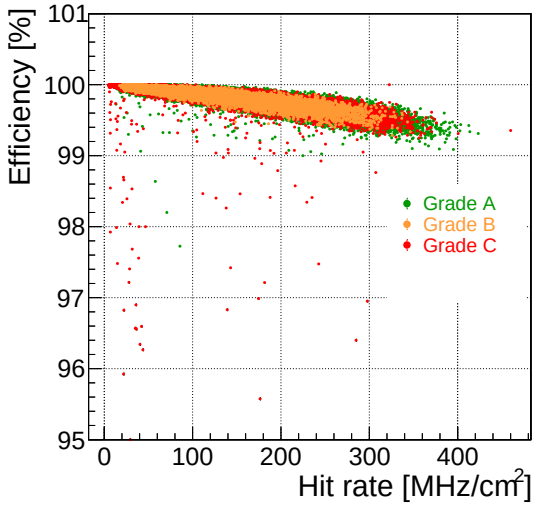

Figure 6.4: Efficiency of ROCs on layer 1 modules as a function of hit rate. All modules which are assigned a grade A or B present an efficiency of above 99% at a hit rate of 300 MHz cm^{-2}.

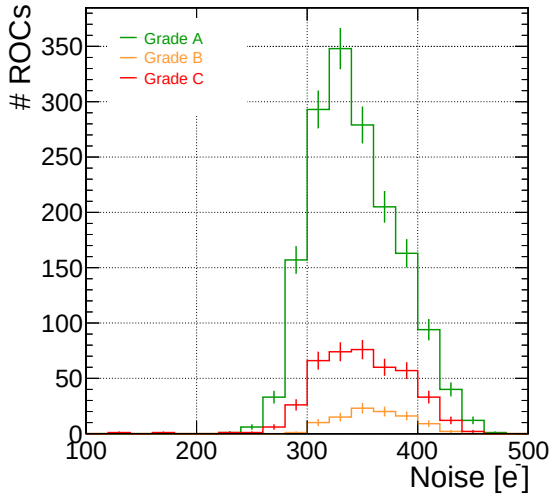

Figure 6.5: Noise of the tested modules when exposed to X-rays. The noise amounts to 350 e$^-$ on average in these conditions.

tion 5.3.3, using frequent resets in order to prevent issues of mismatches between data and timestamp buffers. The efficiency of the ROCs of all modules is shown for different hit rates in Figure 6.4. Each data point corresponds to the efficiency of one ROC, and is coloured according to the assigned grade of the module to which the ROC belongs. The efficiency of all ROCs graded A exceeds 99% at the maximum rate expected in the CMS experiment, which corresponds to 300 MHz cm^{-2}. The efficiency of several ROCs on modules graded C is however considerably lower, decreasing below 96% already at very low rates. One reason for such cases are defects in the double column periphery. This is described in more detail in Section 6.3.3.

6.3.2 Noise

The noise when exposed to X-rays is also evaluated and shown in Figure 6.5. The hit rates during the measurements vary between 150 MHz cm^{-2} and 200 MHz cm^{-2}. As expected from previous measurements, the noise in these conditions is large, averaging 343 ± 38 e$^-$ for modules graded A. Modules with lower grades have a very similar noise level. No grading is applied on the noise level of modules.

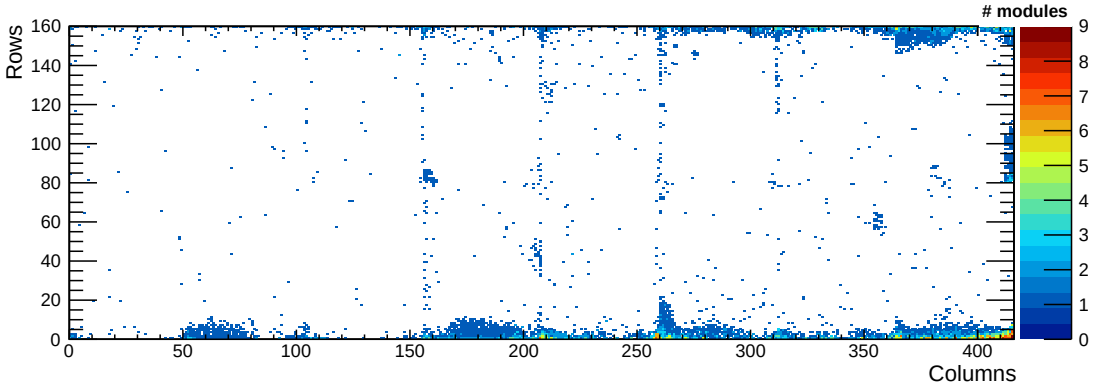

Figure 6.6: Overlay of the bump bonding defects of all tested modules. Most defects are located on the edges of the module.

6.3.3 Observed defects

A variety of defects appeared during the qualification of layer 1 modules in a high hit rate environment. The most common defects are summarised here.

Tests performed in a high hit rate environment are used to evaluate the quality of the bump bonding. Electrically working pixels which record no hits during a sufficiently long data acquisition time are easily identifiable has having a defective connection to the sensor. Figure 6.6 shows an overlay of all defective bump bonds of the 134 tested modules. The majority of the bump bonding problems arise at the edges of the module, and concentrate predominantly on one of its sides. This differs to modules tested for layer 2 of the detector, where defective bump bonds primarily occur at the corners of the ROCs as is illustrated in [175]. These modules are bump bonded using a different setup than modules for layer 1 which explains the varying patterns. The origin of the problems for layer 1 are explained by the fact that the size of the pressure mask applied on the module during bump bonding is barely as large as the module itself. Thus a lower pressure is applied on the edges of the modules.

The main defects which are observed during module qualification in a high hit rate environment are issues involving individual double columns. These defects appear in various constellations, but are all identifiable by irregularities observed when exposing the module to X-rays. Most of these cases are explained by defects in the double column periphery.

One example is described in the previous Section, where wrong addresses lead to hits of pixels in even rows being recorded in an adjacent row. This feature is observed for internal calibrate signals and a similar observation holds for hits created by X-

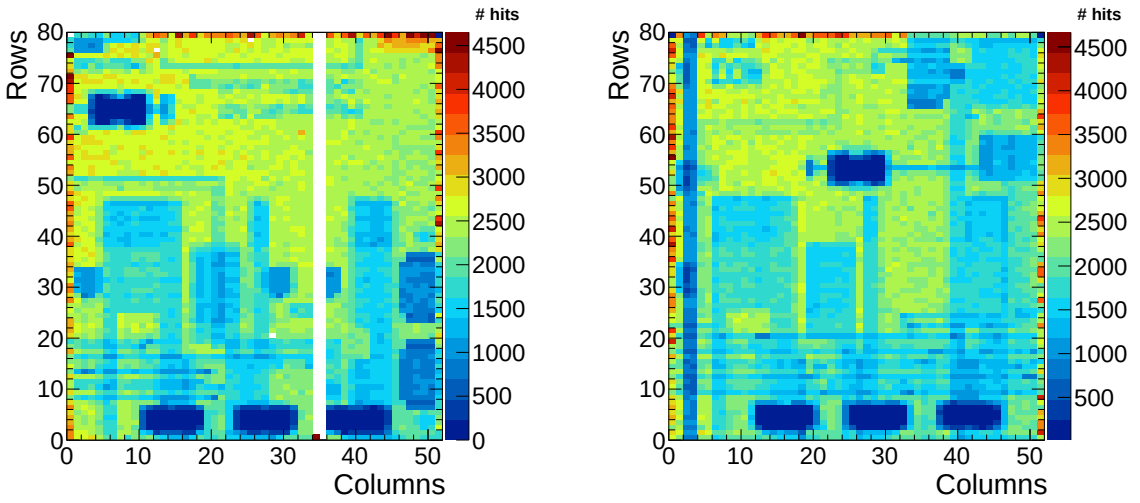

(a) Defective data buffers

(b) Defective timestamp buffers

Figure 6.7: Hit map of a ROC with defective data buffers (a) and defective timestamp buffers (b) in one double column. In the first case, the column sees no hits when exposed to X-rays. In the second case, the efficiency of the problematic double column decreases.

rays. Other cases are related to defective buffers in the double column interface. Two examples are given in Figure 6.7 which shows the hit maps of two ROCs of different modules. In the first example, no pixel except for one records any hit in a full double column. In the second case, one double column registers far less hits than adjacent ones.

Using a dedicated testing procedure, the issue of the first ROC under study is traced back to several defective data buffers in the periphery of the double column, which is illustrated in Figure 6.8. In this test, calibrate signals are injected in each double column until filling all the timestamp buffers. The number of pixels into which pulses are injected per timestamp can be varied. It is then verified if all injected test pulses can be read out. In the example shown here, it can be seen that all hits can be read out when less than 8 timestamp buffer cells are used, injecting 2 pixels per timestamp. When injecting 4 pixels simultaneously, only hits injected in the first 3 timestamp buffers are recorded. Evaluating the total number of hits injected into the data buffers, it can be concluded that there exists a chain of defective data buffers in the double column periphery, beginning at cell 15 or 16. In a similar test, it could be identified that the example shown in Figure 6.7 (right) arises from a defective

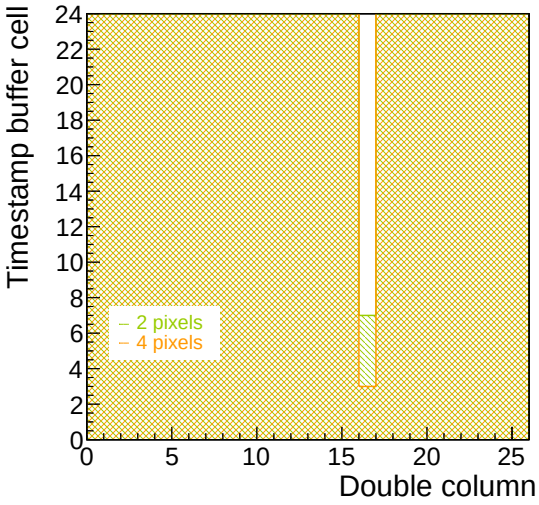

Figure 6.8: Verification of the functionality of timestamp and data buffers. As the number of the timestamp cell from which on calibrate signals are not detected any more depends on the number of pulses injected per timestamp, it can be concluded that double column 16 has defective data buffers.

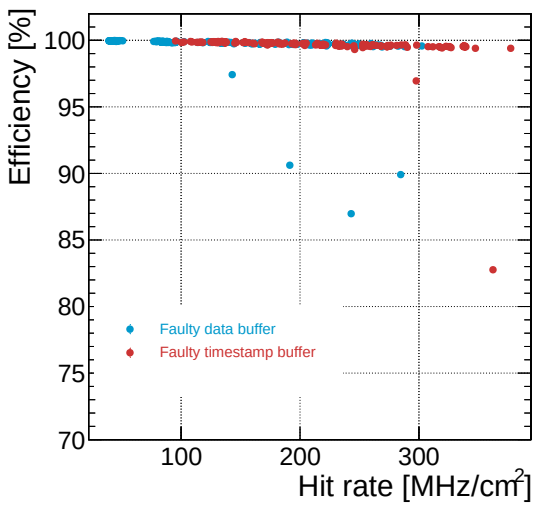

Figure 6.9: Efficiency of ROCs exhibiting issues with buffers in one double column. These double columns have a notably lower efficiency above a certain hit rate.

timestamp buffer in cell 14. In this case, the output of the test is independent on the number of injected hits per timestamp.

These defects lower the efficiency of the ROCs when exposed to X-rays as is illustrated in Figure 6.9. In both cases the efficiency of one ROC of each module decreases significantly above a certain hit rate. The rate at which the efficiency begins to decrease depends on the position and the cell of the defective buffers.

As similar defects were already observed for layer 2 modules which were produced before those of layer 1, the ROC wafer testing was expanded to identify issues with defective buffers [182]. This enabled to already reject problematic chips before module assembly. However, it is clear that the test did not recognise all faulty ROCs.

6.4 Qualification overview

After performing all tests described above, each ROC on the module is being assigned a grade between A and C, the module grade being the worst grade of all its ROCs. A ROC is downgraded either from one of its performance parameters or because of a too high number of defective pixels. When more than 42 pixels (1%) on a ROC are defective, the ROC is graded B, if there are more than 168 (4%), it is graded C. Pixel defects recognised in X-ray tests involve bump bonds, and hot pixels which have to be masked. Furthermore, no module with more than 200 bump bonding defects in total is accepted. Performance parameters taken into account are the efficiency of the ROC, the column uniformity which requires that all columns record a similar number of hits, and the temporal readout uniformity which verifies if the number of recorded hits remains constant over time. These parameters enable to recognise most of the issues arising in the double column periphery, which are described in Section 6.3.3. Grading criteria on the performance parameters are shown in Table 6.1.

Table 6.1: Performance parameters of a ROC leading to a downgrade. These involve the ROCs efficiency when exposed to X-rays, and its column and readout uniformity.

	B	C
Efficiency at $300\,\mathrm{MHz\,cm^{-2}}$	$< 98\%$	$< 95\%$
Column uniformity problems	-	≥ 1
Readout uniformity problems	-	≥ 1

In addition to the grade obtained during the qualification in the high hit rate environment, the module is assigned a grade for its sensor quality and one for its electronic properties. The final grade corresponds to the worst grade of these three.

A total of 141 modules were tested, of which 79 were assigned grade A, 26 grade B and 36 grade C, leading to a failure rate of 28.5%. As 96 modules are needed for installation, enough modules of grade A and B are available to equip the detector.

The main failure reasons are issues with double column defects, affecting 22 modules. Two modules were rejected because of their poor bump bonding quality, and an unusually high leakage current disqualified 3 modules. All other modules graded C present various defects in the electric test and are described in [181].

Modules successfully passing the qualification were installed on the support structure in November and December 2016 at PSI, and connected to the supply tube. The Phase 1 pixel detector was transported to CERN and installed in CMS in February 2017.

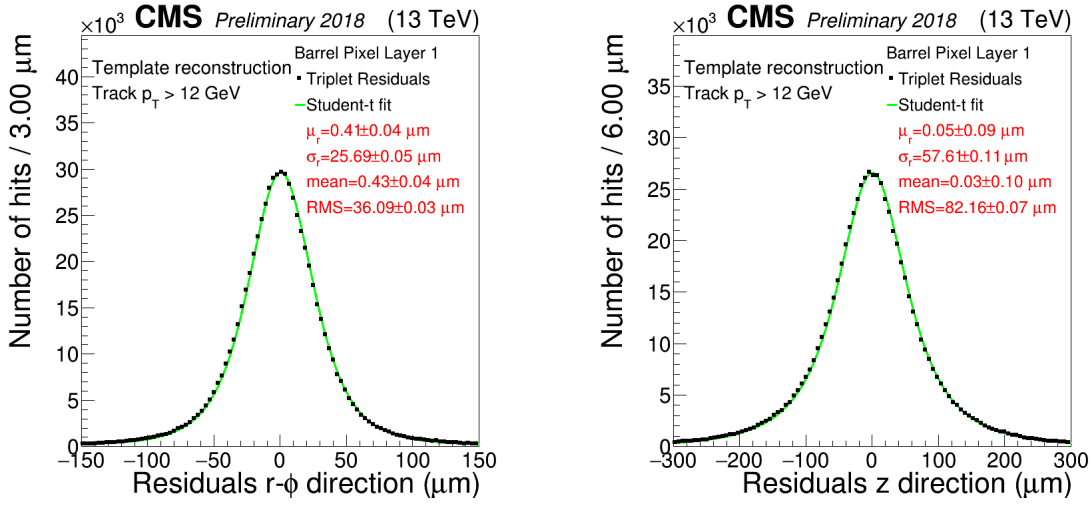

(a) $r-\phi$ direction (b) z direction

Figure 6.10: Residuals of layer 1 in the $r-\phi$ (a) and z (b) direction [183]. The residuals give an upper limit on the position resolution of the innermost layer of the detector.

The detector has been operated in 2017 and 2018 and performed excellently. This is exemplified for instance by its position resolution. Figure 6.10 shows the residuals in the $r-\phi$ and z directions of the innermost layer of the detector. For this measurement, the triplet method is employed, in which signals from two layers in the pixel detector are used to extrapolate the hit position in the third layer of interest. The residual is then evaluated as the difference between the interpolated and the measured hit position. While this method aims to evaluate the position sensitivity, the residual also takes into account effects such as detector alignment and position sensitivity of other detector layers. Although the residuals of layer 1 of the detector are larger than for layers 2 and 3 as the interpolation is performed one-sided only, a width of the residual distribution and thus an upper limit on the position resolution of 25.7 µm in the $r-\phi$ direction and 57.6 µm in the z direction are nonetheless achieved. Figure 6.11 shows the efficiency of each detector layer as a function of the instantaneous luminosity. The hit efficiency of all layers lies above 99% except for a drop to 97.5% at an instantaneous luminosity of $2 \times 10^{34}\,\mathrm{cm}^{-2}\,\mathrm{s}^{-1}$ in layer 1. This is because of the limited frequency of the resets necessary for maintaining the efficiency level as described in Section 5.3.3. Nonetheless, the detector provides collision data of excellent quality for physics analysis.

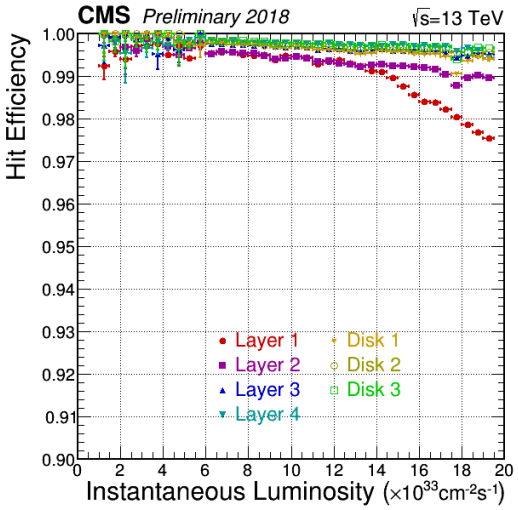

Figure 6.11: Hit efficiency of the four barrel layers and the three endcap disks of the pixel detector as a function of the instantaneous luminosity [183]. Except for layer one where the efficiency drops to 97.5% at an instantaneous luminosity of $2 \times 10^{34}\,\mathrm{cm}^{-2}\,\mathrm{s}^{-1}$, the efficiency of all detector layers consistently lies above 99%.

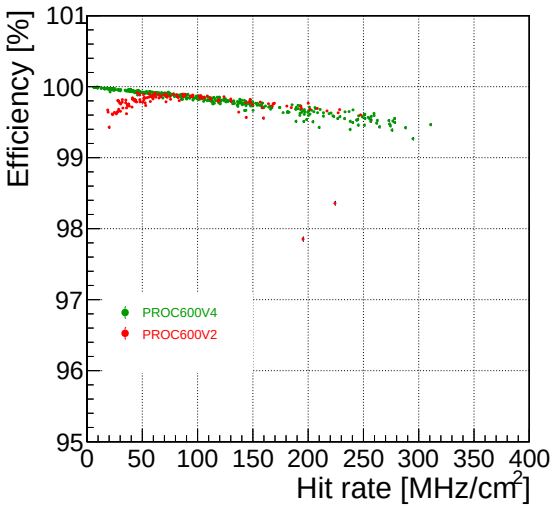

Figure 6.12: Comparison of the efficiency of modules equipped with *PROC600V4* and *PROC600V2* chips. The measurement is performed without any resets. It can be noticed that the efficiency of the newer chip version is higher and more stable throughout the tested hit rate range.

6.5 Modules for the replacement of the innermost layer

As described in Section 4.3.1, the modules mounted on the innermost layer of the Phase I pixel detector present several shortcomings. To improve the performance of the detector for the Run III of the LHC, this layer has been exchanged in 2020. In particular, the readout chip used for the modules has been replaced by an updated version, the *PROC600V4* chip.

Three prototype modules equipped with the newly designed *PROC600V4* chip are tested under X-ray illumination in order to characterise their performance. In particular, the impact of the design changes of the ROC with respect to the previous version are studied. First, it is confirmed that the noise level is indeed reduced for the new chip version as is described in Section 5.3.3. This enables to successfully operate modules at a threshold of down to $1950\,\mathrm{e}^-$, compared to the $4000\,\mathrm{e}^-$ threshold with

which the modules equipped with *PROC600V2* are operated.

In addition, it is verified that the inefficiencies at both low and high rates which are caused by mismatches between the buffers are resolved. This is verified in Figure 6.12, which shows the efficiency of the three tested modules with *PROC600V4* chips, and for comparison one module with the older *PROC600V2* chip version. Here, no resets are applied during the measurement, which reveals the inefficiencies at low rates in particular, where the efficiency is below 99.5%. With the newly designed ROC version, the efficiency approaches 100% at rates below $20\,\mathrm{MHz\,cm^{-2}}$ and remains above 99% up to a rate of $300\,\mathrm{MHz\,cm^{-2}}$ which is the maximum rate expected in the CMS detector during Run III.

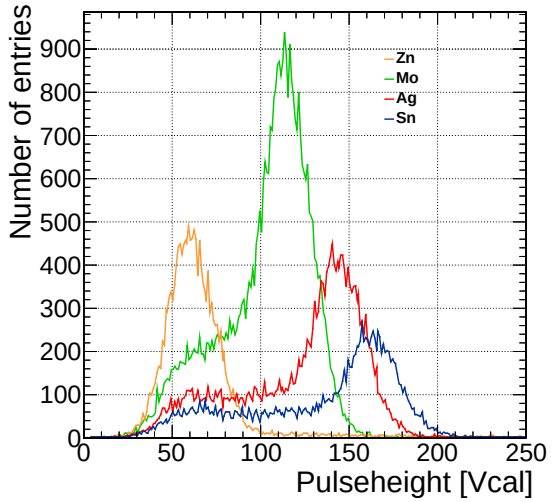

Figure 6.13: Spectrum of the zinc, molybdenum, silver and tin targets measured with a *PROC600V4* chip. All four peaks corresponding to the Kα_1 emission lines can be resolved. The shoulders on the left side of the peaks arise from charge diffusion in the sensor, which in some cases is split up over multiple pixels.

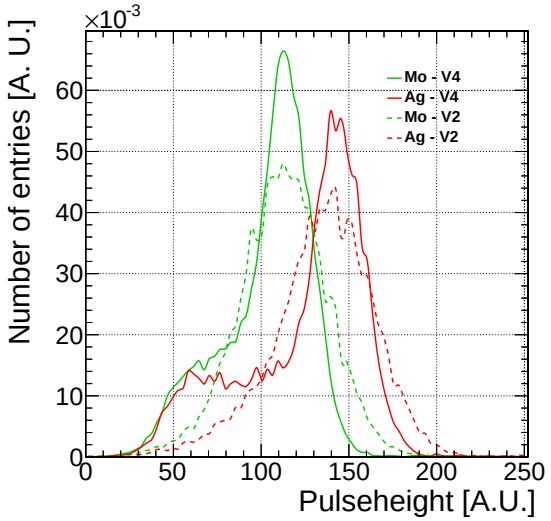

Figure 6.14: Comparison of the spectrum of the Mo and Ag targets measured using a *PROC600V2* and a *PROC600V4* chip. For better visibility, the spectra are smoothed, normalised and superimposed. The peak corresponding to the Kα_1 line is more pronounced for the *PROC600V4* chip.

Furthermore, the pulse height resolution of the ROC is improved. Figure 6.13 shows the spectrum of the four available fluorescent targets measured by a ROC of one of the three prototype modules with the new ROC version. The peaks corresponding

to the Kα_1 lines of the elements are easily identifiable. Two of these spectra are compared in Figure 6.14 to those obtained using *PROC600V2* chips. The peaks corresponding to the Kα_1 emission line of the material are fitted with a Gaussian function. For both emission lines, a distribution width of $\sim$ 23 ADC is obtained with *PROC600V2* and $\sim$ 14 ADC with *PROC600V4*. The width of the peak is thus reduced by $\sim$40% for the *PROC600V4* chip, indicating a much improved pulse height resolution.

This feature enables a more precise energy calibration using the method presented in Section 5.3.2. Averaging between the three tested modules, a calibration slope of $43.72 \pm 0.29\,\mathrm{e^-Vcal^{-1}}$ and an offset of $-442 \pm 18\,\mathrm{e^-}$ are measured.

These measurements show that several of the shortcomings of the *PROC600V2* chip have been resolved in the development of the *PROC600V4* chip. In the beginning of the year 2020 modules with this new chip version were built, qualified and installed in the detector to replace the innermost layer of Phase I upgrade of the CMS pixel detector.

Part II

Search for the associated production of a Higgs boson with a top quark pair in the high p_T phase space

Chapter 7

Motivation

After the discovery of the Higgs boson in 2012 by the ATLAS and CMS collaborations [35, 36], focus has shifted towards evaluating its properties through precision measurements. In this context the associated production of a Higgs boson with a pair of top quarks has gained importance in recent years. Despite its low cross section, this process can now be observed with the increasing luminosity delivered to the experiments by the LHC. Indeed, the precision on the production cross section of this process has increased significantly. The relative error σ_μ/μ on the ratio μ of the measured cross section and the SM predicted one of the $t\bar{t}H$, $H\to b\bar{b}$ process was 1.33 using data collected by the CMS experiment at centre-of-mass energies of 8 TeV [184]. This number decreased to 0.63 using data collected in 2016 [185], and to 0.28 when including the 2017 dataset [186].

Additionally, new Higgs boson production and decay modes have been targeted. For instance, the high p_T phase space region of the Higgs boson in the gluon fusion production mode has been explored in 2019, providing a differential cross section measurement in the combination of the $H \to \gamma\gamma$, $H \to ZZ$ and $H \to b\bar{b}$ decay channels [187].

The second part of this thesis describes a measurement of the $t\bar{t}H$, $H\to b\bar{b}$ process, focusing on final states with top quarks or Higgs bosons produced at large transverse momentum. This Chapter motivates the search for such events. In particular, Section 7.1 describes how a precise measurement of the $t\bar{t}H$, $H\to b\bar{b}$ process improves the understanding of the Higgs sector and of particle physics in general. A thorough overview on the current status of the search for $t\bar{t}H$, $H\to b\bar{b}$ events is given in Section 7.2, and Section 7.3 describes the topology of these events in the high p_T phase space.

7.1 Implications of the $t\bar{t}H$, $H \to b\bar{b}$ process for particle physics

Since the top quark is the most massive particle known to date, its coupling with the Higgs boson is expected to be the largest one in the SM ($c_{Y,t} \sim \mathcal{O}(1)$). However potential deviations from Standard Model predictions could arise in the Yukawa coupling between both particles, which is why a precise measurement of the coupling is necessary.

7.1.1 Measurement of the top quark Yukawa coupling in the $t\bar{t}H$, $H \to b\bar{b}$ process

With the increase of the centre-of-mass energy of the collisions occurring at the LHC from 8 TeV to 13 TeV in 2015, interest in the study of the $t\bar{t}H$ process has grown significantly. This is explained by the considerable increase of the cross section of the process with higher centre-of-mass energies as shown in Figure 3.4. With more refined analysis methods, the decay into a bottom quark pair also becomes targetable, as it gives a better handle on the overwhelming $t\bar{t}$+jets background.

A remarkable property of the Higgs boson is its coupling to all massive particles, which is proportional to their mass as explained in Section 2.2. To verify this property, the Yukawa couplings are measured with increasing precision, as is illustrated in Figure 7.1. This Figure shows the coupling strength between the Higgs boson and different fermions and bosons as a function of their mass. The predicted proportionality between both parameters is verified. Of major interest is the coupling between the Higgs boson and the top quark, as it is the most massive particle known to date, and therefore has the largest Yukawa coupling. However, the measurements of this coupling are so far dominated by the gluon fusion process. While the cross section for this process is largest, the top quark only appears in virtual loops. Thus, BSM physics effects entering the loop cannot be excluded, and might impact the indirect measurement of the top quark Yukawa coupling.

A direct measurement can only be obtained in the associated production of a Higgs boson with a top quark pair, and in the production of a single top quark associated to a Higgs boson. However, the cross section of the latter is seven times smaller than that of the $t\bar{t}H$ process. As the top quarks are present in the final state of the $t\bar{t}H$ process, BSM effects can be excluded in this case.

A precise measurement of the top quark Yukawa coupling is crucial, in particular because it impacts the stability of the electroweak vacuum. The Higgs boson potential

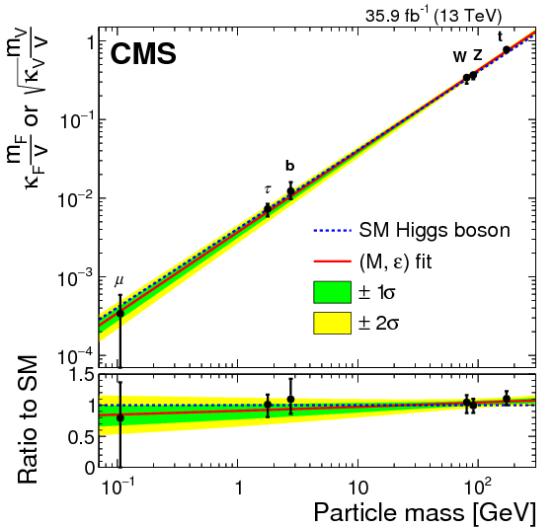

Figure 7.1: Coupling strength of the Higgs boson to massive leptons and quarks as a function of the particles' mass [189]. All measurements to date confirm the proportionality between both quantities.

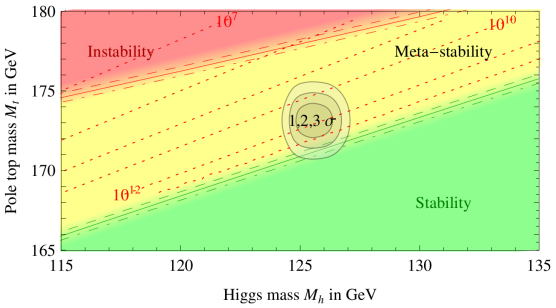

Figure 7.2: Vacuum stability as a function of the top quark and the Higgs boson pole masses [188]. Current experimental results hint that the position of the SM vacuum lies in the meta-stable region of phase space.

shown in Figure 2.2 only takes this form if the Higgs self-coupling parameter λ is positive. However, this parameter is impacted by renormalisation. For instance, top quark loops account negatively to λ and their contribution depends on the value of the top quark Yukawa coupling. If λ becomes negative, field configurations with a lower potential than the known electroweak vacuum arise, leading to an unstable vacuum [188].

Figure 7.2 shows the regions of stability of the electroweak vacuum as a function of the top quark and the Higgs boson pole masses. Current experimental results for both masses as well as their uncertainties are indicated by the circular regions, which indeed lie in the metastable region of the vacuum stability.

7.1.2 BSM effects in the top quark Yukawa coupling at large Higgs boson transverse momentum

When the top quark or the Higgs boson carries a large p_T, their decay products become collimated and cannot be reconstructed into single classical jets. Figure 7.3

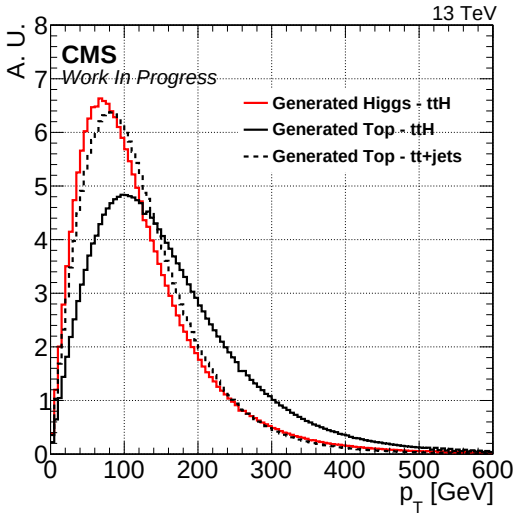

Figure 7.3: Transverse momentum of the Higgs bosons and hadronically decaying top quarks in signal $t\bar{t}H$, $H\to b\bar{b}$ and background $t\bar{t}$+jets events. A significant fraction of events carry objects with a large p_T.

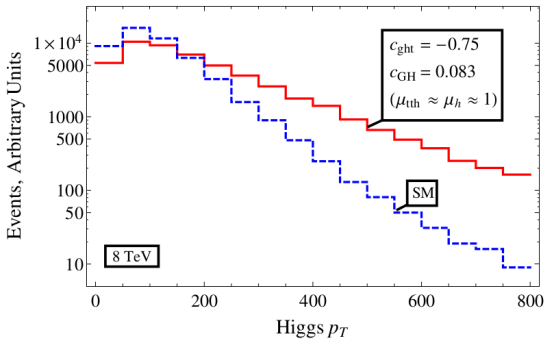

Figure 7.4: Higgs boson transverse momentum in $t\bar{t}H$ events at 8 TeV in the SM case and with the addition of non-zero chromomagnetic dipole and Higgs-gluon kinetic couplings [192]. An increase of events with large Higgs boson p_T is observed in the latter case.

shows the transverse momentum of the Higgs boson and hadronically decaying top quarks in signal $t\bar{t}H$, $H\to b\bar{b}$ events, and in the case of top quarks in $t\bar{t}$+jets events, which constitute the major background to the $t\bar{t}H$, $H\to b\bar{b}$ analysis. While the peaks of the distributions lie below 100 GeV, a number of objects carry a significantly larger transverse momentum reaching several hundreds of GeV, such that reconstructing these objects using dedicated techniques can improve the performance of the analysis.

Furthermore, a difference in the p_T spectra of top quarks is observed between signal and background events, which can help to discriminate between the two and improves the signal-over-background ratio [190, 191]. Details about methods used to reconstruct these high p_T Higgs bosons and top quarks are given in Section 8.1.

Most importantly, an analysis of the $t\bar{t}H$, $H\to b\bar{b}$ process in the high p_T regime can lead to additional insight into the nature of the Yukawa coupling between the top quark and the Higgs boson, which could potentially resolve the instability of the electroweak vacuum [188].

Several BSM theories indeed postulate anomalous couplings between the Higgs

boson and the top quark. For instance, a class of theories predict a different CP nature of the coupling by including a pseudoscalar component to the interaction. In this case, the Lagrangian describing the interaction between both particles can be written as

$$\mathcal{L}_{\text{int}} = -\frac{m_t}{v}\bar{t}(\kappa_t + i\gamma_5\tilde{\kappa}_t)tH \tag{7.1}$$

with the Dirac spinors $\bar{t}$ and t, the top quark mass m_t, the vacuum expectation value v, and the scalar and pseudoscalar couplings κ_t and $\tilde{\kappa}_t$. In the SM case, $\kappa_t = 1$ and $\tilde{\kappa}_t = 0$, since the Higgs boson has spin 0 and parity +. Those parameters can differ from the SM case for instance through heavy fields present in virtual loops. In particular, a parameter $\tilde{\kappa}_t$ different from zero would implicate the existence of a CP-odd boson. This parameter is indirectly constrained by measurements of the electron electric dipole moment d_e [193], which however assume a SM coupling between the electron and the Higgs boson. The current limit on $|d_e| < 1.1 \times 10^{-29}\,\text{e}^-\,\text{cm}$ imposes an upper limit of $\tilde{\kappa}_t < 0.01$. However, additional contributions for instance from supersymmetric scenarios could affect d_e, and thus $\tilde{\kappa}_t$ as well. Therefore a direct measurement of these couplings is essential. These can be performed in the $t\bar{t}H$, tH and $\bar{t}H$ processes, for instance in cross section or invariant mass measurements. Another possibility is to study spin correlations in the top quark pair, which directly translate to the measurable azimuthal angle between the lepton pair and the beam axis in dileptonic $t\bar{t}H$ events. This measurement gains sensitivity in the high p_T regime of the Higgs boson, which is targeted in this thesis [194, 195, 196, 197]. However, so far all measurements, whether direct ones such as in the $t\bar{t}H$ process in the decay to two taus or two photons [198, 199] or indirect ones in top quark pair production [200] and in Higgs boson decays to four leptons, photons or taus [201, 202, 203, 204], strongly favour a pure CP-even top quark Yukawa coupling.

Effective field theories predict new physics at the high energy scale by introducing dimension six couplings of the Higgs boson to particles of the SM. In this case, the amplitude of a process such as $t\bar{t}H$ takes the form

$$\mathcal{A} = \mathcal{A}_{\text{SM}} + c_{\mathcal{O}}\frac{q^2}{\Lambda^2}\mathcal{A}_0 \tag{7.2}$$

where $\mathcal{A}_{\text{SM}}$ designates the momentum independent SM component of the amplitude, $c_{\mathcal{O}}$ a dimensionless constant, Λ the scale at which new physics appears, and q the momentum transfer in the process. Because of the q^2 dependence of the BSM amplitude, the effects of the new physics appear predominantly in the high p_T regime. Thus the Higgs boson typically has a larger transverse momentum than predicted by the Standard Model, while leaving the processes' cross sections unchanged. This

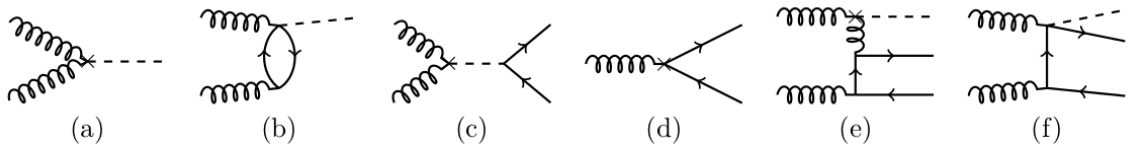

Figure 7.5: Example Feynman diagrams originating from the Higgs-gluon kinetic (a) and the chromomagnetic dipole (b) coupling operators. This leads to additional top quark pair production mechanisms such as those in (c) and (d), and additional $t\bar{t}H$ production modes illustrated in (e) and (f) [192].

applies specifically to the dimension six chromomagnetic dipole coupling (hgt) and the Higgs-gluon kinetic coupling (HG) operators. These can be incorporated in the Lagrangian of the theory as

$$\mathcal{L} = \mathcal{L}_{\mathrm{SM}} + \mathcal{O}_{hgt} + \mathcal{O}_{HG} \tag{7.3}$$

with

$$\mathcal{O}_{hgt} = \frac{c_{hgt}}{\Lambda^2}(\bar{Q}_L H)\sigma^{\mu\nu}T^a t_R G^a_{\mu\nu} \qquad \mathcal{O}_{HG} = \frac{c_{HG}}{2\Lambda^2}(H^\dagger H)G^{\mu\nu}_a G^a_{\mu\nu} \tag{7.4}$$

which lead to additional Feynman diagrams such as those illustrated in Figure 7.5

Both operators thus introduce additional vertices between Higgs bosons and gluons, and modify the kinematics of $t\bar{t}H$, $H\to b\bar{b}$ events, as is illustrated in Figure 7.4. With the chosen coupling strength values of c_{hgt} and c_{HG}, an increase in the number of Higgs bosons with $p_T > 500\,\mathrm{GeV}$ of at least one order of magnitude would be observed [192, 205, 206].

A precise determination of the top quark Yukawa coupling, in particular through studying the Higgs boson p_T profile in $t\bar{t}H$ events, is thus of primordial importance to establish a better understanding of the Higgs sector.

7.2 Current status of the search for the $t\bar{t}H$, $H\to b\bar{b}$ process

The current experimental status on the analysis of the $t\bar{t}H$, $H\to b\bar{b}$ channel is driven by the ATLAS and CMS experiments. The CMS collaboration published an analysis of the data collected in 2016 and 2017, leading to a ratio between the measured cross section of the process and the expected one from the SM (called the signal strength)

of $\mu = 1.15^{+0.32}_{-0.29}$ and an observed significance of 3.9σ [186]. In contrast, the latest published result from the ATLAS collaboration analyses data taken during the full Run II of the LHC, and measures a signal strength of $\mu = 0.43^{+0.36}_{-0.33}$, corresponding to an observed significance of 1.3σ [207].

This new result from the ATLAS collaboration reconstructs the Higgs boson kinematics to provide a measurement within the simplified template cross section formalism [208]. This formalism defines multiple exclusive phase space regions and was developed in order to maximally increase the sensitivity of physics analyses, while minimizing the theory dependence of the results. Additionally, these predefined regions simplify the combination of measurements across different Higgs boson decay channels and results from different experiments. A dedicated analysis category reconstructing Higgs bosons with a transverse momentum larger than 300 GeV is thus provided in the result from the ATLAS collaboration. This individual category leads to a signal strength of $\mu = 0.36^{+0.59}_{-0.55}$, which is compatible with Standard Model expectations.

While the $t\bar{t}H$, $H\to b\bar{b}$ channel has not yet been discovered by either collaboration as the observed significance remains below 5σ, the $t\bar{t}H$ production mode of the Higgs boson was detected by both collaborations in 2018 by combining the decay modes to W and Z bosons, to photons, to τ leptons and to a pair of bottom quarks [209, 210]. Similarly, the decay of the Higgs boson to a pair of bottom quarks could be observed in the same year by combining the results with all other production modes of the Higgs boson [211, 212]. With additional data collected in 2018 and in Run III of the LHC programme and by using refined analysis methods, a direct observation of the $t\bar{t}H$, $H\to b\bar{b}$ process is within reach in the near future.

7.3 Event topology and backgrounds

The search for $t\bar{t}H$, $H\to b\bar{b}$ events is very challenging because of its complicated final state consisting of multiple jets, leptons and missing transverse energy. Furthermore, the signal is hidden by backgrounds whose cross sections are several orders of magnitude larger. These backgrounds mostly consist of the QCD production of a top quark pair in association with additional jets arising from initial or final state radiation.

7.3.1 Final state of $t\bar{t}H$, $H\to b\bar{b}$ events

The associated production of a Higgs boson with a pair of top quarks results in a complex final state. Since the lifetime of top quarks is smaller than the hadronisation time, they decay before hadronising. The most common decay mode of top quarks is

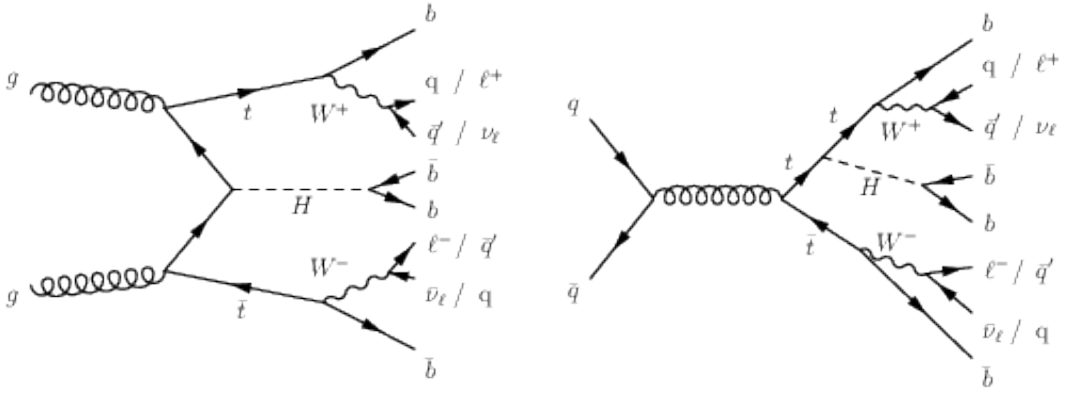

Figure 7.6: Feynman diagrams showing the associated production of a Higgs boson with a pair of top quarks.

into a W boson and a b quark, which has a branching fraction of 0.957 ± 0.034 [15]. The W boson in turn decays either hadronically into a quark and an antiquark, or leptonically into a lepton (electron, muon or tau) and its corresponding neutrino. Thus the final state of $t\bar{t}H$, $H \to b\bar{b}$ events consists of four to eight quarks, of which four are bottom quarks, and between zero and two leptons and neutrinos. Two example Feynman diagrams of the process are shown in Figure 7.6.

Assuming full detector acceptance and perfect resolution, this translates into the following observed objects in the detector: four b-tagged jets, up to four non b-tagged jets, between zero and two leptons, and missing transverse energy (MET) in case at least one of the top quarks decays leptonically. However, it is not always possible to unambiguously associate each generator level particle to a detector level object. While leptons and MET are typically well reconstructed, jets are more difficult. Additionally, not all objects pass the kinematic selections which are applied to the analysis. Three cases can be identified:

- Fully reconstructed events: In this case, every quark can be associated unambiguously to a single jet.
- Fully reconstructed events + ISR/FSR: Each quark can be associated to a jet, but there are additional jets originating from initial or final state radiation.
- Partial reconstruction: Less jets than quarks are present. This scenario occurs when some jets are out of detector acceptance or below the energy threshold. Jets can also be missing when Higgs bosons or top quarks are produced at large

transverse momentum. With higher p_T, the decay products become more and more collimated, and might merge into a single classical jet. This scenario is further investigated in Section 8.3.2.

7.3.2 Backgrounds

The dominant background of the analysis of the $t\bar{t}H$, $H\to b\bar{b}$ process in the leptonic decay channels of the top quark pair is the production of a top quark pair in association with additional jets from QCD radiation ($t\bar{t}$+jets). This background is particularly difficult to handle because of the large difference in cross section of both processes, which equals 0.5085 pb for signal events assuming a Higgs mass of 125 GeV at centre-of-mass energies of 13 TeV, and 831.76 pb for $t\bar{t}$+jets events with a top quark mass of 172.5 GeV [80, 213]. Thus, the theoretically predicted cross section is around three orders of magnitude larger than that of the signal process. In particular the case of two additional b jets ($t\bar{t}$+$b\bar{b}$) is of interest as the final event composition is identical to that of signal $t\bar{t}H$, $H\to b\bar{b}$ events, as becomes apparent when comparing the Feynman diagrams of the signal process in Figure 7.6 and the background process in Figure 7.7. The measured cross section of the $t\bar{t}$+$b\bar{b}$ process even exceeds the theoretically calculated one by a factor of around 1.3, which further reduces the signal-over-background ratio in the $t\bar{t}H$, $H\to b\bar{b}$ analysis [214, 215, 216].

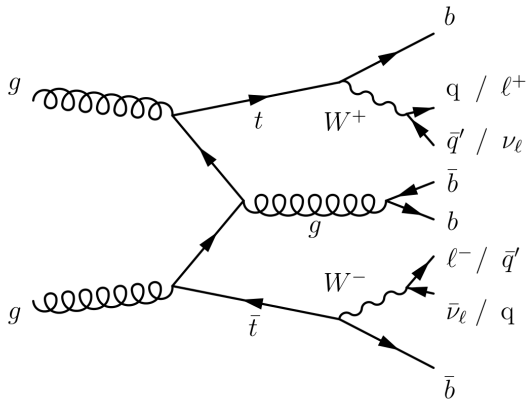

Figure 7.7: Feynman diagram showing the $t\bar{t}$+$b\bar{b}$ process, which constitutes the main background of the $t\bar{t}H$, $H\to b\bar{b}$ analysis.

The $t\bar{t}$+jets background can be subdivided into different categories:

- $t\bar{t}$+$b\bar{b}$: Two additional jets originating each from at least one b hadron are present in the event

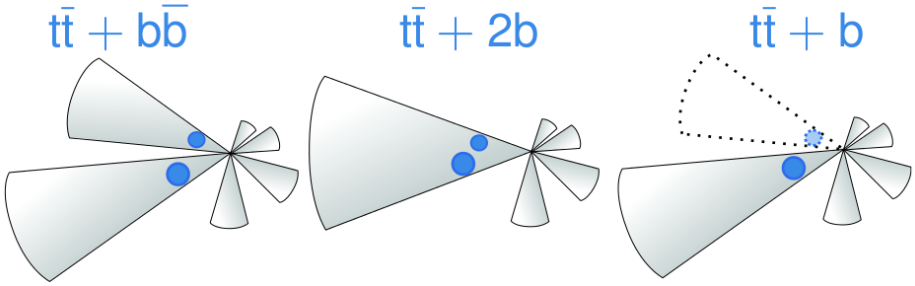

Figure 7.8: Illustration of the $t\bar{t}$+$b\bar{b}$, $t\bar{t}$+b and $t\bar{t}$+2b background contributions. Blue dots represent b hadrons, and cones show the jet reconstruction.

- $t\bar{t}$+b: Exactly one additional jet arising from a single b hadron is present
- $t\bar{t}$+2b: The event contains exactly one additional jet originating from at least two b hadrons. This scenario targets the collinear gluon splitting into a pair of b quarks which cluster into a single jet.
- $t\bar{t}$+$c\bar{c}$: The event has no b-flavoured jets, but at least one jet originating from a charm quark.
- $t\bar{t}$+LF (light flavour): This scenario groups all events which do not contain a c- or b- flavoured jet.

In these definitions the jet flavour is determined by associating jets and partons by spatial distance. The first three contributions are illustrated in Figure 7.8. This splitting enables to better constrain the uncertainties on these backgrounds.

Additional minor backgrounds contributing to the analysis of the $t\bar{t}$H, H→$b\bar{b}$ channel are $t\bar{t}$H events with a different decay mode of the Higgs boson, the production of a top quark pair in association with a W or Z boson (ttW, ttZ), diboson production (WW, ZZ, WZ), single top production, and the production of a W or Z boson with additional jets. These amount to less than 5% of the total background contribution.

Since the final state contains many jets, this analysis also suffers from considerable self-backgrounds since the association between jets and quarks is not unambiguous. For example, there are 15 possibilities to identify the two jets originating from the decay of the Higgs boson in an event with six jets. Using techniques to reconstruct Higgs bosons or top quarks at large transverse momentum can reduce this ambiguity as is explained in Section 9.5.

Chapter 8

Analysis techniques

As the LHC reaches higher energies and increases its luminosity, processes with smaller cross sections become accessible. However, they are typically difficult to disentangle from backgrounds processes which are often several orders of magnitude larger than that of the signal.

In order to isolate signal events, dedicated analysis techniques are necessary. In this work, large-R jets arising from the decay of heavy particles such as top quarks or Higgs bosons are reconstructed. The techniques used for this purpose are detailed in Section 8.1.

To discriminate between signal events and different types of backgrounds, the b tagging likelihood ratio is used. This discriminant solely uses b tagging information and is therefore ideally suited to discriminate between the light and b-flavoured components of the $t\bar{t}$+jets background. It is described in Section 8.2.

Additionally, the matrix element method (MEM) is used to distinguish between signal and background processes, as it is particularly powerful in separating $t\bar{t}H$, $H \to b\bar{b}$ events from $t\bar{t}$+$b\bar{b}$ events. The MEM is described in Section 8.3.

8.1 Jet substructure techniques

Jet reconstruction algorithms, which are described in Section 3.1.3, were developed to combine all hadronisation products originating from a single parton. However, in decays of heavy particles with large p_T such as top quarks or Higgs bosons, the angular separation between the jets in the final state is reduced, since the cone size R_{max} containing all decay products of the heavy particle scales as $R_{\text{max}} \sim \frac{2m}{p_T}$. Thus, reconstructing individual partons using a jet algorithm with a small distance parameter fails when the hadronisation products of neighbouring partons enter the jet.

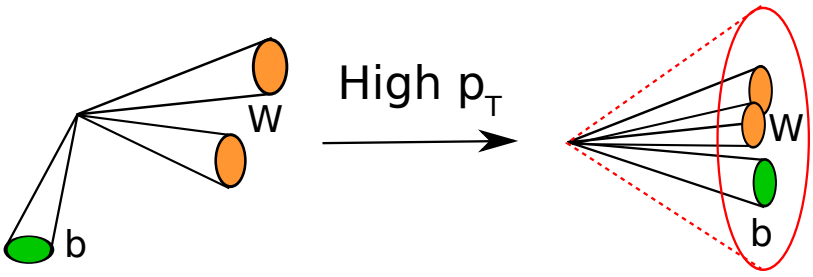

Figure 8.1: Schematics illustrating the decay topology of top quarks depending on its p_T. The higher the p_T, the more collimated the decay products are, allowing to reconstruct the top quark within a large-R jet.

The starting point to correctly reconstruct these massive objects for most of the developed techniques is the construction of large-R jets, which contain all constituents emerging from the decaying particles. This is illustrated in the case of a top quark in Figure 8.1, which shows how its three decay products become more collimated at larger p_T and can be combined into a large-R jet. In the following, various techniques used to identify large-R jets originating from heavy particles with high p_T, known as "boosted" techniques, are described.

8.1.1 Overview of boosted techniques

Over the past years, interest in boosted techniques has grown considerably as the phase space for which they are designed became accessible due to the high collision energies and luminosities generated at the LHC.

The initial approaches focus on cleaning the large-R jets from additional constituents arising for instance from pileup. These so-called grooming techniques are described in Section 8.1.2. After this cleaning, further algorithms can be applied to the large-R jets to analyse their substructure and identify the particle that created the jet.

One class of substructure variables study the energy deposition inside a jet, examples of which are N-subjettiness [217] and energy correlation functions [218]. Both evaluate the likelihood of a jet having a substructure compatible with N centers of energy deposition. Thus it enables to distinguish heavy particles such as top quarks, or W and Higgs bosons from jets emerging from QCD radiation, as they have a 3 or 2-prong structure, which is not the case for QCD jets [219, 220].

Further substructure discriminants reconstruct the clustering history of a jet, examples of which are shower and event deconstruction [221, 222].

While the methods presented above are generic as they can be adapted to the identification of various different particles, other methods are more specific. For instance, a multitude of algorithms have been developed to identify or "tag" top quarks. Examples are the HOTVR [223], the BEST [224], the CMSTopTagger [225] and the HEPTopTaggerV2 (HTT) algorithm [226, 227, 228, 229], which is described in Section 8.1.3.

In the aftermath of the Higgs boson discovery in 2012, interest in tagging high p_T Higgs bosons has grown considerably, resulting in the development of new methods to identify such jets. The decay to a pair of b quarks is particularly interesting as it features the largest branching ratio. Thus, both the CMS and ATLAS collaborations have proposed algorithms to identify these bosons [230, 231, 232]. These are primarily based on correctly interpreting the flavour content of the large-R jets.

In the past few years, machine learning techniques have gained a lot of attention, and have improved the tagging performance of boosted objects considerably, as is shown for instance in the case of top quark tagging [233], where the background rejection of QCD jets of some network architectures improves by a factor two for the same signal efficiency with respect to a simple analytical tagger combining N-subjettiness and jet mass. An even larger improvement is observed in the case of Higgs boson tagging [231, 232].

8.1.2 Jet grooming

An essential part of the reconstruction of heavy particles is the analysis of the constituents of the large-R jets. In particular, constituents originating from other processes than the decay of heavy particles must be identified and removed from the large-R jet. There exist various algorithms which fulfil that purpose, commonly grouped as grooming algorithms. Some examples are filtering [190], soft drop [234], mass-drop [190], trimming [235] or pruning [236].

The filtering algorithm has been developed in conjunction with the mass-drop algorithm [190]. It operates by reclustering all jet components with the Cambridge-Aachen algorithm with a smaller jet parameter $\Delta R_{\text{filt}} = \min(0.3, \frac{\Delta R(j_1,j_2)}{2})$. Here j_1 and j_2 correspond to the two jets arising from the last clustering step in the formation of the original jet. The filtering step consists in conserving only the three subjets with the largest p_T after this reclustering. This number has been optimised for the analysis of jets originating from a two-prong decay (such as W or Higgs bosons), allowing for a contribution from QCD radiating from one of the decay products. The algorithm is illustrated in Figure 8.2.

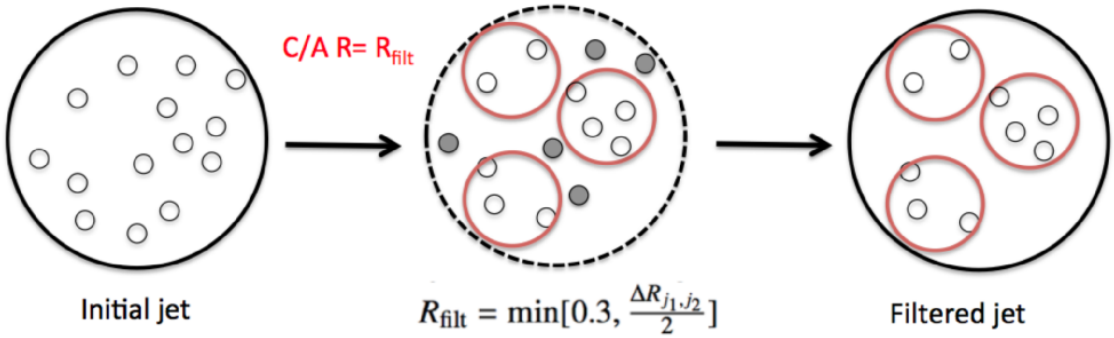

Figure 8.2: Illustration of the filtering algorithm [237]. The filtering algorithm reclusters the jet components with a smaller jet radius, and removes contributions which are not contained in the three subjets with the largest p_T.

8.1.3 HEP Top Tagger

As mentioned previously, top quarks play an important role in many precision measurements of the SM, but also in searches for BSM physics. While top quarks decaying leptonically via a W boson are more easily identifiable since background processes are less important, top quarks decaying into hadrons are often difficult to distinguish from QCD processes. This is why dedicated algorithms have been developed to identify these quarks, such as the HEPTopTaggerV2 (HTT) algorithm [226, 227, 228, 229], which has first been applied in a phenomenological study of the $t\bar{t}H$ process in 2010 [238].

The HTT tagger operates on large-R CA jets with a distance parameter of $R = 1.5$ and with $p_T > 200\,\text{GeV}$. This initial jet is shown in Figure 8.3a. In a first step, the last iterations of the jet clustering algorithm are undone, until the mass of all produced subjets lies below 30 GeV. Furthermore, a subjet j_s which emerges from an unclustering step of jet j is only conserved if $m_{j_s} > 0.2 m_j$. Figure 8.3b illustrates the first unclustering step. After several steps, a jet such as illustrated in Figure 8.3c is obtained, where in this case four subjets are reconstructed. If the number of subjets is below three, the jet is not processed further. Next, the filtering algorithm is applied on three of the obtained subjets. This is done for all the possible combinations of subjets, such as in this example the triplets ABD, ACD, BCD and as is illustrated in Figure 8.3d, ABC. All combinations of three filtered subjets are then reclustered with the CA algorithm using a distance parameter $R_f = \min(0.3, \Delta R_{ij}/3)$ where ΔR_{ij} designates the angular distance between the two closest subjets in the triplet. This creates a new list of subjets, of which only the five with the largest p_T

are conserved as is demonstrated in Figure 8.3e. The triplet leading to the largest mass of the sum of this second list of subjets is chosen, and their constituents are reclustered with the CA algorithm into exactly three subjets, which correspond to the three decay products of the top quark as is illustrated in Figure 8.3f. Those three subjets form the HTT candidate with a mass m_{123} and a joint mass of two subjets m_{ij}. If the p_T of the obtained HTT candidate lies below 200 GeV, the candidate is rejected.

The parameter f_W estimates the compatibility of the mass m_{ij} with the W boson mass, and is shown in Figure 8.4. In this Figure, events are shown in the $\arctan(m_{13}/m_{12})$ versus m_{23}/m_{12} plane. The top quark mass can be written in terms of the subjet masses as

$$m_t^2 \equiv m_{123}^2 \simeq m_{12}^2 + m_{13}^2 + m_{23}^2. \tag{8.1}$$

since the decay products themselves are considered to be massless.

Equation 8.1 thus describes a sphere of radius m_t. The parameters $\arctan(m_{13}/m_{12})$ and m_{23}/m_{12}, which are the azimuthal and the polar angle of a point on the sphere, can thus unambiguously represent the candidate. The variable f_W then describes the distance between the HTT candidate to one of the lines corresponding to $m_{ij} = m_W$ in the $\arctan(m_{13}/m_{12})$ versus m_{23}/m_{12} plane. Setting an upper limit on f_W on the HTT candidates thus corresponds to requiring that the combined mass of two subjets i and j satisfies the condition $m_{ij} = m_W \pm f_W\%$. As shown in Figure 8.4, the variable f_W is clearly discriminating between top quarks and QCD induced jets as the former cluster at small f_W values [226].

Thus m_{123} must fulfil one of the following conditions:

$$0.2 < \arctan\frac{m_{13}}{m_{12}} < 1.3 \qquad \text{and} \qquad R_{min} < \frac{m_{23}}{m_{123}} < R_{max} \tag{8.2}$$

$$R_{min}^2(1 + (\frac{m_{13}}{m_{12}})^2) < 1 - (\frac{m_{23}}{m_{123}})^2 < R_{max}^2(1 + (\frac{m_{13}}{m_{12}})^2) \quad \text{and} \quad \frac{m_{23}}{m_{123}} > 0.35 \tag{8.3}$$

$$R_{min}^2(1 + (\frac{m_{12}}{m_{13}})^2) < 1 - (\frac{m_{23}}{m_{123}})^2 < R_{max}^2(1 + (\frac{m_{12}}{m_{13}})^2) \quad \text{and} \quad \frac{m_{23}}{m_{123}} > 0.35 \tag{8.4}$$

where

$$R_{min} = (1 - f_{W,max})\frac{m_W}{m_t} \qquad \text{and} \qquad R_{max} = (1 + f_{W,max})\frac{m_W}{m_t} \tag{8.5}$$

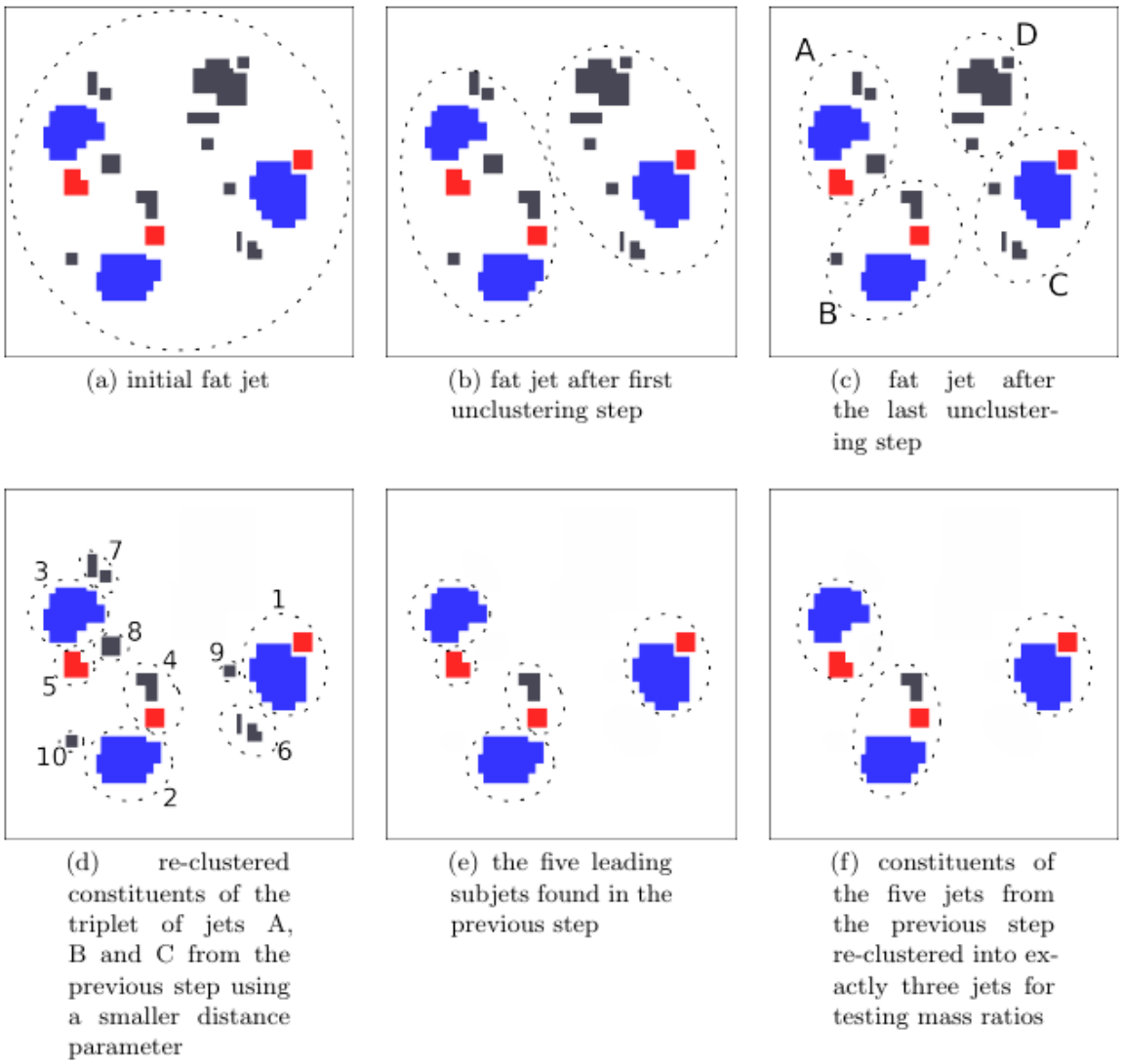

(a) initial fat jet

(b) fat jet after first unclustering step

(c) fat jet after the last unclustering step

(d) re-clustered constituents of the triplet of jets A, B and C from the previous step using a smaller distance parameter

(e) the five leading subjets found in the previous step

(f) constituents of the five jets from the previous step re-clustered into exactly three jets for testing mass ratios

Figure 8.3: Illustration of the HEPTopTagger algorithm. Jet constituents shown in blue represent the top quark's decay products. Emissions from gluon radiation are shown in red and those from pileup and underlying events are depicted in grey. The algorithm reconstructs the three decay products of the top quark and largely removes other contributions [229].

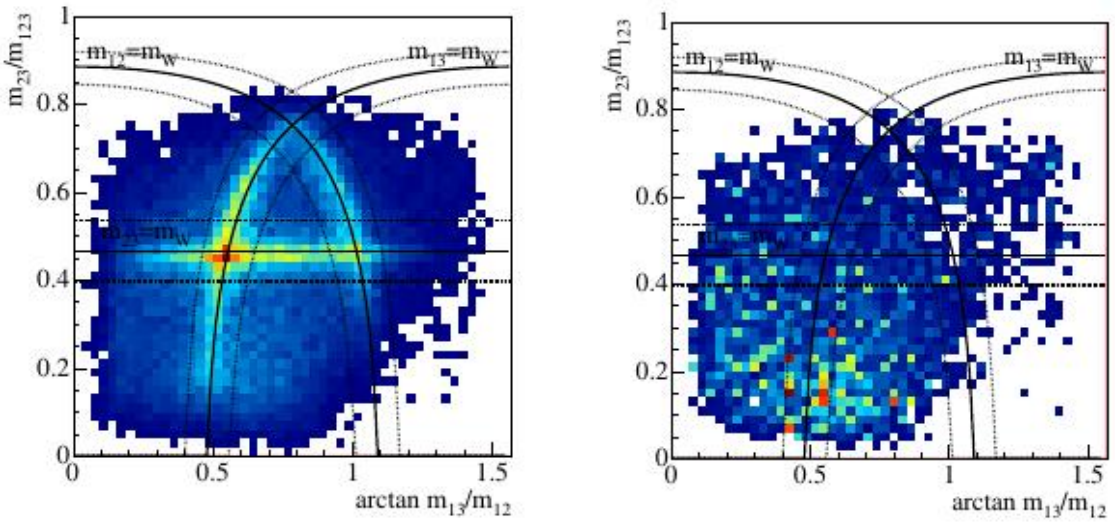

(a) $t\bar{t}$ (b) QCD

Figure 8.4: Distribution of HTT candidates in $t\bar{t}$ (a) and QCD multijet (b) events in the arctan(m_{13}/m_{12}) versus m_{23}/m_{12} plane. Solid black lines represent the cases where the mass of a combination of two subjets directly matches the W mass. Dashed lines show the region with $f_{W,max} = 0.15$ [226]. Top quarks are clustered around the lines where the invariant mass of two of the subjets is compatible with the W mass, while the distribution is mostly uniform for QCD events.

8.2 B tagging likelihood ratio

To discriminate between different contributions to the $t\bar{t}$+jets background, the b tagging likelihood ratio (BLR) is evaluated.

To this aim, a b tagging likelihood function is built from the probability density function $f(\xi|b/l)$ of a jet with a b tagging discriminator ξ to originate from a bottom or a light quark:

$$BL(\vec{\xi}|N_b) = \sum_{i\in\text{perm}} \Big[\prod_{k\in b_i} f(\xi_k|b) \prod_{k\in l_i} f(\xi_k|l) \Big] \tag{8.6}$$

The sum in Equation 8.6 expands over all the possible permutations to assign N_b jets in the event to b quarks, and $\vec{\xi}$ designates the array of the b tagging discriminants of all jets in the event. Selecting the largest element in the sum allows to identify the jets originating from bottom quarks in the event.

A ratio is built from two b tagging likelihoods:

$$BLR(\vec{\xi}) = \frac{BL(\vec{\xi}|4b)}{BL(\vec{\xi}|4b) + BL(\vec{\xi}|2b)} \tag{8.7}$$

Selecting the ratios of the 4 versus 2 b-tagged jets hypothesis optimises the discrimination power between $t\bar{t}$+$b\bar{b}$ events which have 4 b quarks and $t\bar{t}$ + light jet events, which have only two b quarks.

8.3 The matrix element method

The matrix element method (MEM) is an analytical discrimination variable built from multiple event characteristics, in particular the four-momenta of the jets and leptons.

The first theoretical motivation for the method arose several decades ago [239], and first experimental applications followed at the Tevatron accelerator notably for a top quark mass measurement [240], and the discovery of single top quark production [241, 242]. The application of the method to the $t\bar{t}$H, H→$b\bar{b}$ process was first motivated in [243] and later applied both by the ATLAS and CMS experiments [184, 244].

8.3.1 Definition

This Section details the implementation of the MEM in the case of the analysis of the $t\bar{t}$H, H→$b\bar{b}$ process.

The MEM computes the probability of an event with observables $\mathbf{y}$ (kinematics of all measured particles) to originate from a process $\boldsymbol{\theta}$ with an associated matrix element $\mathcal{M}_\theta$ as follows

$$\begin{aligned} P(\mathbf{y}, \boldsymbol{\theta}) = \sum_{k=1}^{N_\alpha} \int \frac{dx_1 dx_2}{2x_1 x_2 s} \int \prod_{i=1}^{n} \frac{d^3 p_i}{2(2\pi)^3 E_i} \\ \times \delta^4(q_1 + q_2 - \sum_{i=1}^{n} p_i) \\ \times f(x_1) f(x_2) \\ \times \mathcal{R}(\tilde{\boldsymbol{\rho}}_T, \boldsymbol{\rho}_T) \\ \times |\mathcal{M}_\theta(q_1, q_2, p_1, ..., p_n)|^2 \\ \times W(\mathbf{y}|\mathbf{p}) \end{aligned} \tag{8.8}$$

where $q_{1,2}$ represent the momenta of the colliding partons. Since their momenta cannot be measured, an integration is performed over the momentum fractions $x_{1,2}$ of both partons, involving the parton distribution functions $f(x_i)$. The two first lines of equation 8.8 also include the phase space element of the 2→n scattering process.

The matrix element $\mathcal{M}_\theta(q_1, q_2, p_1, ..., p_n)$ depends on the kinematics of the colliding partons, and on those of the final state particles $\mathbf{p}$. These are however not known as only the detector observables $\mathbf{y}$ are measurable. To estimate the kinematics of the final state particles from the observables, transfer functions $W(\mathbf{y}|\mathbf{p})$ are evaluated for jets and leptons. These functions give the probability to measure properties $\mathbf{y}$ from a parton level state $\mathbf{p}$. Similarly a transfer function $\mathcal{R}(\tilde{\boldsymbol{\rho}}_T, \boldsymbol{\rho}_T)$ is evaluated for the measured missing transverse momentum $\tilde{\rho}$ [245].

A further complication arises from the fact that jet kinematics are affected by different uncertainty sources as will be described in Section 9.4, each modifying the observables vector $\mathbf{y}$ to a vector $\mathbf{y}' = \mathbf{y} + \delta\mathbf{y}$. These need to be propagated to the MEM probability as they affect the transfer functions used in the integration. To optimize the available computing resources, thus avoiding a full recalculation for every uncertainty source, the MEM probability is evaluated by promoting the transfer function to a vector containing all sets of kinematics as

$$W(\mathbf{y}|\mathbf{p}) \quad \rightarrow \quad \begin{pmatrix} W(\mathbf{y}|\mathbf{p}) \\ W(\mathbf{y} + \delta\mathbf{y_1}|\mathbf{p}) \\ ... \\ W(\mathbf{y} + \delta\mathbf{y_n}|\mathbf{p}) \end{pmatrix} \tag{8.9}$$

thus treating all sources simultaneously [245].

Lastly, a sum is performed over N_α possibilities to associate all measured jets to the parton level quarks. Using symmetries and physical considerations, N_α does not need to correspond to all possibilities for this association. An event with six jets is considered here for illustration. From b tagging, four jets which are most likely those into which the four b quarks hadronise, can be singled out. Of those four b-tagged jets, two must arise from the decay of the Higgs boson into b quarks. There are 6 possibilities to choose those two quarks. Since current techniques to measure the charge of b-tagged jets still lead to large mistag rates [246], no charge information is used for those jets. Thus, another two permutations are needed to associate both remaining b-flavoured jets to the b and $\bar{b}$ quarks arising from the decay of the two top quarks. In total, this amounts to 12 permutations to associate all jets to parton level quarks.

Several simplifications are made here. For instance, in the case of dileptonic events, it is assumed that the charge of the lepton can be measured unambiguously.

Similarly, the mistag rate in identifying the four jets arising from the b quarks is neglected. Lastly, in the case of semileptonic events, the remaining, non b-flavoured jets are not permutated over the light quarks since the matrix element is symmetric under this permutation [245]. Reducing the number of permutations significantly reduces the computation time of the MEM probability.

Finally, a discriminant is built from the MEM probability calculated under the signal and the background hypotheses as

$$P_{s/b} = \frac{P(\boldsymbol{y}|\boldsymbol{s})}{P(\boldsymbol{y}|\boldsymbol{s}) + \kappa \cdot P(\boldsymbol{y}|\boldsymbol{b})} \tag{8.10}$$

where κ has been optimised to 0.1 to reach an optimal discriminator performance, as is detailed in [245].

8.3.2 Misreconstructed events

In the ideal case, one jet is reconstructed per parton. However, because of energy thresholds and detector acceptance, jets can escape detection. The MEM is adapted in order to cover the cases where less jets than expected are reconstructed. To this aim, the space of observables is extended as $\mathbf{y} \rightarrow \mathbf{y'} = (\mathbf{y}, (E_q, \mathbf{e}_q)_{\mathrm{q}\in\mathrm{lost}})$, with the energy E_q and three-momentum $\mathbf{e}_q$ of the lost jets. This translates into a modified MEM probability:

$$P(\mathbf{y}) \rightarrow P'(\mathbf{y'}) = \frac{1}{\sigma'} \frac{d\sigma_i}{d\mathbf{y} \prod_{\mathrm{q}\in\mathrm{lost}} dE_q d\mathbf{e}_q} \tag{8.11}$$

Since the kinematics of the non-reconstructed jets is by definition unknown, an integral is performed over the volume outside of the detector acceptance $\tilde{\mathrm{A}}$:

$$P(\mathbf{y}) = \int_{\tilde{\mathrm{A}}} \Big[\prod_{\mathrm{q}\in\mathrm{lost}} dE_q d\mathbf{e}_q \Big] P'(\mathbf{y'}) \tag{8.12}$$

$$= \int ... \times \prod_{\mathrm{q}\in\mathrm{lost}} \Big[\int_{|\eta_q| \leq \eta_{\mathrm{cut}}} d\Omega_q \varepsilon(E_q, \eta_q) ... + \int_{|\eta_q| \geq \eta_{\mathrm{cut}}} d\Omega_q ... \Big] \times ... \tag{8.13}$$

where both origins for missing jets (energy below the threshold or jet out of detector acceptance) have been factorised. The probability that a quark of energy E_q and pseudorapidity η_q forms a jet with an energy below the threshold is given by

$$\varepsilon(E_q, \eta_q) = \int_0^{E_{\mathrm{cut}}(\eta_q)} dE_j W(E_j|E_q) \tag{8.14}$$

where the transfer function $W(E_j|E_q)$ is used [245]. A third explanation for missing jets arises from top quarks or Higgs bosons with a large transverse momentum, as their decay products can merge.

Contrarily, many events will contain QCD radiation, such that more jets are reconstructed than expected from the number of quarks. In this situation, the MEM is evaluated by ignoring all jets in a permutation which are not associated to one of the quarks. Finally, a sum is performed over all possible combinations in the computation of the MEM [245].

Thus it is possible to apply the MEM to real collider data with a limited detector acceptance and in the presence of additional QCD jets.

8.3.3 Transfer functions

The matrix element method integrates over the parton level kinematics $\mathbf{p}$. As these are not known, they are related to the kinematics of the observed particles via transfer functions $W(\mathbf{y}|\mathbf{p})$. These transfer functions must normalise to unity as

$$\int_{\mathcal{A}} d\mathbf{y} W(\mathbf{y}|\mathbf{p}) = 1 \tag{8.15}$$

Transfer functions for leptons, jets and MET are evaluated separately to account for the difference in reconstruction efficiency of the detector for these particles.

Given the excellent performance of the CMS detector in reconstructing lepton kinematics (see Section 3.2), a simple delta function is used to model their transfer functions.

A multivariate normal distribution is used to represent the transfer functions for the missing transverse energy:

$$W_{\mathrm{MET}}(\mathbf{p}_T|\sum_k \mathbf{p}_k) = \frac{1}{2\pi|\Sigma|^{1/2}} \exp\left[-\frac{1}{2}(\mathbf{p}_T - \sum_k \mathbf{p}_k)^T \Sigma^{-1} (\mathbf{p}_T - \sum_k \mathbf{p}_k)\right] \tag{8.16}$$

with $\Sigma = \sigma_{\mathrm{MET}}\mathbf{I}$ and $\sigma_{\mathrm{MET}} = 30$ GeV, which approximatively corresponds to the detector resolution.

For jets, transfer functions are directly measured using Monte Carlo simulation. Dedicated transfer functions are evaluated according to the jets' flavour and kinematics. To evaluate these transfer functions, the p_T of jets arising from the hadronisation of quarks within a given kinematic range is sampled and fitted with a double Gaussian distribution:

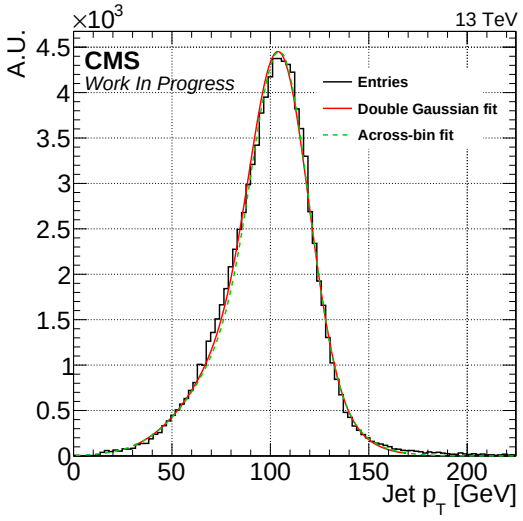

Figure 8.5: Transfer function for jets associated to quarks with low pseudorapidity in the p_T range $[100 - 102]$ GeV. The distribution peaks at the value of the quark p_T, and both fit methods model the distribution well.

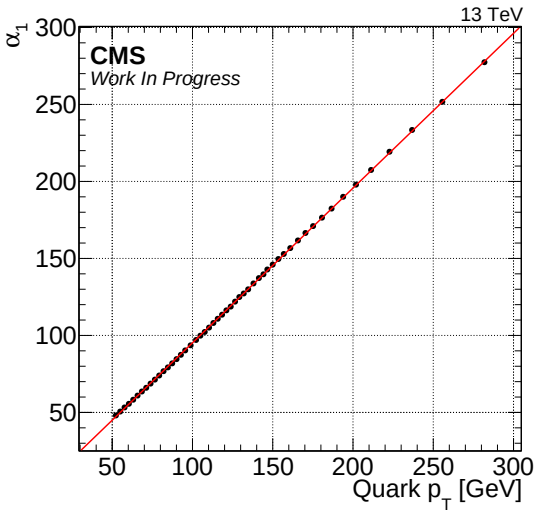

Figure 8.6: Across-bin fit of the α_1 parameter as a function of p_T. The parameter evolves linearly with p_T.

$$TF(p_T|p_{T,\text{gen}}) = N\left[0.7\exp\left(\frac{p_{T,\text{gen}} - p_T - \alpha_1}{\alpha_2}\right)^2 + 0.3\exp\left(\frac{p_{T,\text{gen}} - p_T - \alpha_3}{\alpha_2 + \alpha_4}\right)^2\right]. \tag{8.17}$$

For practical purposes, a polynomial across-bin fit in p_T is then performed on all four parameters ($\alpha_{i,\, i\in[1,4]}$) of the double Gaussian fit. These polynomial fits allow to reconstruct the measured transfer functions over the entire kinematic range [245, 247]. Figure 8.5 illustrates the transfer function for b-flavoured jets associated to quarks with $|\eta| < 1$ and $p_T \in [100 - 102]$ GeV. Both the double Gaussian and the reconstruction from the across-bin fit model the distribution well. The across-bin fit of the α_1 parameter is shown in Figure 8.6. In this Figure, each data point corresponds to the extracted α_1 parameter in one p_T bin.

The transfer functions must be evaluated separately for different jet types. Here, examples are shown for anti-k_T jets with a distance parameter of 0.4 (AK4), HTT

subjets and subjets of anti-k_T jets with a distance parameter of 0.8 (AK8 subjets). The transfer functions for AK8 subjets have only been derived for b quarks, as AK8 jets will be used to reconstruct Higgs boson candidates. For comparison of all three jet types, transfer functions for quarks with a p_T of 100 GeV are shown in Figure 8.7. Similarly, the parameters $\alpha_{i,\, i\in[1,4]}$ are shown in Figure 8.8

All transfer functions are evaluated on a simulated sample of $t\bar{t}H$, $H\to b\bar{b}$ events, and a matching criteria of $\Delta R\,(\text{jet,quark}) = 0.3$, using $\Delta R = \sqrt{(\Delta\eta)^2 + (\Delta\phi)^2}$.

8.3.4 Technical implementation

The technical implementation of the MEM is not part of this work. Details are presented in [245], of which this Section only gives a brief overview.

Several packages are used to perform the calculation of the MEM probabilities. For the evaluation of the matrix elements, `OpenLoops` is used [128, 129]. The parton distribution functions are evaluated from the `CTEQ6.6` [248] set using the `LHAPDF` software [249]. The `Vegas` algorithm [250] is used together with the the `CUBA` package [251] for the numerical integration. The computation of the MEM is performed on the worldwide LHC Computing Grid which provides adequate computing resources. Using this infrastructure, a Monte Carlo sample containing eight million $t\bar{t}H$, $H\to b\bar{b}$ events can be processed in simultaneous batches of 2000 events, each of which having a computation time of around two hours.

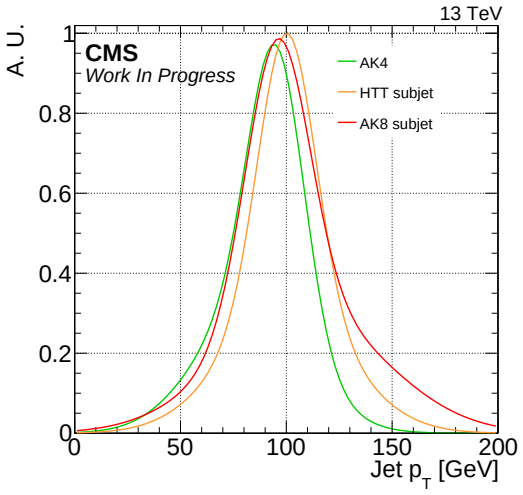

(a) b quarks, $\eta < 1$

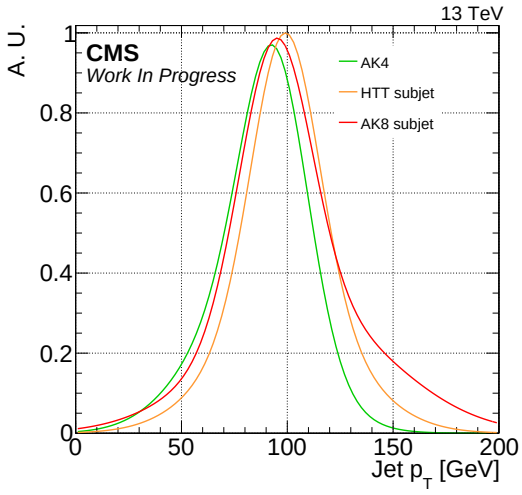

(b) b quarks, $\eta > 1$

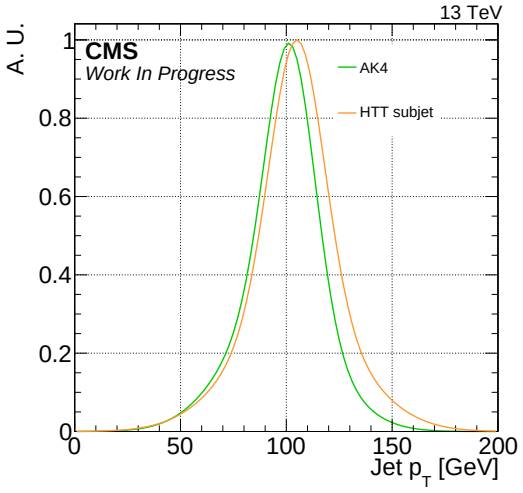

(c) light quarks, $\eta < 1$

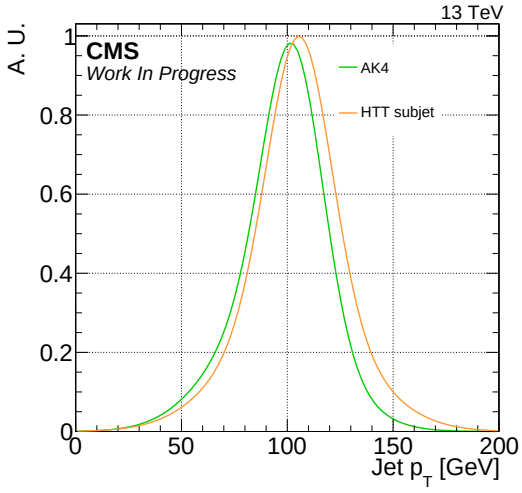

(d) light quarks, $\eta > 1$

Figure 8.7: Transfer functions for AK4 jets, AK8 subjets and HTT subjets for quarks with $p_T = 100\,\text{GeV}$. These are evaluated separately for b quarks (a,b) and light quarks (c,d), as well as for $\eta < 1$ (a,c) and $\eta > 1$(b,d).

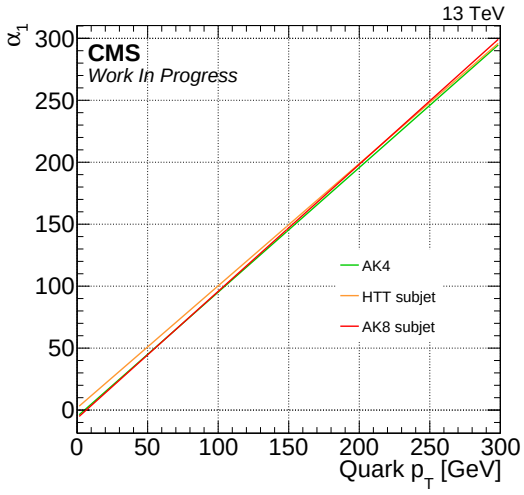

(a) α_1

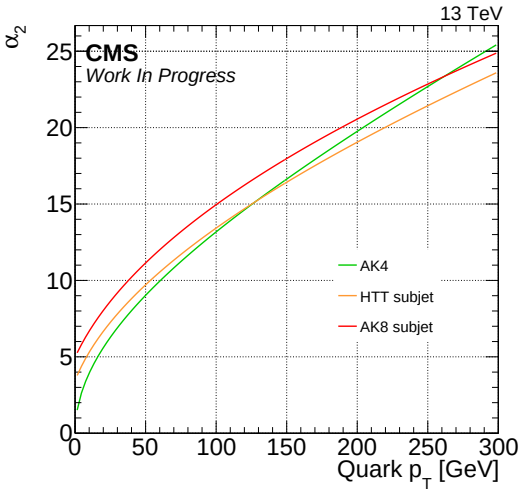

(b) α_2

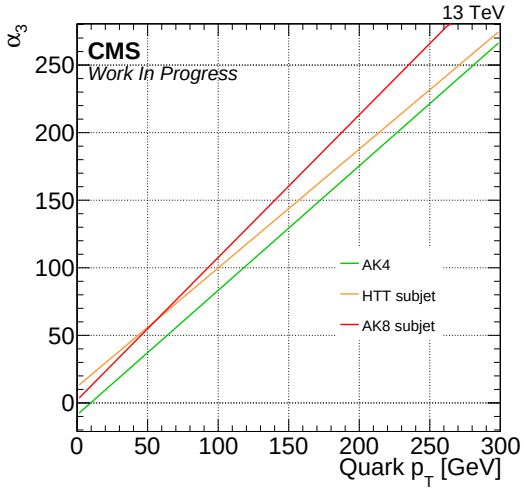

(c) α_3

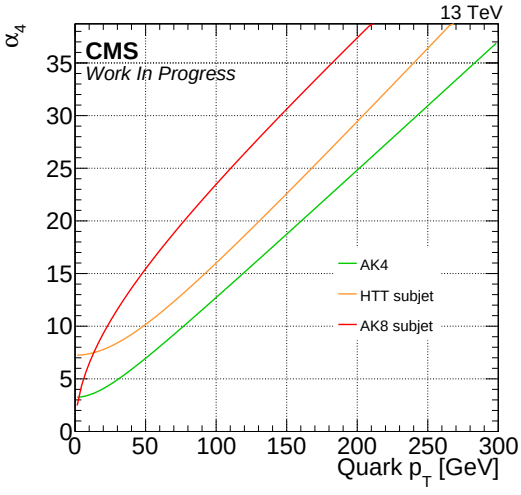

(d) α_4

Figure 8.8: Parameters α_i of the across-bin fits of the transfer functions for AK4 jets, AK8 subjets and HTT subjets corresponding to b quarks with $p_T = 100\,\text{GeV}$ and $\eta < 1$.

Chapter 9

Analysis strategy

This thesis presents a search for $t\bar{t}H$, $H \to b\bar{b}$ events with high momentum Higgs bosons or top quarks, analysing the dataset collected in 2017 by the CMS experiment in proton-proton collisions at a centre-of-mass energy of $\sqrt{s} = 13\,\text{TeV}$, which corresponds to an integrated luminosity of 41.5 fb.

The analysis results will be compared to a standard analysis selection similar to the one presented in [245] to quantify the gain of including the substructure techniques presented in Section 8.1.

Section 9.1 details the datasets and simulated samples used in the analysis, and Section 9.2 presents the quality requirements which must be fulfilled by muons, electrons, jets, and missing transverse energy. Additionally, the selection criteria for large-R jets used in the analysis of the high p_T phase space of $t\bar{t}H$, $H \to b\bar{b}$ events are presented. The event selection is described in Section 9.3, and the measurement uncertainties are presented in Section 9.4. Finally, the merging strategy of the boosted techniques and the MEM as well as the event categorisation are explained in Section 9.5 and the statistical analysis of the data is presented in Section 9.6.

9.1 Data and simulation samples

Events are selected from the dataset collected in 2017 by the CMS experiment and are split based on the decay mode of the top quark pair:

- Fully hadronic channel (FH): both top quarks fully decay into hadrons.
- Semileptonic channel (SL): one of the top quarks decays into hadrons, the other one into a bottom quark, a lepton and a neutrino.

- Dileptonic channel (DL): a lepton is produced in the decay of both top quarks.

The analysis focuses on the leptonic decay channels (SL and DL) of the top quark pair. Even though the branching ratio of these channels is smaller than in the fully hadronic case, the presence of leptons facilitates the identification of such events, and frees the analysis from contributions from QCD multijet events.

Therefore semileptonic and dileptonic trigger paths are used. In the electron channel, the trigger threshold is set to 32 GeV or 28 GeV depending on the trigger path. In the muon channel, leptons with $p_T > 27$ GeV are triggered. In the double electron channel, a p_T threshold of 23 GeV is set on the leading electron, and 12 GeV on the subleading electron. The corresponding trigger thresholds for the dimuon channel are 17 GeV and 8 GeV. Finally, in the muon/electron dilepton channel, three trigger paths are considered. The corresponding trigger thresholds are for the muon/electron pair 12 GeV/23 GeV, 23 GeV/12 GeV and 8 GeV/23 GeV.

For comparison with data, Monte Carlo (MC) simulations are used to model the signal and background processes. All samples are generated assuming a Higgs boson mass of 125 GeV and a top quark mass of 175.2 GeV. The hard scattering of events is simulated with the Powheg v.2 [124, 125, 126, 127], the MADGRAPH5_aMC@NLO [123] or the Pythia 8 [130] generators, where the first two generators simulate events at next-to-leading order in perturbation theory, and Pythia 8 at leading order. In the simulation, the NNPDF3.1 parton distribution set [252] is used. Furthermore, Pythia 8 is also used to simulate parton showering and hadronisation. Underlying events are parametrised using the CP5 tune, together with a parameter $h_{\text{damp}} = 237.9$ GeV [253]. The detector simulation is implemented using the Geant4 generator [131, 254].

Table 9.1 shows all simulated MC samples used in the analysis. Most samples are generated using the five flavour scheme, which assumes massless b quarks. Several samples simulating the single top quark production process are however generated using the four flavour scheme, which does not make that assumption.

9.2 Object selection

As this analysis focuses on the semileptonic and dileptonic decay modes of the top quark pair, the final state of $t\bar{t}H$, $H \to b\bar{b}$ events consists of one or two leptons (in this analysis, only electrons or muons are considered, which also includes leptonic tau decays), missing transverse energy (since neutrinos cannot be detected) and several jets. Jets are additionally divided into b-tagged jets, which likely arise from the

Sample	Generator	Cross section [pb]
$t\bar{t}H$, H→$b\bar{b}$	Powheg	0.295 [80]
$t\bar{t}H$, H→non-$b\bar{b}$	Powheg	0.212 [80]
$t\bar{t}$+jets - DL	Powheg	88.34 [213]
$t\bar{t}$+jets - SL	Powheg	365.45 [213]
$t\bar{t}$+jets - FH	Powheg	377.96 [213]
Single top (s)	MG5_aMC@NLO	6.96 [255]
Single top (t)	Powheg	136.02 [255]
Single antitop (t)	Powheg	80.95 [255]
Single top (tW)	Powheg	35.85 [255]
Single antitop (tW)	Powheg	35.85 [255]
$t\bar{t}$+W, W→ $\ell\nu$	MG5_aMC@NLO	0.1792 [256]
$t\bar{t}$+W, W→ qq	MG5_aMC@NLO	0.3708 [256]
$t\bar{t}$+Z, W→ $\ell\ell, \nu\nu$	MG5_aMC@NLO	0.2589 [256]
$t\bar{t}$+Z, W→ qq	MG5_aMC@NLO	0.6012 [256]
WW	Pythia 8	118.7 [257]
WZ	Pythia 8	65.54 [257]
ZZ	Pythia 8	15.83 [257]
Z + jets, Z→ $\ell\ell$ - 0 jets	MG5_aMC@NLO	4620.52 [258]
Z + jets, Z→ $\ell\ell$ - 1 jets	MG5_aMC@NLO	859.59 [258]
Z + jets, Z→ $\ell\ell$ - 2 jets	MG5_aMC@NLO	338.26 [258]
W + jets, W→ $\ell\nu$ - 0 jets	MG5_aMC@NLO	50131.98 [258]
W + jets, W→ $\ell\nu$ - 1 jets	MG5_aMC@NLO	8426.09 [258]
W + jets, W→ $\ell\nu$ - 2 jets	MG5_aMC@NLO	3172.96 [258]

Table 9.1: Simulated MC samples for signal and background processes of the $t\bar{t}H$, H→$b\bar{b}$ analysis.

hadronisation of a b quark, and into light jets, which originate from up, down, charm and strange quarks, as well as from gluons.

All objects used in the analysis are built from particle flow objects using the algorithm described in Section 3.3.6. To increase the purity of the reconstructed objects, several quality criteria are applied.

9.2.1 Leptons

To increase the purity of the leptons used in the analysis, selection criteria are applied.

	SL channel	DL channel	
		Leading muon	Subleading muon
$p_T >$ [GeV]	29	25	15
$\|\eta\| <$	2.4	2.4	2.4
Identification	Tight	Tight	Tight
Relative isolation iso(μ)/pt	0.15	0.25	0.25

Table 9.2: Selection criteria for muons in the semileptonic (SL) and dileptonic (DL) channels.

Muons

Muons are required to satisfy kinematic selections on their transverse momentum p_T and their pseudo-rapidity $|\eta|$.

A muon identification criterion is further applied to disentangle muons originating from the hard process (prompt muons) from non-prompt muons. These arise for instance from misidentified hadrons or from decays of b quarks or mesons. The identification criterion is built amongst others from tracker and muon chamber hit information [118, 259].

Lastly, an isolation requirement is applied to distinguish prompt muons from QCD radiation processes. For this purpose, an isolation variable is computed as

$$\text{iso}(\mu) = \sum_{\Delta R<0.4} p_T^{\text{CH}} + \max\left(0, \sum_{\Delta R<0.4} [E_T^{\text{NH}} + E_T^{\gamma} - \frac{1}{2} p_T^{\text{PU}}]\right) \tag{9.1}$$

where p_T and E_T denote the transverse momentum and energy of charged hadrons (CH), neutral hadrons (NH) or photons (γ) originating from the primary vertex, as well as of hadrons originating from pileup processes (PU). The factor 1/2 is estimated from simulation and gives the fraction of neutral over charged particle production in pileup processes. The isolation variable thus sums over the momenta of all particles contained within a cone of 0.4 around the muon [260, 110]. All mentioned selections are summarised in Table 9.2.

Electrons

Selection criteria on electrons are applied similarly to those for muons in order to select objects produced in weak boson decays, and to suppress jets falsifying electron

	SL channel	DL channel	
		Leading electron	Subleading electron
$p_T >$ [GeV]	30	25	15
$\|\eta\| <$	2.4	2.4	2.4
Identification	Tight	Tight	Tight

Table 9.3: Selection criteria for electrons in the semileptonic (SL) and dileptonic (DL) channels.

signals. In a first step, kinematic selections are imposed. An isolation measure is defined as

$$\text{iso}(e) = \sum_{\Delta R<0.3} p_T^{\text{CH}} + \max\left(0, \sum_{\Delta R<0.3} [E_T^{\text{NH}} + E_T^{\gamma} - \rho A(\eta)]\right) \tag{9.2}$$

where the pileup components are written in terms of the mean pileup energy ρ and the effective area $A(\eta)$.

A combined electron identification criterion, which is based on electromagnetic shower shapes, is then defined using a multivariate discriminator. This discriminator also contains a selection on the electron's relative isolation [261]. A summary of the selections is given in Table 9.3.

9.2.2 Jets and missing transverse momentum

Jets are reconstructed with the anti-k_T algorithm and a distance parameter of 0.4 (AK4 jets). Tracks that don't originate from the primary vertex are removed using the charged hadron subtraction algorithm (CHS). This eliminates charged contributions from pileup [74].

Because of the non-linearity of the detector response to the deposited energy of a particle and because of an offset originating from pileup effects, the measured energy generally does not exactly correspond to that of the generated parton. Thus both the jet energy scale (JES) and the jet energy resolution (JER) need to be corrected in data and simulation using jet energy corrections (JECs) [262].

Contributions from pileup are estimated in a QCD dijet sample by comparing the resulting jet kinematics in two separate samples, of which one is processed including pileup effects. The calculated correction for pileup effects depends on the energy density, the area and the kinematics of the jets. Remaining η dependent differences are corrected using the random cone method [116]. The detector response is then

	SL channel	DL channel	
		Leading 2 jets	Other jets
$p_T >$ [GeV]	30	30	20
$\|\eta\| <$	2.4	2.4	2.4
Identification	Tight	Tight	Tight
Pileup identification	Loose	Tight	Tight

Table 9.4: Selection criteria for jets in the semileptonic (SL) and dileptonic (DL) channels.

accounted for by comparing the p_T of generator level jets and of reconstructed ones. For this a precise simulation of the detector geometry is necessary. Final residual corrections on the pseudorapidity of jets are evaluated from a QCD dijet sample by comparison with the barrel reference region. Similarly, residual p_T corrections are evaluated using Z/γ+jets samples. All JECs are applied sequentially to obtain the final, corrected jet kinematics [262, 263].

After including jet energy corrections, selection criteria are applied on jets. As for leptons, these involve kinematic requirements. Further criteria aim to identify and reject jets originating from pileup. This is implemented in a MVA discriminant, which is based on the association of tracks to the primary vertex, the topology of the jet and the object multiplicity [264]. A series of selections on deposited energy fractions are also applied via the jet's identification flag [265]. Lastly, all jets within a distance of 0.4 to a lepton passing the selections are removed. The selection criteria are summarised in Table 9.4.

The DeepCSV algorithm is used to identify jets originating from the decay of bottom quarks [120]. This deep neural network based tagger uses information on displaced tracks as well as on secondary vertices to build a discriminant between jets originating from bottom quarks, and those originating from light or charm quarks or gluons. A jet is considered as a b-tagged jet if it passes the medium working point of the algorithm. At this working point, a tagging efficiency of 70% is achieved at a mistagging rate of 1% for light quarks and gluons, and 20% for charm quarks.

The missing transverse energy (MET) is defined as the negative vectorial sum of the transverse momenta of all visible particles:

$$E_T^{miss} = |-\sum_i \vec{p}_{T,i}| \tag{9.3}$$

The MET originates from the neutrinos produced in leptonic top quark decays,

and the JEC corrections applied to jets are propagated to its calculation.

9.2.3 Boosted objects

High p_T top quarks and Higgs bosons are reconstructed using the methods described in Section 8.1.

Preselection

Higgs boson candidates are constructed using anti-k_T jets with a distance parameter of 0.8 (AK8 jets) from which constituents originating from pileup are removed with the PUPPI algorithm [75]. The PUPPI algorithm filters out charged particles which are compatible with tracks that do not originate at the primary vertex, and lowers the weight of neutral particles which likely originate from pileup. Only large-R jets with $p_T > 300\,\text{GeV}$ and $|\eta| < 2.4$ are considered. For further discrimination against other particles, the double b-tag algorithm (bb-tag) [231] is employed, which enables to distinguish jets with a two-prong, b-flavoured structure, from other types of jets. This gives a strong handle to identify jets originating from Higgs bosons from those arising from QCD radiation or top quarks. The bb-tag algorithm is based on a multivariate technique (MVA), which uses several track-based variables, as well as variables related to the vertex of the event.

Top candidates are built using the HEPTopTagger (HTT) algorithm described in Section 8.1.3, starting from Cambridge-Aachen jets with a distance parameter of 1.5. Since there are no hadronically decaying top quarks in the dileptonic channel, top candidates are only reconstructed in the semileptonic channel. HTT candidates are required to satisfy $p_T > 200\,\text{GeV}$ and $|\eta| < 2.4$.

The selected p_T thresholds are driven by the minimum jet radius R_{min} which contains all decay products of the Higgs boson or the top quark, as is illustrated in Figure 9.1. As expected, R_{min} decreases faster with p_T for the Higgs boson than for the top quark because of its lower mass. The Figure shows that the minimum p_T required such that the decay products of top quarks are contained within a jet with a cone size of 1.5 is roughly 200 GeV, and similarly for Higgs bosons and a cone size of 0.8, the p_T must exceed around 300 GeV.

Boosted decision tree for top quark tagging

To improve the discrimination against other particles, an additional selection is performed on top candidates produced by the HTT algorithm. Three variables are used for the discrimination, the candidate mass, the m_W compatibility variable f_W defined

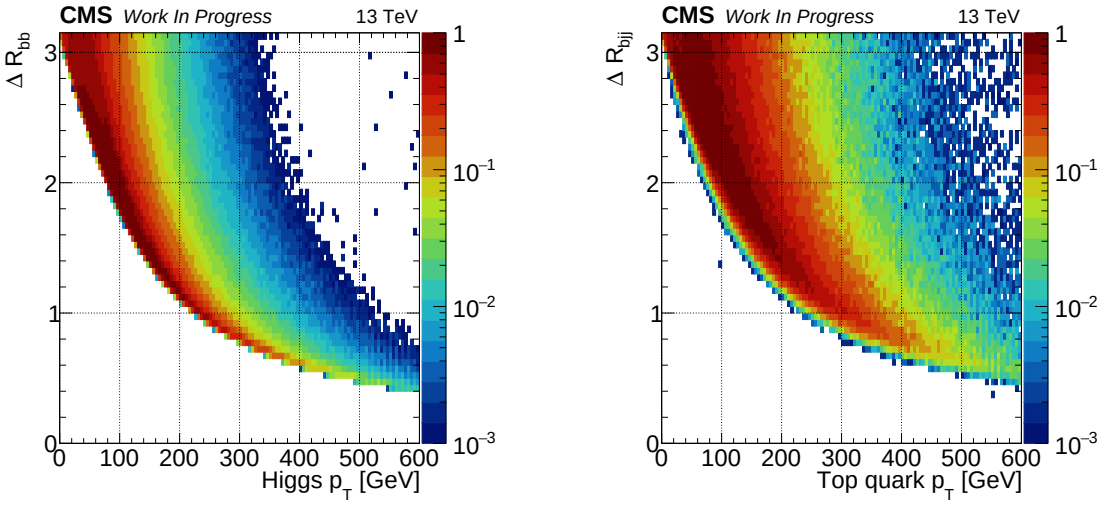

(a) Higgs boson (b) Top quark

Figure 9.1: Minimum angular distance containing the two decay products of the Higgs boson (a) and all three decay products of the top quark (b) as a function of the particles' transverse momentum. As expected, this distance scales as $R_{\text{min}} \sim \frac{2m}{p_T}$.

in Section 8.1.3, and ΔR(HTT,lep), which corresponds to the distance between the candidate and the lepton in semileptonic events.

These three variables are processed by a boosted decision tree (BDT), implemented with the scikit-learn package [266]. The training and testing datasets are built from samples of $t\bar{t}H$, $H \to b\bar{b}$ and $t\bar{t}$+jets events, where the top decays are semileptonic. To avoid selection biases these samples are orthogonal to the samples used at later stages of the analysis. The hard interaction in both samples is modelled with the Powheg generator at next-to-leading order. Pythia is used to simulate parton showering and hadronisation processes. In both samples, top quark candidates ("signal") and background jets are selected as follows:

- Select generated hadronically decaying top quarks with $p_T > 200\,\text{GeV}$ and $|\eta| < 2.4$
- Remove HTT candidates with $p_T < 200\,\text{GeV}$ and $|\eta| > 2.4$
- HTT candidates within an angular distance below 0.6 to a generated, hadronically decaying top quark form the signal jet collection, other candidates constitute the background.

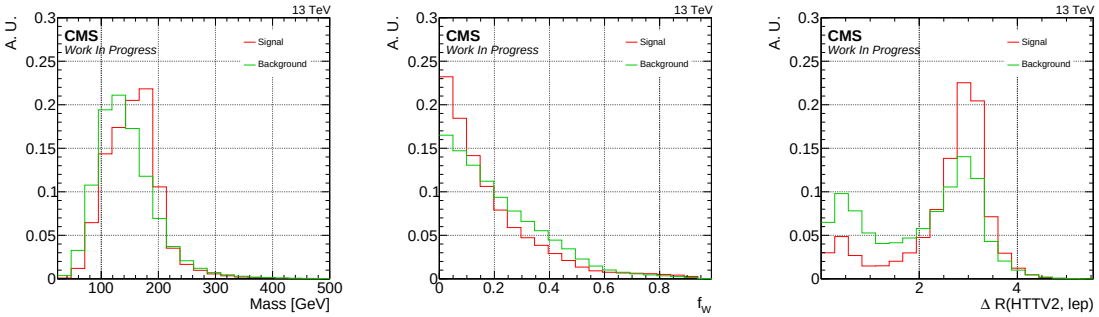

(a) Mass (b) f_W (c) ΔR(HTT,lep)

Figure 9.2: Input variables used for the training of the top quark identification BDT, which are the HTT mass (a), the f_W variable (b), and the candidate's distance to the lepton (c). These differ between signal and background jets.

The BDT is trained on individual jets. Jets which are obtained from both samples are mixed, such that the final datasets contain about 50% of jets from each sample. The obtained dataset is then separated into two, to form a sample for training the BDT, and one for its testing. Each of those samples contains around 1.3M events.

Figure 9.2 shows the input variables which are used in the training of the BDT. All distributions show some discrimination between signal and background jets. The BDT is trained with a learning rate of 0.05, the maximum depth is 2 and 3000 estimators are used.

Figure 9.3 shows the BDT score for signal and background jets, in the training and the test sample. Importantly the distributions are similar in both samples for both types of jets. This indicates that the BDT does not overtrain, as it is not learning any noise features of the training sample.

The performance of identifying Higgs boson and top quark candidates is summarised in Figure 9.4, which shows a receiver operating characteristics (ROC) curve. It illustrates the efficiency of identifying true Higgs bosons or top quarks (ε_S) as a function of the misidentification rate for other types of jets (ε_B). An area under the curve of 0.75 is achieved for Higgs boson tagging and of 0.71 for top quark tagging.

Optimisation procedure

After building discriminants for the identification of top quark and Higgs boson candidates, the working point of these discriminants is chosen. It is optimised simultaneously on events containing at least one HTT and one Higgs boson candidate

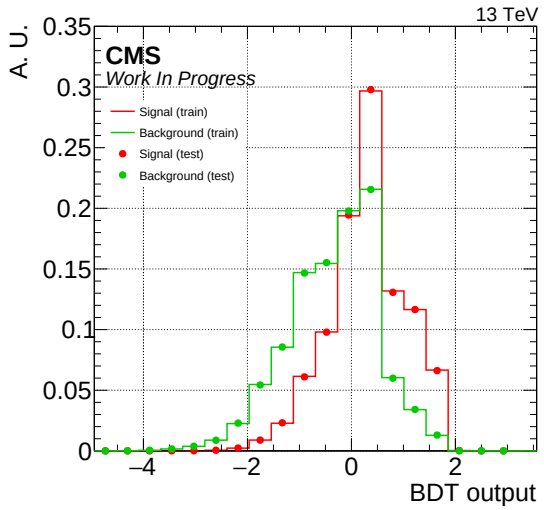

Figure 9.3: Output distribution of the top quark identification BDT for signal and background jets in the training and test samples. A discrimination between signal and background jets is clearly noticeable.

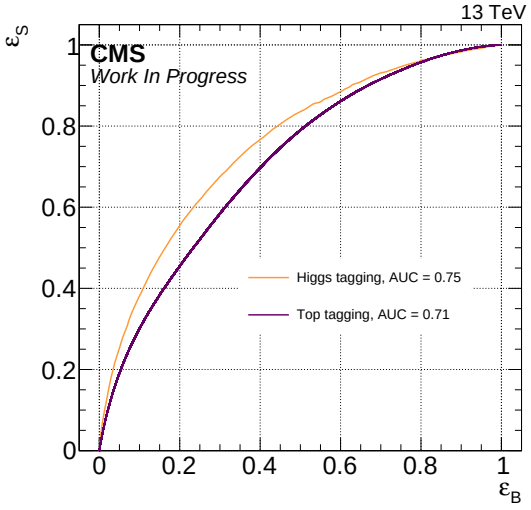

Figure 9.4: Receiver operating curve for the top quark identification BDT, and for the Higgs boson selection based on its bb-tag score.

passing the preselection. Signal events are taken from a $t\bar{t}H$, $H\to b\bar{b}$ sample, while background events are selected from a $t\bar{t}$+jets sample in which the top quark pair decays semileptonically, and which must not contain more than 2 b-tagged jets.

Figure 9.5 shows the signal-over-background ratio S/B (a) and the simultaneous Higgs boson and top quark tagging efficiency ε_{HT} (b) as a function of the selection on the Higgs boson candidate bb-tag and the top quark BDT discriminator scores. Clearly, the efficiency to correctly identify the candidates increases with more stringent selections on the discriminators. However, this reduces the sensitivity of the analysis, as the S/B ratio decreases. Thus, the working point is optimised on the product of the efficiency ε_{HT} and the S/B ratio, which is illustrated in Figure 9.6. A bb-tag score within $[0.3, 0.6, 0.8, 0.9]$ is further required to simplify the application of scale factors to correct for different tagging efficiencies in data and simulation, as is explained in Section 9.3. Given these constraints, the maximum of the product $\varepsilon_{HT} \cdot S/B$ is found at (0.32, 0.6) for the (top quark, Higgs boson) discriminator scores, which is the working point that is chosen for this analysis, and which is marked in Figures 9.5 and 9.6.

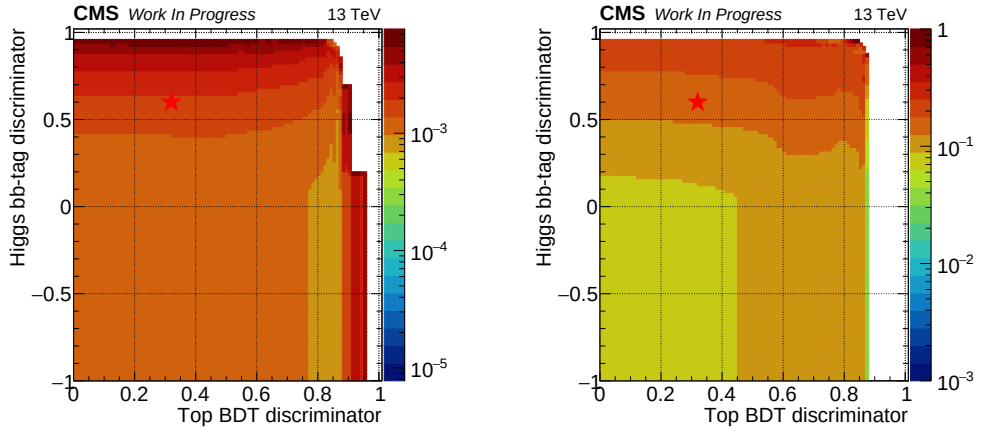

(a) S/B (b) ε_{HT}

Figure 9.5: Signal-over-background ratio S/B (a) and the simultaneous Higgs boson and top quark tagging efficiency ε_{HT} (b) as a function of the Higgs candidate bb-tag and the top quark identification BDT score. The red star indicates the selected working point.

Figure 9.7 shows the efficiency of this selection as a function of the generated top quark or Higgs boson p_T in semileptonic $t\bar{t}H$, $H\to b\bar{b}$ events. Candidates are associated to the generator level objects using a matching criteria of $\Delta R < 0.6$. The tagging efficiency ε is defined as the number of candidates passing the selections on p_T and $|\eta|$ (solid lines) or on p_T, $|\eta|$, and bb-tag/BDT score (dashed lines) which are matched to generator level objects, divided in both cases by the total number of generated Higgs bosons or hadronically decaying top quarks. The tagging efficiency increases with larger p_T of the generated object, and reaches a plateau at full efficiency at around 500 GeV when only considering kinematic selections. The plateau is reached at higher p_T for Higgs boson candidates, since the minimum p_T required from these candidates is larger than for HTT candidates. Applying the optimised selections on the bb-tag or the BDT score leads to slightly lower tagging efficiencies. For Higgs boson candidates, the efficiency decreases by around 10% at large p_T, and for HTT candidates, the efficiency loss is around 30%. Thus, the optimised selection sets rather loose requirements on the candidates.

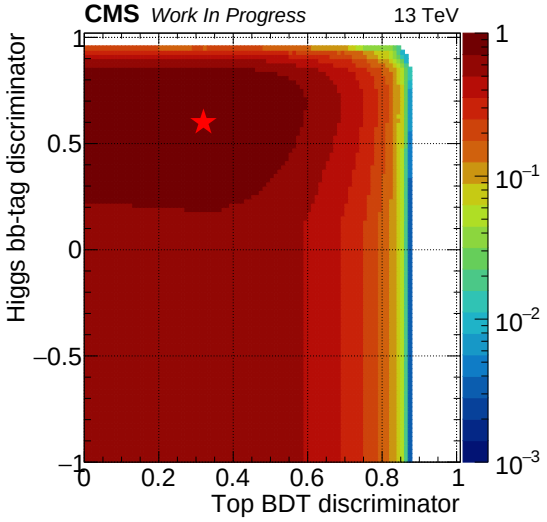

Figure 9.6: Normalised product of the S/B and ε_{HT} variables as a function of the Higgs candidate bb-tag and the top quark identification BDT score. The red star indicates the selected working point, which corresponds to the maximum of the histogram.

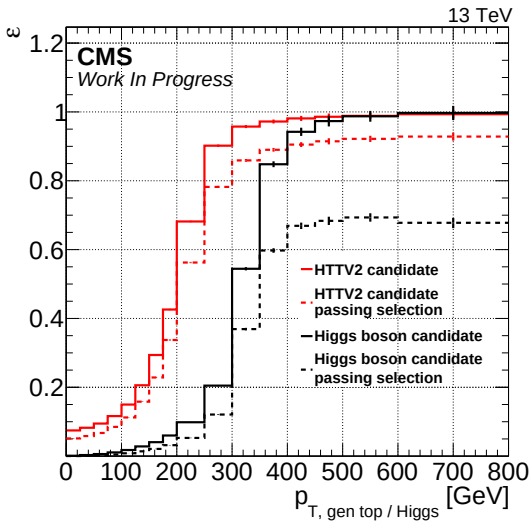

Figure 9.7: Tagging efficiency for top quarks and Higgs bosons using HTT and AK8 candidates respectively. Solid lines show the tagging efficiency applying only kinematic selections, whereas dashed lines include selections on the HTT BDT score and the AK8 bb-tag score.

9.3 Event selection

Using the analysis objects satisfying the mentioned requirements, events compatible with the $t\bar{t}H$, $H\to b\bar{b}$ signal are selected.

Event cleaning is performed with MET filters, which remove problematic events due to detector noise, badly reconstructed vertices and beam halo effects. A total of 8 filters are applied on data, and 7 on MC simulation. Additionally each valid event must contain at least one primary vertex satisfying the criteria detailed in Section 3.3.6.

The SL and DL analysis channels are then reconstructed. DL events must contain exactly two opposite-signed leptons as defined in Section 9.2. Additionally the invariant mass of the lepton pair m_{ll} should exceed 20 GeV to remove contributions from decays of heavy resonances and from low-mass Drell-Yan processes. Furthermore, it must be outside of the window $[76, 106]$ GeV and the MET is required to be

larger than 40 GeV for events with two leptons of the same flavour to suppress events involving Z boson decays.

SL events contain exactly one lepton, with no additional leptons passing the subleading selections in Tables 9.2 and 9.3. The MET needs to exceed 20 GeV in order to suppress contributions from QCD events.

In both channels, only events with at least 4 jets including 2 or more b-tagged jets are considered. Events in which the W bosons decay into a tau lepton are indirectly included in the analysis if the taus decay to electrons or muons.

To account for residual differences between data and simulation, MC events are reweighted. The global event weight is a product of individual scale factors, correcting for generator, pileup, trigger, lepton, b tagging and L1 prefiring effects:

- Generator: Events are scaled using the process cross sections such that the event yields in simulation correspond to the same integrated luminosity than the collected data.

- Pileup: The pileup distribution in simulation is rescaled such that it agrees with the measured one in data. This is necessary as the MC samples are produced before the data collection period is over, such that the distribution is not known at processing time. For this purpose each event is assigned a weight.

- Trigger efficiency: As the trigger efficiency differs in data and simulation, a scale factor is applied to adjust the latter one to that in data. In the SL event categories, this factor depends on the p_T and η of the triggering lepton, and in the DL categories on the p_T of both leptons [267].

- Lepton efficiency: Events are also scaled to account for different lepton reconstruction efficiencies in data and simulation. These corrections consist of a component to correct for differences in the electron reconstruction and identification, and a component accounting for the discrepancies in the muon identification and isolation criteria [267].

- B tagging efficiency: To correct for different b tagging efficiencies in data and in simulation, scale factors are applied. These are derived using a tag and probe approach, and are evaluated separately for light-flavoured and heavy-flavoured jets. For c-flavoured jets, a weight of one is used [268].

- Prefiring correction: A gradual timing shift of the electromagnetic calorimeter was not taken into account during data taking by the trigger system, such that trigger primitives at large values of η were linked to an earlier bunch crossing. As

two consecutive bunch crossings cannot be processed by the L1 trigger system, it follows that some events are rejected by their own deposits in the endcaps of the ECAL. The probability for this to occur is evaluated and used to reweight each event in simulation [269].

- Top quark / Higgs boson tagging efficiency: Similarly to the other cases above, the efficiency to identify top quarks and Higgs bosons differs in simulation and data. Scale factors are used to correct for this effect. For the Higgs boson candidate, corrections are derived centrally by the CMS collaboration [268]. For top quark candidates, these weights are calculated separately in a phase space enriched in top quark pair events decaying semi-leptonically. Selected events contain a single muon with a $p_T > 30\,\text{GeV}$ and $|\eta| < 2.1$ and no other leptons, have a missing transverse momentum larger than 40 GeV and the p_T of the leptonically decaying W boson (reconstructed from the missing transverse momentum and the muon) must exceed 200 GeV. This selection is orthogonal to that of the analysis as only events with at most 2 b-tagged jets are considered. In the calculation, lepton, generator, trigger, b tagging and pileup weights are applied as described above. Control distributions showing the MET and the three variables used in the top quark tagging BDT are shown in Figure 9.8. The tagging efficiency is then calculated as the ratio of the number of top quark candidates which are within an angular distance of 0.6 to a generated top quark passing the selected working point on the BDT, divided by the total number of candidates. In data, the number of top quark candidates which are associated to generated top quarks is estimated by subtracting the unmatched contribution from simulation in both the nominator and the denominator. With this, an event weight of 0.982 ± 0.059 is obtained.

9.4 Systematic uncertainties

Uncertainties affecting the measurement of the $t\bar{t}H$ process are divided into statistical and systematic uncertainties. While statistical uncertainties are reduced when increasing the size of the dataset, this is not the case for systematic uncertainties, as they account for calibration uncertainties in detectors or unknowns in theoretical predictions. As is shown in Chapter 10, this analysis is dominated by systematic uncertainties, which is why their sources are described in the following, and summarised in Table 9.5. These sources are further categorised into experimental and theoretical uncertainties. In the final results, uncertainties affecting different analysis categories in the same way are treated as fully correlated.

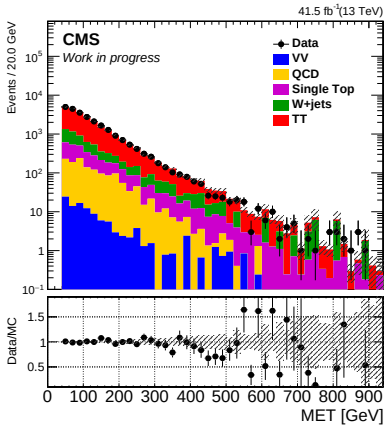

(a) MET

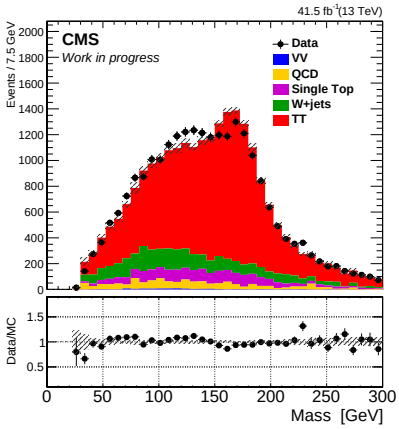

(b) Candidate mass

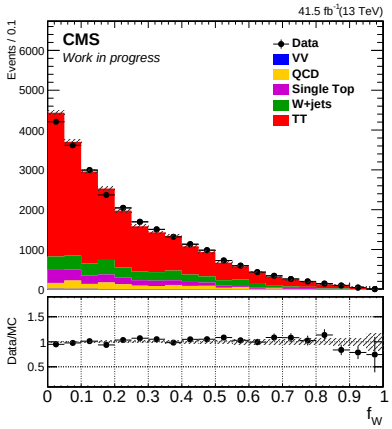

(c) Candidate f_W

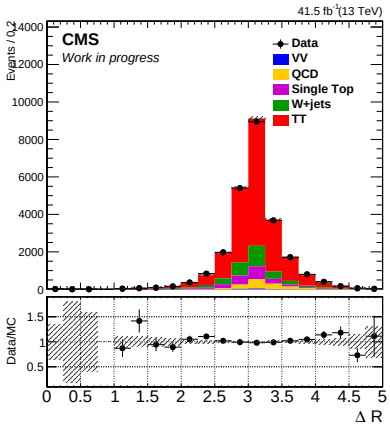

(d) Candidate ΔR(HTT,lep)

Figure 9.8: Modelling of some event and tagger variables such as the MET (a), the top quark candidate mass (b), the f_W variable (c), and the distance ΔR(HTT,lep) to the lepton (d) in the phase space used for the evaluation of the top quark candidate weight.

9.4.1 Experimental uncertainties

Experimental uncertainties arise from uncertainties on the event weights presented above, or from uncertainties in detector calibrations. These affect all signal and background MC samples equally.

- MC sample size: As the size of the samples used to model signal and background processes is limited, the predicted event yields are affected by statistical fluctuations. These are modelled using the Barlow-Beeston method [270], where a nuisance parameter is applied to each histogram bin, scaling its number of expected entries. For bins with more than 10 effective entries, a Gaussian prior is assumed on the nuisance parameter, otherwise a Poisson distribution is used.

- Luminosity: All MC samples are rescaled according to the measured integrated luminosity of the dataset. An uncertainty of 2.3% is assigned to the luminosity measurement of the dataset collected by the CMS experiment in 2017 [271].

- Lepton efficiency: Events are rescaled to correct for different lepton reconstruction efficiencies in data and simulation. Those scale factors carry uncertainties, which are propagated to the discriminant as a shape uncertainty. Given that the overall impact of the uncertainty on the final results is small, a single uncertainty combining statistical and systematic effects on the scale factor is used. Using the same justification, uncertainties on the electron reconstruction and identification scores are combined to a single nuisance parameter, and similarly for the muon identification and isolation parameters [267].

- Trigger efficiency: Uncertainties on the trigger efficiency scale factors are propagated to the final result by modifying the event scale factor, similarly than in the previous case. They are considered correlated across the event categories, but uncorrelated among the single electron, single muon and dileptonic trigger paths [267].

- L1 Prefiring: Uncertainties on the weight correcting the L1 prefiring issue are accounted by propagating the provided uncertainties to the discriminant shape [269].

- Pileup: The cross section of inelastic proton-proton collisions is estimated to be 69.2 mb with an uncertainty of 4.6% [272]. The uncertainty on the pileup weight is thus evaluated by propagating the uncertainties on the cross section to the final result.

- Jet energy corrections: As these corrections apply to individual jets and thus by construction also to the MET, the uncertainties are taken into account by recalculating the discriminator value with each variation of the jet and MET kinematics. These uncertainties can therefore also change the event categorisation, as the jet and event selection is applied separately for all the uncertainty variations.

  Jet energy resolution uncertainties are taken into account by increasing and decreasing the difference between the measured and the generator level jet energy by one standard deviation.

  Jet energy scale corrections are split into 19 different uncorrelated sources, each of which is assigned a dedicated uncertainty. This splitting provides a much improved modelling of the corrections with respect to applying a single uncertainty, and is possible because of progress in the detector simulation and calibration. These sources can be grouped into four categories:

  - Uncertainties affecting the absolute energy scale of the jet, which are derived in a global fit using the Z+jet, γ+jet and QCD multijet MC samples. This uncertainty has a time dependent component to model the degradation of the detector properties with time.
  - Uncertainties on the jet relative pseudorapidity corrections, which are needed to homogenise the barrel and encap region's detector response.
  - Uncertainties on the pileup offset correction, which removes contributions from pileup processes in the jets.
  - Uncertainties on the jet flavour correction, which is modelled differently in data and simulation [273].

- B tagging: Three sources of uncertainties are considered on the scale factors applied to correct for different b tagging efficiencies in data and simulation:

  - Jet energy corrections: The uncertainties on the jet energy scale and resolution directly affect the b tagging scale factors as well, as they depend on the jet kinematics. The b tagging scale factor is thus also recalculated considering the up and down variations of the 19 uncertainty sources mentioned above simultaneously to shifting the jet kinematics.
  - Purity of the heavy and light flavour components in the samples used for the evaluation of the scale factors: Two nuisance parameters are assigned to this uncertainty, one for the heavy flavour and one for the light flavour

components, and correspond to the contamination of heavy (light) flavour jets in the light (heavy) flavour phase space.

– Statistical uncertainties arise from the limited size of the MC samples used to evaluate the b tagging scale factors. Two nuisance parameters are assigned to these uncertainties for each of the two flavour components. One of these nuisance parameters describes an overall, linear tilt of the b tagging discriminator distribution, while the second, quadratic term governs higher-order distortions in the distribution shape.

No scale factors are derived specifically for charm jets, which is why they are assigned a scale factor of one together with an uncertainty twice larger than that of b flavoured jets.

These uncertainties are propagated as a modified event weight towards the final result [268].

- Top quark / Higgs boson reconstruction efficiency: Uncertainties on the corresponding scale factors are treated as modified scale factors to the final result.

9.4.2 Theory uncertainties

Theoretical uncertainties arise from the limited precision of theoretical predictions on the processes considered in the analysis, such as cross sections or parton distribution functions.

- Background normalisation uncertainty: As the normalisation of the $t\bar{t}$+jets backgrounds is affected by large theoretical uncertainties, it is treated as a freely floating parameter which is determined by the fit on data. A common parameter $t\bar{t}$+B is used for the $t\bar{t}$+$b\bar{b}$, $t\bar{t}$+2b and $t\bar{t}$+b background components, while the $t\bar{t}$+$c\bar{c}$ normalisation is modelled with a separate rate parameter.

- Inclusive cross section: The inclusive cross section of the processes included in the analysis is calculated to at least NLO accuracy, and is affected by uncertainties on the QCD scale (renormalisation and factorisation scales), as well as on the choice of the parton distribution functions (PDF). These uncertainties affect the rate of the processes, and are treated as correlated if the uncertainty is common to different processes and uncorrelated otherwise. The rate uncertainty on the QCD scales varies between 13% for the $t\bar{t}W$ process and 1% for the V+jets process. The uncertainty on the PDF description varies between 2% and 4% depending on the process.

- PDF shape: The uncertainty on the shape of the PDF set is estimated by reweighting the final discriminants using different PDF sets. The total uncertainty is taken as the envelope of all PDF variations.

- μ_R, μ_F scale: Shape uncertainties arising from uncertainties in the renormalisation scale μ_R and the factorisation scale μ_F in the calculation of the matrix element are obtained by varying the scales independently by a factor 0.5 and 2, which translate to modified event weights and discriminant shapes.

- Parton shower uncertainties: To estimate the uncertainties of effects of initial (ISR) and final state radiation (FSR) which arise from uncertainties on the choice of α_S in the simulation of the parton shower, the scale is varied by a factor $\sqrt{2}$ and $1/\sqrt{2}$ using a similar procedure than described for the μ_R and μ_F scale uncertainties above. ISR and FSR shower uncertainties are treated as uncorrelated.

- ME-PS matching and underlying event: To improve the modelling of the jet multiplicity in simulation, MC samples are produced with the customised underlying event tune CP5, which governs the importance of ISR, and a parameter h_{damp}, which sets the scale for the gluon emission cross section. Uncertainties on both parameters are estimated using dedicated MC samples with varied values of the h_{damp} parameter and event tune. Given the limited size of these samples, these uncertainties only model normalisation effects, and are compatible with an absence of shape variations.

9.5 Event categorisation

This analysis builds upon the analysis of the 2016 collision data from the CMS experiment published in [245]. As this result does not make use of boosted techniques, its strategy and event categorisation are denoted as the resolved analysis in the following.

Resolved analysis

In this analysis strategy, only events with at least three b-tagged jets according to the medium working point of the DeepCSV algorithm are considered, and events must contain at least one lepton, which allows to reduce the amount of QCD background.

Events are split according to their jet and b jet multiplicities. The matrix element method discriminator described in Section 8.3 is used in categories with four or more

Source	Type	Affected processes
Integrated luminosity	Rate	All
Lepton Reconstruction	Shape + Rate	All
Trigger efficiency	Shape + Rate	All
L1 prefiring correction	Shape + Rate	All
Pileup	Shape + Rate	All
Jet energy scale (19 sources)	Shape + Rate	All
Jet energy resolution	Shape + Rate	All
Top / Higgs selection efficiency	Shape + Rate	All
B tagging weights (8 sources)	Shape + Rate	All
Renormalisation / Factorisation scale	Rate	All
PDF ($gg, qg, q\bar{q}$)	Rate	All
PDF shape	Shape	$t\bar{t}$+jets, $t\bar{t}$H, H→$b\bar{b}$ processes
μ_R, μ_F	Shape + Rate	$t\bar{t}$+jets processes
PS scale ISR, FSR	Shape + Rate	$t\bar{t}$+jets processes
Hdamp, tune uncertainties	Rate	$t\bar{t}$+jets processes
tt+ HF crosssections	Rate	$t\bar{t}$+jets processes
MC sample size	Shape	All
$t\bar{t}$+B, $t\bar{t}$+$c\bar{c}$ normalisations	Free floating	$t\bar{t}$+B, $t\bar{t}$+$c\bar{c}$

Table 9.5: Summary of all uncertainties applied to the analysis of the $t\bar{t}$H, H→$b\bar{b}$ process. For each source of uncertainty its effect on the discriminant distribution is indicated (rate changing parameter or shape modifier), as well as the processes on which they apply.

b-tagged jets, as this method is particularly powerful in discriminating $t\bar{t}$H, H→$b\bar{b}$ events from the main background in this phase-space, the $t\bar{t}$+$b\bar{b}$ process. While the signal sensitivity of events with a lower number of b-tagged jets is reduced, events with exactly three of these jets are used to constrain the various components of the $t\bar{t}$+jets background, which in turn contributes to improve the analysis sensitivity in the signal enriched categories. Thus the following resolved analysis categories are used in the SL and DL categories:

- SL: ≥ 6 jets, ≥ 4 b-tagged jets, 5 jets, ≥ 4 b-tagged jets, 4 jets, 4 b-tagged jets, ≥ 6 jets, 3 b-tagged jets, 5 jets, 3 b-tagged jets, 4 jets, 3 b-tagged jets
- DL: $\geq$4 jets, ≥ 4 b-tagged jets, ≥ 4 jets, 3 b-tagged jets

Figure 9.9 illustrates the event composition in these categories. Clearly, categories with larger number of b-tagged jets contain a higher fraction of signal events.

Combination of MEM with substructure methods

The analysis is expanded by using substructure methods to include events with a Higgs boson or a top quark with a large p_T. The approach presented here analyses events containing such a candidate in separate categories, and combines these with the resolved analysis ones, ensuring that these are mutually exclusive.

Figure 9.10 illustrates the event selection in the boosted analysis. First, so-called resolved jets are identified according to the selection criteria given in Section 9.2, and if at least three b-tagged jets are found, the event is treated as in the resolved analysis. If this is not the case, boosted top quark or Higgs boson candidates are reconstructed. If any of these candidates fulfil the criteria defined in Section 9.2, their subjets (2 in the case of the Higgs boson candidate, three for top quark candidates) are isolated. Resolved jets located within an angular distance of 0.3 to these subjets are discarded. If a top quark candidate has been identified, its subjet with the largest b tagging score is selected as a b-tagged jet, while to other two form light-flavoured jets. For Higgs boson candidates, both subjets are classified as b-tagged jets. In addition to these jets, resolved b-tagged jets are considered, starting with those having the largest b tagging score, until the event contains at most four b-tagged jets. All remaining resolved b-tagged jets are discarded. If a top quark candidate is found, all resolved light jets are similarly discarded, but if only a Higgs candidate is identified, these jets are conserved. No top quark candidate is accepted in the dileptonic analysis channel.

If the newly formed list of b-tagged jets, consisting of a mixture of subjets and resolved jets, contains four elements, it is used to calculate the MEM. Otherwise the event is discarded. The event composition of the boosted categories used in the analysis are shown in Figure 9.9.

In addition, substructure techniques can help to simplify the calculation of the MEM, as identifying a Higgs boson or a top quark candidate can be used to reduce the number of permutations that are considered in the MEM computation. In particular, when a top quark candidate is found, one b-tagged jet is unambiguously identified as originating from a top quark decay. This leaves three permutations to associate the remaining three b-tagged jets to the quarks into which the Higgs boson and the other top quark decay. Similarly when a Higgs boson candidate is found, only two permutations need to be considered. Finally, only one permutation remains when both candidates are identified. As is shown in Section 10.3, this considerably reduces the computation time of the MEM.

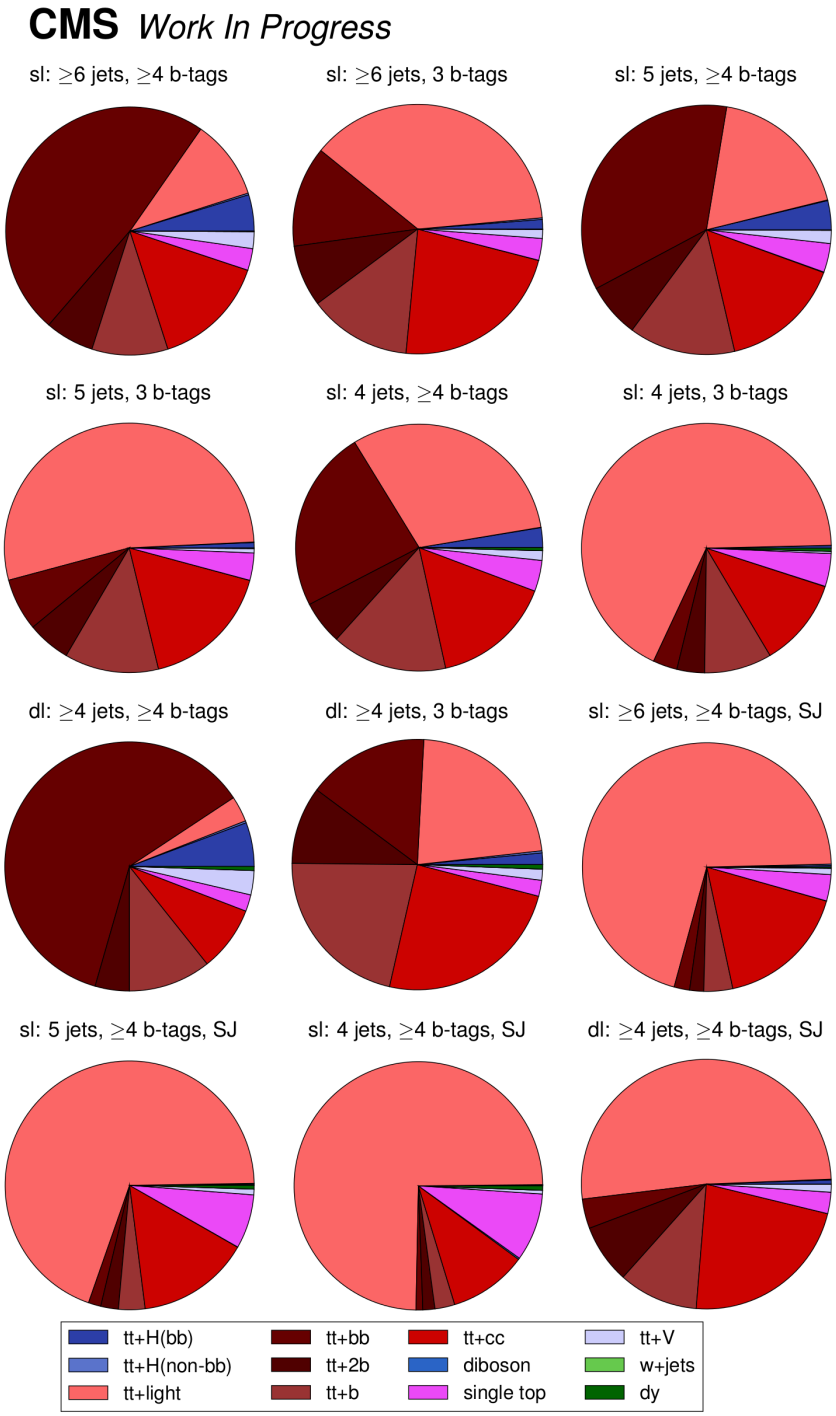

Figure 9.9: Event composition of all categories used in the resolved and the boosted analysis. Categories with larger numbers of b-tagged jets are dominated by contributions from $t\bar{t}H$, $H \to b\bar{b}$ and $t\bar{t}+b\bar{b}$ events. Boosted categories only contain a minor fraction of signal events.

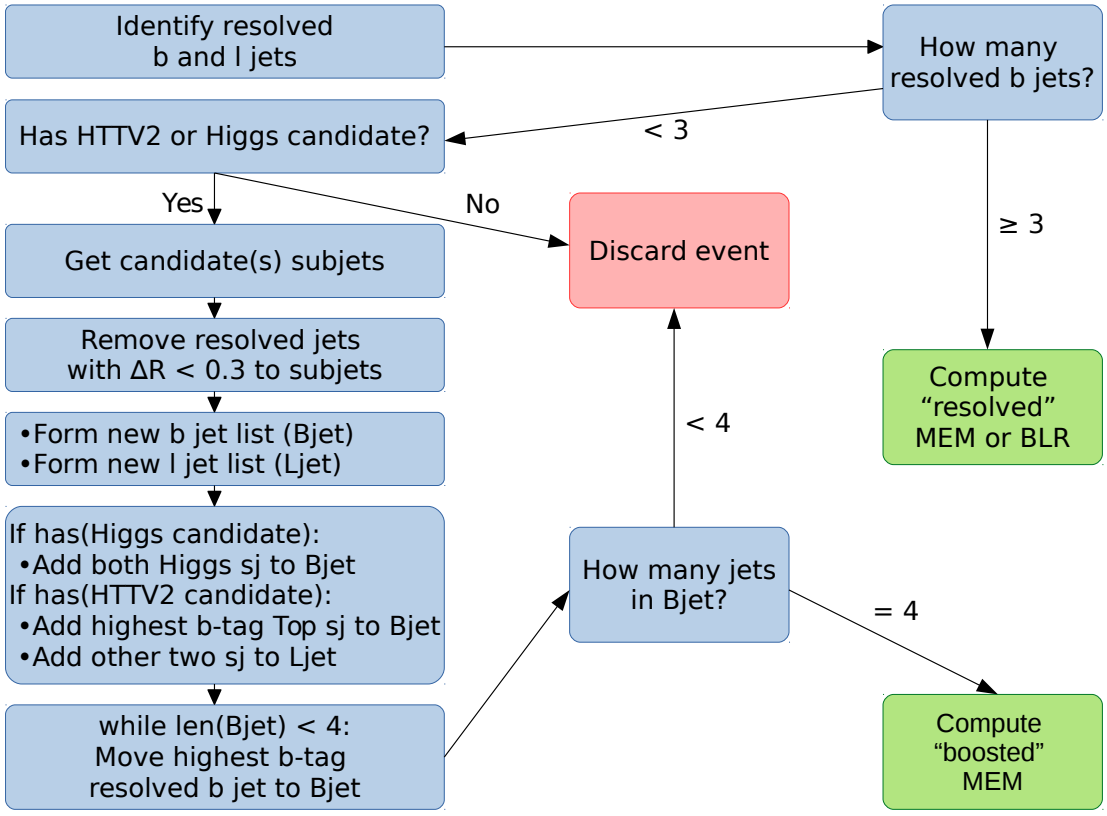

Figure 9.10: Schematics illustrating the analysis strategy in the boosted categories.

Discriminants

Depending on the analysis category different discriminating variables are used to reconstruct signal events. In categories with four b-tagged jets (in both the resolved and the boosted case), the Matrix Element Method (MEM) is used. In the resolved analysis, these four jets are the four jets leading to the largest b tagging likelihood ratio, whereas in the boosted case the jets are a mixture of resolved jets and subjets. The MEM hypothesis that is chosen depends on the number of observed jets. With six or more jets in the SL analysis channel, the fully reconstructed hypothesis (SL-$2_l2_h2_t$) is used, as two light quarks, both b quarks from the Higgs boson and both b quarks from the two top decays have been reconstructed. In events with less than six jets, the hypotheses SL-$1_l2_h2_t$ and SL-$0_l2_h2_t$ are used, where the integration is performed over the missing quarks as described in Section 8.3.2. In the boosted

analysis, the SL-$i_l 2_h 2_t$-sj hypothesis is used, where i indicates the number of reconstructed light-flavoured jets, and which uses the same integration procedure than the SL-$i_l 2_h 2_t$ hypothesis, but with a modified jet selection. In the boosted categories, the MEM can also be calculated with a reduced set of permutations as described above, defined as SL-$i_l 2_h 2_t$-sj-fix$_{\text{top/higgs}}$ which indicates which permutations are fixed in the integration. For events with only three reconstructed b-tagged jets, the BLR is used as a discriminator between signal and background events. Table 9.6 summarises the discriminators used in all analysis categories and shows which categories are used in the resolved and the boosted analysis strategy.

In an alternative result that is presented in the following chapter, the BLR is used in all resolved categories, and the average pseudorapidity between all jets discriminates between signal and background events in the boosted categories.

9.6 Statistical analysis of the data

Even after the object and event selections, the $t\bar{t}H$, $H\to b\bar{b}$ signal is still hidden by large contributions from background processes, in particular $t\bar{t}$+jets events. This is why simply counting the number of events in each analysis category, or searching for a mass peak around the Higgs boson mass would not lead to any significant result. To resolve this issue a maximum likelihood template fit is carried out to extract the signal strength modifier of the $t\bar{t}H$, $H\to b\bar{b}$ process $\mu = \frac{\sigma_{t\bar{t}H}}{\sigma_{t\bar{t}H,SM}}$, which gives the ratio of the measured cross section and the predicted one from the SM. This implies that for data distributed exactly according to the SM predictions, a signal strength of one is expected, which corresponds to the hypothesis H_1 under test. The aim of the analysis is to exclude the null hypothesis (H_0), which corresponds to the case $\mu = 0$ where there is no contribution from the signal.

The template fit normalises the signal and background distributions such that their sum best represents the data distribution. The fit accuracy thus depends strongly on the distinctiveness of the templates used for the signal and background distributions. Similarly, the goodness of the fit depends on the choice of the template and on the correct assessment of the uncertainties affecting the distributions. These uncertainties are described in Section 9.4.

Each of the templates representing a variable x used in the fit is represented as a histogram, where $\mathbf{n} = (n_1, n_2, ..., n_N)$ gives the number of events in each histogram bin. The expected number of events in each bin is estimated based on the expected number of signal s_i and background b_i events:

	Analysis category	Discriminant	Alternative discriminant
Resolved analysis	SL, ≥ 6 jets, ≥ 4 b-tags	MEM, SL-$2_l2_h2_t$	
	SL, ≥ 6 jets, 3 b-tags	BLR	
	SL, 5 jets, ≥ 4 b-tags	MEM, SL-$1_l2_h2_t$	
	SL, 5 jets, 3 b-tags	BLR	
	SL, 4jets, ≥ 4 b-tags	MEM, SL-$0_l2_h2_t$	
	SL, 4 jets, 3 b-tags	BLR	
	DL, ≥ 4 jets, ≥ 4 b-tags	MEM, DL-2_h2_t	
	DL, ≥ 4 jets, 3 b-tags	BLR	
Boosted analysis	SL, ≥ 6 jets, ≥ 4 b-tags, SJ	MEM, SL-$2_l2_h2_t$-sj	MEM, SL-2_l2_h2t-sj-fix$_{\text{top}}$ MEM, SL-$2_l2_h2_t$-sj-fix$_{\text{higgs}}$ MEM, SL-$2_l2_h2_t$-sj-fix$_{\text{top, higgs}}$
	SL, ≥ 6 jets, ≥ 4 b-tags, no SJ	MEM, SL-$2_l2_h2_t$	
	SL, ≥ 6 jets, 3 b-tags	BLR	
	SL, 5 jets, ≥ 4 b-tags, SJ	MEM, SL-$1_l2_h2_t$-sj	MEM, SL-$1_l2_h2_t$-sj-fix$_{\text{higgs}}$
	SL, 5 jets, ≥ 4 b-tags, no SJ	MEM, SL-$1_l2_h2_t$	
	SL, 5 jets, 3 b-tags	BLR	
	SL, 4jets, ≥ 4 b-tags, SJ	MEM, SL-$0_l2_h2_t$-sj	MEM, SL-$0_l2_h2_t$-sj-fix$_{\text{higgs}}$
	SL, 4jets, ≥ 4 b-tags, no SJ	MEM, SL-$0_l2_h2_t$	
	SL, 4 jets, 3 b-tags	BLR	
	DL, ≥ 4 jets, ≥ 4 b-tags, SJ	MEM, DL-2_h2_t-sj	MEM, DL-2_h2_t-sj-fix$_{\text{higgs}}$
	DL, ≥ 4 jets, ≥ 4 b-tags, no SJ	MEM, DL-2_h2_t	
	DL, ≥ 4 jets, 3 b-tags	BLR	

Table 9.6: Summary of the discriminants used in all analysis categories. By default, the MEM is used in categories with at least four b-tagged jets. When only three b-tagged jets are present, the BLR is used.

$$\mathcal{E}[n_i] = b_i(\theta) + \mu s_i(\theta) \tag{9.4}$$

where μ is the signal strength parameter, and the expected numbers of signal and background events depend on a set of nuisance parameters θ. These describe the effect of the uncertainty sources on the observed number of events in each bin. It is assumed that the observed number of events n_i in a discrete distribution obeys to a Poisson distribution, such that

$$\mathcal{P}_i(n_i|\mathcal{E}[n_i]) = \frac{\mathcal{E}[n_i]^{n_i}}{n_i!} e^{-\mathcal{E}[n_i]} \tag{9.5}$$

Thus, the likelihood function describing the likeliness of the measured data to distribute according to μ and θ is given by

$$\mathcal{L}(\text{data}|\mu,\theta) = \prod_i^N \frac{[b_i(\theta) + \mu s_i(\theta)]^{n_i}}{n_i!} e^{-[b_i(\theta)+\mu s_i(\theta)]} \cdot p(\tilde{\theta}|\theta) \tag{9.6}$$

The parameter $\tilde{\theta}$ gives the values of the nuisance parameters as constrained by data. The function $p(\tilde{\theta}|\theta)$ is linked to the probability density function $p(\theta|\tilde{\theta})$ by the Bayes theorem

$$p(\theta|\tilde{\theta}) \approx p(\tilde{\theta}|\theta) \cdot \pi(\theta) \tag{9.7}$$

with the prior $\pi(\theta)$.

The choice of the probability density function depends on the type of uncertainty. Generally, two different types are considered:

- Rate uncertainties only affect the normalisation of a distribution, but not its shape. They are modelled using a log-normal distribution

$$p(\theta|\tilde{\theta}) = \frac{1}{\sqrt{2\pi}\theta \ln\kappa} e\Big[- \frac{(\ln\theta - \ln\tilde{\theta})^2}{2(\ln\kappa)^2} \Big] \tag{9.8}$$

  with the scale parameter $\kappa = 1 + \sigma/\mu^2$.

- Shape uncertainties on the contrary affect the shape of the distributions. They are assumed to follow a Gaussian distribution

$$p(\theta|\tilde{\theta}) = \frac{1}{\sqrt{2\pi}\sigma} e\Big[- \frac{(\theta - \tilde{\theta})^2}{2\sigma^2} \Big] \tag{9.9}$$

  with the variance σ of the normal distribution.

A profile likelihood ratio is built as

$$\lambda(\mu) = \frac{\mathcal{L}(\mu, \hat{\hat{\theta}})}{\mathcal{L}(\hat{\mu}, \hat{\theta})} \tag{9.10}$$

where $\hat{\mu}$ and $\hat{\theta}$ are the parameters under which the likelihood function is maximised, and $\hat{\hat{\theta}}$ depends on μ and describes the set of nuisance parameters which maximise the likelihood function for a fixed value of μ.

Practically, finding the maximum of the likelihood function might surpass the numerical precision of the machine when computing the product of many numbers below one, which is why the negative logarithm q_μ of that function is minimised instead:

$$q_\mu = -2 \ln \lambda(\mu) \tag{9.11}$$

Only values of $\hat{\mu} \geq 0$ are considered as the analysis is searching for an excess of events which cannot be explained by the sole presence of the background [274].

A large measured value of the test statistics q_μ therefore describes an incompatibility with the hypothesis under test. This is formalised by calculating the so-called p-value

$$p_\mu = \int_{q_\mu,\text{obs}}^{\infty} f(q_\mu|\mu = 0) dq_\mu \tag{9.12}$$

where $f(q_\mu|\mu = 0)$ denotes the probability density function of the test statistics under the H_0 hypothesis. It can be computed by producing toy datasets following the background only model. However, the smaller the observed p-value and the larger the discovery potential, the more toy datasets are necessary to model the tail of the distribution.

To overcome this issue, Wald's theorem is used to evaluate an analytic formulation of the probability density function $f(q_\mu|\mu')$ [275]. The theorem states that for a sufficiently large dataset, the test statistics can be approximated by

$$-\ln \lambda(\mu) \simeq \frac{(\mu - \hat{\mu})^2}{\sigma^2} + \mathcal{O}(\frac{1}{\sqrt{N}}). \tag{9.13}$$

Here, μ is the signal strength under test, $\hat{\mu}$ its estimator, and the width σ corresponds to the standard deviation of μ which is obtained from the covariance matrix of $\mathcal{L}(\text{data}|\mu, \theta)$

$$V^{-1} = E\Big[\frac{\partial \ln \mathcal{L}}{\partial \theta_i \theta_j}\Big]. \tag{9.14}$$

Thus, the Wald theorem implies that for a large dataset, $\hat{\mu}$ follows a Gaussian distribution with a mean μ. In this approximation, the p-value can easily be computed as

$$p_0 = 1 - \Phi(\sqrt{q_0}) \tag{9.15}$$

with Φ the cumulative of the Gaussian distribution of $\hat{\mu}$. From this, the significance level of the measurement is extracted as $S = \sqrt{p_0}$. The LHC experiments have adopted a convention that a significance of 3σ is necessary to claim an observation of a process. When 5σ are exceeded, a discovery is announced. For smaller expected significances, the same approximation is used to set an upper limit on μ at a confidence level of $1 - \alpha$ as

$$\mu_{\text{up}} = \hat{\mu} + \sigma\Phi^{-1}(1 - \alpha). \tag{9.16}$$

This corresponds to claiming that the presence of a signal with a signal strength of μ_{up} or higher is excluded at a confidence level $1 - \alpha$.

To compute the expected significance of a signal, the so-called Asimov dataset is used. This dataset sets the values of s_i and b_i as expected from the SM and corresponds to evaluating the p-value of the probability density function $f(q_0|\mu = 1)$ by integrating from its median to infinity [276, 277].

Chapter 10

Results

This Chapter presents the results of the analysis in the $t\bar{t}H$, $H \to b\bar{b}$ channel, focusing on a search for events with a Higgs boson or a top quark with a large p_T, using the dataset collected by the CMS experiment in 2017. Section 10.1 verifies the object and event selections presented in the previous Chapter in a control region of the analysis. Several discrepancies found during this process related to b tagging are described and investigated in Section 10.2. The expected sensitivity of the resolved analysis is shown in Section 10.3. Section 10.4 presents an observed mismodelling in the MEM distribution and Section 10.5 finally presents the results of the search for $t\bar{t}H$, $H \to b\bar{b}$ events using the BLR and the average pseudorapidity between jets as discriminating variables.

10.1 Control region

To validate the object definitions, the event selection, and the application of event weights, event yields and distribution shapes for the jet and b-tagged jet multiplicities, the lepton and jet p_T, the MET and the number of primary vertices are compared between expectations from simulation and measured data. Results for the SL and the DL channel are shown in Figures 10.1 and 10.2 respectively, where in both cases events with at least four jets including at least two b-tagged ones are considered.

Generally a good agreement between data and simulation is observed in these distributions. Several variables however are less well modelled by simulation. For example, the number of primary vertices per event is underestimated. This disagreement is however expected as MC samples are produced ahead of the data collection period, such that the exact distribution is not known at production time. Additionally, the event yields at large jet multiplicities are underestimated in simulation. This

feature arises from a theoretical mismodelling of the parton shower. However, the mismodelling in bins of large numbers of b-tagged jets per event, where an excess of data is observed, was not expected. Investigations on this behaviour are presented in the following Section.

10.2 B tagging scale factors

Based on the disagreement in the b-tagged jet multiplicity in data and simulation shown in Figures 10.1 and 10.2, several issues involving the b tagging scale factors, which are applied to the analysis, were identified.

10.2.1 Data to simulation mismodelling

Although the effect is still within the systematic uncertainties in the SL channel, a significant excess of events with many b-tagged jets is observed in data in Figures 10.1 and 10.2 (top right). While the yields for events with exactly two b-tagged jets are similar in data and simulation, there are 20% more events with four b-tagged jets in data than in simulation in the SL channel. This disagreement arises from a combination of two distinct effects.

One issue involves an underestimation of the cross section of the $t\bar{t}$+$b\bar{b}$ background, which mostly affects bins with large b-tagged jet multiplicities in the distributions. This is because the background is dominated by the $t\bar{t}$+$b\bar{b}$ process for such events, while the largest background contribution for events with lower numbers of b-tagged jets are $t\bar{t}$+light events.

A second contributing factor is the application of b tagging scale factors, which are described in Section 9.3 and which are needed to correct for different b tagging efficiencies in data and simulation. Figure 10.3 shows the data to simulation agreement for semileptonic events without applying b tagging scale factors. Comparing with the result including b tagging scale factors in Figure 10.1, the agreement between data and simulation in the number of b-tagged jets is much improved, while the agreement in the jet multiplicity is mostly unaffected. Several aspects of the calculation of these scale factors have thus been investigated to understand these differences.

Firstly, the environments in which the analysis is performed and the one in which the scale factors are derived differ. While these are also measured in a phase space enriched in $t\bar{t}$+jets events, in this case only dileptonic events with exactly two b-tagged jets and no additional jets are considered. This selection is further referred to as the heavy flavour (HF) selection. Clearly, the environment in which the $t\bar{t}H$, $H\rightarrow b\bar{b}$ analysis is performed, in particular in the SL channel which is used here

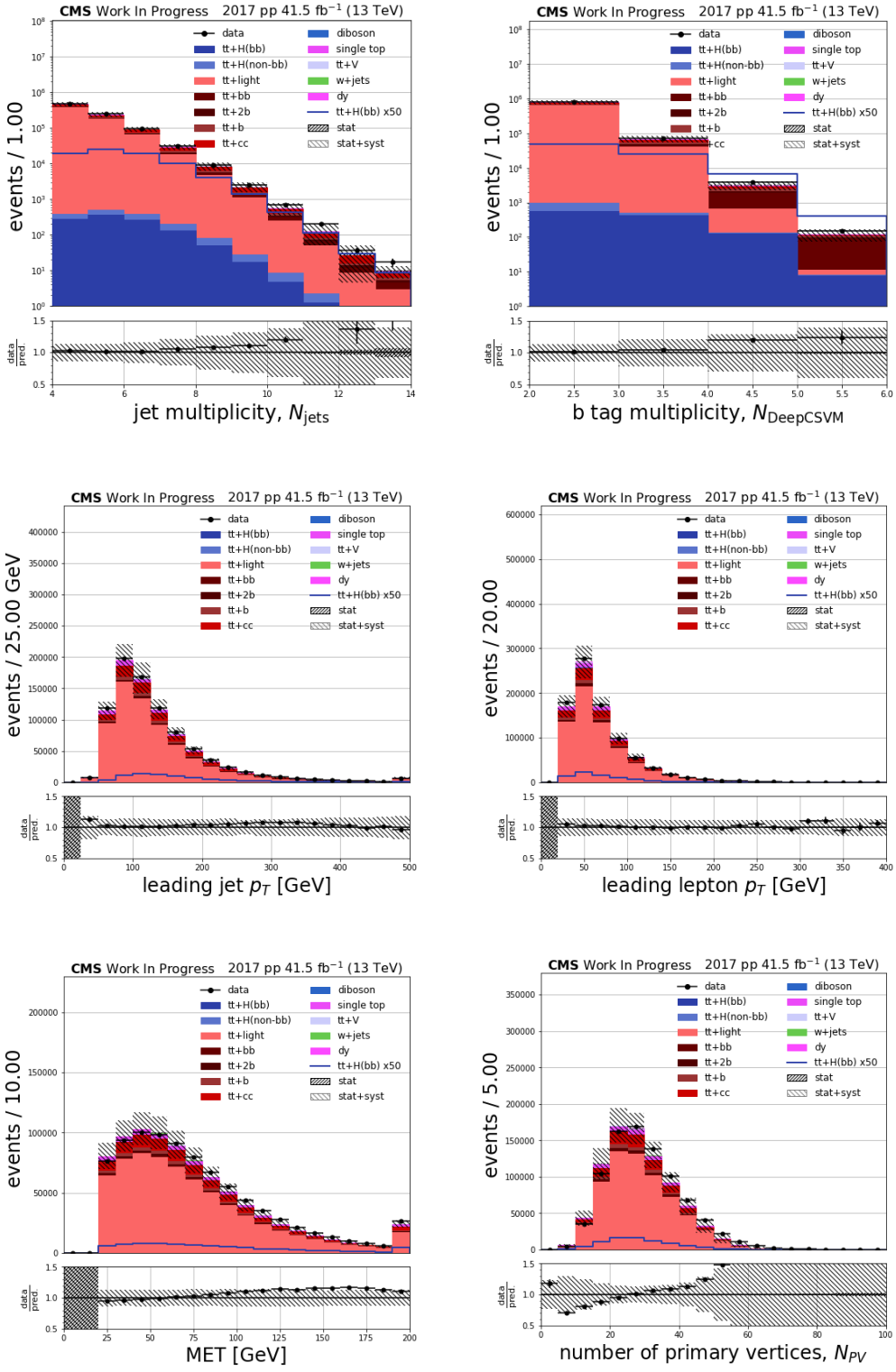

Figure 10.1: Comparison of event variable shapes between data and simulation for SL events with at least four jets, amongst which at least 2 must be b-tagged. The uncertainty band includes statistical and systematic uncertainties. Most variables present a good agreement.

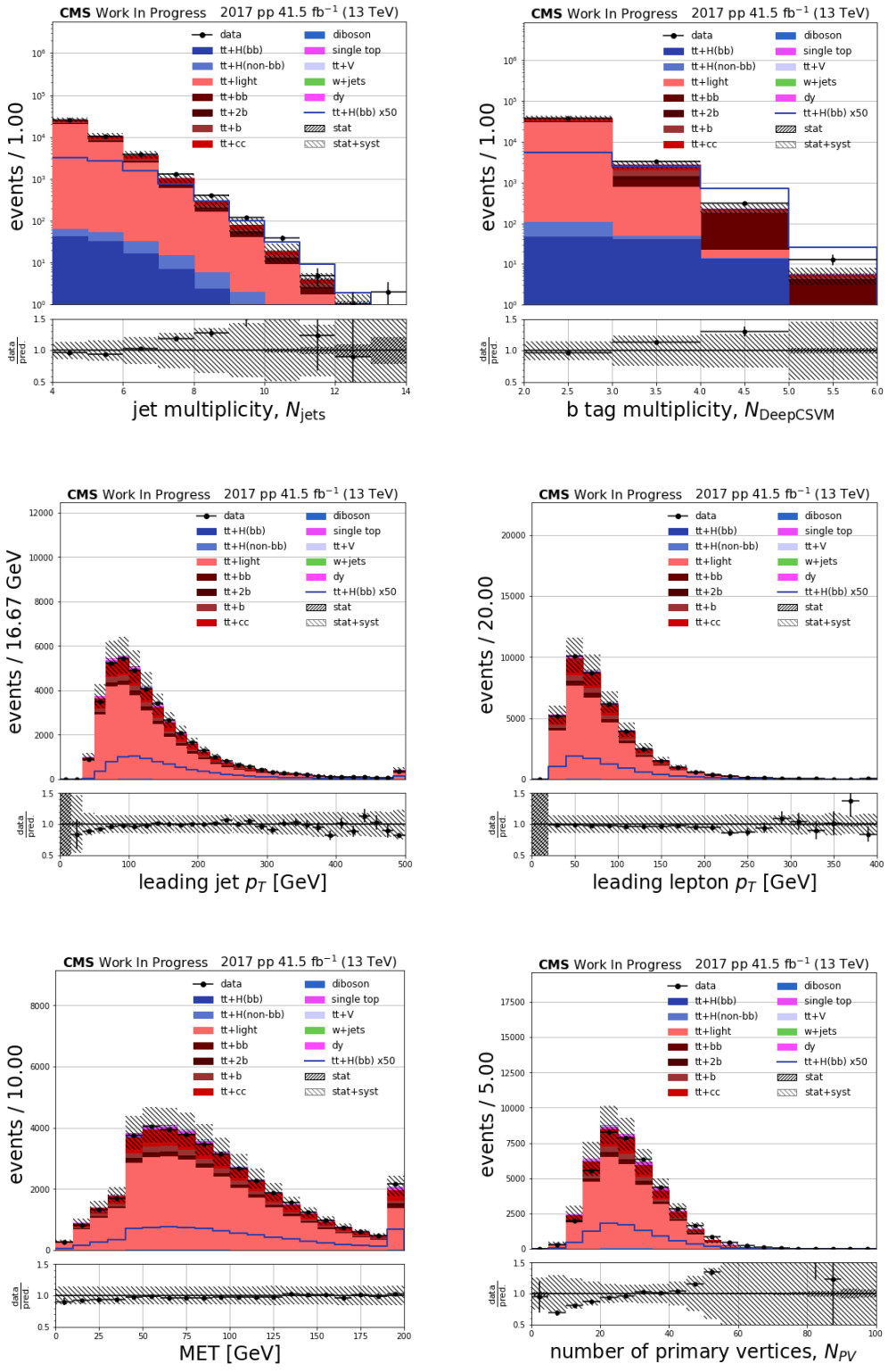

Figure 10.2: Comparison of event variable shapes between data and simulation for DL events with at least four jets, amongst which at least 2 must be b-tagged. The uncertainty band includes statistical and systematic uncertainties. Most variables present a good agreement and discrepancies are contained within the uncertainties.

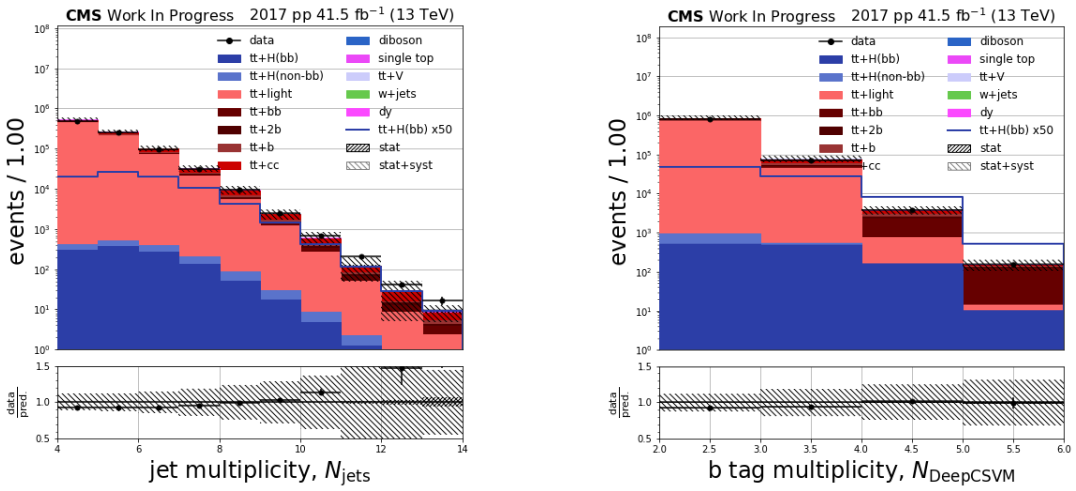

(a) Jet multiplicity

(b) B tagged jet multiplicity

Figure 10.3: Data to MC agreement in the jet (a) and b-tagged jet (b) multiplicities without applying b tagging scale factors. In this case, a much better modelling of the b tagged multiplicity is seen.

for comparison, has a larger number of reconstructed objects per solid angle. This is verified in Figure 10.4, which shows the number of additional jets (regardless of whether they satisfy the selection criteria in Section 9.2.2) within an angular distance of 0.8 to jets passing those selections. Results are presented as a function of the b-tagged jet multiplicity. This shows that on average 20% of jets in the HF environment have at least one additional jet in their vicinity, while this number is almost twice as large in the $t\bar{t}H$, $H\rightarrow b\bar{b}$ environment. This figure even increases in bins with larger numbers of b-tagged jets, reaching 60% for jets in events with at least five b-tagged jets.

The denser environment in the $t\bar{t}H$, $H\rightarrow b\bar{b}$ analysis impacts the reconstruction of the secondary vertex (SV) of jets originating from b quarks. To describe the performance of the SV reconstruction, the angular distance ΔR (vertex, jet) between the jet axis and the axis between the primary and the secondary vertex is calculated, where the SV leading to the smallest distance ΔR (vertex, jet) is used. Figure 10.5a proves that the angular distance is much lower for jets originating from bottom and charm quarks, which are expected to possess a secondary vertex, compared to jets originating from other types of quarks.

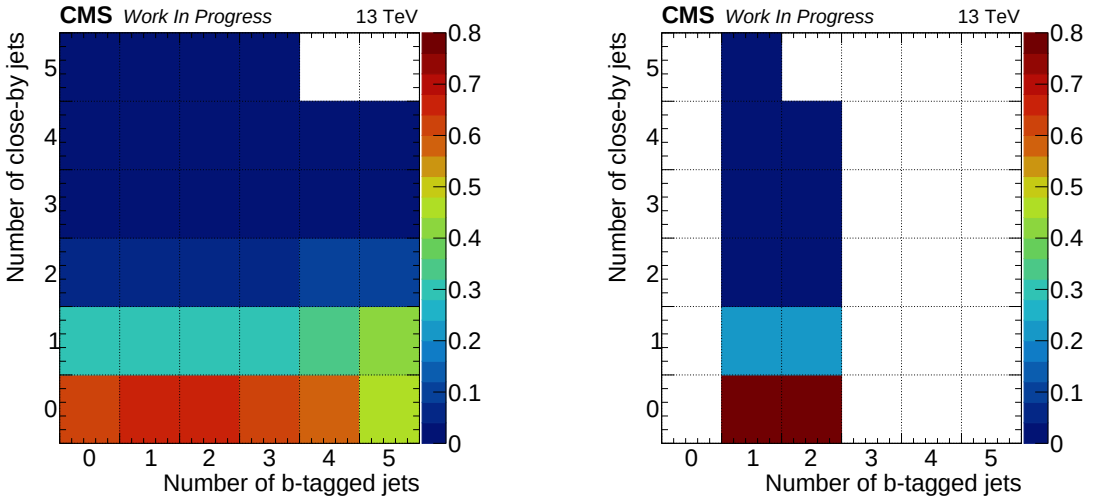

(a) $t\bar{t}H$, $H\to b\bar{b}$ (b) HF

Figure 10.4: Number of close-by jets (with $\Delta R = 0.8$) as a function of the number of b-tagged jets per event in the $t\bar{t}H$, $H\to b\bar{b}$ and the HF environments. Each column is normalised to unity. Additional jets are more likely found in the environment of analysis jets in the phase space targeted by the $t\bar{t}H$, $H\to b\bar{b}$ analysis.

The angular distance between the axis of b-flavoured jets and their closest SV is shown for the SL $t\bar{t}H$, $H\to b\bar{b}$ and the HF environments in Figure 10.5b. On average, this angular distance is smaller for b-flavoured jets in the HF environment. This is expected, as with additional jets close to the jet under consideration, the probability for additional tracks originating from a different particle interfering with the SV reconstruction increases. Similarly the angular distance between jet axis and vertex position slightly increases with the number of b-tagged jets in $t\bar{t}H$, $H\to b\bar{b}$ events as is shown in Figure 10.5c.

This behaviour is exemplified when studying the dependence of the average angular distance ΔR (vertex, jet) on the number of tracks associated to the secondary vertices shown in Figure 10.5d. Only tracks satisfying the criteria mentioned in Section 3.3.6 are considered. For b-flavoured jets, the angular distance constantly decreases with a larger number of tracks associated to the SVs, as this improves the vertex interpolation. Contrarily for c-flavoured jets, a decrease of ΔR (vertex, jet) is observed for low numbers of associated tracks, followed by a slight rise. This can be explained by the fact that the SV created by charm quarks typically have a lower number of tracks than those created by bottom quarks, so that SVs with a larger

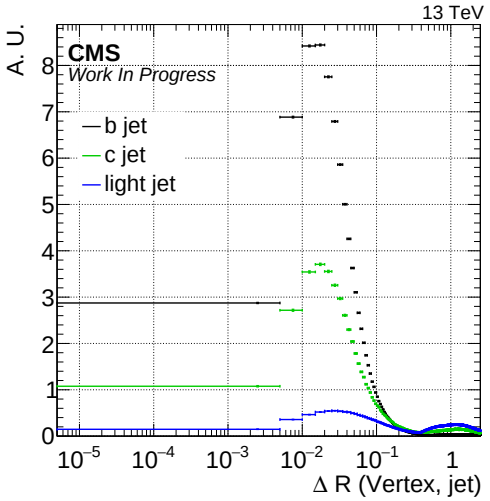

(a) Jet flavour

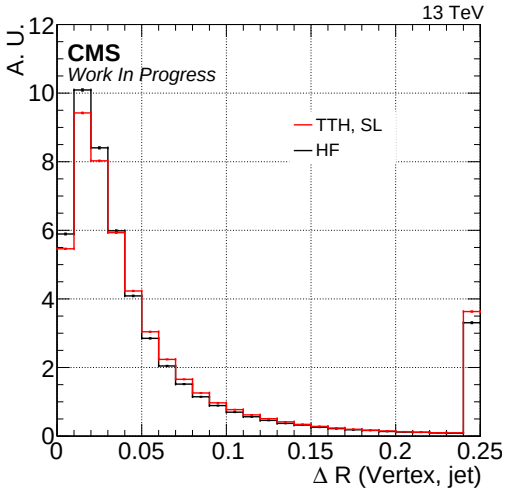

(b) Environment dependence

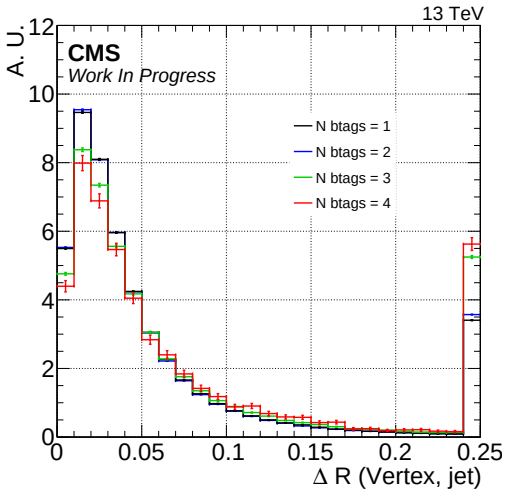

(c) B jet multiplicity dependence

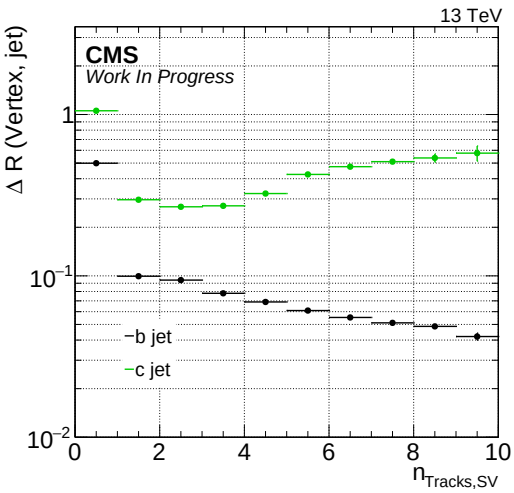

(d) N_{tracks} dependence

Figure 10.5: Alignment of the secondary vertex with the jet axis as a function of the jet hadron flavour (a), the phase space (b), the number of b-tagged jets in $t\bar{t}H$, $H\rightarrow b\bar{b}$ events (c) and the number of tracks associated to the SV (d). Generally, the alignment improves in less dense environments, and for well reconstructed b-flavoured jets.

number of associated tracks are more likely to originate from another particle, or to contain additional tracks from other particles. In both cases, this leads to a worse vertex reconstruction, and thus larger values of ΔR (vertex, jet).

Since the number of tracks associated to the SV is used to evaluate the b tagging score of a jet in the DeepCSV tagger, this quantity will have an effect on the b tagging efficiency. This is shown in Figure 10.6a, which shows the scale factor, defined as the ratio of the efficiency of correctly identified b-flavoured jets in data divided by that in simulation, as a function of the number of tracks of the jet's SV. This scale factor is evaluated in dileptonic $\mathrm{t\bar{t}}$ events, containing exactly two jets. To increase the purity of this selection in data, a tag-and-probe approach is used, applying selection criteria on the tag jets such as minimum b tagging discriminant score, without imposing selections on the probe jet on which the scale factor is evaluated. This scale factor is calculated for three different working points of the b tagging algorithm. Figure 10.6a shows that the scale factor varies considerably with the number of tracks associated to the SV, reaching values between 0.65 for jets without any properly reconstructed vertex tracks and 1 for jets with many well reconstructed tracks associated to the SV.

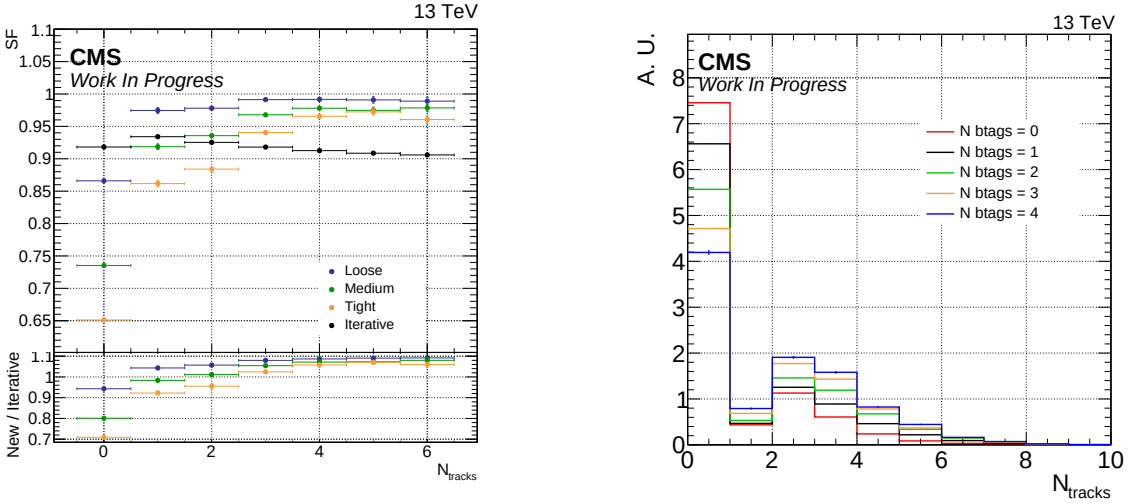

(a) Scale factor

(b) N_{track} vs. $N_{\mathrm{b\ jets}}$

Figure 10.6: Scale factor as a function of the number of tracks of its associated secondary vertex (a) and average number of tracks associated to the secondary vertex as a function of the number of b-tagged jets in the event (b).

For comparison, Figure 10.6a also shows for the same jets the scale factor which is used by default in black. Clearly, these have only a very minor dependency on

the number of tracks associated to the SV, thus being in disagreement with the scale factors computed specifically as a function of this variable. Figure 10.6b shows the average number of tracks associated per SV as a function of the number of b-tagged jets in $t\bar{t}H$, $H\to b\bar{b}$ events. As expected the average number of tracks increases with additional b-tagged jets. Therefore the more b-tagged jets the event possesses, the more the b tagging SF will be underestimated, as in the region with larger numbers of tracks, the scale factor used in the analysis is 5-10% lower than expected from this study.

Given the time scale of this analysis, it was not possible to use these conclusions concretely to correct for the mismodelling observed in Figures 10.1 and 10.2, and to study its correlation with the theoretical uncertainties in the modelling of the $t\bar{t}+b\bar{b}$ background, which also affect the data to simulation agreement. It is expected that the mismodelling will not significantly impact the results of the analysis as it is mostly contained within the systematic uncertainties affecting the distributions. Furthermore the normalisation of the $t\bar{t}$+HF background is left freely floating which also compensates for this mismodelling.

10.2.2 Shape distortions

Additionally, it was observed that distributions which are independent of b tagging, such as the jet p_T, are distorted when applying b tagging scale factors. In order to correct for this effect, a correction factor is derived from simulation along the lines of the procedure in [278]. This correction factor depends on the number of jets and the H_T of the event, and is derived for events passing all selection criteria of the main analysis except of the requirement on the b-tagged jet multiplicity. It is then calculated as the ratio of the weighted number of events after and before applying b tagging scale factors. Separate correction factors are evaluated for the SL and DL channels, and for the $t\bar{t}H$, $H\to b\bar{b}$, the $t\bar{t}$+B (combining the $t\bar{t}+b\bar{b}$, $t\bar{t}$+b and $t\bar{t}$+2b backgrounds), the $t\bar{t}+c\bar{c}$ and the $t\bar{t}$+LF processes. The latter ones are also used for all other minor backgrounds of the analysis. Figures 10.7 and 10.8 show the correction factors in each of these channels and processes. All values lie between 0.8 and 1.5.

Figure 10.9 verifies the validity of these correction factors in the SL $t\bar{t}H$, $H\to b\bar{b}$ selection. As expected, these do not affect the shape of the b tagging score distribution after applying the b tagging scale factors. However, it can be seen that the H_T, the jet multiplicity and the jet p_T distributions are restored to their shape before application of the scale factors. These correction factors are thus applied in all analysis categories and are already included in Figures 10.1 and 10.2.

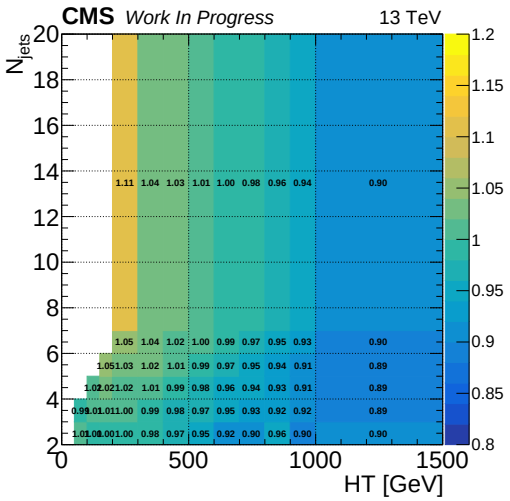

(a) SL - $t\bar{t}H$, $H \to b\bar{b}$

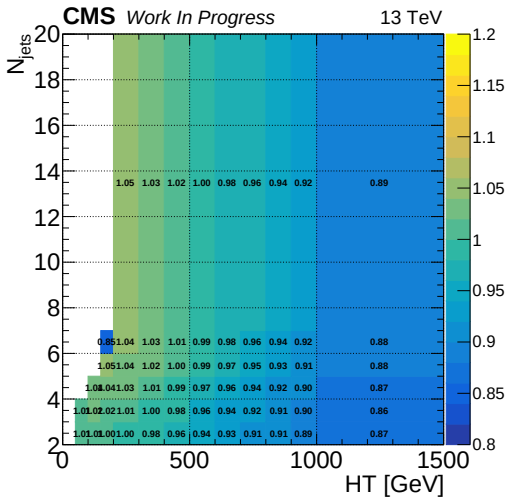

(b) SL - $t\bar{t}+b\bar{b}$

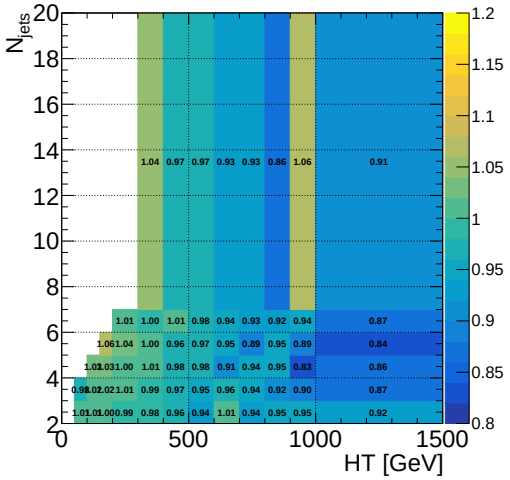

(c) SL - $t\bar{t}+c\bar{c}$

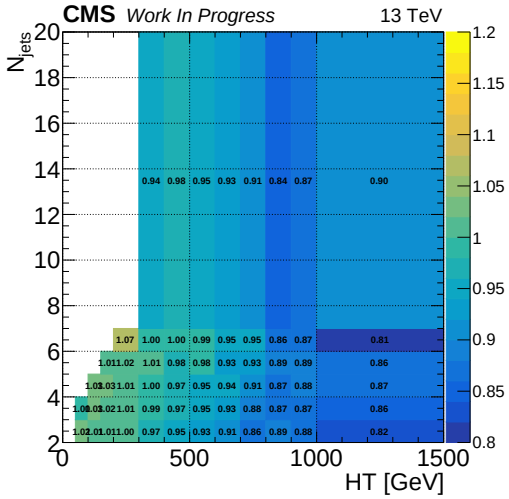

(d) SL - $t\bar{t}$+light

Figure 10.7: B tagging correction factors rectifying the shape distortions appearing when applying b tagging scale factors in the SL channel.

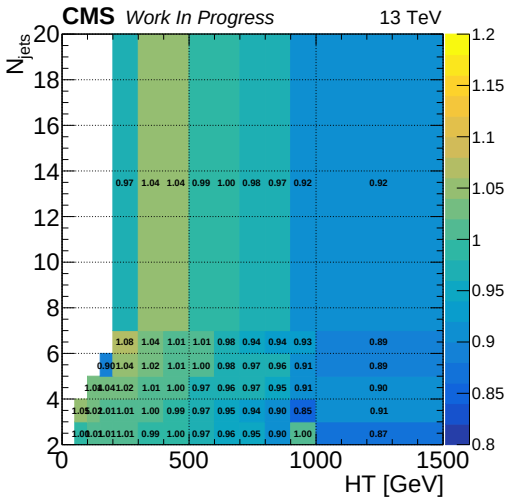

(a) DL - $t\bar{t}H$, $H \to b\bar{b}$

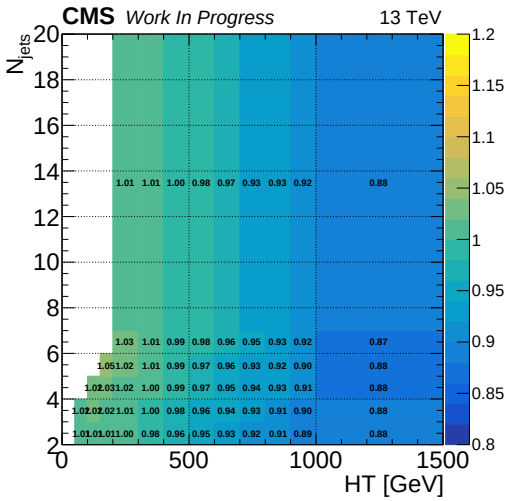

(b) DL - $t\bar{t}+b\bar{b}$

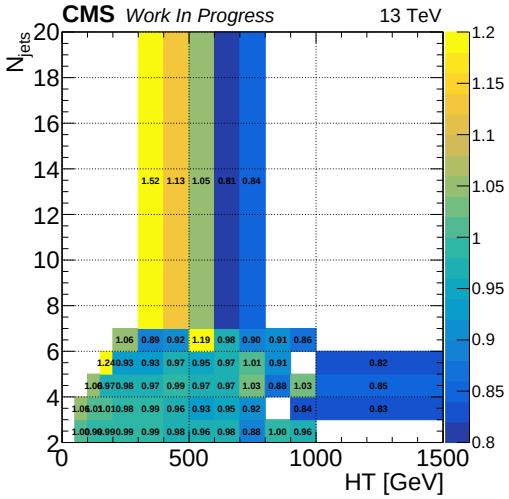

(c) DL - $t\bar{t}+c\bar{c}$

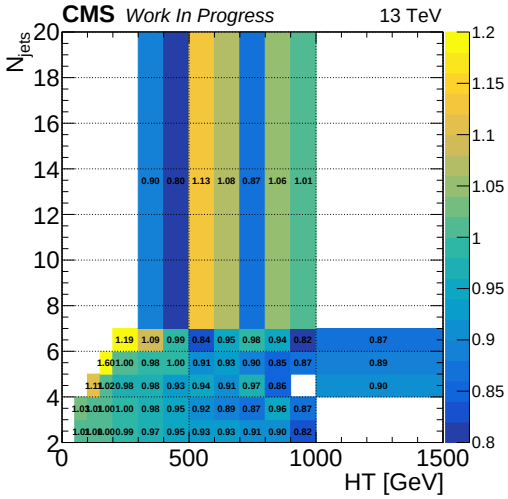

(d) DL - $t\bar{t}$+light

Figure 10.8: B tagging correction factors rectifying the shape distortions appearing when applying b tagging scale factors in the DL channel.

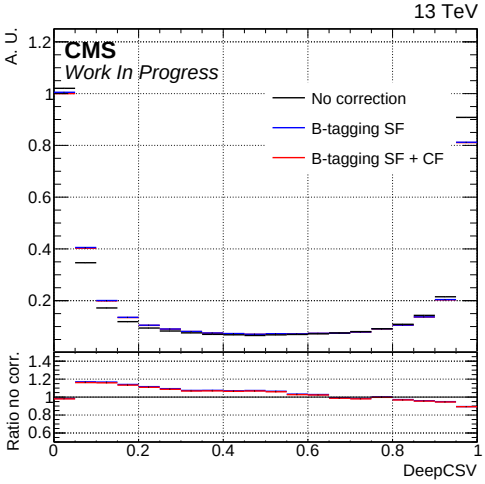

(a) b tagging discriminant

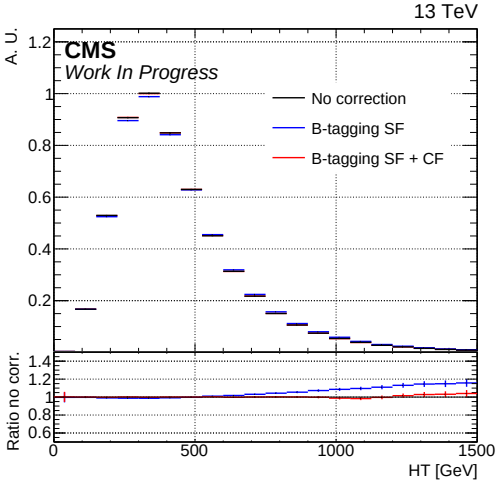

(b) H_T

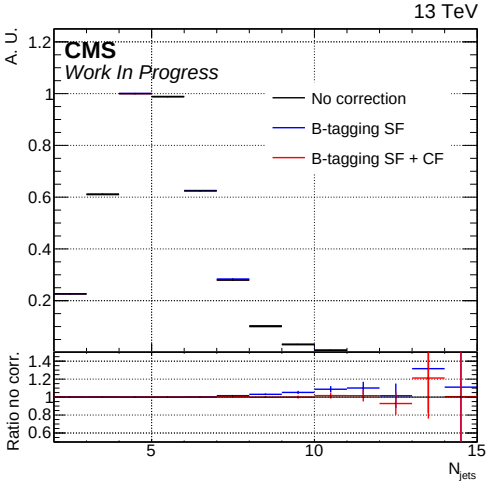

(c) Jet multiplicity

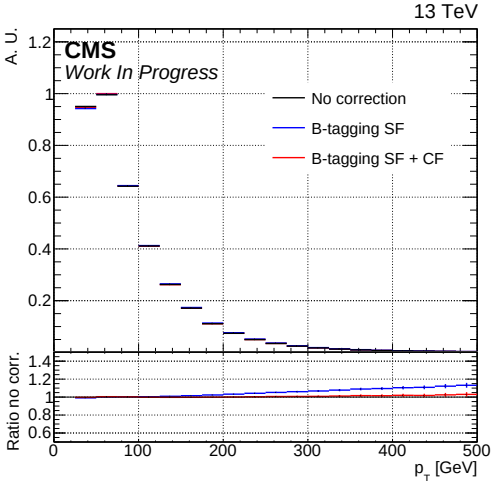

(d) Jet p_T

Figure 10.9: Effect of the b tagging correction factors on the jet b tagging score (a), the event H_T (b), the number of jets per event (c), and the jet p_T (d). While the correction factors leave the b tagging score distribution unchanged, they restore all other distributions to their shape before applying b tagging scale factors.

10.3 Expected performance of the boosted selection

Using an Asimov dataset which is defined in Section 9.6, the expected performance of the analysis in the boosted phase space using the MEM discriminant is presented.

10.3.1 MEM performance for boosted events

In a first step, the performance of the MEM for events with a boosted candidate, which is denoted the boosted MEM and described in Section 9.5, is evaluated. This is motivated by the assumption that when the top quark or the Higgs boson are produced at large p_T and their decay products are very collimated, they are easier to reconstruct when using dedicated substructure methods than with standard jet algorithms. Thus if these methods allow a better measurement of each jet's kinematics, the accuracy of the MEM would improve. The performance of the boosted MEM is expected to differ from that of the MEM in resolved categories as the input lists of jets are different. While it consists of AK4 jets in the resolved case, it is a mixture of such jets and of subjets in the boosted case.

Figure 10.10a compares the performance of the resolved and the boosted MEM. Separate curves are shown for events which only fulfil the resolved event selection (in solid black), events for which both variants of the MEM can be calculated (in dashed black when the resolved MEM is calculated and in dashed red when the boosted MEM is used), and for events only passing the boosted event selection (in solid red). The performance of the boosted MEM variant with fixed permutations is also shown in solid orange (for events which do not fulfil the resolved event selection) and in dashed orange (for events where this is the case).

This Figure shows that the resolved MEM performance always exceeds that of the boosted MEM. For events which fulfil the selection criteria of the resolved and the boosted analysis, the discriminator performance degrades from an area under the ROC curve of 0.29 using the resolved MEM to 0.34 with the boosted MEM. For events which only pass the boosted event selections, an area under the ROC curve of 0.42 is achieved. A further loss in performance is observed when fixing the permutation of the subjets obtained from a top quark or a Higgs boson candidate in the MEM calculation. This can be explained when considering the definition of the MEM in Section 8.3.1. As the total probability consists of a sum of the probabilities of all permutations, the total probability can only be lower when removing some cases. If the correct permutation is amongst those conserved, the performance will be similar since the correct permutation has a considerably larger probability than the

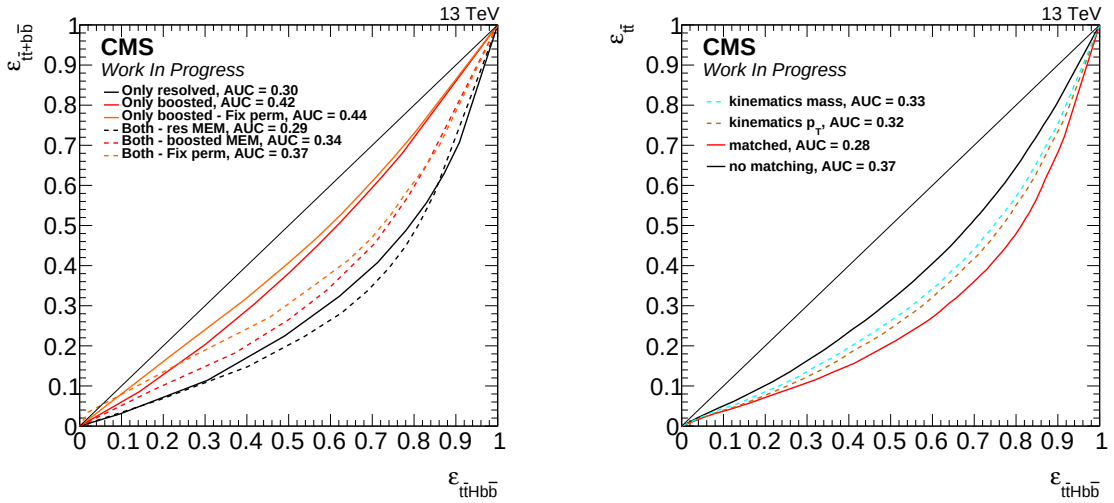

(a) All events (b) Events with boosted top quark

Figure 10.10: ROC curves describing the performance of the MEM. On the left, its performance in the resolved and the boosted case is compared. On the right, the impact of quark and kinematic matching on the MEM performance for events with a boosted top quark candidate is evaluated. The performance is quantified with the area under the curve (AUC), for which smaller values indicate better separation power.

other ones, thus dominating the total probability. If however the assignment of the subjets to the quarks is wrong, the correct permutation might be discarded, and thus considerably lowering the MEM performance. This is why the global performance of the MEM is lower in this case, and this strategy will not be used to extract the results of the boosted analysis.

The loss of performance of the boosted MEM calculated using all possible permutations can be explained when investigating the reconstruction of the boosted objects. Figure 10.11 shows the top quark and Higgs boson p_T and mass at generator level, as reconstructed by two (for the Higgs boson) or three (for the top quark) AK4 jets and the one of the boosted candidates. While the mass distributions of the top quark and the Higgs boson candidates are closer to the generator level mass for both objects, the p_T distributions are distorted. These are well modelled when reconstructing the objects with AK4 jets, however the boosted candidates shift the distributions towards larger transverse momenta.

A second aspect which explains the performance loss are higher failure rates in

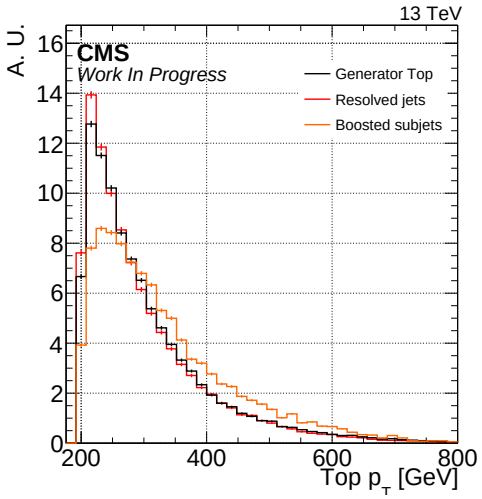

(a) Top candidate p_T

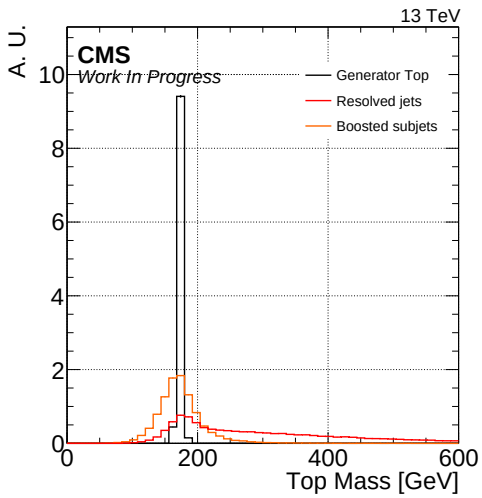

(b) Top candidate mass

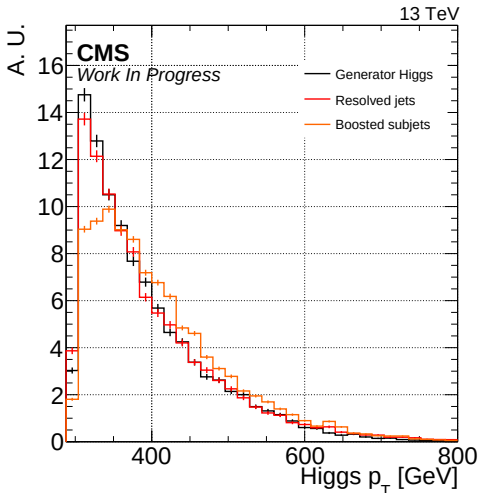

(c) Higgs candidate p_T

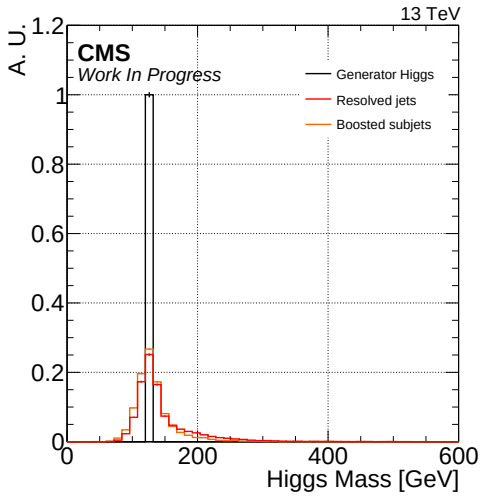

(d) Higgs candidate mass

Figure 10.11: Comparison of the kinematics of the top quark (a,b) and the Higgs boson (c,d) as reconstructed from AK4 jets or subjets with the generator level quantities. While boosted objects improve the mass resolution with respect to resolved jets, they distort the p_T spectrum.

	Higgs [%]	Hadronic top [%]	Leptonic top [%]	Full event [%]
Resolved	81	38	94	28
Boosted - only Higgs	26	25	87	6
Boosted - only Top quark	62	18	84	11
Boosted - both candidates	19	24	89	6

Table 10.1: Matching fractions of jets and subjets to quarks in the resolved and the boosted analysis. A considerable drop is observed when boosted objects are used.

correctly associating subjets to quarks with respect to the resolved case, as illustrated in Table 10.1. This Table shows the matching fractions of all final state particles in the $t\bar{t}H$, $H\rightarrow b\bar{b}$ analysis (Higgs boson, hadronically and leptonically decaying top quarks) for resolved events and for events with either a boosted Higgs boson candidate, a boosted top quark candidate or both. A particle is considered matched if all of the quarks in which it decays are within an angular distance of 0.3 to either AK4 jets (in the resolved analysis, for the leptonically decaying top quark, and for the hadronically decaying one or the Higgs boson when the object wasn't reconstructed using boosted methods), or to Higgs boson or top quark candidate subjets. It is observed that the matching fractions considerably drop when including either of the two boosted candidates in the analysis. For example the matching fraction drops from 81% in the resolved case to 26% when reconstructing the Higgs boson with a boosted candidate, and further deteriorates to 19% when the event also has a boosted top quark candidate. This indicates that in many cases, the substructure algorithms do not correctly identify the Higgs boson or the top quarks, and sometimes a top quark is mistakenly considered as a Higgs boson candidate, and the other way around.

Figure 10.10b investigates the impact of these two aspects on the boosted MEM performance for events which contain a top quark candidate. Separate curves are shown for events where the top quark candidate's subjets are matched to the generator level quarks (meaning that their respective angular distance is below 0.3), and where either the top quark candidate's p_T or its mass is within 20 GeV of that of the generated top quark. Clearly, these conditions are not independent of each other, as the kinematics are usually close to the generator level ones when the correct subjets have been identified.

When only the p_T or the mass of the top quark candidate is well reconstructed but the subjet matching is incomplete, a performance increase of 8% is achieved. If instead all three subjets are matched to the generated quarks, an area under the ROC curve of 0.28 is achieved, which even surpasses the performance of the resolved MEM. It can be concluded that both criteria impact the MEM performance, and in particular

when the subjets are matched to the generator level quarks, the performance of the resolved MEM is recovered.

These observations indicate that the algorithms chosen to identify high p_T top quarks or Higgs boson candidates have a limited efficiency and often miss the correct object. Especially when they mistakenly identify another final state object, this affects the performance of the MEM considerably. These conclusions motivate why events which satisfy both the resolved and the boosted selection criteria are treated using the resolved strategy.

10.3.2 Expected sensitivity of the boosted analysis

To verify the validity of the analysis and to evaluate its expected sensitivity, an Asimov dataset is used as described in Section 9.6. This pseudo-dataset can be built from simulation either assuming the presence of a signal according to SM expectations ($\mu = 1$) or assuming no presence of signal ($\mu = 0$).

In a first step, the so-called pulls and constraints of the fit on the nuisance parameters are studied in Figure 10.12. These pulls and constraints correspond to the mean and the width of the distribution $(\hat{\theta} - \theta_0)/\Delta\theta$ where θ_0 represents the values of the nuisance parameters before the fit, and $\Delta\theta$ is the uncertainty on the prefit nuisance parameter. The presence of large pulls would indicate a wrong modelling of the uncertainties, while large under- or over-constraints arise from an unreasonable uncertainty assigned to the nuisance parameter. By definition, no pulls are expected to appear in either the signal+background or the background model fit on the $\mu = 0$ dataset and the size of the constraints should be comparable, which is verified in Figure 10.12a. Similarly, it is verified in Figure 10.12b that the signal+background fit on the $\mu = 1$ dataset exerts no pulls on the nuisances. Small positive and negative pulls of less than 0.2 are however observed in particular for some of the JEC uncertainties for the background-only fit of this dataset. These arise from differences in the background-only model and the signal+background dataset. For both datasets, the maximum constraints are of the order of 50% and occur for nuisance parameters related to b tagging, implying that the prior uncertainties are rather large on these nuisances.

Table 10.2 gives the best-fit values and the expected significance in the resolved and boosted analysis categories evaluated on an Asimov dataset. Given the larger statistics in the SL channel, the channel drives the overall sensitivity of the resolved analysis, for which a significance of 2.11 is expected. As expected from the low performance of the MEM in the boosted categories, these have no major impact on the analysis sensitivity. As can be seen from the expected signal strength, the analysis

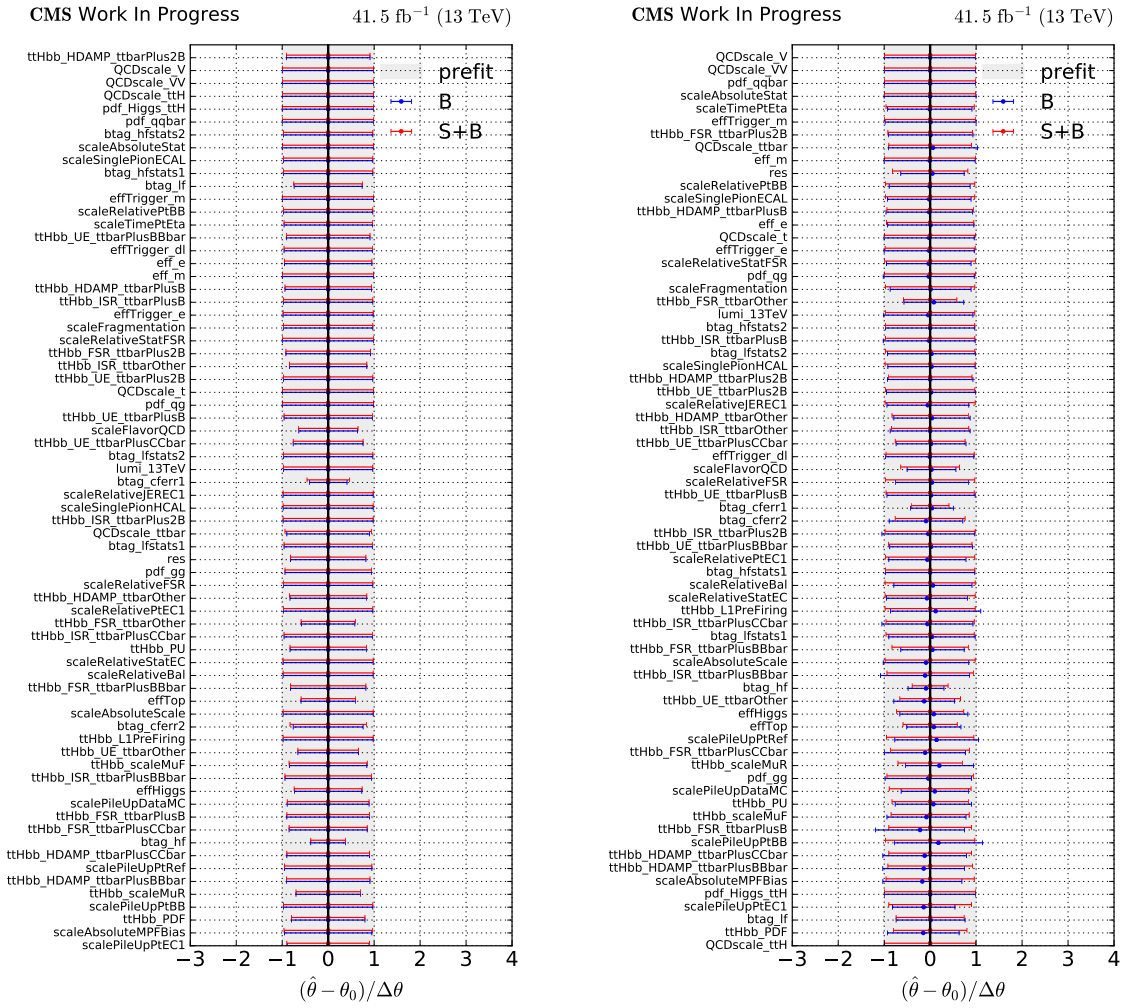

(a) $\mu = 0$ (b) $\mu = 1$

Figure 10.12: Pulls and constraints on the nuisance parameters evaluated for the signal+background model (red) and the background model only (blue) for the $\mu = 0$ (a) and the $\mu = 1$ (b) Asimov datasets for the boosted analysis. The nuisances specific to the boosted analysis are only mildly constrained.

is dominated by systematic uncertainties.

While the sensitivity of the boosted analysis is not significantly improved with respect to the resolved analysis, the computation time can be drastically reduced when using these methods, as is shown in Table 10.3. This is because reconstructing boosted

	$\hat{\mu}\pm$ tot ($\pm$ stat $\pm$ syst)	Significance
SL resolved	$1^{+0.58}_{-0.55}\left(\begin{smallmatrix}+0.28 & +0.51\\ -0.27 & -0.48\end{smallmatrix}\right)$	1.80
DL resolved	$1^{+1.11}_{-1.98}\left(\begin{smallmatrix}+0.64 & +0.91\\ -0.60 & -0.77\end{smallmatrix}\right)$	1.02
SL + DL resolved	$1^{+0.51}_{-0.48}\left(\begin{smallmatrix}+0.25 & +0.45\\ -0.25 & -0.40\end{smallmatrix}\right)$	2.11
SL boosted	1^{+9}_{-11}	0.06
SL + DL boosted	1^{+9}_{-11}	0.07
SL + DL resolved + boosted	$1^{+0.51}_{-0.47}\left(\begin{smallmatrix}+0.25 & +0.44\\ -0.25 & -0.40\end{smallmatrix}\right)$	2.15

Table 10.2: Best-fit values $\hat{\mu}$ and expected significance in the SL and DL categories and for the combined fit in the resolved and boosted analysis categories using an Asimov dataset. A expected significance of 2.15 is expected in the combined analysis.

objects allows to remove permutations in the MEM computation, either because jets originating from ISR or FSR can be identified and removed from the analysis (such as in the SL-$2_l2_h2_t$-sj hypothesis), or by directly removing wrong permutations.

10.4 Mismodelling of the MEM distribution

During the unblinding procedure, a large mismodelling of the MEM discriminant has been observed. Especially in the most signal sensitive analysis categories, a sizeable excess of data is observed at large MEM values above 0.85, close to where the $t\bar{t}H$, $H\to b\bar{b}$ signal is expected, as can be seen in Figure 10.13.

This disagreement has been traced back to the integration strategy of the MEM probability itself, and in particular to the treatment of the jet energy corrections described in Section 8.3.1. Figure 10.14a shows the shape of the MEM distribution for SL events in data when computing the MEM as a scalar integral, and when using a vector containing 26 times the same value than in the scalar case, as described in Section 8.3.1. Naively a similar output is expected in both cases. However the shape between both cases differs significantly in the region of high MEM values, where a disagreement of up to 20% is observed, which is precisely where the large discrepancy between data and simulation is detected. Figure 10.14b compares the ratio between the vector and the scalar case to the statistical uncertainty on the scalar integration, which is computed using Poissonian errors and error propagation. Clearly, the difference between the distributions is not covered by this uncertainty which points

Analysis category	Total time [s]	$t\bar{t}H$, $H\to b\bar{b}$ hypothesis [s]	$t\bar{t}+b\bar{b}$ hypothesis [s]
SL-$2_l2_h2_t$	49.9 ± 33.78	18.15 ± 13.12	32.48 ± 22.68
SL-$1_l2_h2_t$	45.54 ± 13.1	16.08 ± 4.94	29.49 ± 8.53
SL-$0_l2_h2_t$	145.26 ± 32.41	55.24 ± 16.4	103.83 ± 27.21
DL-2_h2_t	105.16 ± 28.18	36.52 ± 10.96	69.52 ± 19.28
SL-$2_l2_h2_t$-sj	23.99 ± 10.34	8.51 ± 3.94	15.5 ± 6.75
SL-$1_l2_h2_t$-sj	44.32 ± 12.71	15.88 ± 5.04	28.56 ± 8.83
SL-$0_l2_h2_t$-sj	143.47 ± 32.96	53.84 ± 15.98	99.57 ± 26.62
DL-2_h2_t-sj	102.67 ± 28.35	35.79 ± 10.94	67.71 ± 19.38
SL-2_l2_h2t-sj-fix$_{\text{top}}$	6.01 ± 1.77	2.18 ± 0.68	3.83 ± 1.14
SL-$0_l2_h2_t$-sj-fix$_{\text{higgs}}$	6.57 ± 5.87	2.52 ± 2.34	4.05 ± 3.66
SL-$2_l2_h2_t$-sj-fix$_{\text{top, higgs}}$	2.0 ± 0.66	0.75 ± 0.24	1.25 ± 0.47
SL-$1_l2_h2_t$-sj-fix$_{\text{higgs}}$	7.48 ± 2.67	2.81 ± 0.91	4.66 ± 1.96
SL-$0_l2_h2_t$-sj-fix$_{\text{higgs}}$	25.99 ± 8.92	9.64 ± 2.95	16.35 ± 6.71
DL-2_h2_t-sj-fix$_{\text{higgs}}$	17.6 ± 5.83	6.33 ± 1.96	11.27 ± 4.22

Table 10.3: Computation times of the MEM discriminant in the different analysis categories. The total time is given, as well as the individual times for the signal $t\bar{t}H$, $H\to b\bar{b}$ and the background $t\bar{t}+b\bar{b}$ MEM hypothesis. Using substructure methods reduces the computation time, especially when removing permutations.

to a deeper problem in the integration, as different numerical implementations of the integral should not have such a strong impact on the shape.

Given that no explanation for this unexpected behaviour has been found yet, no signal extraction using the MEM distribution is presented. Instead it will be performed using an alternative set of discriminants.

10.5 Signal extraction

The signal is extracted using the BLR distribution in all resolved analysis categories, and the average η between jets in the boosted categories. This variable is shown in Figure 10.15 in the SL and DL control regions with at least four jets amongst which two must be b-tagged. The agreement between data and simulation is within uncertainties. Given the lower discrimination power of these variables, in particular in distinguishing the $t\bar{t}H$, $H\to b\bar{b}$ signal from the $t\bar{t}+b\bar{b}$ background, a worse sensitivity is expected than with the MEM approach.

A combined fit is performed on all resolved and boosted analysis categories simultaneously to extract the signal strength from data. In a first step, the validity of the

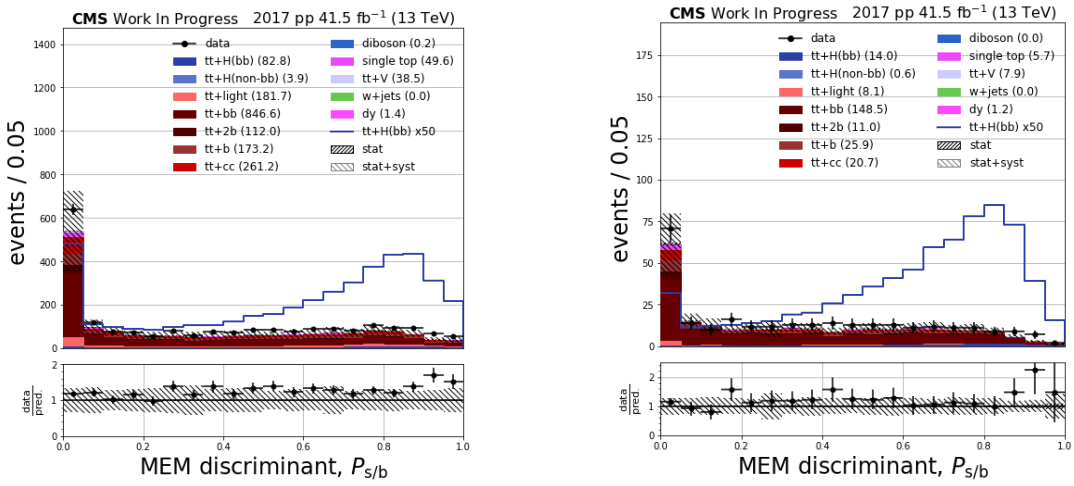

(a) SL (b) DL

Figure 10.13: MEM distribution in the SL, $\geq$ 6 jets, $\geq$ 4 b-tagged jets (a) and DL, $\geq$ 4 jets, $\geq$ 4 b-tagged jets (b) categories. A large excess of events in data at large MEM values is observed.

fit is controlled by evaluating the pulls and constraints on the nuisance parameters by the fit, which are presented in Figure 10.16. The nuisance parameters with the largest constraints are related to the b tagging and jet energy correction uncertainties and are constrained by up to 50% of the prior value. This is expected because events are selected in different jet and b-tagged jet multiplicities, such that differences in the reconstruction of these jets in the analysis categories will impact the performance of the fit. Additionally, while the fitted value for most nuisance parameters is within 1σ of the expected value, two nuisance parameters describing the uncertainty on the effect of initial state radiation and on the factorisation scale are set to around -1.5.

The freely floating rate parameters for the $t\bar{t}$+B and $t\bar{t}$+$c\bar{c}$ normalisations are optimized by the fit to $1.23^{+0.22}_{-0.22}$ and $1.1^{+0.4}_{-0.5}$ respectively. These parameters are above unity, because as expected, they compensate for the mismodelling originating from the b tagging scale factors, which led to an excess of data in the analysis categories.

This is verified in Figures 10.17 (SL, $\geq$ 4 b-tagged jets), 10.18 (SL, = 3 b-tagged jets) and 10.19 (DL + boosted category), which show the prefit and postfit distributions in all analysis categories. These prove that indeed, the excess of data which is present predominantly in the categories with four b-tagged jets is completely re-

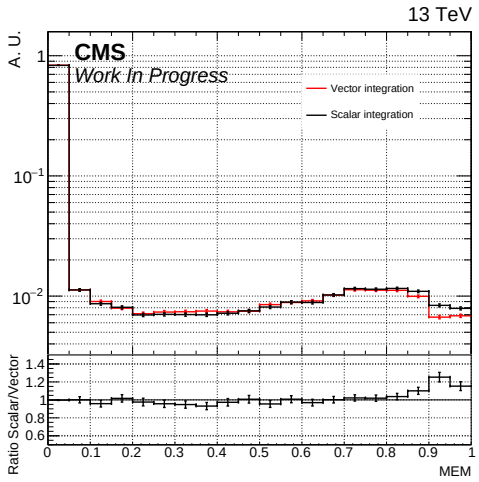

(a) MEM distribution shape

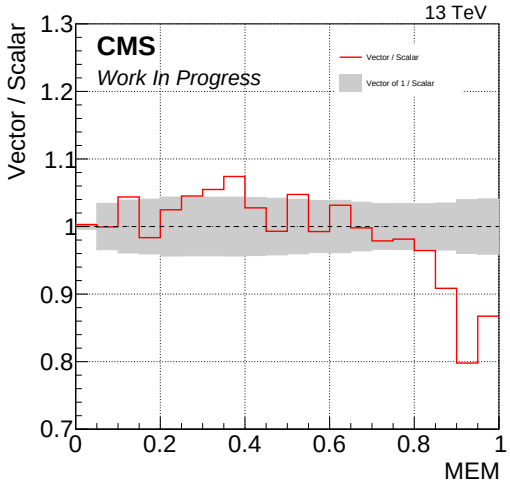

(b) Comparison with statistical uncertainty

Figure 10.14: Comparison of the shape of the MEM distribution for all events in the SL category for the vector and the scalar integration method (a) and comparison of their ratio with the statistical uncertainty on the shape (b). The choice of the integration method strongly affects the high-MEM region.

solved in the postfit distributions, leading to a good agreement between data and simulation in those distributions. Additionally the uncertainties are smaller in those distributions as expected from the constrained nuisance parameters.

Table 10.4 lists the best-fit values for the signal strength parameter $\hat{\mu}$ and the observed significance. When combining all resolved analysis categories, a best-fit μ of $3.82^{+3.78}_{-4.48}$ is found, corresponding to a significance of 0.84. When additionally combining with the boosted selection, a best-fit value $\hat{\mu}$ of $0.47^{+3.34}_{-3.41}$, and a significance of 0.14 are observed. Therefore, there is an underfluctation of signal events in the boosted phase-space region. Nonetheless all values in all presented analysis categories are compatible with each other within uncertainties and with SM expectations.

The impact of each nuisance parameter on the signal strength is shown in Figure 10.20. These are obtained by evaluating the shift of the best-fit μ after varying each nuisance parameter one by one by one standard deviation up and down around its postfit value. The nuisance parameters which most strongly impact $\hat{\mu}$ are the background normalisation parameters, which is expected given the poor separation of the chosen discriminators between the signal and the $\mathrm{t\bar{t}}$+jets backgrounds.

The effect of the nuisances on the uncertainty on the signal strength are studied

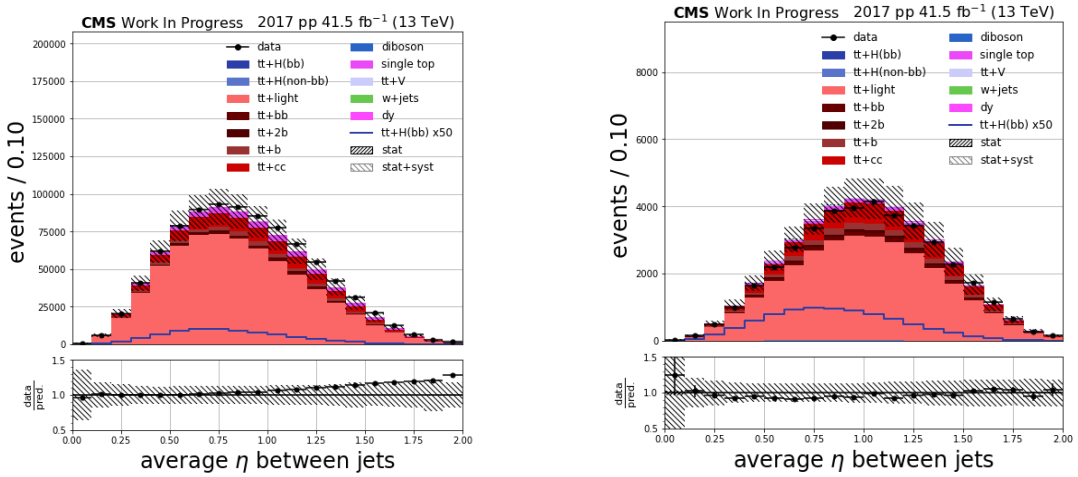

(a) SL (b) DL

Figure 10.15: Distribution of the average η between jets in the SL, ≥ 4 jets, ≥ 2 b-tagged jets (a) and DL, ≥ 4 jets, ≥ 2 b-tagged jets (b) control regions. The data to simulation ratio agrees within uncertainties.

as well. This is performed for groups of nuisance parameters separately by evaluating the difference of the uncertainty on the signal strength between the fit involving all nuisances and a similar fit performed while freezing all nuisance parameters except the ones of interest, assuming that all nuisances are uncorrelated. Results for this test are given in Table 10.5. The uncertainty on the signal strength parameter is dominated by systematic uncertainties, to which the theoretical uncertainties contribute most. However the individual uncertainties in the theory and experimental groups cannot be added in quadrature, as there in fact exist correlations amongst them, which is shown in Figure 10.21 such that the assumption does not fully hold. This is the case for instance between the b tagging and the background normalisation uncertainties. Additionally the uncertainty on the $\mathrm{t\bar{t}}$+B background normalisation strongly anticorrelates with the signal strength with $\rho = -0.7$. This is expected given that this process is the main background to the analysis.

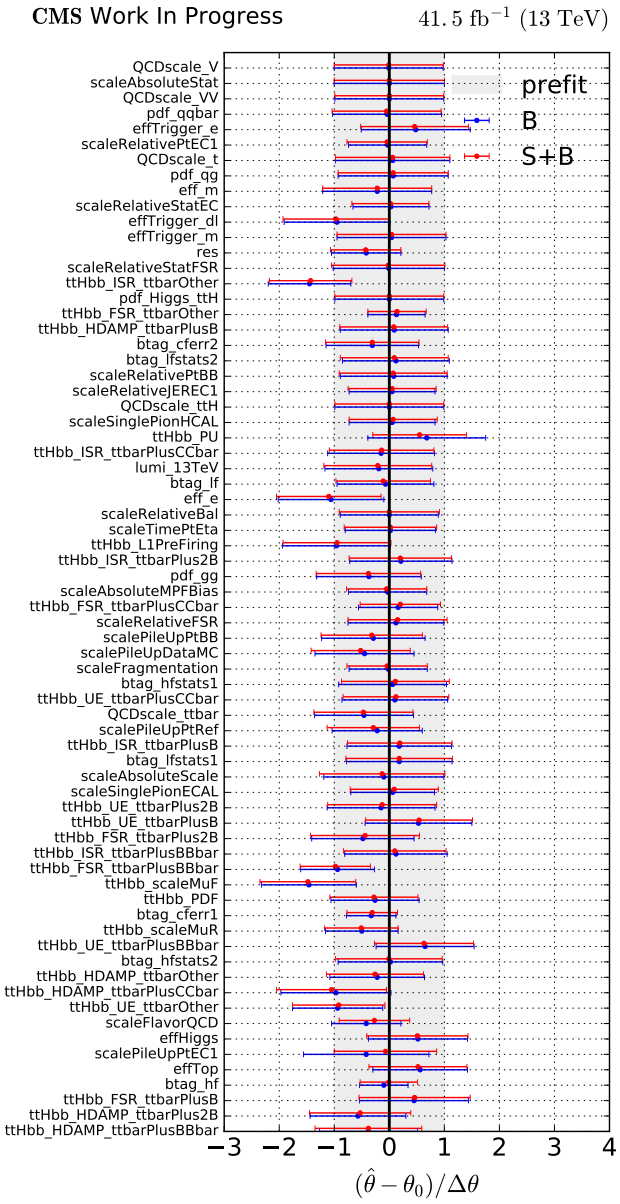

Figure 10.16: Pulls and constraints on the nuisance parameters evaluated for the signal+background model (red) and the background model only (blue) fit. The largest constraints are of the order of 50%, and most best-fit values for the nuisance parameters are within one standard deviation of their prefit value.

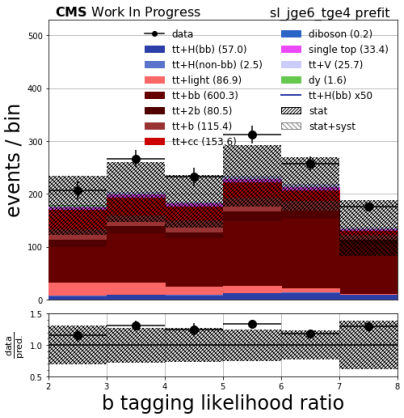

(a) SL, $\geq$ 6 jets, $\geq$ 4 b-tags - prefit

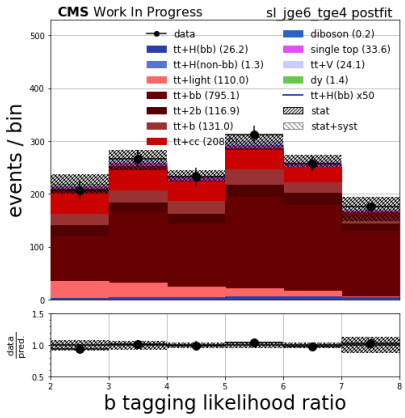

(b) SL, $\geq$ 6 jets, $\geq$ 4 b-tags - postfit

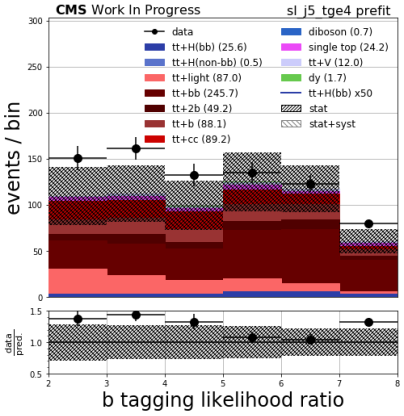

(c) SL, 5 jets, $\geq$ 4 b-tags - prefit

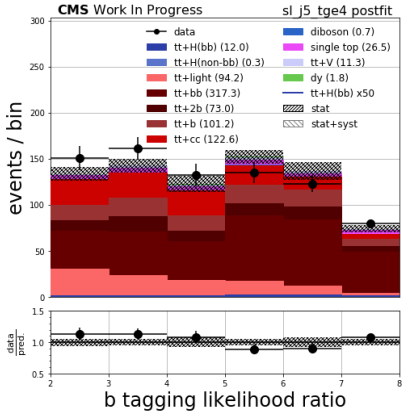

(d) SL, 5 jets, $\geq$ 4 b-tags - postfit

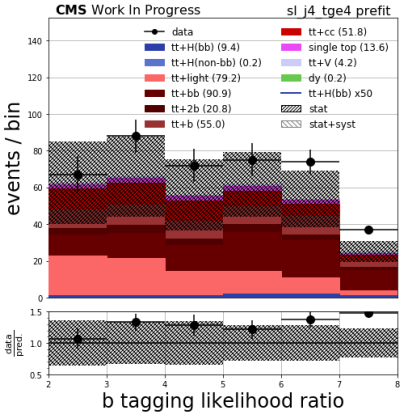

(e) SL, 4 jets, $\geq$ 4 b-tags - prefit

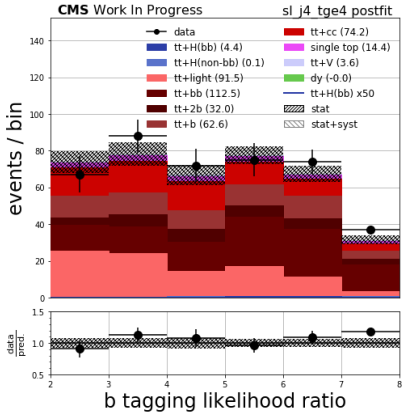

(f) SL, 4 jets, $\geq$ 4 b-tags - postfit

Figure 10.17: Pre- (left) and postfit plots in the semileptonic channel in categories with at least four b-tagged jets.

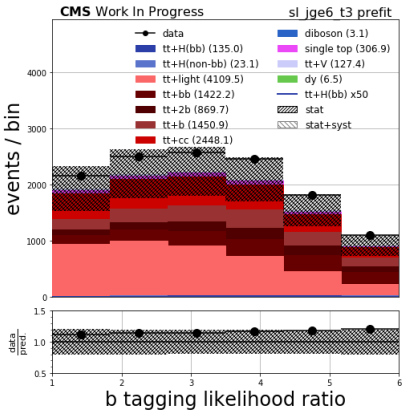

(a) SL, ≥ 6 jets, 3 b-tags - prefit

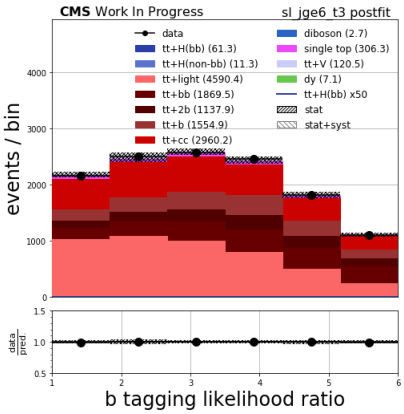

(b) SL, ≥ 6 jets, 3 b-tags - postfit

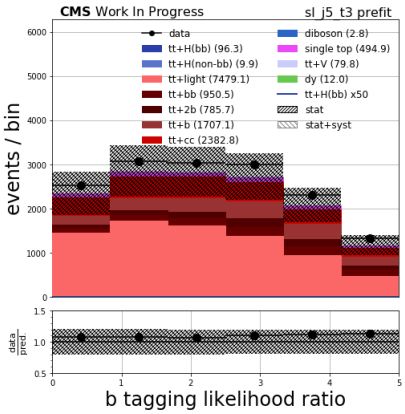

(c) SL, 5 jets, 3 b-tags - prefit

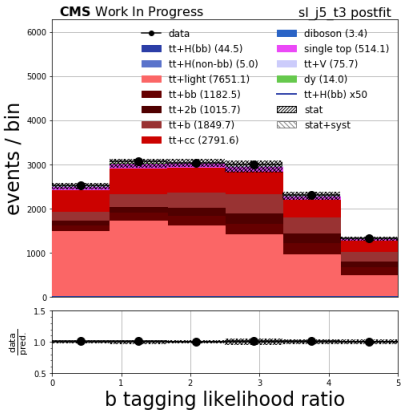

(d) SL, 5 jets, 3 b-tags - postfit

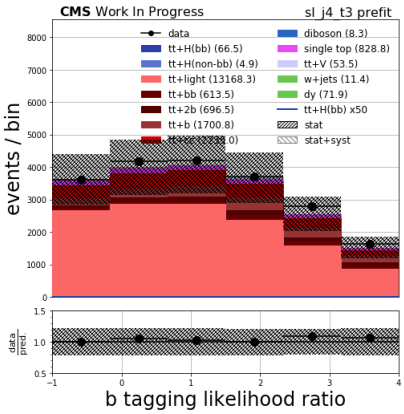

(e) SL, 4 jets, 3 b-tags - prefit

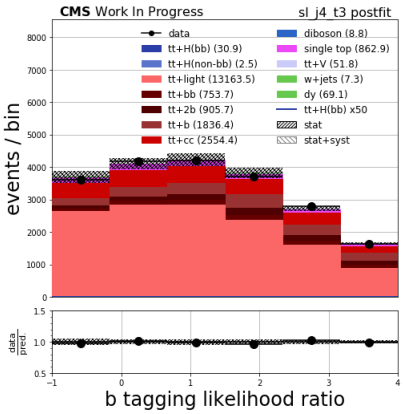

(f) SL, 4 jets, 3 b-tags - postfit

Figure 10.18: Pre- (left) and postfit plots in the semileptonic channel in categories with exactly three b-tagged jets.

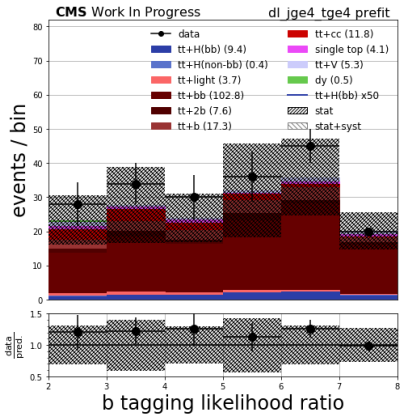

(a) DL, $\geq$ 4 jets, $\geq$ 4 b-tags - prefit

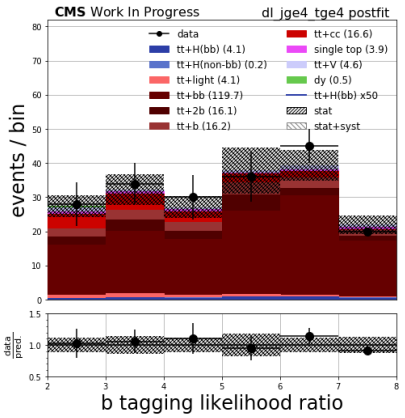

(b) DL, $\geq$ 4 jets, $\geq$ 4 b-tags - postfit

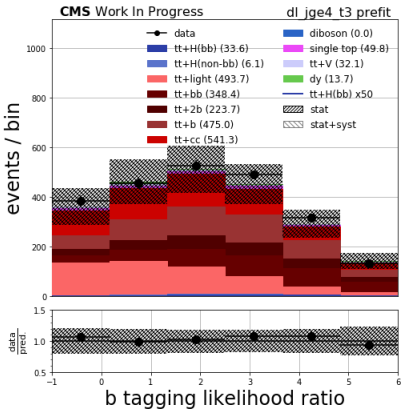

(c) DL, $\geq$ 4 jets, 3 b-tags - prefit

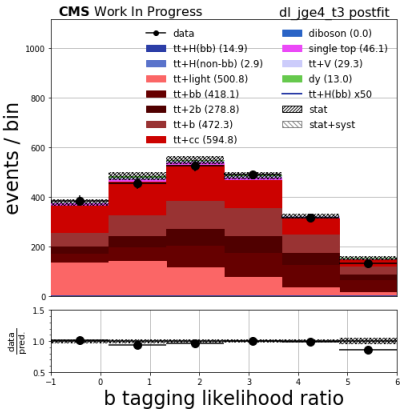

(d) DL, $\geq$ 4 jets, 3 b-tags - postfit

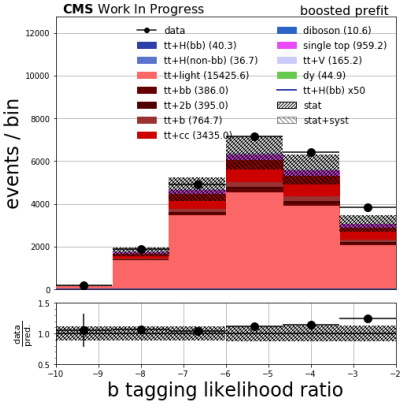

(e) SL, DL boosted - prefit

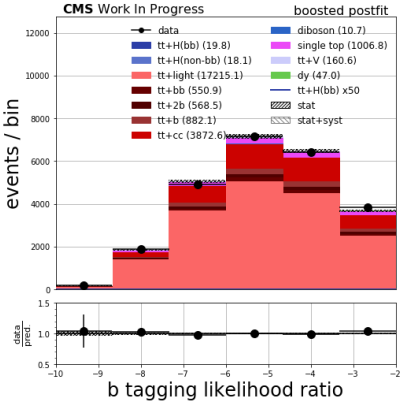

(f) SL, DL boosted - postfit

Figure 10.19: Pre- (left) and postfit plots in the dileptonic and the boosted analysis categories.

	$\hat{\mu}\pm$ tot ($\pm$ stat $\pm$ syst)	Significance observed (expected)
SL	$2.67^{+3.84}_{-3.70}$ $\left(\begin{smallmatrix}+2.05 & +3.25\\ -2.23 & -2.95\end{smallmatrix}\right)$	0.72 (0.31)
DL	$1.15^{+6.87}_{-7.69}$ $\left(\begin{smallmatrix}+4.62 & +5.08\\ -5.54 & -5.33\end{smallmatrix}\right)$	0.17 (0.16)
SL + DL combined	$3.82^{+3.78}_{-4.48}$ $\left(\begin{smallmatrix}+0.36 & +3.77\\ -0.36 & -4.47\end{smallmatrix}\right)$	0.84 (0.34)
SL + DL + Boosted combined	$0.47^{+3.34}_{-3.41}$ $\left(\begin{smallmatrix}+0.36 & +3.32\\ -0.36 & -3.40\end{smallmatrix}\right)$	0.14 (0.39)

Table 10.4: Best-fit values of the signal strength parameter $\hat{\mu}$ and observed and expected significance of the analysis.

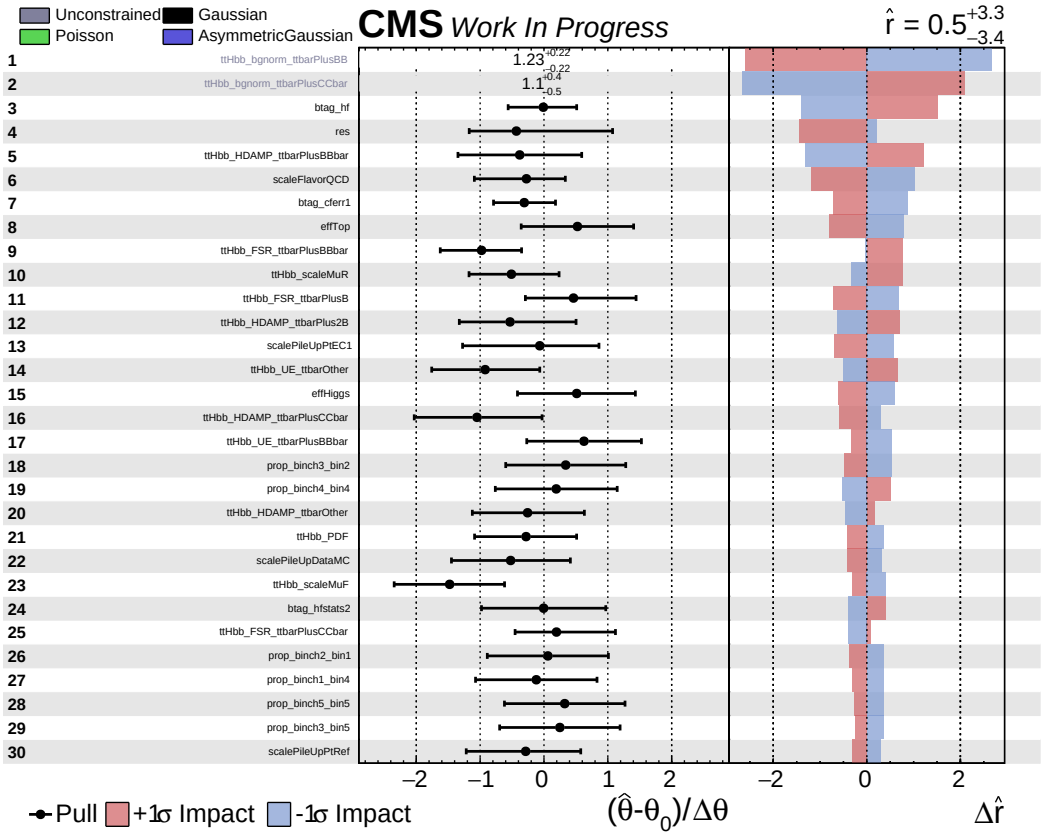

Figure 10.20: Impacts of the nuisance parameters on the signal strength. The largest impacts arise from the normalisations of the main backgrounds to the analysis.

	$-\Delta\mu$	$+\Delta\mu$
Background normalization	-1.01	+1.01
ISR, FSR	-0.85	+0.82
MC tune, hdamp	-0.96	+0.92
Theory	-2.46	+2.26
MC statistics	-0.11	+0.11
JEC	-0.11	+0.13
B tagging	-0.56	+0.59
Top / Higgs selection	-0.05	+0.05
Experimental	-0.85	+0.95
Systematic	-3.40	+3.32
Statistic	-0.36	+0.36
Total	-3.41	+3.34

Table 10.5: Uncertainties on the best-fit signal strength parameter for the different uncertainty sources. The uncertainty on $\hat{\mu}$ is dominated by theoretical systematic uncertainties.

10.6 Outlook

This work presents a search for $t\bar{t}H$, $H\to b\bar{b}$ events, including a selection targeting events with large Higgs boson or top quark p_T using the dataset collected in 2017 by the CMS experiment.

In the resolved case, a significance of 0.84 has been observed. An important aspect in improving upon this result is to find a valid solution to the mismodelling of the MEM distribution, which would provide a much stronger discriminant between the signal and the main background $t\bar{t}$+jets. Additionally, developing track dependant b tagging scale factors would correct the mismodelling in the b-tagged jet multiplicities which would also improve the sensitivity of the analysis. Furthermore an improved modelling of the $t\bar{t}+b\bar{b}$ background would reduce the uncertainty linked to the normalisation of this process, which is one of the largest uncertainties affecting the final result. Several measurements from the CMS and ATLAS collaborations have studied this process, and measured a cross section up to 40% larger than predictions at NLO, with an uncertainty of around 30% [279, 280]. Along these lines, new theoretical predictions have been developed. Indeed, the models used in this analysis are simulated using the five-flavour scheme, in which additional b jets are mostly produced in the parton shower. However, these additional jets largely arise from gluon splittings in

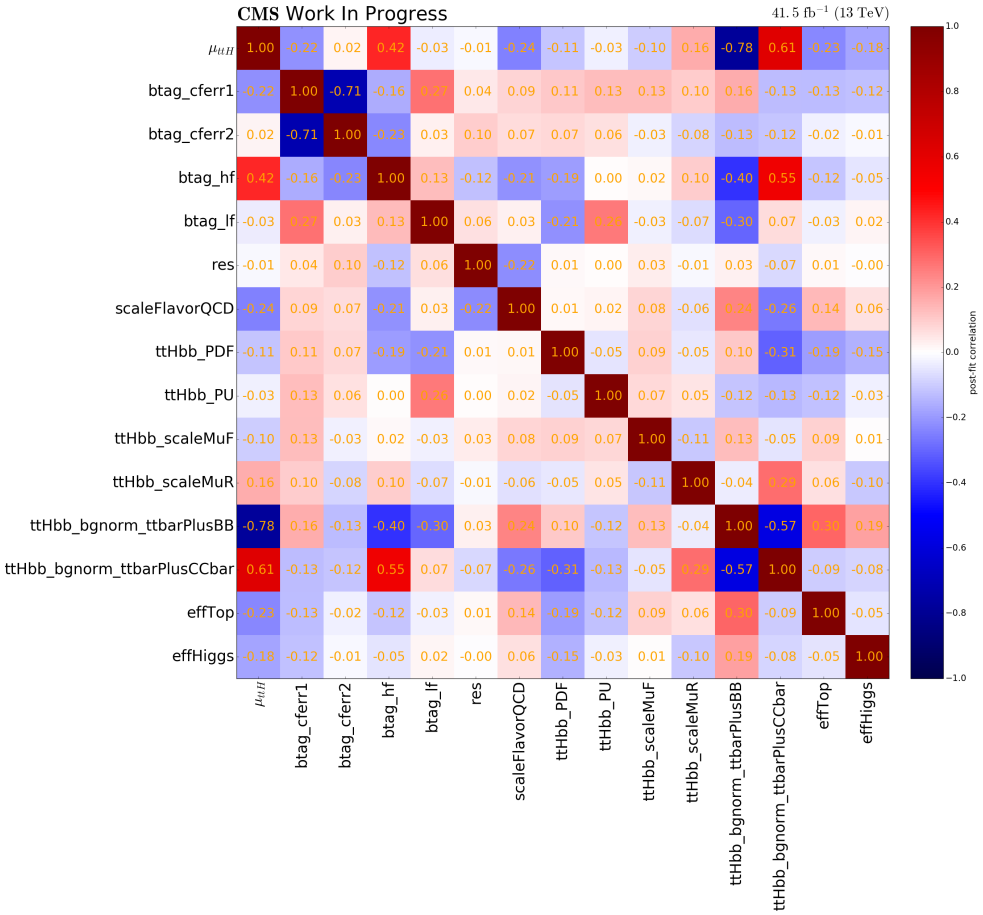

Figure 10.21: Correlations between the signal strength and the nuisance parameters. Strong correlations between the nuisances related to b tagging (*btag_cferr[1,2]*, *btag_[hf,lf]*) and to the background normalisations (*ttHbb_bgnorm_ttbarPlusBB*, *ttHbb_bgnorm_ttbarPlusCCbar*) and the signal strength exist. Correlations between the nuisances related to the JECs, the theory uncertainties and the uncertainties on the selection of the boosted objects are less important.

the final state. A model using these new developments has recently been developed and would improve the modelling of the main background of the analysis [281].

Unfortunately, the sensitivity of the boosted analysis presented here hardly improves upon that of the resolved analysis. The reasons leading to this poor performance were shown in Section 10.3.1. Therefore in order to use this phase space efficiently and to measure the top quark Yukawa coupling, large improvements in cor-

rectly identifying the top quark and Higgs boson candidates are essential. As briefly summarised in Section 8.1.1, several new methods improving the tagging performance of heavy objects have been developed simultaneously to this work. One example for Higgs boson tagging is the DeepDoubleB tagger developped by the CMS collaboration [232], whose efficiency is compared to that of the double b-tag algorithm used in this work in Figure 10.22a. For similar signal efficiencies, this new tagger reaches a mistag rate five times lower than the double b-tag algorithm. Similarly, new machine learning based taggers outperform the performance of classical taggers such as the HTTV2 algorithm as is shown in Figure 10.22b. Here the performance of the HTTV2 algorithm is comparable to that of the combined tagger of N-subjettiness and candidate mass. This tagger has a twice lower background rejection compared to more recent machine learning tools at similar signal efficiencies. Using these more modern tools would therefore considerably increase the analysis sensitivity. Combining this analysis with data collected in 2016 and 2018 would also be beneficial as with the additional statistics, more stringent selections on the boosted objects can be used which would help to increase the signal fractions in the analysis categories.

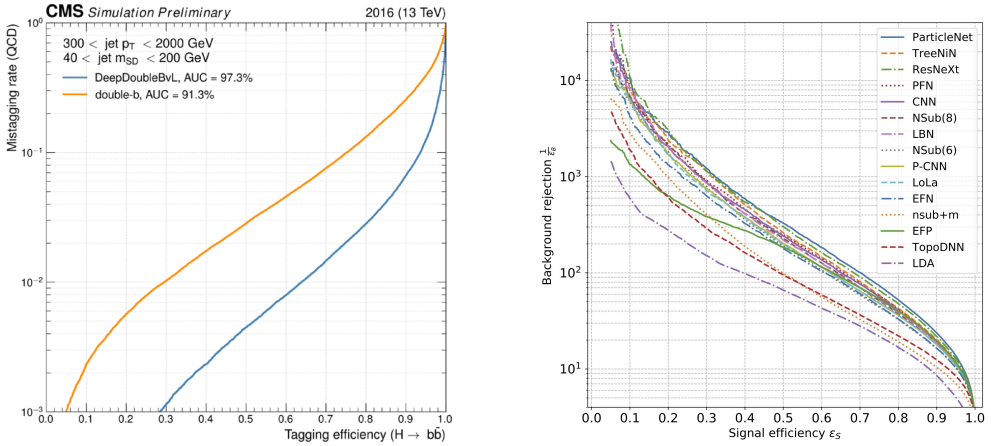

(a) Higgs boson tagging (b) Top quark tagging

Figure 10.22: Performance of the DeepDoubleB and the double b tagger for Higgs boson tagging (a) and of various machine learning algorithms for top quark tagging (b) [232, 233]. These algorithms improve upon the methods used in this work.

Chapter 11

Conclusion

While the discovery of the Higgs boson in 2012 marked an important milestone in the history of particle physics as it completed the SM, a number of open questions remain in the quest to understand Nature around us at its most fundamental level. The most promising path forward to solve these questions at the high-energy frontier are precision measurements to potentially find discrepancies with respect to SM expectations.

Of particular interest is the Yukawa coupling with the top quark, which is the heaviest fundamental particle known to date. A direct measurement of this property is possible in the associated production of a Higgs boson with a top quark pair — which is the focus of this thesis — even though this channel is difficult to reconstruct because of large background contributions and a complex final state.

This analysis uses different approaches to discriminate between signal and background events. For example the matrix element method builds a discriminant from the probabilities of an event to originate from either of the processes, evaluating their matrix elements from the measured kinematics of the event, while the BLR deeply exploits the b tagging information of the jets. This analysis also includes a selection targeting events where the top quark or the Higgs boson is produced at large transverse momentum. Dedicated techniques such as the HEPTopTaggerV2 and the bb-tag algorithm are used to reconstruct these objects.

This work uncovered a dependence of the b tagging scale factors used to correct for different tagging efficiencies in data and simulation on the number of tracks belonging to a jet. This knowledge thus contributes to a better understanding on how to measure more accurate scale factors. Additionally it was found that the MEM is very sensitive to small differences in the numerical integration procedure, which need to be understood in the future. Deploying better understood analytically derived

discriminants, a best-fit signal strength of $0.47^{+3.34}_{-3.41}$ has been measured in a combined fit, which is compatible with Standard Model expectations. The sensitivity of the analysis is driven by the resolved and not the boosted selection.

To improve the sensitivity of the analysis in the high p_T regime, advancements in algorithms designed to identify heavy resonances are crucial. Several options have already been proposed and are now either already in use by analyses performed by the ATLAS and CMS collaborations or being adapted from working in a controlled environment to actual collision data. Alongside with larger datasets collected in other years, a better sensitivity can be obtained. However this result already proves that this regime can be targeted and used for future analyses.

Alongside with these improvements, a better modelling of systematic uncertainties is necessary, as these impact the sensitivity of the analysis of the $t\bar{t}H$, $H\rightarrow b\bar{b}$ process most. Improved theoretical modelling of the main backgrounds to the analysis will positively impact the analysis sensitivity as well.

However, performing analyses with high sensitivities is only possible with a detector measuring high-quality data. Thus, maintaining the excellent performance of the CMS detector is essential. Particularly important in the search for $t\bar{t}H$, $H\rightarrow b\bar{b}$ events is the pixel detector, which records particle tracks, and is necessary to determine the charge and momentum of particles. To cope with increasing luminosities, the CMS pixel detector was exchanged with a newly designed version, which improves upon the performance of the previous one while dealing with denser environments.

This work was crucial to verify that the modules of the innermost detector layer, which are used to measure interactions with particles and preprocess the gathered information, are functional. This involved verifying the radiation tolerance of the readout chips built into these modules. By irradiating test samples to increasing rates using a proton beam, it is shown that no significant damage is created at the doses expected to be delivered to the readout chips during their expected lifetime in the detector. Furthermore calibrations are provided to adjust operation parameters to maintain the same detector response throughout its use in the CMS experiment.

An additional contribution to the successful installation of the pixel detector inside the experiment was the quality assessment of every single module that was later installed onto the support structure. This enabled to identify faulty components or defects introduced during module production, such that the detector was equipped only with modules satisfying stringent quality criteria. The detector with this innermost layer has been used in the CMS experiment in 2017 and 2018 and has collected data with excellent quality for physics analyses, such as the one presented in the first part of this thesis.

A further upgrade of the pixel detector is planned in the middle of the decade

to prepare for conditions during the High-Luminosity programme of the LHC. The design and development of this detector significantly benefits from experience gathered during construction and operation of the version to which this work contributed. With the immense datasets which will be collected by the ATLAS and the CMS experiments in this new LHC phase an improved sensitivity in the $t\bar{t}H$, $H\rightarrow b\bar{b}$ analysis and its high p_T phase space are expected. More importantly, this additional data will bring new insights into the laws governing Nature and contribute to answering the remaining open questions regarding the fundamental constituents of our universe.

Bibliography

[1] B. Pullman and A. Reisinger, *The Atom in the History of Human Thought*. Oxford University Press, 2001.

[2] A. Kenny, *Ancient Philosophy*. No. Bd. 1 in Ancient Philosophy, Clarendon Press, 2004.

[3] J. Dalton, *A New System of Chemical Philosophy*. William Dawson & Sons, 1808.

[4] J. J. Thomson, *Cathode rays*, Philosophical Magazine Series 5, vol. 44, pp. 293–316, 1897.

[5] E. Rutherford, *The scattering of α and β particles by matter and the structure of the atom*, The London, Edinburgh, and Dublin Philosophical Magazine and Journal of Science, vol. 21, no. 125, pp. 669–688, 1911.

[6] J. Chadwick, *The existence of a neutron*, Proc. R. Soc. Lond. A, vol. 136, no. 830, 1932.

[7] M. Gell-Mann, *A schematic model of baryons and mesons*, Physics Letters, vol. 8, no. 3, pp. 214 – 215, 1964.

[8] G. Zweig, *An SU(3) model for strong interaction symmetry and its breaking. Version 2*, Developments in the quark theory of hadrons. Vol. 1. 1964 - 1978, pp. 22–101, 1964.

[9] D. Griffiths, *Introduction to elementary particles*. Wiley, 2008.

[10] G. Altarelli and J. Wells, *Gauge Theories and the Standard Model*. Springer International Publishing, 2017.

[11] B. Pontecorvo, *Mesonium and anti-mesonium*, Sov. Phys. JETP, vol. 6, p. 429, 1957.

[12] Y. Fukuda *et al.*, *Evidence for oscillation of atmospheric neutrinos*, Phys. Rev. Lett., vol. 81, pp. 1562–1567, 1998.

[13] N. Cabibbo, *Unitary Symmetry and Leptonic Decays*, Phys. Rev. Lett., vol. 10, pp. 531–533, 1963.

[14] M. Kobayashi and T. Maskawa, *CP-Violation in the Renormalizable Theory of Weak Interaction*, Progress of Theoretical Physics, vol. 49, no. 2, pp. 652–657, 1973.

[15] M. Tanabashi *et al.*, *Review of Particle Physics*, Phys. Rev. D, vol. 98, p. 030001, 2018.

[16] B. Lillie, L. Randall, and L.-T. Wang, *The Bulk RS KK-gluon at the LHC*, JHEP, vol. 2007, no. 09, pp. 074–074, 2007.

[17] R. M. Harris, C. T. Hill, and S. J. Parke, *Cross Section for Topcolor Z' decaying to top-antitop*, arXiv preprint hep-ph/9911288, 1999.

[18] P. Dirac, *The quantum theory of the electron*, Proc. R. Soc. Lond. A, vol. 117, no. 778, 1928.

[19] C. D. Anderson, *The Positive Electron*, Phys. Rev., vol. 43, pp. 491–494, 1933.

[20] Wikimedia Commons, *Standard Model of Elementary Particle Physics*. `https://upload.wikimedia.org/wikipedia/commons/0/00/Standard_Model_of_Elementary_Particles.svg`. Accessed on 04-11-2019.

[21] S. Weinberg, *A Model of Leptons*, Phys. Rev. Lett., vol. 19, pp. 1264–1266, 1967.

[22] S. L. Glashow, *Partial-symmetries of weak interactions*, Nuclear Physics, vol. 22, no. 4, pp. 579 – 588, 1961.

[23] A. Salam, *Weak and Electromagnetic Interactions*, Conf. Proc. C, vol. C680519, pp. 367–377, 1968.

[24] G. Arnison *et al.*, *Experimental Observation of Isolated Large Transverse Energy Electrons with Associated Missing Energy at* $\sqrt{s} = 540$ *GeV*, PLB, vol. 122B, pp. 103–116, 1983.

[25] M. Banner *et al.*, *Observation of Single Isolated Electrons of High Transverse Momentum in Events with Missing Transverse Energy at the CERN anti-p p Collider*, PLB, vol. 122B, pp. 476–485, 1983.

[26] G. Arnison *et al.*, *Experimental Observation of Lepton Pairs of Invariant Mass Around 95 GeV/c^2 at the CERN SPS Collider*, PLB, vol. 126B, pp. 398–410, 1983.

[27] P. W. Higgs, *Broken Symmetries and the Masses of Gauge Bosons*, Phys. Rev. Lett., vol. 13, pp. 508–509, 1964.

[28] F. Englert and R. Brout, *Broken Symmetry and the Mass of Gauge Vector Mesons*, Phys. Rev. Lett., vol. 13, pp. 321–323, 1964.

[29] G. S. Guralnik, C. R. Hagen, and T. W. B. Kibble, *Global Conservation Laws and Massless Particles*, Phys. Rev. Lett., vol. 13, pp. 585–587, 1964.

[30] J. Ellis, M. K. Gaillard, and D. V. Nanopoulos, *A Historical Profile of the Higgs Boson. An Updated Historical Profile of the Higgs Boson*, no. arXiv:1504.07217, CERN-PH-TH-2015-098, p. 22 p, 2015.

[31] Y. Nambu, *Quasi-Particles and Gauge Invariance in the Theory of Superconductivity*, Phys. Rev., vol. 117, pp. 648–663, 1960.

[32] J. Goldstone, *Field theories with Superconductor solutions*, Il Nuovo Cimento (1955-1965), vol. 19, no. 1, pp. 154–164, 1961.

[33] J. Goldstone, A. Salam, and S. Weinberg, *Broken Symmetries*, Phys. Rev., vol. 127, pp. 965–970, 1962.

[34] C. Z. Yuan and M. Mulders, eds., *Proceedings, 3rd Asia-Europe-Pacific School of High-Energy Physics (AEPSHEP 2016): Beijing, China, October 12-25 2016. 3rd Asia-Europe-Pacific School of High-Energy Physics*, (Geneva), CERN, 2018.

[35] The ATLAS Collaboration, *Observation of a new particle in the search for the Standard Model Higgs boson with the ATLAS detector at the LHC*, PLB, vol. 716, no. 1, pp. 1 – 29, 2012.

[36] The CMS Collaboration, *Observation of a new boson at a mass of 125 GeV with the CMS experiment at the LHC*, PLB, vol. 716, no. 1, pp. 30 – 61, 2012.

[37] The CMS Collaboration, *A measurement of the Higgs boson mass in the diphoton decay channel*, no. CMS-PAS-HIG-19-004, 2019.

[38] T. van Ritbergen and R. G. Stuart, *Complete two loop quantum electrodynamic contributions to the muon lifetime in the Fermi model*, Phys. Rev. Lett., vol. 82, pp. 488–491, 1999.

[39] M. Steinhauser and T. Seidensticker, *Second order corrections to the muon lifetime and the semileptonic B decay*, PLB, vol. B467, pp. 271–278, 1999.

[40] T. van Ritbergen and R. G. Stuart, *On the precise determination of the Fermi coupling constant from the muon lifetime*, Nuclear Physics B, vol. 564, no. 3, pp. 343 – 390, 2000.

[41] The CMS Collaboration, *Summaries of CMS cross section measurements*. `https://twiki.cern.ch/twiki/bin/view/CMSPublic/PhysicsResultsCombined`. "Accessed on 19-1-2019".

[42] CERN, *LHC Guide*. `https://cds.cern.ch/record/2255762`, 2017.

[43] S. P. Martin, *A Supersymmetry Primer*, Advanced Series on Directions in High Energy Physics, p. 1–98, 1998.

[44] The CMS Collaboration, *CMS Supersymmetry Physics Results*. "Accessed on 09-12-2019".

[45] The ATLAS Collaboration, *ATLAS News: Highlights from EPS 2019 - SUSY Summary Plot July 2019*. 2019.

[46] N. Arkani–Hamed, S. Dimopoulos, and G. Dvali, *The hierarchy problem and new dimensions at a millimeter*, PLB, vol. 429, no. 3, pp. 263 – 272, 1998.

[47] L. Randall and R. Sundrum, *Large Mass Hierarchy from a Small Extra Dimension*, Phys. Rev. Lett., vol. 83, pp. 3370–3373, 1999.

[48] M. J. Dugan, H. Georgi, and D. B. Kaplan, *Anatomy of a composite Higgs model*, Nuclear Physics B, vol. 254, pp. 299 – 326, 1985.

[49] M. J. Strassler and K. M. Zurek, *Echoes of a hidden valley at hadron colliders*, PLB, vol. 651, no. 5, pp. 374 – 379, 2007.

[50] The BABAR Collaboration, *Measurement of an excess of $\overline{B} \to D^{(*)}\tau^-\overline{\nu}_\tau$ decays and implications for charged Higgs bosons*, Phys. Rev. D, vol. 88, p. 072012, 2013.

[51] The Belle Collaboration, *Measurement of the τ Lepton Polarization and $R(D^*)$ in the Decay $\overline{B} \to D^*\tau^-\overline{\nu}_\tau$*, Phys. Rev. Lett., vol. 118, p. 211801, 2017.

[52] The LHCb Collaboration, *Measurement of the Ratio of the $B^0 \to D^{*-}\tau^+\nu_\tau$ and $B^0 \to D^{*-}\mu^+\nu_\mu$ Branching Fractions Using Three-Prong τ-Lepton Decays*, Phys. Rev. Lett., vol. 120, p. 171802, 2018.

[53] The CMS Collaboration, *Measurement of angular parameters from the decay $B^0 \to K^{*0}\mu^+\mu^-$ in proton–proton collisions at $\sqrt{s} = 8\,\text{TeV}$*, PLB, vol. 781, pp. 517 – 541, 2018.

[54] O. S. Brüning *et al.*, *LHC Design Report.* CERN Yellow Reports, Geneva: CERN, 2004.

[55] J. Schwinger, *On the Classical Radiation of Accelerated Electrons*, Phys. Rev., vol. 75, pp. 1912–1925, 1949.

[56] W. Herr and B. Muratori, *Concept of luminosity.* `https://cds.cern.ch/record/941318`, 2006.

[57] S. D. Drell and T.-M. Yan, *Massive Lepton-Pair Production in Hadron-Hadron Collisions at High Energies*, Phys. Rev. Lett., vol. 25, pp. 902–902, 1970.

[58] K. Rabbertz, *Jet Physics at the LHC*, Springer Tracts Mod. Phys., vol. 268, pp. pp.1–214, 2017.

[59] J. Rojo *et al.*, *The PDF4LHC report on PDFs and LHC data: Results from Run I and preparation for Run II*, J. Phys G., vol. 42, p. 103103, 2015.

[60] The NNPDF collaboration and others, *Parton distributions for the LHC Run II*, JHEP, vol. 2015, no. 4, p. 40, 2015.

[61] Y. L. Dokshitzer, *Calculation of the Structure Functions for Deep Inelastic Scattering and e+ e- Annihilation by Perturbation Theory in Quantum Chromodynamics.*, Sov. Phys. JETP, vol. 46, pp. 641–653, 1977.

[62] V. Gribov and L. Lipatov, *Deep inelastic electron scattering in perturbation theory*, PLB, vol. 37, no. 1, pp. 78 – 80, 1971.

[63] G. Altarelli and G. Parisi, *Asymptotic freedom in parton language*, Nuclear Physics B, vol. 126, no. 2, pp. 298 – 318, 1977.

[64] G. Sterman and S. Weinberg, *Jets from Quantum Chromodynamics*, Phys. Rev. Lett., vol. 39, pp. 1436–1439, 1977.

[65] G. C. Blazey *et al.*, *Run II Jet Physics: Proceedings of the Run II QCD and Weak Boson Physics Workshop*, 2000.

[66] G. Arnison *et al.*, *Hadronic Jet Production at the CERN Proton - anti-Proton Collider*, PLB, vol. 132B, p. 214, 1983.

[67] G. P. Salam and G. Soyez, *A practical seedless infrared-safe cone jet algorithm*, JHEP, vol. 2007, no. 05, pp. 086–086, 2007.

[68] T. Plehn, *Lectures on LHC physics; 2nd ed.* Lecture Notes in Physics, Springer, 2015.

[69] S. D. Ellis and D. E. Soper, *Successive combination jet algorithm for hadron collisions*, Phys. Rev. D, vol. 48, pp. 3160–3166, 1993.

[70] Y. Dokshitzer *et al.*, *Better jet clustering algorithms*, JHEP, vol. 1997, no. 08, pp. 001–001, 1997.

[71] M. Wobisch and T. Wengler, *Hadronization corrections to jet cross-sections in deep inelastic scattering*, in *Monte Carlo generators for HERA physics. Proceedings, Workshop, Hamburg, Germany, 1998-1999*, pp. 270–279, 1998.

[72] M. Cacciari, G. P. Salam, and G. Soyez, *The anti-kt jet clustering algorithm*, JHEP, vol. 2008, no. 04, pp. 063–063, 2008.

[73] The CMS Collaboration, *Public CMS Luminosity Information*. `https://twiki.cern.ch/twiki/bin/view/CMSPublic/LumiPublicResults`. Accessed on 01-12-2019.

[74] The CMS Collaboration, *Pileup Removal Algorithms*, CMS-PAS-JME-14-001, 2014.

[75] D. Bertolini *et al.*, *Pileup per particle identification*, JHEP, vol. 2014, no. 10, p. 59, 2014.

[76] The ATLAS Collaboration, *Tagging and suppression of pileup jets with the ATLAS detector*, no. ATLAS-CONF-2014-018, 2014.

[77] T. Sjöstrand and M. van Zijl, *A multiple-interaction model for the event structure in hadron collisions*, Phys. Rev. D, vol. 36, pp. 2019–2041, 1987.

[78] J. Abelleira *et al.*, *High-Energy LHC design*, Journal of Physics: Conference Series, vol. 1067, p. 022009, 2018.

[79] LHC Higgs Cross Section Working Group, *Higgs cross sections for HL-LHC and HE-LHC* . `https://twiki.cern.ch/twiki/bin/view/LHCPhysics/HiggsEuropeanStrategy`. Accessed on 01-12-2019.

[80] LHC Higgs Cross Section Working Group, *SM Higgs production cross sections at $\sqrt{s}$ = 13-14 TeV (CERN Report 3)*. `https://twiki.cern.ch/twiki/bin/view/LHCPhysics/CERNYellowReportPageAt1314TeV2014`. Accessed on 01-12-2019.

[81] The CMS Collaboration, *Evidence for the direct decay of the 125 GeV Higgs boson to fermions*, Nature Phys., vol. 10, pp. 557–560, 2014.

[82] The CMS Collaboration, *Limits on the Higgs boson lifetime and width from its decay to four charged leptons*, Phys. Rev. D, vol. 92, p. 072010, 2015.

[83] CERN. `https://home.cern/`. Accessed on 10-12-2019.

[84] L. Arnaudon *et al.*, *Linac4*. Technical Design Report, 2006.

[85] The Antiproton Decelerator. `https://home.cern/science/accelerators/antiproton-decelerator`. Accessed on 10-12-2019.

[86] The ISOLDE Radioactive Ion Beam facility. `http://isolde.web.cern.ch/`. Accessed on 10-12-2019.

[87] E. Mobs, *The CERN accelerator complex*, OPEN-PHO-ACCEL-2018-005, 2018.

[88] CERN, *LEP design report*. CERN Yellow Reports, 1984.

[89] The CMS Collaboration, *Technical proposal*. LHC Technical Proposal, 1994.

[90] The ATLAS Collaboration, *ATLAS: Detector and physics performance technical design report. Volume 1*, 1999.

[91] The ALICE Collaboration, *The ALICE experiment at the CERN LHC*, JINST, vol. 3, no. 08, p. S08002, 2008.

[92] The LHCb Collaboration, *The LHCb Detector at the LHC*, JINST, vol. 3, p. S08005, 2008.

[93] T. Sakuma, *Cutaway diagrams of CMS detector*, 2019.

[94] The CMS Collaboration, *Description and performance of track and primary-vertex reconstruction with the CMS tracker*, JINST, vol. 9, no. 10, p. P10009, 2014.

[95] The CMS Collaboration, *CMS Technical Design Report for the Pixel Detector Upgrade*. No. CERN-LHCC-2012-016. CMS-TDR-11 in Technical Design Report, 2012.

[96] The CMS Collaboration, *The CMS tracker system project*. Technical Design Report, Geneva: CERN, 1997.

[97] The CMS Collaboration, *Tracker technical design report*. Technical Design Report, 1998.

[98] The CMS Collaboration, *The CMS tracker: addendum to the Technical Design Report*. Technical Design Report, Geneva: CERN, 2000.

[99] M. Livan and R. Wigmans, *Calorimetry for collider physics: an introduction*. Unitext for physics, Springer, 2019.

[100] The CMS Collaboration, *The CMS electromagnetic calorimeter project*. Technical Design Report, Geneva: CERN, 1997.

[101] The CMS Collaboration, *Performance of electron reconstruction and selection with the CMS detector in proton-proton collisions at* $\sqrt{s}$ = 8TeV, JINST, vol. 10, p. P06005, 2015.

[102] The CMS Collaboration, *Energy calibration and resolution of the CMS electromagnetic calorimeter in pp collisions at* $\sqrt{s}$*= 7 TeV*, JINST, vol. 8, no. 09, p. P09009, 2013.

[103] The CMS Collaboration, *The CMS hadron calorimeter project*. Technical Design Report, Geneva: CERN, 1997.

[104] The CMS Collaboration, *CMS luminosity measurement for the 2017 data-taking period at* $\sqrt{s} = 13$ TeV, no. CMS-PAS-LUM-17-004, 2018.

[105] V. D. Elvira, *Measurement of the Pion Energy Response and Resolution in the CMS HCAL Test Beam 2002 Experiment*, no. CMS-NOTE-2004-020, 2004.

[106] The CMS Collaboration, *The CMS muon project*. Technical Design Report, Geneva: CERN, 1997.

[107] The CMS Collaboration, *Performance of the CMS drift tube chambers with cosmic rays*, JINST, vol. 5, no. 03, p. T03015, 2010.

[108] The CMS Collaboration, *Performance of the CMS cathode strip chambers with cosmic rays*, JINST, vol. 5, no. 03, p. T03018, 2010.

[109] P. Paolucci *et al.*, *CMS Resistive Plate Chamber overview, from the present system to the upgrade phase I*, JINST, vol. 8, no. 04, p. P04005, 2013.

[110] The CMS Collaboration, *Performance of the CMS muon detector and muon reconstruction with proton-proton collisions at* $\sqrt{s}$ = 13TeV, JINST, vol. 13, p. P06015, 2018.

[111] S. Cittolin, A. Rácz, and P. Sphicas, *CMS The TriDAS Project: Technical Design Report, Volume 2: Data Acquisition and High-Level Trigger. CMS trigger and data-acquisition project*. Technical Design Report, Geneva: CERN, 2002.

[112] The CMS Collaboration, *The CMS trigger system*, JINST, vol. 12, p. P01020, 2017.

[113] K. Bos *et al.*, *LHC computing Grid: Technical Design Report. Version 1.06 (20 Jun 2005)*. Technical Design Report, Geneva: CERN, 2005.

[114] The CMS Collaboration, *Particle-flow reconstruction and global event description with the CMS detector*, JINST, vol. 12, p. P10003, 2017.

[115] The CMS Collaboration, *Description and performance of track and primary-vertex reconstruction with the CMS tracker*, JINST, vol. 9, no. 10, p. P10009, 2014.

[116] The CMS Collaboration, *Jet energy scale and resolution in the CMS experiment in pp collisions at 8 TeV*, JINST, vol. 12, no. 02, p. P02014, 2017.

[117] The CMS Collaboration, *Performance of photon reconstruction and identification with the CMS detector in proton-proton collisions at* $\sqrt{s}$ *= 8 TeV*, JINST, vol. 10, no. 08, p. P08010, 2015.

[118] The CMS Collaboration, *Performance of CMS Muon Reconstruction in pp Collision Events at* $\sqrt{s} = 7$ *TeV*, JINST, vol. 7, p. P10002, 2012.

[119] W. Adam *et al.*, *Reconstruction of electrons with the Gaussian-sum filter in the CMS tracker at the LHC*, J. Phys G., vol. 31, no. 9, p. N9–N20, 2005.

[120] The CMS Collaboration, *Identification of heavy-flavour jets with the CMS detector in pp collisions at 13 TeV*, JINST, vol. 13, no. 05, p. P05011, 2018.

[121] M. H. Seymour and M. Marx, *Monte Carlo Event Generators*, 2013.

[122] N. Metropolis and S. Ulam, *The Monte Carlo Method*, Journal of the American Statistical Association, vol. 44, no. 247, pp. 335–341, 1949.

[123] J. Alwall *et al.*, *The automated computation of tree-level and next-to-leading order differential cross sections, and their matching to parton shower simulations*, JHEP, vol. 2014, no. 7, 2014.

[124] P. Nason, *A New Method for Combining NLO QCD with Shower Monte Carlo Algorithms*, JHEP, vol. 2004, no. 11, p. 040–040, 2004.

[125] S. Frixione, P. Nason, and C. Oleari, *Matching NLO QCD computations with parton shower simulations: the POWHEG method*, JHEP, vol. 2007, no. 11, p. 070–070, 2007.

[126] S. Alioli *et al.*, *A general framework for implementing NLO calculations in shower Monte Carlo programs: the POWHEG BOX*, JHEP, vol. 2010, no. 6, 2010.

[127] H. Hartanto *et al.*, *Higgs boson production in association with top quarks in the POWHEG BOX*, Phys. Rev. D, vol. 91, no. 9, 2015.

[128] F. Cascioli, P. Maierhöfer, and S. Pozzorini, *Scattering Amplitudes with Open Loops*, Phys. Rev. Lett., vol. 108, no. 11, 2012.

[129] F. Buccioni *et al.*, *OpenLoops 2*, EPJC, vol. 79, no. 10, 2019.

[130] T. Sjöstrand *et al.*, *An introduction to PYTHIA 8.2*, Computer Physics Communications, vol. 191, p. 159–177, 2015.

[131] S. Agostinelli *et al.*, *Geant4—a simulation toolkit*, Nucl. Instrum. Methods Phys. Res. A, vol. 506, no. 3, pp. 250 – 303, 2003.

[132] S. M. Seltzer and M. J. Berger, *Evaluation of the collision stopping power of elements and compounds for electrons and positrons*, Int. J. Appl. Radiat. Isot., vol. 33, no. 11, pp. 1189 – 1218, 1982.

[133] S. M. Seltzer and M. J. Berger, *Improved procedure for calculating the collision stopping power of elements and compounds for electrons and positrons*, Int. J. Appl. Radiat. Isot., vol. 35, no. 7, pp. 665 – 676, 1984.

[134] L. Rossi *et al.*, *Pixel Detectors - From Fundamentals to Applications*. Particle Acceleration and Detection, Springer-Verlag, 2006.

[135] H. Spieler, *Semiconductor Detector Systems*, vol. 12 of *Series on Semiconductor Science and Technology*. Oxford University Press, 2005.

[136] W. Shockley, *Currents to Conductors Induced by a Moving Point Charge*, Journal of Applied Physics, vol. 9, no. 10, pp. 635–636, 1938.

[137] S. Ramo, *Currents Induced by Electron Motion*, Proceedings of the IRE, vol. 27, no. 9, pp. 584–585, 1939.

[138] E. Belau *et al.*, *Charge collection in silicon strip detectors*, Nucl. Instrum. Methods Phys. Res., vol. 214, no. 2, pp. 253 – 260, 1983.

[139] F. Ragusa and L. Rolandi, *Tracking at LHC*, New Journal of Physics, vol. 9, no. 9, pp. 336–336, 2007.

[140] M. Backhaus, *High bandwidth pixel detector modules for the ATLAS Insertable B-Layer*. PhD thesis, Universität Bonn, 2014.

[141] R. Gluckstern, *Uncertainties in track momentum and direction, due to multiple scattering and measurement errors*, Nuclear Instruments and Methods, vol. 24, pp. 381 – 389, 1963.

[142] D. Curtin and C. B. Verhaaren, *Discovering uncolored naturalness in exotic Higgs decays*, JHEP, vol. 2015, no. 12, pp. 1–36, 2015.

[143] LHC Commissioning, *LHC schedules and luminosity forecasts*. `https://lhc-commissioning.web.cern.ch/lhc-commissioning/schedule/HL-LHC-plots.htm`. Accessed on 17-07-2019.

[144] The CMS Collaboration, *CMS Phase 1 heavy flavour identification performance and developments*, CMS-DP-2017-013, 2017.

[145] L. Feld *et al.*, *The DC-DC conversion power system of the CMS Phase-1 pixel upgrade*, JINST, vol. 10, no. 01, p. C01052, 2015.

[146] Paul Scherrer Institute (PSI), *CDCT – Project contributions*. `https://www.psi.ch/en/ltp-electronics/cdct-projects`. Accessed on 19-07-2019.

[147] J. H. Hoß, *Search for Supersymmetry with Multiple Charged Leptons at $\sqrt{s}$ = 13 TeV with CMS and Radiation Tolerance of the Readout Chip for the Phase I Upgrade of the Pixel Detector*. PhD thesis, ETH Zürich, 2017.

[148] P. Eller, *Associated Z+Higgs Boson Production in the Leptonic+Beauty Final State and the Upgrade of the Pixel Detector at CMS*. PhD thesis, ETH Zürich, 2015.

[149] B. Meier, *CMS pixel detector with new digital readout architecture*, JINST, vol. 6, no. 01, p. C01011, 2011.

[150] CMS Pixel Collaboration, *Digital ROC documentation*. `https://twiki.cern.ch/twiki/bin/viewauth/CMS/Psi46dig`. Accessed on 19-07-2019.

[151] G. Apollinari *et al.*, *High-Luminosity Large Hadron Collider (HL-LHC): Technical Design Report*. CERN Yellow Reports, Geneva: CERN, 2017.

[152] Danek Kotlinski, *Personal conversation*, 2018.

[153] W. Adam *et al.*, *The CMS Phase-1 Pixel Detector Upgrade*, JINST, vol. 16, no. 02, p. P02027, 2021.

[154] The CMS Collaboration, *Technical Proposal for the Phase-II Upgrade of the CMS Detector*. No. CERN-LHCC-2015-010. CMS-TDR-15-02 in Technical Design Report, 2015.

[155] M. Garcia-Sciveres and J. Christiansen, *Development of pixel readout integrated circuits for extreme rate and radiation*. No. CERN-LHCC-2013-002, 2013.

[156] D. Ta *et al.*, *Serial powering: Proof of principle demonstration of a scheme for the operation of a large pixel detector at the LHC*, Nucl. Instrum. Methods Phys. Res. A, vol. 557, no. 2, pp. 445 – 459, 2006.

[157] M. Karagounis *et al.*, *An integrated Shunt-LDO regulator for serial powered systems*, ESSCIRC 2009 - Proceedings of the 35th European Solid-State Circuits Conference, pp. 276 – 279, 2009.

[158] C. Claeys and E. Simoen, *Radiation Effects in Advanced Semiconductor Materials and Devices*, vol. 57 of *Springer Series in Materials Science*. Springer-Verlag, 2002.

[159] T.-P. Ma and P. V. Dressendorfer, *Ionizing radiation effects in MOS devices & circuits*. John Wiley & Sons, 1989.

[160] T. R. Oldham and F. B. McLean, *Total ionizing dose effects in MOS oxides and devices*, IEEE Trans. Nucl. Sci., vol. 50, no. 3, pp. 483–499, 2003.

[161] C. T. Sah, *Origin of Interface States and Oxide Charges Generated by Ionizing Radiation*, IEEE Trans. Nucl. Sci., vol. 23, no. 6, pp. 1563–1568, 1976.

[162] F. Faccio and G. Cervelli, *Radiation-induced edge effects in deep submicron CMOS transistors*, IEEE Trans. Nucl. Sci., vol. 52, no. 6, pp. 2413–2420, 2005.

[163] W. Snoeys *et al.*, *Layout techniques to enhance the radiation tolerance of standard CMOS technologies demonstrated on a pixel detector readout chip*, Nucl. Instrum. Methods Phys. Res. A, vol. 439, no. 2, pp. 349 – 360, 2000.

[164] Karlsruher Institut für Technologie (KIT). `https://www.kit.edu/`. Accessed on 03-04-2020.

[165] Institute of Experimental Particle Physics, KIT, *ETP Proton Irradiation*. `https://www.etp.kit.edu/english/264.php`. Accessed on 09-07-2019.

[166] National Institute of Standards and Technology (NIST), *Stopping-Power & Range Tables for Electrons, Protons, and Helium Ions*. `https://www.nist.gov/pml/stopping-power-range-tables-electrons-protons-and-helium-ions`. Accessed on 10-07-2019.

[167] M. T. Meinhard, *Analysis of X-radiation in the module calibration setup and Vcal calibration with filters*, 2014. Semesterarbeit, ETH Zürich.

[168] *PXAR - Pixel eXpert Analysis Readout*. `https://twiki.cern.ch/twiki/bin/viewauth/CMS/Pxar`, 2019. Accessed on 26-07-2019.

[169] S. Spannagel, B. Meier, and H. C. Perrey, *The pxarCore Library - Technical Documentation, Reference Manual, and Sample Applications*, no. CMS-NOTE-2016-001, 2015.

[170] *elComandante: Installation and Software Guide*. `https://twiki.cern.ch/twiki/bin/viewauth/CMS/ElComandante`, 2016. Accessed on 26-07-2019.

[171] M. Meinhard *et al.*, *Performance of the modules for layer 1 of the CMS phase 1 pixel detector upgrade*, JINST, vol. 12, no. 12, p. C12002, 2017.

[172] A. Starodumov, P. Berger, and M. Meinhard, *High rate capability and radiation tolerance of the PROC600 readout chip for the CMS pixel detector*, JINST, vol. 12, no. 01, p. C01078, 2017.

[173] V. Gromov *et al.*, *A Radiation Hard Bandgap Reference Circuit in a Standard 0.13 μm CMOS Technology*, IEEE Trans. Nucl. Sci., vol. 54, no. 6, pp. 2727–2733, 2007.

[174] D. Hilbiber, *A new semiconductor voltage standard*, ISSCC Digest Technical Papers, vol. VII, pp. 32–33, 1964.

[175] V. R. Tavolaro, *Study of the differential Higgs boson production in the diphoton decay channel with CMS and characterisation and calibration of detector modules for the Phase1 upgrade of the pixel detector*. PhD thesis, ETH Zürich, 2018.

[176] National Institute of Standards and Technology (NIST), *X-Ray Transition Energies Database*. `https://www.nist.gov/pml/x-ray-transition-energies-database`, 2018. Accessed on 08-07-2019.

[177] Burkhalter, Stephan, *Personal conversation*, 2019.

[178] Paul Scherrer Institut (PSI). `https://www.psi.ch/en`. Accessed on 10-12-2019.

[179] ETH Zürich. `https://ethz.ch/de.html`. Accessed on 10-12-2019.

[180] *Module Result Web*. `https://twiki.cern.ch/twiki/bin/viewauth/CMS/MoReWeb`, 2015. Accessed on 08-08-2019.

[181] D. H. Zhu, *Search for Long-Lived Heavy Neutral Leptons and Detector Modules for the CMS Pixel Phase 1 Upgrade*. PhD thesis, ETH Zürich, 2020.

[182] Berger, Pirmin, *Personal conversation*, 2016.

[183] The CMS Collaboration, *The Performance plots for Phase 1 Pixel Detector*. `https://twiki.cern.ch/twiki/bin/view/CMSPublic/PixelOfflinePlotsOctober2018`. "Accessed on 08-06-2020".

[184] The CMS Collaboration, *Search for a Standard Model Higgs Boson Produced in Association with a Top-Quark Pair and Decaying to Bottom Quarks Using a Matrix Element Method*, Eur. Phys. J., vol. C75, no. 6, p. 251, 2015.

[185] The CMS Collaboration, *Search for* $\mathrm{t\bar{t}H}$ *production in the* $\mathrm{H} \to \mathrm{b\bar{b}}$ *decay channel with leptonic* $\mathrm{t\bar{t}}$ *decays in proton-proton collisions at* $\sqrt{s} = 13$ *TeV*, JHEP, vol. 03, p. 026. 59 p, 2018.

[186] The CMS Collaboration, *Measurement of* $\mathrm{t\bar{t}H}$ *production in the* $\mathrm{H} \to \mathrm{b\bar{b}}$ *decay channel in* $41.5\,\mathrm{fb}^{-1}$ *of proton-proton collision data at* $\sqrt{s} = 13\,\mathrm{TeV}$, no. CMS-PAS-HIG-18-030, 2019.

[187] The CMS Collaboration, *Measurement and interpretation of differential cross sections for Higgs boson production at* $\sqrt{s}$*=13TeV*, PLB, vol. 792, p. 369–396, 2019.

[188] G. Degrassi *et al.*, *Higgs mass and vacuum stability in the Standard Model at NNLO*, JHEP, vol. 2012, no. 8, 2012.

[189] The CMS Collaboration, *Combined measurements of Higgs boson couplings in proton–proton collisions at* $\sqrt{s}$*=13 TeV*, EPJC, vol. 79, no. 5, 2019.

[190] J. M. Butterworth *et al.*, *Jet Substructure as a New Higgs-Search Channel at the Large Hadron Collider*, Phys. Rev. Lett., vol. 100, no. 24, 2008.

[191] T. Plehn, G. P. Salam, and M. Spannowsky, *Fat Jets for a Light Higgs Boson*, Phys. Rev. Lett., vol. 104, p. 111801, 2010.

[192] J. Bramante, A. Delgado, and A. Martin, *Cornering a hyper Higgs boson: Angular kinematics for boosted Higgs bosons with top pairs*, Phys. Rev. D, vol. 89, no. 9, 2014.

[193] J. Brod, U. Haisch, and J. Zupan, *Constraints on CP-violating Higgs couplings to the third generation*, JHEP, vol. 2013, no. 11, 2013.

[194] J. Ren, L. Wu, and J. M. Yang, *Unveiling CP property of top-Higgs coupling with graph neural networks at the LHC*, PLB, vol. B802, p. 135198, 2020.

[195] A. V. Gritsan *et al.*, *Constraining anomalous Higgs boson couplings to the heavy flavor fermions using matrix element techniques*, Phys. Rev., vol. D94, no. 5, p. 055023, 2016.

[196] M. R. Buckley and D. Gonçalves, *Boosting the Direct CP Measurement of the Higgs-Top Coupling*, Phys. Rev. Lett., vol. 116, no. 9, 2016.

[197] J. Ellis *et al.*, *Disentangling Higgs-Top Couplings in Associated Production*, JHEP, vol. 04, p. 004, 2014.

[198] The CMS Collaboration, *Measurements of* $\mathrm{t\bar{t}}H$ *production and the CP structure of the Yukawa interaction between the Higgs boson and top quark in the diphoton decay channel*, Phys. Rev. Lett., vol. 125, p. 061801. 18 p, 2020.

[199] The ATLAS Collaboration, *Study of the CP properties of the interaction of the Higgs boson with top quarks using top quark associated production of the Higgs boson and its decay into two photons with the ATLAS detector at the LHC*, Phys. Rev. Lett., vol. 125, p. 061802. 21 p, Apr 2020.

[200] The CMS Collaboration, *Measurement of the top quark Yukawa coupling from* $\mathrm{t\bar{t}}$ *kinematic distributions in the dilepton final state at* $\sqrt{s} = 13$ TeV, no. CMS-PAS-TOP-19-008, 2020.

[201] The ATLAS Collaboration, *Measurement of the Higgs boson coupling properties in the* $H \to ZZ^* \to 4l$ *decay channel at* $\sqrt{s}$*=13 TeV with the ATLAS detector*, JHEP, vol. 2018, no. 3, 2018.

[202] The ATLAS Collaboration, *Measurements of Higgs boson properties in the diphoton decay channel with 36 fb-1 of pp collision data at* $\sqrt{s}$*=13 TeV with the ATLAS detector*, Phys. Rev. D, vol. 98, no. 5, 2018.

[203] The CMS Collaboration, *Measurements of the Higgs boson width and anomalous HVV couplings from on-shell and off-shell production in the four-lepton final state*, Phys. Rev. D, vol. 99, no. 11, 2019.

[204] The CMS Collaboration, *Constraints on anomalous HVV couplings from the production of Higgs bosons decaying to* τ *lepton pairs*, Phys. Rev. D, vol. 100, no. 11, 2019.

[205] F. Maltoni, E. Vryonidou, and C. Zhang, *Higgs production in association with a top-antitop pair in the Standard Model Effective Field Theory at NLO in QCD*, JHEP, vol. 2016, no. 10, 2016.

[206] C. Degrande *et al.*, *Probing top-Higgs non-standard interactions at the LHC*, JHEP, vol. 2012, no. 7, 2012.

[207] The ATLAS Collaboration, *Measurement of the Higgs boson decaying to b-quarks produced in association with a top-quark pair in pp collisions at* $\sqrt{s} = 13$ *TeV with the ATLAS detector*, no. ATLAS-CONF-2020-058, 2020.

[208] D. de Florian *et al.*, *Handbook of LHC Higgs Cross Sections: 4. Deciphering the Nature of the Higgs Sector*. No. CERN-2017-002, 2016.

[209] The ATLAS Collaboration, *Observation of Higgs boson production in association with a top quark pair at the LHC with the ATLAS detector*, PLB, vol. 784, pp. 173 – 191, 2018.

[210] The CMS Collaboration, *Observation of* $t\bar{t}H$ *Production*, Phys. Rev. Lett., vol. 120, p. 231801, 2018.

[211] The ATLAS Collaboration, *Observation of* $H \to b\bar{b}$ *decays and VH production with the ATLAS detector*, PLB, vol. 786, pp. 59 – 86, 2018.

[212] The CMS Collaboration, *Observation of Higgs Boson Decay to Bottom Quarks*, Phys. Rev. Lett., vol. 121, p. 121801, 2018.

[213] LHC Physics Group, *NNLO+NNLL top-quark-pair cross sections*. `https://twiki.cern.ch/twiki/bin/view/LHCPhysics/TtbarNNLO`. Accessed on 07-02-2020.

[214] The CMS Collaboration, *Measurement of the* $\mathrm{t\bar{t}b\bar{b}}$ *production cross section in the all-jet final state in pp collisions at* $\sqrt{s} = 13$ *TeV*, no. arXiv:1909.05306. CMS-TOP-18-011-003, 2019.

[215] The CMS Collaboration, *Measurement of the cross section for* $\mathrm{t\bar{t}}$ *production with additional jets and b jets in proton-proton collisions at* $\sqrt{s} = 13$ TeV, no. CMS-PAS-TOP-18-002, 2019.

[216] The CMS Collaboration, *Measurements of* $\mathrm{t\bar{t}}$ *cross sections in association with b jets and inclusive jets and their ratio using dilepton final states in pp collisions at* $\sqrt{s} = 13$ TeV, PLB, vol. 776, p. 355–378, 2018.

[217] J. Thaler and K. Van Tilburg, *Identifying boosted objects with N-subjettiness*, JHEP, vol. 2011, no. 3, 2011.

[218] A. J. Larkoski, G. P. Salam, and J. Thaler, *Energy correlation functions for jet substructure*, JHEP, vol. 2013, no. 6, 2013.

[219] The CMS Collaboration, *Search for massive resonances decaying into WW, WZ, ZZ, qW, and qZ with dijet final states at $\sqrt{s} = 13$ TeV*, Phys. Rev. D, vol. 97, p. 072006, 2018.

[220] The CMS Collaboration, *Measurement of the jet mass in highly boosted $\mathrm{t\bar{t}}$ events from pp collisions at $\sqrt{s} = 8$ TeV*, EPJC, vol. 77, no. 7, 2017.

[221] D. E. Soper and M. Spannowsky, *Finding top quarks with shower deconstruction*, Phys. Rev., vol. D87, p. 054012, 2013.

[222] D. E. Soper and M. Spannowsky, *Finding physics signals with event deconstruction*, Phys. Rev., vol. D89, no. 9, p. 094005, 2014.

[223] T. Lapsien, R. Kogler, and J. Haller, *A new tagger for hadronically decaying heavy particles at the LHC*, Eur. Phys. J., vol. C76, no. 11, p. 600, 2016.

[224] J. S. Conway *et al.*, *Identification of High-Momentum Top Quarks, Higgs Bosons, and W and Z Bosons Using Boosted Event Shapes*, Phys. Rev., vol. D94, no. 9, p. 094027, 2016.

[225] The CMS Collaboration, *A Cambridge-Aachen (C-A) based Jet Algorithm for boosted top-jet tagging*, no. CMS-PAS-JME-09-001, 2009.

[226] T. Plehn *et al.*, *Stop reconstruction with tagged tops*, JHEP, vol. 2010, no. 10, 2010.

[227] G. Kasieczka *et al.*, *Resonance Searches with an Updated Top Tagger*, JHEP, vol. 2015, no. 6, 2015.

[228] C. Anders *et al.*, *Benchmarking an even better top tagger algorithm*, Phys. Rev. D, vol. 89, no. 7, 2014.

[229] G. Kasieczka, *Search for Resonances Decaying into Top Quark Pairs Using Fully Hadronic Decays in pp Collisions with ATLAS at $\sqrt{s} = 7\,TEV$*. PhD thesis, Universität Heidelberg, 2013.

[230] The ATLAS Collaboration, *Identification of boosted Higgs bosons decaying into b-quark pairs with the ATLAS detector at 13 TeV*, Eur. Phys. J., vol. C79, no. 10, p. 836, 2019.

[231] The CMS Collaboration, *Identification of double-b quark jets in boosted event topologies*, no. CMS-PAS-BTV-15-002, 2016.

[232] The CMS Collaboration, *Performance of Deep Tagging Algorithms for Boosted Double Quark Jet Topology in Proton-Proton Collisions at 13 TeV with the Phase-0 CMS Detector*, no. CMS-DP-2018-046, 2018.

[233] G. Kasieczka *et al.*, *The Machine Learning landscape of top taggers*, SciPost Physics, vol. 7, no. 1, 2019.

[234] A. J. Larkoski *et al.*, *Soft drop*, JHEP, vol. 2014, no. 5, 2014.

[235] D. Krohn, J. Thaler, and L.-T. Wang, *Jet Trimming*, JHEP, vol. 02, p. 084, 2010.

[236] S. D. Ellis, C. K. Vermilion, and J. R. Walsh, *Techniques for improved heavy particle searches with jet substructure*, Phys. Rev. D, vol. 80, no. 5, 2009.

[237] The ATLAS Collaboration, *Performance of jet substructure techniques for large-R jets in proton-proton collisions at* $\sqrt{s} = 7$ *TeV using the ATLAS detector*, JHEP, vol. 2013, no. 9, 2013.

[238] T. Plehn, G. P. Salam, and M. Spannowsky, *Fat Jets for a Light Higgs*, Phys. Rev. Lett., vol. 104, p. 111801, 2010.

[239] K. Kondo, *Dynamical Likelihood Method for Reconstruction of Events with Missing Momentum. I. Method and Toy Models*, Journal of the Physical Society of Japan, vol. 57, no. 12, pp. 4126–4140, 1988.

[240] V. M. Abazov *et al.*, *A precision measurement of the mass of the top quark*, Nature, vol. 429, pp. 638–642, 2004.

[241] T. Aaltonen *et al.*, *Observation of Electroweak Single Top-Quark Production*, Phys. Rev. Lett., vol. 103, no. 9, 2009.

[242] The D0 Collaboration, *Evidence for production of single top quarks*, Phys. Rev. D, vol. 78, p. 012005, 2008.

[243] P. Artoisenet *et al.*, *Unravelling* $t\bar{t}h$ *via the Matrix Element Method*, Phys. Rev. Lett., vol. 111, no. 9, p. 091802, 2013.

[244] The ATLAS Collaboration, *Search for the Standard Model Higgs boson produced in association with top quarks and decaying into $b\bar{b}$ in pp collisions at $\sqrt{s}$= 8 TeV with the ATLAS detector*, EPJC, vol. 75, no. 7, 2015.

[245] J. Pata, *Search for the Production of the Higgs Boson in Association with a Top Quark Pair with CMS at $\sqrt{s}$ = 13 TeV*. PhD thesis, ETH Zürich, 2018.

[246] The ATLAS Collaboration, *A new tagger for the charge identification of b-jets*, no. ATL-PHYS-PUB-2015-040, 2015.

[247] M. Meinhard, *Reconstruction of $t\bar{t}H$, $H \to b\bar{b}$ events using the matrix element method and substructure techniques*, no. arXiv:1812.08458, 2018.

[248] P. M. Nadolsky *et al.*, *Implications of CTEQ global analysis for collider observables*, Phys. Rev. D, vol. 78, no. 1, 2008.

[249] A. Buckley *et al.*, *LHAPDF6: parton density access in the LHC precision era*, EPJC, vol. 75, no. 3, 2015.

[250] G. P. Lepage, *A new algorithm for adaptive multidimensional integration*, Journal of Computational Physics, vol. 27, no. 2, pp. 192 – 203, 1978.

[251] T. Hahn, *Cuba - a library for multidimensional numerical integration*, Computer Physics Communications, vol. 168, no. 2, p. 78–95, 2005.

[252] The NNPDF Collaboration and others, *Parton distributions from high-precision collider data*, no. arXiv:1706.00428, 2017.

[253] The CMS Collaboration, *Extraction and validation of a new set of CMS pythia8 tunes from underlying-event measurements*, EPJC, vol. 80, no. 1, 2020.

[254] J. Allison *et al.*, *Recent developments in Geant4*, Nucl. Instrum. Methods Phys. Res. A, vol. 835, pp. 186 – 225, 2016.

[255] LHC Physics Group, *NNLO single-top channel cross sections*. `https://twiki.cern.ch/twiki/bin/view/LHCPhysics/SingleTopRefXsec`. Accessed on 09-02-2020.

[256] A. Kulesza *et al.*, *Associated production of a top quark pair with a heavy electroweak gauge boson at NLO+NNLL accuracy*, EPJC, vol. 79, no. 3, 2019.

[257] LHC Physics Group, *Standard Model Cross Sections for CMS at 13 TeV*. https://twiki.cern.ch/twiki/bin/viewauth/CMS/StandardModelCrossSectionsat13TeV. Accessed on 09-02-2020.

[258] D. Morse, S. Cooper, and K. Long, *Corrected Cross Sections for Binned V+jet Samples*. https://indico.cern.ch/event/673253/#2-corrected-cross-sections-for, 2017. Accessed on 09-02-2020.

[259] The CMS Collaboration, *Performance of CMS Muon Reconstruction in pp Collision Events at $\sqrt{s} = 7$ TeV*, JINST, vol. 7, no. 10, p. P10002, 2012.

[260] The CMS Collaboration, *Search for neutral Higgs bosons decaying to tau pairs in pp collisions at s =7 TeV*, PLB, vol. 713, no. 2, pp. 68 – 90, 2012.

[261] The CMS Collaboration, *Performance of electron reconstruction and selection with the CMS detector in proton-proton collisions at s= 8 TeV*, JINST, vol. 10, no. 06, p. P06005, 2015.

[262] The CMS Collaboration, *Determination of jet energy calibration and transverse momentum resolution in CMS*, JINST, vol. 6, no. 11, p. P11002, 2011.

[263] The CMS Collaboration, *Calculation of Residual Energy Correction for b Jets Using Z+b Events in 8 TeV pp Collisions*, no. CMS-PAS-JME-13-001, 2014.

[264] The CMS Collaboration, *Jet identification in high pile-up environment (PileupJetID)*. https://twiki.cern.ch/twiki/bin/viewauth/CMS/PileupJetID#Information_for_13_TeV_data_anal. "Accessed on 30-1-2020".

[265] The CMS Collaboration, *Jet algorithms performance in 13 TeV data*, no. CMS-PAS-JME-16-003, 2017.

[266] F. Pedregosa *et al.*, *Scikit-learn: Machine Learning in Python*, Journal of Machine Learning Research, vol. 12, pp. 2825–2830, 2011.

[267] The CMS Collaboration, *Reference muon ID, isolation and trigger efficiencies for 2017 data*. https://twiki.cern.ch/twiki/bin/view/CMS/MuonReferenceEffs2017. "Accessed on 22-7-2020".

[268] The CMS Collaboration, *Heavy flavour tagging for 13 TeV data in 2017 and 94X MC*. //https://twiki.cern.ch/twiki/bin/viewauth/CMS/BtagRecommendation94X. "Accessed on 22-7-2020".

[269] The CMS Collaboration, *Reweighting recipe to emulate Level 1 ECAL prefiring*. `https://twiki.cern.ch/twiki/bin/viewauth/CMS/L1ECALPrefiringWeightRecipe`. Accessed on 15-07-2020.

[270] R. Barlow and C. Beeston, *Fitting using finite Monte Carlo samples*, Computer Physics Communications, vol. 77, no. 2, pp. 219 – 228, 1993.

[271] The CMS Collaboration, *CMS luminosity measurement for the 2017 data-taking period at* $\sqrt{s}$ *= 13 TeV* . `//http://cms-results.web.cern.ch/cms-results/public-results/preliminary-results/LUM-17-004/index.html`. "Accessed on 23-7-2020".

[272] The CMS Collaboration, *Utilities for Accessing Pileup Information for Data*. `//https://twiki.cern.ch/twiki/bin/viewauth/CMS/PileupJSONFileforData#Recommended_cross_section`. "Accessed on 23-7-2020".

[273] The CMS Collaboration, *Jet energy scale uncertainty sources*. `//https://twiki.cern.ch/twiki/bin/view/CMS/JECUncertaintySources#Main_uncertainties_2017_94X`. "Accessed on 23-7-2020".

[274] G. Cowan *et al.*, *Asymptotic formulae for likelihood-based tests of new physics*, EPJC, vol. 71, no. 2, 2011.

[275] A. Wald, *Tests of Statistical Hypotheses Concerning Several Parameters When the Number of Observations is Large*, Transactions of the American Mathematical Society, vol. 54, no. 3, pp. 426–482, 1943.

[276] R. J. Barlow, *Statistics: a guide to the use of statistical methods in the physical sciences*. Manchester physics series, Chichester: Wiley, 1989.

[277] G. Cowan, *Statistical data analysis*. Oxford Science Publications, 1998.

[278] The CMS Collaboration, *Measurement of* $\mathrm{t\bar{t}H}$ *and tH in the* $\mathrm{H \to b\bar{b}}$ *channel with the full Run 2 data sample*, To be published.

[279] The CMS Collaboration, *Measurement of the* $\mathrm{t\bar{t}b\bar{b}}$ *production cross section in the all-jet final state in* pp *collisions at* $\sqrt{s} = 13$ TeV, no. CMS-PAS-TOP-18-011, 2019.

[280] The ATLAS Collaboration, *Measurements of inclusive and differential fiducial cross-sections of* $\mathrm{t\bar{t}}$ *production with additional heavy-flavour jets in proton-proton collisions at* $\sqrt{s} = 13$ TeV *with the ATLAS detector*, JHEP, vol. 2019, no. 4, 2019.

[281] T. Ježo *et al.*, *New NLOPS predictions for* $\mathrm{t\bar{t}} + b$*-jet production at the LHC*, EPJC, vol. 78, no. 6, 2018.

Acknowledgements

I would like to thank Professor Rainer Wallny for accepting me as a PhD student in his group, and for his valuable guidance throughout the course of my thesis. Special thanks also go to Professor Günther Dissertori for sharing his profound knowledge of particle physics, for accepting to serve as co-referee for my PhD defense, and for entrusting me with the organisation of the exercises classes and the exam of his lecture.

Dr. Mauro Donegà's support and supervision were invaluable, as his oversight over my status and progress enabled me to complete this thesis. I am particularly grateful to Professor Gregor Kasieczka and Dr. Joosep Pata for introducing me to the $t\bar{t}H$, $H \to b\bar{b}$ analysis, and for readily answering my questions, even after their time at ETH. Furthermore, I am profoundly indebted to Dr. Alessandro Calandri for sharing his deep expertise in b tagging, for guiding me through the last months of my PhD, as well as for helping with the endorsement of my thesis results. Dr. Malte Backhaus also deserves my gratitude for his advice on many hardware-related issues I came across over the years. Thanks also go to Dr. Andrey Starodumov for initiating the irradiation campaign of the readout chips, which provided the main results of the hardware section of my thesis.

Dear Gregor, Malte, and Mauro: I truly appreciate all of your comments on the various drafts of my thesis — alongside with improving the quality of the work I've learned so much from your valuable feedback!

I am also infinitely grateful to Christina Reißel for joining me in this endeavour for the past three years. She has not only been the best colleague one could possibly hope for, but also became a true and fantastic friend.

This work would not have been possible in such good conditions without the assistance of the technical and administrative staff at IPA. Thank you Rosa, Caroline, Gabriela, Gabriele, Bettina, Jennifer, Bruno, Patrick and Robert!

My time at ETH has been accompanied by lots of ups and downs (b tagging scale factors - I'm talking about you!), but the ups are the ones I will remember for the rest of my life. In particular, I truly appreciated the fantastic atmosphere of our

group on the E floor in HPK which I have Christina, Pirmin, Daniele, Jan^2, Lukas, Franz, David, Gianluca, Marie, Simon, Luca, Alessandro, Kaustuv, Krunal, Gaël, Diego, Micha, Christian^2, Malte, Bane, Mauro, Gregor, Joosep, Maria Giulia, Anne-Mazarine, Alejandro, Felix, Parisa and Pascal (in random order, apologies to those whom I might have forgotten) to thank for. I will miss all of you! Our occasional group dinners, hikes, floating trips down the Limmat, barbecues, birthday cakes, SOLA runs and others contributed to making me feel at home here in Zürich. Even on the toughest days, knowing that I would be meeting all of you for lunch gave me the motivation to come to work in the morning. It also meant a lot to me that some of you came to see me at one of my concerts, and the second day of the week will always be Superkondituesday!

Last but not least, I am beyond grateful to my entire family, my boyfriend and my friends. You not only ignited my interest in science and motivated me to study physics, but also supported me these past years. I would not have had the strength to finish this thesis if it wasn't for you!